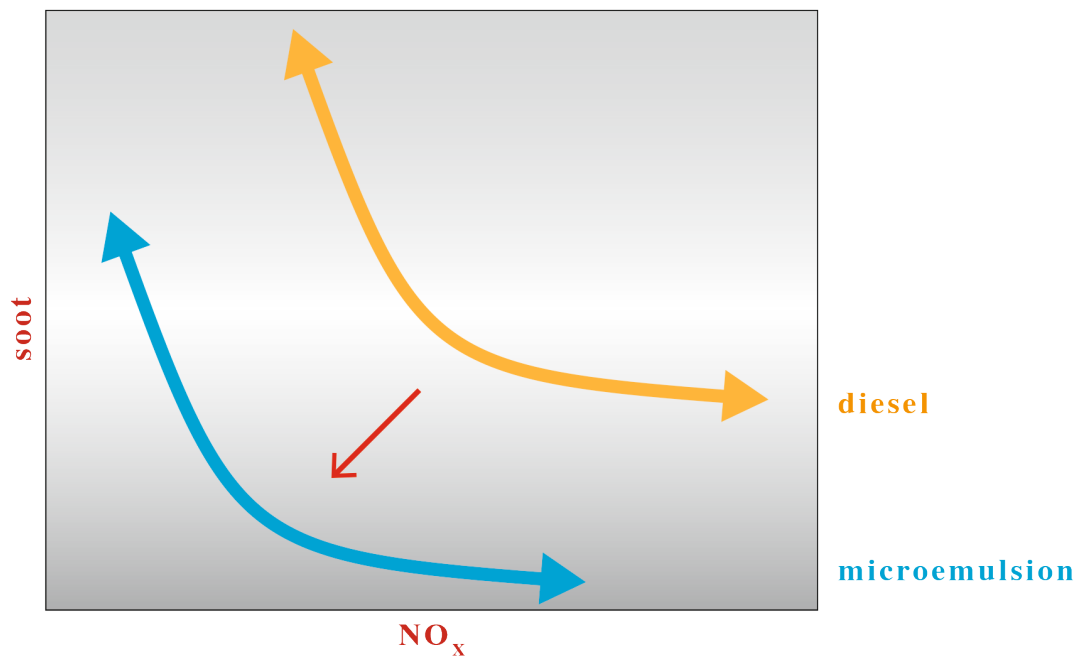


“Green” Microemulsions and Nanoemulsions as Alternative Fuels

Setareh Maleknia



Cuvillier Verlag Göttingen
Internationaler wissenschaftlicher Fachverlag



“Green” Microemulsions and Nanoemulsions as Alternative Fuels





“Green” Microemulsions and Nanoemulsions as Alternative Fuels

Inaugural-Dissertation

zur

Erlangung des Doktorgrades

der Mathematisch-Naturwissenschaftlichen Fakultät

der Universität

zu Köln

vorgelegt von

Setareh Maleknia

aus Teheran (Iran)

Köln

März 2014



Bibliografische Information der Deutschen Nationalbibliothek

Die Deutsche Nationalbibliothek verzeichnet diese Publikation in der Deutschen Nationalbibliografie; detaillierte bibliografische Daten sind im Internet über <http://dnb.d-nb.de> abrufbar.

1. Aufl. - Göttingen : Cuvillier, 2014

Zugl.: Köln, Univ., Diss., 2014

Berichterstatter:

Prof. Dr. Reinhard Strey

Prof. Dr. Christof Simon

Tag der mündlichen Prüfung: 21.05.2014

© CUVILLIER VERLAG, Göttingen 2014

Nonnenstieg 8, 37075 Göttingen

Telefon: 0551-54724-0

Telefax: 0551-54724-21

www.cuvillier.de

Alle Rechte vorbehalten. Ohne ausdrückliche Genehmigung des Verlages ist es nicht gestattet, das Buch oder Teile daraus auf fotomechanischem Weg (Fotokopie, Mikrokopie) zu vervielfältigen.

1. Auflage, 2014

Gedruckt auf umweltfreundlichem, säurefreiem Papier aus nachhaltiger Forstwirtschaft.

ISBN 978-3-95404-912-7

eISBN 978-3-7369-4912-6



Meiner lieben Familie



Kurzzusammenfassung

Die Verbrennung von wasserhaltigen Diesel-Kraftstoffen bewirkt eine simultane Reduktion der Ruß- sowie der NO_x-Emissionen, d.h. sie vermeiden partiell den sogenannten *Ruß-NO_x trade-off*. Bereits 2003 wurden von *Nawrath et al.* die Vorteile der Anwendung von mikroemulgierten Kraftstoffen zum Patent angemeldet [DE 10334897A13]. Im Rahmen dieser Arbeit wurden neue, temperaturinvariante, hoch effiziente Kraftstoff-Mikroemulsionen des Typs Wasser/Gefrierschutzmittel - Dieseldieselkraftstoff - Ölsäure/Monoethanolamin/Ölsäure-diethanolamid mit Wasseranteilen von bis zu 24 Gew.% formuliert, die geeignete physikalische Eigenschaften für die kommerzielle Anwendung aufweisen. Die Struktur dieser Wasser-in-Kraftstoff Mikroemulsionen wurde mittels Kleinwinkelneutronenstreuung (SANS) und dynamischer Lichtstreuung (DLS) untersucht. Im Hinblick auf eine Mikroemulgierung kurz vor der Einspritzung wurde die Bildungskinetik von mikroemulgierten Kraftstoffen bei einer Variation des Wassergehaltes und der Temperatur mittels Durchlicht in einer Stopped-Flow Basiseinheit aufgezeichnet. Es stellte sich heraus, dass sich die Mikroemulsionen unter annähernd realen Verbrennungsbedingungen aufgrund von höheren Temperatur- und Druckbedingungen sogar schneller bilden. Unerwarteterweise wurden bei den Untersuchungen der Mikroemulsions-Formulierungen neuartige Wasser-in-Kraftstoff Nanoemulsionen (< 200 nm) erzielt, die eine erhebliche Reduzierung des Tensidgehaltes aufweisen; ein interessanter ökonomischer Aspekt. Beide untersuchten Kraftstoff-Klassen eignen sich für ein betriebspunktabhängiges „On Injector“-Blending von Wasser (einschließlich Anti-Korrosions Additiv und Schmiermittel) und Diesel (einschließlich Tensid-Mischung), sie mischen sich innerhalb von Millisekunden in der dem Hauptinjektor vorgeschalteten Mischkammer. Dieses Verfahren vermeidet zusätzlich die Kontaminierung des Einspritzsystems mit Wasser, da nur solche Wassermengen zugeführt werden, welche sofort eingespritzt werden. Abgasemissionen, Ruß-Struktur und -Größenverteilung von wasserhaltigen Kraftstoffen wurden im Vergleich zu purem Dieseldieselkraftstoff analysiert. Die Ergebnisse zeigen, dass die Anwendung von betriebspunktabhängigen wasserhaltigen Kraftstoffen zu einer drastischen Reduktion des Rußes von bis zu 98 % (FSN) sowie der Stickoxide von bis zu 62 % führt.

Abstract

Combustion of water-containing diesel fuels results in a simultaneous reduction of soot and NO_x-emissions, i.e. they partially avoid the so-called *soot-NO_x trade-off*. Already in 2003 *Nawrath et al.* advertised in a patent application [DE 10334897A13] the advantageous application of microemulsified fuels. In the frame of the present work new temperature invariant, highly efficient fuel microemulsions of the type water/antifreeze - diesel fuel - oleic acid/monoethanolamine/oleic acid diethanolamide containing up to 24 wt.% water with appropriate physical characteristics for commercial applications were formulated. The structure of these water-in-fuel microemulsions was studied using small angle neutron scattering (SANS) and dynamic light scattering (DLS). Aiming for microemulsification right before injection, the formation kinetics of microemulsified fuels varying the water content and the temperature was recorded via transmitted light in a stopped-flow system. It turned out that microemulsions form even faster approaching combustion conditions, because of high temperature and pressure conditions. As unexpected reward of the investigations on formulation of microemulsion fuels, novel water-in-fuel nanoemulsions (< 200 nm) were obtained featuring substantial reduction of surfactant content, an interesting economical aspect. Both investigated fuel classes are suitable for load point dependent “on injector”-blending of water (including anti-corrosion agent and lubricant) and diesel (including surfactant-blend) which are mixed within milliseconds in the mixing chamber from the upstream main injector. This procedure in addition avoids contamination of the injection system with water, as only those amounts of water are added that are immediately injected. Exhaust gas emissions, soot-structure and size distribution of water containing fuels compared to pure diesel fuel were analysed. The results show that using load-dependent water containing fuels yield a drastic reduction of soot up to 98 % (FSN) as well as nitrogen oxide emissions up to 62 %.

Acknowledgment

Die vorliegende Arbeit entstand im Zeitraum von Februar 2011 bis März 2014 am Institut für Physikalische Chemie der Universität zu Köln unter der wissenschaftlichen Leitung von Herrn *Prof. Dr. Reinhard Strey*. Ich danke ihm, dass ich in seiner Arbeitsgruppe dieses interessante, fachübergreifende und spannende Thema bearbeiten durfte. Weiterhin möchte ich ihm für die Unterstützung meiner Arbeit und für die große Diskussionsbereitschaft danken, wie auch das Vertrauen in der Bearbeitung des zweijährigen Forschungsprojektes. Für den Freiraum, den er mir bei der Forschung des innovativen Themas gegeben hat, bin ich sehr dankbar.

Innerhalb des Projektes kam es zur Zusammenarbeit mit der Hochschule Trier unter der wissenschaftlichen Leitung von Herrn *Prof. Dr. Christof Simon*. An dieser Stelle danke ich für die Übernahme des Zweitgutachtens und der netten Kooperation während meiner Arbeit. Zusätzlich möchte ich mich für sein großes Interesse an meinen Untersuchungen danken.

Herrn *Prof. Dr. Gerd Meyer* danke ich für die Übernahme des Prüfungsvorsitzes.

Für die Durchsicht und Korrektur der Arbeit möchte ich *Dipl.Chem. Dirk Steidung* und *M. Sc. Sascha Dauwe*, sowie *Dr. Helge Klemmer* danken. Bei Helge möchte ich mich außerdem dafür bedanken, dass er mich auch in die Stopped-Flow Anlage eingewiesen hat und immer hilfsbereit war, falls kleine oder größere Fragen zu lösen waren. Für die effektive, lustige und auch nette Arbeitszeit im Labor sind meine Laborkollegen *Dr. Lars Menger*, *Dipl. Chem. Dirk Steidung* und *M. Sc. Sascha Dauwe* mit verantwortlich.

Dipl.-Ing. (FH) M. Eng. Heinrich Dörksen und *Dipl.-Ing. Peter Dittmann* danke ich für die nette Zusammenarbeit innerhalb des zweijährigen Projektes. Beide standen mir zur Seite als Fragen bezüglich der motortechnischen Seite aufkamen.

Bei *Dipl.Chem. Silke Quester* möchte ich mich für die schönen REM-Bilder bedanken.

Dipl.Chem. Anna Klemmer war immer hilfsbereit und immer offen für Fragen, die Sie schließlich zusammen mit mir immer beantwortet hat.



Mit *Dipl.Chem. Nadja Wulff* habe ich mein ganzes Studium durchlebt! Du warst privat als auch in der Uni immer für mich da. Deinem Mann *Dr. Pascal Wulff* danke ich, dass er mich in die Thematik der Mikroemulsionen eingewiesen hat.

M. Sc. Carola Harbauer, M. Sc. Yvonne Pütz und *Dr. Helge Klemmer* danke ich für die Hilfestellung bei der Auswertung der SANS-Daten, wie auch bei der Durchführung der Messungen in München.

Dr. Lada Bemert danke ich, dass sie dieses Projekt, welches ich während meiner Promotionszeits bearbeiten durfte, ins Leben gerufen hat.

M. Sc. Richard Meisenheimer, Yaseen Qawasmi und *Felicitas Bröhl* danke ich für die tatkräftige Unterstützung bei der Formulierung und Charakterisierung von Wasser-Diesel Mikroemulsionen.

Jerome Gonzales hat mir bei Grafik-Fragen weitergeholfen und war stets hilfsbereit. Meinen Freundinnen und meinem Freund *Dennis* danke ich, dass sie mir abwechslungsreiche Wochenenden im Ausgleich zu den langen Labortagen gebracht haben.

Dem Arbeitskreis von *Prof. Dr. Reinhard Strey* möchte ich mich für die stets tolle Arbeitsatmosphäre während meiner Diplom- als auch Promotionszeit bedanken.

Der Firma *Wall-Chemie, Frank Zimmermann* und *Dipl. Chem. Jürgen Hedtfeld* danke ich für die Bereitstellung der Tenside und der kooperativen Zusammenarbeit innerhalb des Forschungsprojektes.

Ein großer Dank gilt auch der feinmechanischen Werkstatt unter der Leitung von *Herbert Metzner*.

Der FVV danke ich für die finanzielle Unterstützung, wie auch den Kooperationspartnern, *HS Trier* und *VKA Aachen* für die erfolgreiche und konstruktive Zusammenarbeit.

Ein besonderer Dank geht an meine ganze Familie, die mich während der Zeit meiner wissenschaftlichen Tätigkeit unterstützt und motiviert hat. Ich liebe Euch und bin glücklich Euch zu haben! Meiner Mami gilt ein ganz besonderer Dank!!



Content

1	Introduction	1
1.1	Motivation	2
1.2	Water containing fuels	5
1.3	Task description	7
2	Fundamentals	9
2.1	Microemulsions	9
2.1.1	Phase behaviour	10
2.1.2	Phase prism	11
2.1.3	$T(\gamma)$ -section	12
2.1.4	Efficiency	15
2.1.5	Technical grade surfactant	17
2.1.6	Temperature invariance	18
2.1.7	High pressure phase behaviour	19
2.1.8	Trajectory of the middle phase	20
2.1.9	Additives	21
2.1.10	Amphiphilic film	22
2.1.11	Compounds	25
2.2	Emulsions	28
2.2.1	Types of emulsions	29
2.2.2	Emulsification methods	30
2.2.3	Compounds	34
2.3	Microstructure and formation kinetics	37
2.3.1	Dynamic light scattering	37
2.3.2	Small angle neutron scattering	39
2.3.3	Formation kinetics	40
2.4	Combustion parameters	42
2.4.1	Diesel injection	46
2.4.2	Diesel spray atomisation	49
2.4.3	Internal combustion emissions	50
2.4.4	Aftertreatment	56



3	Water Containing Fuels.....	61
3.1	Water fuel microemulsions	61
3.1.1	Influence of n -variation on the phase behaviour	62
3.1.2	Influence of δ -variation on the phase behaviour	64
3.1.3	Influence of ε -variation on the phase behaviour	66
3.1.4	Influence of ψ -variation on the phase behaviour	69
3.1.5	Influence of α -variation on the phase behaviour	71
3.1.6	Optimised systems	74
3.2	Physical properties	80
3.3	Microstructure	90
3.3.1	DLS-measurements	90
3.3.2	SANS-measurements	92
3.4	Stopped-flow measurement	95
3.5	Water fuel nanoemulsions	100
3.5.1	Aqueous phase	100
3.5.2	Dynamic light scattering	103
4	Combustion Results	109
4.1	On injector-blending	109
4.2	Microemulsion combustions experiments	112
4.2.1	NO _x -emissions	113
4.2.2	Filter smoke number (FSN) and opacity	114
4.2.3	Particulate mass	116
4.2.4	Number of particle	117
4.2.5	Particulate matter composition	119
4.2.6	Unburnt hydrocarbons	120
4.2.7	Carbon monoxide and carbon dioxide	121
4.2.8	Spray behaviour	122
4.3	Nanoemulsion combustion experiments	127
4.3.1	NO _x -emissions	127
4.3.2	Filter smoke number (FSN) and opacity	129
4.3.3	Unburnt hydrocarbons	130



4.3.4	Carbon monoxide and carbon dioxide	131
4.3.5	Scanning electron microscope (SEM)	132
4.4	Comparison of microemulsions and nanoemulsions	143
4.4.1	NO _x -emissions	143
4.4.2	Filter smoke number (FSN) and opacity	144
5	Summary	147
6	Experimental Section	151
6.1	Chemicals	151
6.2	Measuring methods	152
7	Appendix	169
7.1	X-points and utilisable efficiency	169
7.1.1	Diesel fuel microemulsion	169
7.2	Physical properties	172
7.3	DLS-measurements	173
7.4	Combustion measurements	175
7.5	Corrosion-test	178
7.6	Scanning electron microscopy	179
7.7	Abbreviations and Symbols	181
7.8	Literature	186





1 INTRODUCTION

The most efficient power source among all known types of internal combustion engines is the direct injected diesel engine. Due to its high efficiency, low fuel consumption and longevity, the diesel engine, invented by *Dr. Rudolph Diesel* in the 1890s [1], is also the most common drive system.

However, internal combustion engines are significant contributors to air pollution, which negatively influences human health and the environment [2-4] and are known as a contributor to global warming [5, 6]. Growing concerns about emission of nitrogen oxides (NO_x) and especially diesel particulates lead to a substantial urgency to reduce exhaust gas emissions from diesel engines in terms of a sustainable climate policy. The European Union (EU) aims to introduce stricter limits on pollutant emissions from light road vehicles since 1992 with the EURO I to EURO VI (Sept. 2014) stages [7] and will legislate even stricter terms in the years to come. The necessity of such jurisdiction dates back to the late nineteenth century, in which the demand for crude oil started to accelerate with the invention of the internal combustion engine and became one of the most essential commodities traded worldwide.

Petroleum liquids are non-renewable resources, thus *Hubbert* has developed a method to forecast future production of crude oil. In 1956, *Hubbert* hypothesised that the world oil production follows a “bell-shaped” curve and has already reached its peak in 1970 in the United States [8]. His model gained worldwide popularity and was used to forecast oil production worldwide with a peak before 2010 [9-12]. Henceforth, not only exhaust gas emissions, but also fuel consumption, have been drastically reduced due to a conscious handling of non-renewable resources [13,14].

Besides limited availability due to decreasing fossil resources and growing energy consumption, the pollutant emission represents another problem of fossil fuel. Application of renewable biofuels can overcome both of these problems. Alternative fuels are not from petroleum origin and have a respectively high heating value [15]. 1st generation of alternative fuels such as fatty acid methyl ester (FAME) are based on grain crops, such as rape-seed, grain and maize. The 2nd generation of biogenic fuels is based on biogenic energy such as GtL (Gas-to-Liquid) or BtL (Biomass-to-Liquid). The conversion of coal, natural gas and biomass into liquid hydrocarbons is accessible by the well-known *Fischer-Tropsch* synthesis [16]. Biofuels are already available on the market in the form of bioethanol for gasoline engines and FAME for diesel engines. Small amounts of these components (up to 10 %) are used for

blending in gasoline and diesel with an advantage that no modification of the fuel system is necessary [17].

A further approach to overcome the depletion of fossil fuels is to use electric, hybrid electric and fuel-cell powered drive train technologies which are the most promising vehicle solutions in the future. Hybrid technology is commercially available since 1997 and the sales figures are expected to rise considerably until 2023 [18]. Hybrid vehicles add a parallel electric motor with the combination of batteries in the combustion engine. In order to replace combustion engines entirely, fundamental problems like an efficient storage capacity, durability and its lower power output have to be solved [19].

1.1 Motivation

The combustion products of diesel fuel under ideal conditions (complete combustion) are water and carbon dioxide. Residues of incomplete combustion are mainly carbon monoxide, nitrogen oxides, unburnt hydrocarbons and particulate matter. Due to several factors influencing the combustion as the fuel/air ratio of the fuel spray, the short time available for the mixture formation, the temperature during combustion and the increased penetration depth, inefficient combustion with increased emissions is observed.

Development of advanced after-treatments systems and other internal engine modifications has been motivated by the growing interest in reducing the formation of pollutant during combustion. In-cylinder emission control technology and combustion optimisation are the key to reduce emissions and fuel consumption. Suitable combustion chamber geometry [20], favourable fuel injection pressure [21] or optimal fuel/air ratio [22] improve combustion. Another option to achieve maximum power with minimal consumption and exhaust emission lies in the optimisation of the fuel itself. Physical properties of the fuel (*e.g.* viscosity, density and surface tension) affect the evaporation behaviour and the fuel atomisation [23,24]. Due to a changed fuel composition by adding cetane improver or oxygenates [25-27] soot- or NO_x -emissions are reduced. The advantage of a modified fuel composition is not only the reduction of exhaust emissions, but also a decline in CO_2 -emission due to the use of biogenic blends: renewable raw materials are characterised by their CO_2 -neutral combustion and can therefore be subtracted from the balance [28, 29].

The main pollutants from diesel engines are soot and nitrogen oxides (NO_x). The so-called *soot- NO_x trade-off* describes the contradictory formation of soot and NO_x in the combustion chamber of diesel engines. A simultaneously reduction of both emissions is very difficult as by rising the combustion temperature, the emission of soot declines while the emission of

NO_x increases. In contrast, the emission of NO_x is reduced at the expense of an increased soot-formation at lower combustion temperatures.

One promising, economically efficient and simple way to reduce the emissions and improve the fuel conversion efficiency of diesel engines is the addition of water into the combustion chamber. A number of potential benefits are offered in the combustion of water containing fuel. One effect is based on the volatility difference between water and fuel, which can lead to the so-called microexplosions. The microexplosions of the primary droplet are followed by the secondary atomization producing a number of fine-sized secondary droplets which consequently enhances the fuel/air ratio in the combustion and reduces the flame temperature. Hence, the formation of *Zeldovich* NO is suppressed and an improved combustion efficiency is observed [30]. Due to a changed chemical reaction mechanism by applying water into fuel, a further positive effect is observed. At higher temperatures ($> 2000 \text{ K}$) water causes an increased concentration of radicals ($\cdot\text{OH}$, $\cdot\text{O}$, $\cdot\text{O}_2\text{H}$) in the combustion chamber, leading to an effective oxidation of soot precursors (C_2H_2 , C_2H_4 and unburnt hydrocarbons) [31].

The combination of both effects includes the potential benefit to reduce both hazardous emissions while avoiding the *soot- NO_x trade-off*. Water can be introduced into the combustion chamber in various ways. The University of Applied Science in Trier developed a stratified injection of water and different blending systems in order to improve the response time [32,33]. The recent generated *in injector*-blending allows the generation of appropriate water/fuel-mixing ratios with an even reduced response time due to direct injection of water into the fuel-channel of the injector [34]. The addition of water may also happen in the form of microemulsions or nanoemulsions. Due to finer dispersed water droplets during combustion, an increased positive effect occurs [35]. Ordinary emulsions and microemulsions differ mainly in their thermodynamic stability and surfactant concentration. Thermodynamically stable microemulsions are translucent in appearance and show a homogenous, nanoscale structure of order 10 nm. Thermodynamically unstable emulsions appear white because of their droplet sizes of order 1 μm [36,37]. Generally, more surfactant is required to formulate thermodynamically stable microemulsions (including ultralow interfacial tension [38]) and is thus favoured regarding storage due to its long-term stability. A relatively new, special kind of emulsions can appear transparent with droplet sizes of order 100 nm. They are called nanoemulsions and, interestingly, require a reduced amount of surfactant compared to thermodynamically stable microemulsions.

Both types show different combustion characteristics even if the initial water content is the same [35]. This effect is based upon different size distribution of the dispersed water droplets in a fuel droplet as schematically shown in figure 1-1.

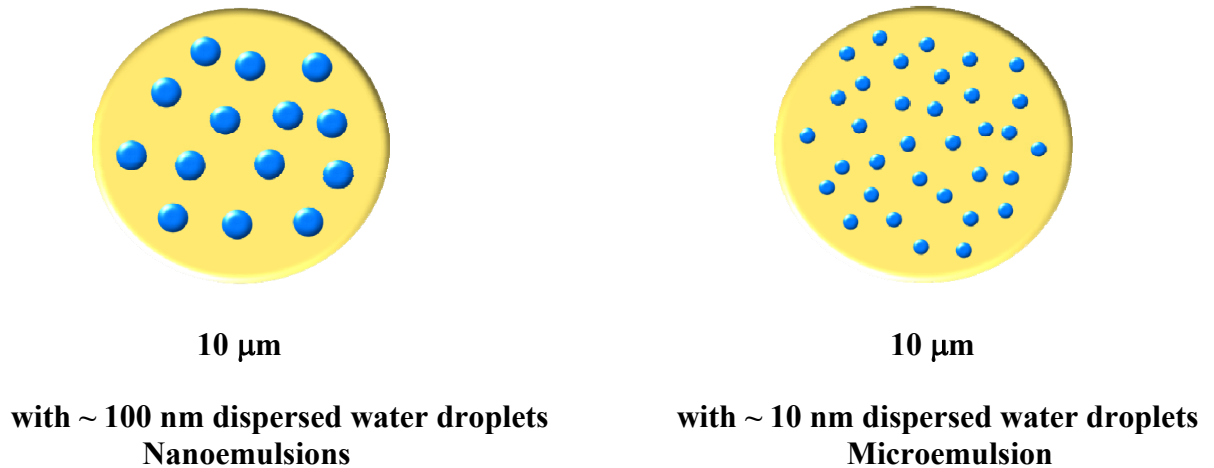


Figure 1-1: Schematic illustration of the dispersed water droplets inside a typical fuel droplet of the spray. Nanoemulsions feature larger-scaled dispersed water droplets (~ 100 nm) with a lower number density of water droplets in a fuel droplet (left). Smaller-scaled size distribution of the dispersed water droplets (~ 10 nm) are generated by microemulsions with a accordingly higher number density of water droplets in a fuel droplet (right).

The evaporation of the water droplets in water containing fuels may be accompanied by microexplosions which are not observed in the combustion of pure diesel droplet. Due to volatility difference between the water and the fuel, this phenomenon depends on the size of the dispersed water droplets [39].

1.2 Water containing fuels

The first investigation on water containing fuels started in the 1940s by the NACA during the Second World War by spraying a mixture of water/ethanol/methanol into the air intake of aircraft engines in order to cool the engines while decreasing the combustion temperature [40].

Cornet and *Nero* published in 1954 the systematic investigations of emulsified diesel fuel and observed an improved efficiency with a simultaneous slight reduction of fuel specific consumption [41]. *Feuermann* formulated and patented the first gasoline-water emulsion in 1979 by mixing gasoline, water and non-ionic surfactants and observed a reduction of pollutants during combustion [42]. *Velji et al.* showed a reduction of NO_x -, CO- and soot-emissions by increasing the water content [43]. *Kadota et al.* studied the microexplosion phenomena during combustion while using water fuel emulsions [30]. A lowered combustion temperature was observed which leads to a reduced NO_x -emission. 2005 *Mathis et al.* studied the influence of water on primary soot particle diameter and particle number size distribution in the exhaust of a diesel engine. The diameter of soot particles from the water-diesel emulsion were determined using scanning electron microscopy and were slighter larger than from diesel fuel [44]. The investigations described were related to emulsion-fuels which contained a small proportion of surface active agents in order to provide a kinetically stable mixture.

Despite decades of research activity indicating positive results, and the intense need to improve emissions due to tightening regulatory requirements, no widespread application of water-in-fuel emulsions exists today. AquazoleTM (Lubrizol Corp.) and PuriNOxTM (Elf Aquitaine) water-in-diesel emulsion formulations were commercially available in the mid-2000's, but eventually removed from the market [45]. Most likely the inherent limited stability of emulsions and corrosion effects in the fuel injection system critically hampers application of water-in-fuel emulsions.

Microemulsions containing gasoline, kerosene, diesel and fuel oil with water-soluble additives and surfactant-blends of fatty acid derivatives, poly-alkanolamine, sorbitan esters and nonylphenol were patented in 1975 by *McCoy* [46]. *Schwab et al.* formulated cryogenic stable water-diesel fuel microemulsion with a combination of dimethylethanolamine and long-chained fatty acids as surfactants [47]. Additionally, investigations on vegetable oil-microemulsions for use in internal combustion engines were studied in 1984 and 1985 [48-50]. *Huzbun et al.* reported the use of microemulsions in 1986 containing 7 wt.% water, tertiary butyl alcohol as major component and a blend of ionic- and non-ionic surfactants [51].

In 2006, *Davis* studied water-in-fuel microemulsions based on fatty acid amines and observed water domains below 0.1 μm [52].

A wide variety of investigations on microemulsions as fuel were studied in the group of *Prof. Strey*. Temperature invariant microemulsions containing water (up to 45 wt.%), diesel fuel and a blend of ionic- and non-ionic surfactants were formulated by *Nawrath* and *Rottländer* [53, 54]. The potential benefit using water-fuel microemulsions while reducing both the soot- and NO_x -emission was patented by *Strey*, *Nawrath* and *Sottmann* in 2003 with the title “Microemulsions and their use as fuel” [55]. This patent claims the use of the bicontinuous area in fuel-microemulsions which represents the state with a minimum amount of surfactant forming a single phase microemulsion and an ultra-low interfacial tension. *Bemert* published her dissertation in 2008 with a systematically investigation of the influence of different types of surfactants and additives on the phase behaviour. Combustion experiments showed the positive effect on pollutant emissions while applying water containing fuels [56]. *Lif et al.* compared microemulsions and emulsions in terms of emissions and spray behaviour. Both systems represent a promising approach to reduce emissions of NO_x and particulate matter [57-59]. *Wulff*'s work is also an evidence for overcoming the *soot- NO_x trade-off* [60]. *Menger* has recently studied the microemulsified fuels under nearly realistic conditions using the test vehicle of the workgroup of *Prof. Strey*. A reduction of toxic emissions over all loads was concluded to require an adjustment of water content on the engine map and through an on-demand water admixing [61].

Industry shows interest in water containing fuels. In 2006, the *Rheinbahn* in Düsseldorf started a practical test using water-in-fuel emulsions [62]. *MAN, Fuel Emulsions International* and *Nonox Ltd.* are developing effective emulsion fuel system technologies which are already used in diesel engines, cruise liners, and commercial ships [63-65].

All these studies show the potential benefit of water containing fuels in order to reduce the emissions of health hazardous and improve burning efficiency. The application would greatly be facilitated or even made commercially attractive, if certain aim are fulfilled. As such

- the water containing fuel should be mixed right before injection,
- it should contain as less as possible surfactant,
- the surfactant should be of biological origin,
- the fuel system should not be contaminated by water,
- the water content should be adjustable to the engine map.

1.3 Task description

The multiplicity of studies of microemulsified fuels confirmed the presumed positive effects of microemulsions on the exhaust gas emissions in diesel engines [53, 54, 56, 60, 61]. However, an improvement potential exists applying catalyst-free (ash-free), bio-derived surfactants which were not used in previous studies leading to inefficient combustion. Hence, one goal of this thesis was the formulation of an efficient, temperature invariant, practice-oriented fuel microemulsion including fully combustible, ash-free surfactants of biological origin while also considering crucial physical properties.. Here, an interdisciplinary cooperation (FVV-project) with the *University of Applied Sciences in Trier* and the *Rheinisch-Westfälische Technische Hochschule Aachen* (RWTH Aachen) should allow a detailed examination of the influence of these water containing fuels on the exhaust emissions and spray behaviour. To this end, inexpensive, fully combustible and “green” surfactants and additives were to be introduced into an initial system of the type water/ammonium nitrate/ethanol - diesel - oleic acid/monoethanolamine/oleic acid diethanolamide. Here, the surfactant mixture was to be optimised to guarantee the one-phase state at storage conditions in winter and during combustion (temperature invariant state). Keeping an eye on the engine requirements, physical characteristics of the microemulsified fuels were to be measured evaluating the spray behaviour in accordance with EN 590. Regarding the microemulsification approaching injection conditions, the formation kinetics of such systems were to be analysed for different temperatures and water-content. Furthermore, the structure of water-in-fuel microemulsions was to be determined using small angle neutron scattering (SANS) and dynamical light scattering (DLS).

The second goal of this thesis was to formulate economically more appealing, low surfactant content nanoemulsion fuels for load point dependent on injector-blending of water and diesel streams milliseconds before injection into the combustion chamber. Here, the surfactant blend was to be optimised in order to utilise the ultra-low interfacial tension to form small-scaled dispersed water droplets. The influence by varying the HLB-value and surfactant was to be studied using dynamic light scattering (DLS). In order to be able to use nanoemulsified fuels for the on injector-blending system, a separate aqueous- and oleic-phase was to be prepared. Based on the formulation of the nanoemulsion, the aqueous phase was to be added with a suitable, efficient anti-corrosion agent and lubricant.

Finally, in industrial combustion tests the influence of water- and surfactant-content on exhaust gas emissions and spray behaviour was to be clarified, thereby also comparing the pollutant emissions of microemulsions and nanoemulsions. In particular, scanning electron



microscopy (SEM) was to be applied to characterise the soot-structure and aggregation behaviour.



2 FUNDAMENTALS

A fundamental background is needed to understand the present results and techniques in this work. The first sub-chapter (2.1) provides an introduction in microemulsions and their binary systems. In the following sub-chapter (2.2) the properties and different preparation methods for emulsions are explained. The techniques applied for structural and formation kinetics investigations are introduced in sub-chapter (2.3) A basic knowledge of combustion parameters and emission formation is given in the last sub-chapter (2.4).

2.1 Microemulsions

Microemulsions are thermodynamically stable, macroscopically homogenous, optically isotropic, nanostructured systems of at least three components [66]. Microemulsions are formed spontaneously upon mixing a hydrophilic, a hydrophobic and an amphiphilic component. Two of these three components are immiscible, like water (polar component) and oil (non-polar). The amphiphilic nature of the third component allows adsorbing to the interface between the hydrophilic and hydrophobic component. The amphiphilic component features a hydrophilic and a hydrophobic subsection causing a reduction of the interfacial tension between these two immiscible components by forming an amphiphilic film. As a consequence, a nanodisperse mixture of these components forms a thermodynamically stable microemulsion [67]. The first microemulsion was recognised by *Schulmann* and *Hoar* in 1943 [68]. A classification of microemulsions was denoted by *Winsor* in three types of phase equilibria [69]. The temperature-, pressure and component-dependant phase behaviour of microemulsions is closely related to the evolution of the microstructure. Further fundamental backgrounds were observed by *Kahlweit* and *Strey*, which are described and reviewed in this chapter.

In the following, a brief introduction into the application of microemulsions is given. Due to the unique properties of microemulsions, they have been used in various branches of industry. Intensive research on microemulsions was started by the two oil crises in 1973 and 1979. The use of microemulsions was of high interest in terms of enhanced oil recovery. Oil-wells were pumped with water-surfactant mixtures in order to extract the left over crude oil [70]. Microemulsions gained an important role as drug delivery vehicles in the pharmaceutical industry due to their improved bioavailability. Certain drugs were solubilised in

microemulsions and penetrated into the blood circuit while being protected from degradation, hydrolysis and oxidation [71, 72]. A large field of application for microemulsions is the cosmetic industry. Many cosmetic ingredients can be solubilised in the swollen micelles of microemulsions and may enhance diffusion and transport through various barriers [73, 74]. Furthermore, microemulsions can also be used in washing processes in addition to conventional liquid detergents. An enhanced removal of contaminants from solid surfaces by the extremely low interfacial tension in microemulsions is observed [75, 76]. Another possible and important application of microemulsions is the use as *nano insulation materials* in order to save energy by improving thermal insulation of buildings [77]. In textile industry, microemulsions are used in textile finishing and impregnation [78]. Further examples for applications can be found in food and agrochemical industry [79, 80], in chemical reactions e.g. to produce ultrafine particles [81], for polymerisation [82] and as solvent for electrochemical reactions [83].

2.1.1 Phase behaviour

In simply ternary systems that contain water (A), an alkane (B) and a non-ionic surfactant (C) the main properties of microemulsions can be observed [84]. The fairly universal phase behaviour of all systems of this type can be presented in a phase prism with the temperature axis as the ordinate and the *Gibbs* phase triangle A-B-C as the base [66, 85]. The complex temperature-dependent phase behaviour of the ternary system can be understood by considering the three independent binary systems water - oil (A - B), water - surfactant (A - C) and oil - surfactant (B - C). The binary systems represent the three sides of the phase prism, as shown in figure 2-1. A miscibility gap over the entire experimental temperature range dominates the binary system water - oil (A - B). The binary oil - surfactant (B - C) mixture shows a lower miscibility gap with a critical point cp_{α} at a critical temperature T_{α} which is located below 0 °C. The binary system water - surfactant (A - C) features a lower miscibility gap with an upper critical point which is mostly below the melting point of the mixture. An upper closed miscibility gap with lower critical point cp_{β} at the critical temperature T_{β} is found at higher temperatures. The locations of cp_{α} and cp_{β} depend on the nature of the components and are related to the behaviour of the ternary system. These two critical points deliver an explanation for the temperature-dependant phase behaviour: with increasing temperature the solubility of non-ionic surfactant in water decreases while the solubility in oil increases.

An inverse phase behaviour is observed for ionic surfactants. The binary system, consisting of water - ionic surfactant, shows a deviant behaviour. Compared to the binary system water - non-ionic surfactant, only a lower miscibility gap with the critical point cp_β occurs. The nomenclature remains the same but a contrary trend is noticed: with increasing temperature the solubility of ionic surfactant in water increases while the solubility in oil decreases.

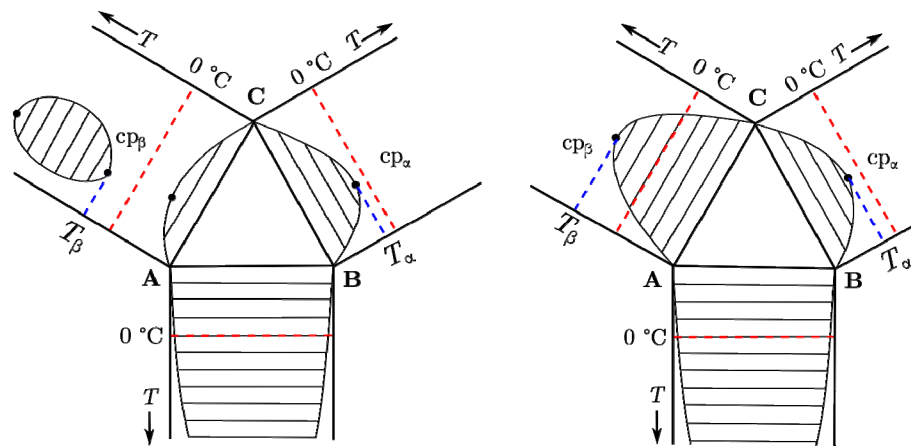


Figure 2-1: Schematic drawing of the unfolded phase prism of the ternary mixture A-B-C (left: non-ionic system; right: ionic system), showing the phase diagrams of the three corresponding binary systems A - B, B - C and A - C (according to [66] taken from [86]).

By increasing the chain length of the surfactant, various mesophases are observed [87]. Micelles (L_1 -phase) are formed above the critical micelle concentration (cmc) in mixtures of low surfactant concentration. With increasing surfactant concentration liquid crystalline phases are formed. First, a sponge-like bicontinuous L_3 -phase at low surfactant concentrations is formed. The bicontinuous phase consists of a surfactant double layer film between two independent water domains. At higher concentrations the highly viscous lamellar phase L_α is observed. Liquid crystalline mesophases as cubic (V_1), or hexagonal (H_1) phases occur with increasing the surfactant concentration. An inverse micellar region (L_2) is formed at very high surfactant concentrations.

2.1.2 Phase prism

The ternary system containing water (A), oil (B) and a non-ionic surfactant (C) is shown in figure 2-2. When the critical temperature T_β at the critical point cp_β is reached, the binary water - surfactant mixture phase separates. At this critical point cp_β , the critical line cl_β starts and proceeds to the critical end point cep_β at the temperature T_1 . Furthermore, the critical line

cl_α at the critical point cp_α starts to proceed into the phase prism until it ends in the critical endpoint cep_α at the temperature T_u . The critical end points cep_α and cep_β build the edges of the *critical conode* and encircle the three-phase area. By increasing the chain length of the oil in the system water - oil - non-ionic surfactant, the solubility of the surfactant in oil increases while the solubility in water decreases. Therefore, T_α shifts to higher temperatures. In the following, an easier determination of the entire phase diagram is introduced.

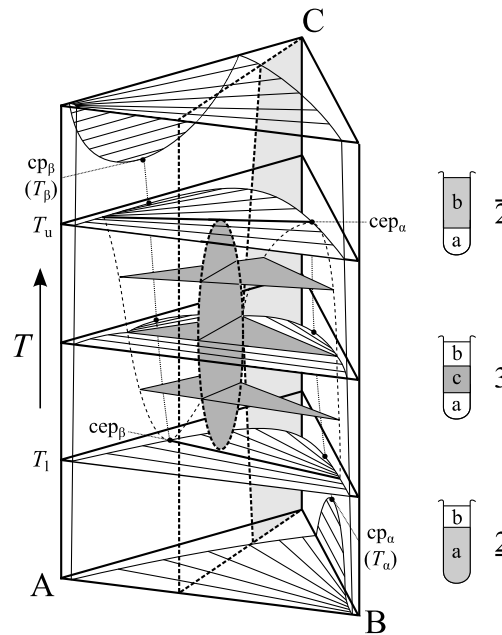


Figure 2-2: *Gibbs* phase prism showing the temperature-dependent phase behaviour of a ternary system containing water (A) - oil (B) - non-ionic surfactant (C) (according to [67] taken from [86]).

2.1.3 $T(\gamma)$ -section

In figure 2-3 a section through the phase prism at constant oil to water-plus-oil mass fraction α is shown.

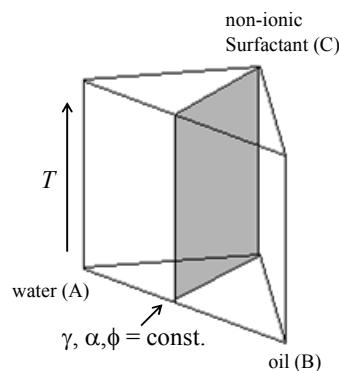


Figure 2-3: Schematic drawing of the phase prism to show temperature-dependent phase behaviour of ternary microemulsions. The section through the phase prism at constant mass fraction α is highlighted in grey.

To perform a $T(\gamma)$ -section, the mass fraction of surfactant γ is added to the binary system water - oil. The number and the type phases are studied visually under variation of the sample temperature. The mass fraction α of oil in the mixture of water and oil is given by:

$$\alpha = \frac{m_B}{m_A + m_B} \quad (1)$$

where m_A is the mass of water and m_B the mass of oil. The mass fraction of surfactant in the ternary system is defined as:

$$\gamma = \frac{m_C}{m_A + m_B + m_C} \quad (2)$$

where m_C is the mass of surfactant.

In order to compare the volumes of the excess phases in the three-phase region, the volume fraction of oil ϕ in the mixture of water and oil is used:

$$\phi = \frac{V_B}{V_A + V_B} \quad (3)$$

while V_A is the volume of water and V_B the volume of oil.

The volume fraction of surfactant ϕ_C in the mixture is defined as:

$$\phi_C = \frac{V_C}{V_A + V_B + V_C} \quad (4)$$

while V_C is the volume of surfactant.

After performing such a section through the phase prism as shown in figure 2-3, a phase diagram of the type, which is schematically shown in figure 2-4, is obtained.

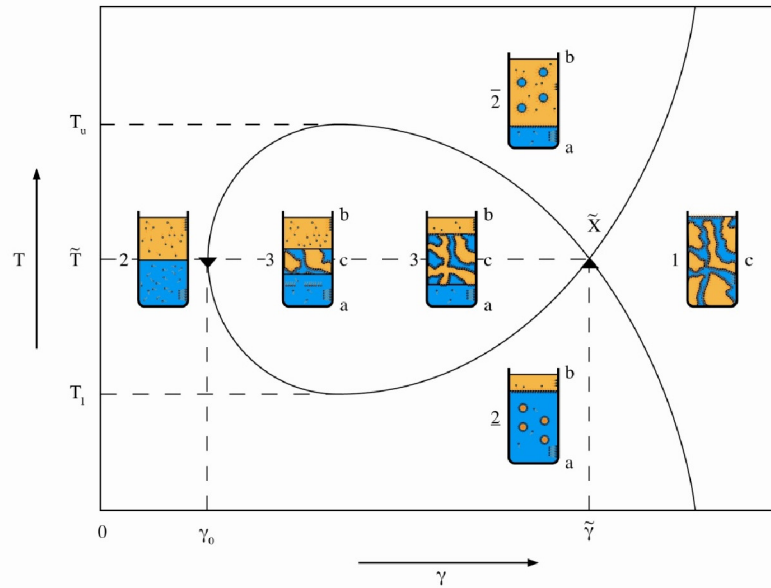


Figure 2-4: Schematic drawing of a $T(\gamma)$ -section through the ternary prism A - B - C (non-ionic surfactant) at $\phi = 0.5$. At γ_0 , the macroscopic interface and the solvents are saturated with surfactant monomers. For $\gamma_0 < \gamma < \tilde{\gamma}$ the three phase region 3 is found between T_l and T_u . At larger surfactant mass fractions $\gamma > \tilde{\gamma}$, microemulsions are formed (redrawn and modified from [60]).

By increasing surfactant mass fraction γ , the phase states in the $T(\gamma)$ -section, the so called “Fish tail”-cut, can easily be determined. At the critical value γ_0 , the macroscopic interface and the solvents are saturated with surfactant monomers. By increasing the surfactant mass fraction above γ_0 , a three-phase body appears between T_l and T_u . A surfactant-rich middle-phase coexists with an oil- and water-excess phase. At lower temperatures ($< T_l$) the excess surfactant will preferentially dissolve in the water-phase. Consequently, oil swollen micelles in water coexist with an oil-excess phase: the two-phase state $\underline{2}$ is found. For higher temperatures than T_u , the amphiphilic film is bent around the water and the state $\overline{2}$ is observed. The excess surfactant molecules dissolve within the oil phase; water-swollen inverse micelles coexist with a water-excess phase. By further increasing the surfactant amount at intermediate temperatures, the volume of the surfactant-rich phase increases, while the volumes of the two excess phases decrease. At $\tilde{\gamma}$, the characteristic X-point of the well-known fish-tail point is finally achieved. A sufficiently amount of surfactant is added and the excess phases are fully solubilised; the volume of the three-phase region increases until it meets the one-phase region at the X-point. The X-point defines the minimum amount of surfactant to solubilise water and oil (efficiency of the surfactant) as well as its temperature \tilde{T} . For ionic surfactants inverse phase behaviour is observed.

2.1.4 Efficiency

The X-point is defined by the mass-fraction $\tilde{\gamma}$ where the minimum amount of the chosen surfactant is needed to reach the one-phase region and marks the efficiency of the surfactant. Therefore, the location of the X-point depends on the molecular structure of the surfactant and thus on its Hydrophilic-Lipophilic Balance (HLB) [88]. Surfactants have an amphiphilic nature and are large molecules that have both hydrophilic and hydrophobic ends. The hydrophilic polar end is composed of ethoxy groups; the hydrophobic non-polar end consists of a large carbon chain containing carbon atoms. Figure 2-5 shows a schematic drawing of a non-ionic surfactant (e.g. *n*-alkypolyethylene glycol ether with the common structure formula $\text{CH}_3(\text{CH}_2)_{i-1}\text{O}(\text{CH}_2\text{CH}_2\text{O})_j\text{H} = \text{C}_i\text{E}_j$, *i* describes the number of carbon atoms of the hydrophobic chain and *j* the number of ethoxy groups of the hydrophilic block).

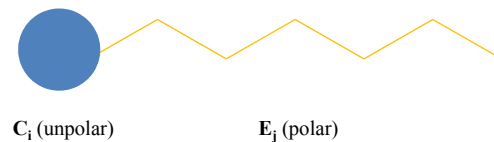


Figure 2-5: Schematic drawing of an amphiphilic molecule.

Due to economic aspects, the microemulsions should contain as less surfactant as possible. Hence, the location of the X-point by changing the surfactant structure parameters *i* and *j* is examined in figure 2-6 and allows the comparison between surfactants with different molecular structures.

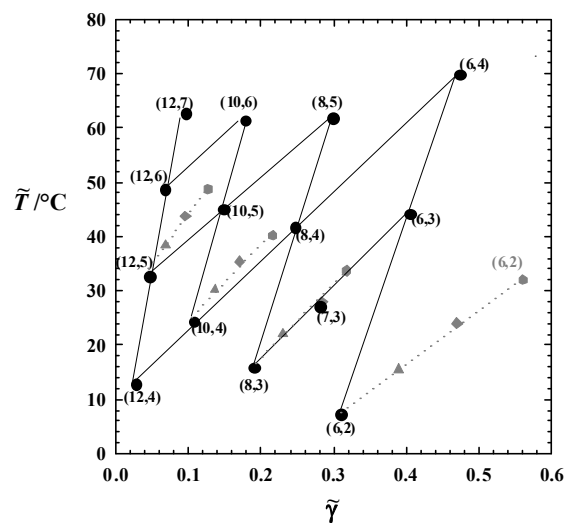


Figure 2-6: X-points of various H_2O - *n*-octane - C_iE_j as a function of $\tilde{\gamma}$ and phase inversion temperature T_m at $\phi = 0.5$. Surfactant structure parameters *i* and *j* (hydrophilic and hydrophobic block) influence the efficiency and the phase inversion temperature T_m (according to [89], taken from [90]).

Systematic trends can be observed by plotting a function of the mass fraction $\tilde{\gamma}$ and temperature \tilde{T} . The ethoxy group j is increased from two to seven, while the hydrophobic chain length i is varied from six to twelve. With increasing hydrophobic chain length i , the X-point shifts to lower surfactant mass fractions and lower temperature \tilde{T} . The surfactant becomes more hydrophobic and the solubilisation efficiency increases. Due to longer alkyl chains, the lamellar mesophase L_α extends and almost touches the X-point. With increasing j , \tilde{T} increases, the surfactant becomes more hydrophilic and the efficiency is reduced.

A systematic variation with the chain length k of the n -alkane also shows an influence on the efficiency. With increasing chain length, the X-point shifts to higher temperatures and the surfactant becomes less efficient; the solubility of a surfactant with given hydrophilic chain length in an alkane with larger chain length k is decreased [91].

Efficiency Boosting Effect

In order to increase the efficiency of microemulsions, small amounts of amphiphilic block copolymers of the type poly(ethylene-propylene)-co-(polyethylene-oxide) (PEP $_x$ -PEO $_y$, with x and y as molar weight per block) to conventional microemulsions can drastically improve the efficiency of surfactants, called *efficiency boosting effect*. The solubilisation capacity of the polymer-surfactant mixture compared to the solubilisation efficiency of the pure surfactant is enhanced [92, 93]. The mass fraction δ is defined as:

$$\delta_{\text{poly}} = \frac{m_{\text{polymer}}}{m_{\text{polymer}} + m_{\text{surfactant}}} \quad (5)$$

while m_{polymer} is the mass of block copolymer, $m_{\text{surfactant}}$ the mass of surfactant.

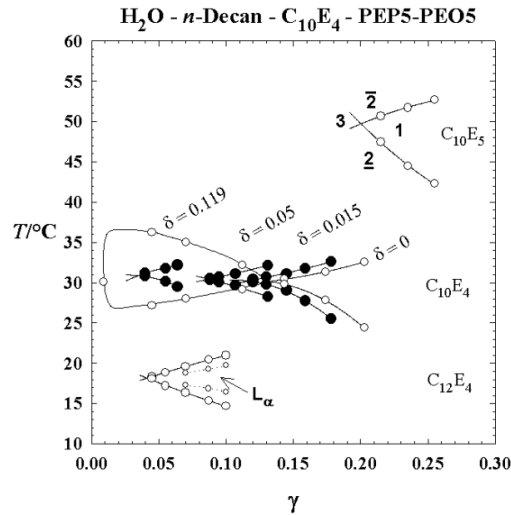


Figure 2-7: Phase diagram of $\text{H}_2\text{O} - n\text{-decane} - \text{C}_{10}\text{E}_4/\text{PEP5} - \text{PEO5}$ at $\phi = 0.5$ for various mass fractions δ_{poly} . Upon increasing δ_{poly} the phase boundaries are shifted to lower surfactant mass fractions γ while T_m remains constant (taken from [92]).

2.1.5 Technical grade surfactant

The previous characterisations were referred to systems with pure surfactants, whose chemical structures and impurities are clearly defined. Pure surfactants with purity $> 99\%$ are usually just used for scientific researches on microemulsions. In terms of economic aspects, technical grade surfactants are used for commercial applications. The main difference between those two surfactants is a broad distribution of the degree of ethoxylation and in the chain length. On the other hand unknown impurities of not fully converted educts also influence the phase behaviour.

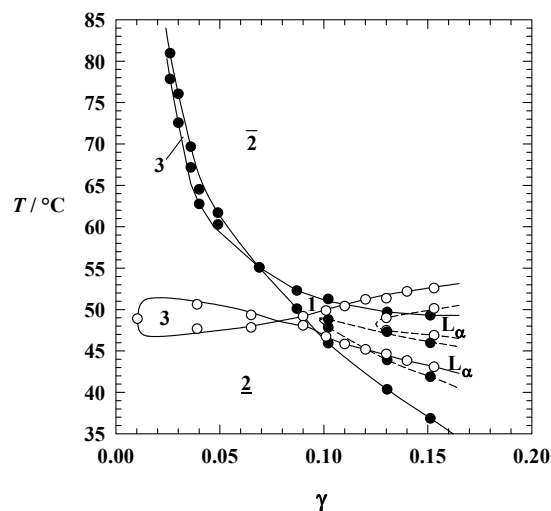


Figure 2-8: Phase behaviour of pure and technical surfactant in the system $\text{H}_2\text{O} - n\text{-octane} - \text{C}_{12}\text{E}_6$ at $\phi = 0.5$. Full circles represent the pure quality while the hollow circles represent the technical analog DA-6 (taken from [94]).

As shown in figure 2-8, the phase boundaries are shifted to higher temperatures and show a distorted shape. This effect is based on a broader distribution of chain lengths and degree of ethoxylation. The chain length is directly related to the polarity of the molecule and can lead to a better monomer solubilisation of individual components. Hence, extraction effects occur and deform the phase boundaries. The hydrophobic surfactant components extract into the oil-phase, which lead to a more hydrophilic surfactant at the interface and shift the phase boundaries to higher temperatures.

2.1.6 Temperature invariance

Temperature invariance in a water-fuel microemulsion is the first essential condition for the use as fuels. The stability of the one-phase region over the entire temperature range has to be ensured. Temperature invariance has to cover a temperature range between -10 °C and 90 °C in order to guarantee a one-phase microemulsion during combustion process and storage. In winter at low temperatures and in the injection system at high temperatures the one-phase region is required. *Kahlweit* and *Strey* [95] examined the combination of non-ionic and ionic surfactants in the system: H₂O/salt - oil - nio/io surfactant whereat the relation of non-ionic to ionic surfactant is defined by the mass fraction δ :

$$\delta = \frac{m_{\text{ionic surfactant}}}{m_{\text{non-ionic surfactant}} + m_{\text{ionic surfactant}}} \quad (6)$$

In figure 2-9 a), the trend of the PIT (*phase inversion temperature*) as a function of the mass fraction δ is shown.

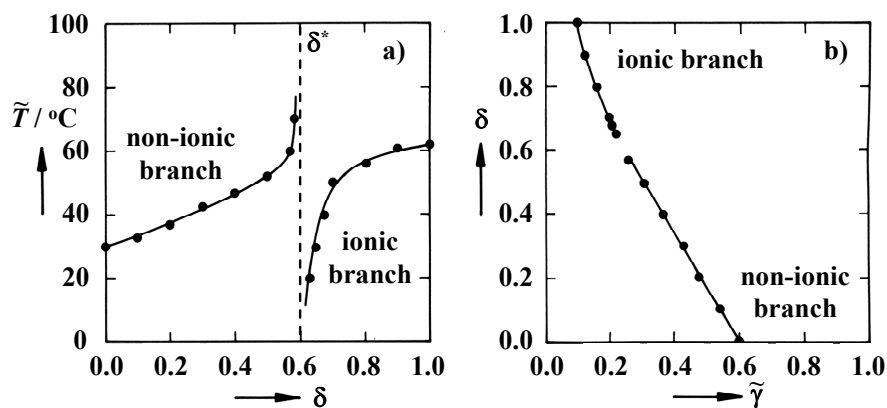


Figure 2-9: Trajectory a) of the phase inversion temperature as a function of the ionic surfactant mass fractions δ in the system H₂O - *n*-decane - C₄E₁/AOT at $\alpha = 0.5$ and $\varepsilon = 0.01$. Trajectory b) of the ionic surfactant mass fractions δ in the same system as a function of $\tilde{\gamma}$. The phase behaviour passes from ionic to non-ionic at the critical ionic surfactant ratio δ^* (taken from [95]).

The system starts with a pure non-ionic surfactant ($\delta = 0.0$) with a non-ionic branch. With increasing amount of ionic surfactant, the PIT increases. This effect is based on the increasing hydrophilicity of the amphiphilic film. Starting from the pure ionic system ($\delta = 1.0$), the PIT of the ionic branch decreases with increasing amount of non-ionic surfactant; the amphiphilic film becomes more hydrophobic. Both branches get closest at $\delta \approx 0.6$, where PIT of the non-ionic branch escalates and the PIT of the ionic branch drastically declines. Accordingly, the one-phase region expands over the relatively small δ^* -region and the one-phase microemulsion is stable over a wide temperature range.

2.1.7 High pressure phase behaviour

The previous phase behaviour of ternary non-ionic microemulsion systems was described at atmospheric pressure. In order to ensure a one-phase microemulsion during the combustion process at higher pressures, the pressure- and temperature independence of the phase behaviour has to be studied.

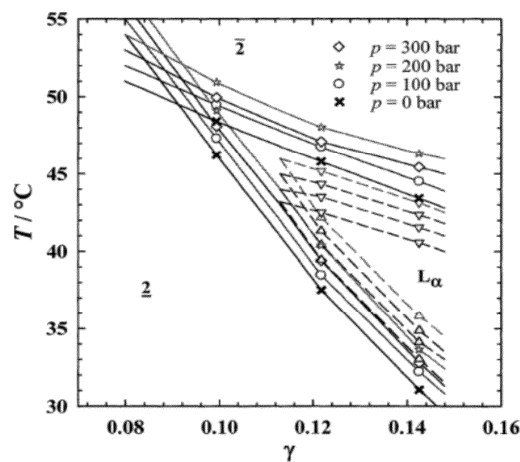


Figure 2-10: Phase behaviour of the system H_2O - diesel - C_{13}E_5 at $\alpha = 0.5$ with increasing pressure (from $p = 0 - 300$ bar) (taken from [96]).

In figure 2-10 a systematic trend of the system H_2O - diesel - C_{13}E_5 with increasing pressure from $p = 0 - 300$ bar can be observed. The phase boundaries and the X-point are minimal shifted to higher temperatures by increasing the pressure. Comparing the location of the X-point at atmospheric pressure and at 300 bar, a shifting of $\Delta T = 4^\circ\text{C}$ is observed.

The effect is based upon a stronger hydration of the hydrophobic head group with increased pressure which leads to an increased volume of the head group. Thereby, a distinctive

curvature of the amphiphilic film enclosing the oil occurs. The change of curvature can be compensated with an increased temperature.

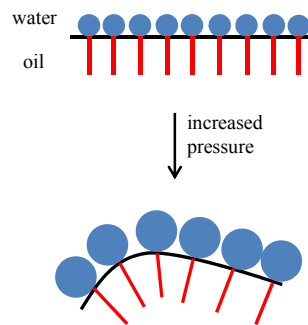


Figure 2-11: Schematic drawing of the curvature of the amphiphilic film with increasing pressure (redrawn from [97]).

2.1.8 Trajectory of the middle phase

The trajectory of the middle phase (respectively the trajectory of the X-point) illustrates a systematic course inside the complex phase prism (see figure 2.2). A typical sigmoidal slope, connecting the critical end points cep_β and cep_α , is featured in the projection onto the T - A - B surface. An appropriate way to exhibit the trajectory of the X-points is the projection onto both the A - B - C base and the front face (the A - B - T plane of the prism). *Sottmann* demonstrated the parabolic shape of the trajectory of the middle phase (figure 2-12), which are scalable for all kinds of microemulsion systems [98, 99].

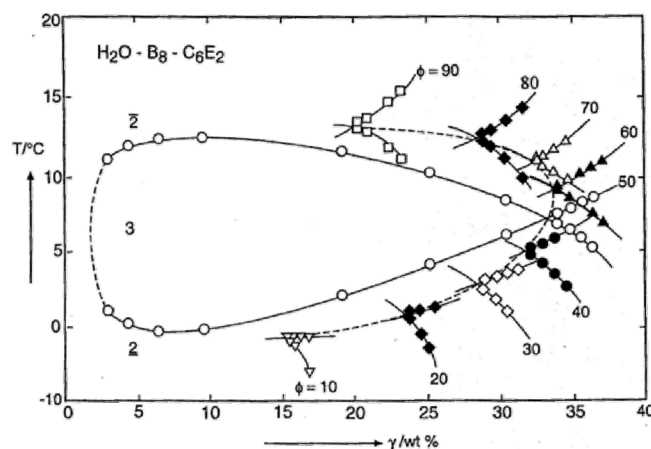


Figure 2-12: Trajectory of the X-points of the system A - B - non-ionic surfactant as a function of the surfactant mass fraction γ at various ϕ (taken from [98]).

2.1.9 Additives

For the use of microemulsions as alternative fuels, additives are added to improve the phase behaviour of microemulsions.

Alcohols

The influence of alcohols (C_iE_0) on the phase behaviour depends on the carbon chain length i . Short-chained alcohols $i \leq 3$ are completely soluble in water and function as a co-solvent while increasing the solubilisation of surfactant in water; the upper miscibility gap of the binary system water - surfactant is reduced [100]. Consequently, the PIT is shifted to higher temperatures. Due to the amphiphilic nature of short-chained alcohols, they insert into the amphiphilic film and operate as an inefficient co-surfactant. Simultaneously, the formation of liquid crystalline phases is reduced by the destabilising effect of short-chained alcohols on the amphiphilic film. Alcohols with a carbon chain length $i \geq 3$ function as a co-surfactant as well as a co-solvent in oil [100-102]. The alcohol in the oil causes a higher hydrophilicity and the miscibility gap of the system oil - surfactant is shifted to lower temperatures. The first property increases the efficiency of the system since the alcohol dissolves in the interface. The mass fraction ψ in the aqueous compound is given by:

$$\psi = \frac{m_{\text{alcohol}}}{m_A} \quad (7)$$

Electrolyte

Hofmeister systematically studied the influence of lyotropic salts on the solubility of organic agents in water. Anions appear to have a larger effect than cations and are usually graded: $\text{SO}_4^{2-} > \text{CrO}_4^{2-} > \text{CO}_3^{2-} > \text{Cl}^- > \text{NO}_3^- > \text{ClO}_3^-$; $\text{Li}^+ > \text{K}^+ > \text{Na}^+ > \text{NH}_4^+ > \text{Mg}^{2+}$. The *Hofmeister series* can also be transferred to non-ionic surfactants. The effect is resulted from changes in the water structure based on the solubility and the electronegativity of the lyotropic salts [103]. The influence of electrolytes on non-ionic surfactants differs than the one on ionic surfactants. While the influence on non-ionic surfactants is based on the *Hofmeister series*, the influence on ionic surfactants is based on the ionic strength of the electrolytes [104]. The electrostatic interference between electrolyte and surfactant can reduce the size of the electrical double layer (*Debye length*) and therefore influence the curvature of the amphiphilic film.

Hydrotopic salts influence the hydrophilicity of surfactants by requiring water for hydration; less water molecules can solubilise the surfactant head group. Consequently, the surfactant head group becomes more hydrophob.

The mass fraction ε in the aqueous compound is given by:

$$\varepsilon = \frac{m_{\text{salt}}}{m_A} \quad (8)$$

2.1.10 Amphiphilic film

The most interesting property of microemulsions is the variety of microstructures. The structural properties of microemulsions can be determined by small angle neutron scattering (SANS), scanning electron microscopy (SEM) and conductivity measurements.

In figure 2-13 the microstructure of the ternary system A - B - C (non-ionic surfactant) is shown in a $T(\gamma)$ -section.

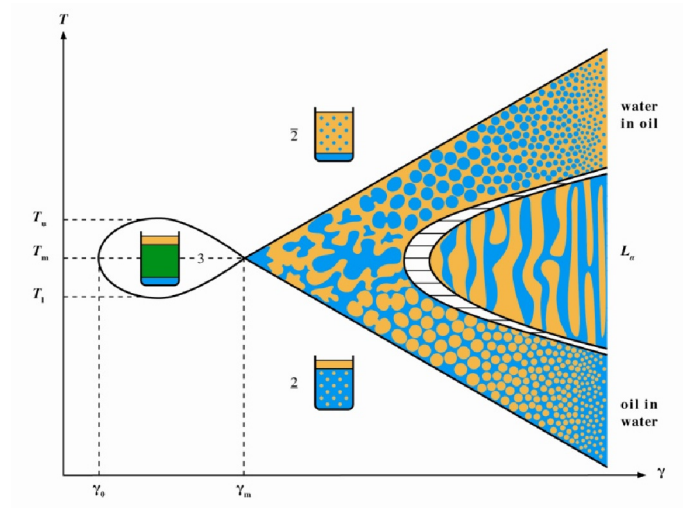


Figure 2-13: Schematic $T(\gamma)$ -section of the ternary system A - B - C (non-ionic surfactant) at $\phi = 0.5$ with the related structure (redrawn after [67]).

The nature and properties of the amphiphilic film are essential for the variety of microstructures. The mathematical approach of *Helfrich* expresses the total bending energy of the membrane as function of its shape [105,106]. *Strey* observed that the main parameter determining the microstructure is the local curvature of the amphiphilic interfacial film [67].

The principal curvature at each point is given by the two principal curvature radii r_1 and r_2

$$c_i = \frac{1}{r_i} \quad (9)$$

A spherical membrane a) and the saddle-shaped structure (bicontinuous phase) b) are shown in figure 2-14.

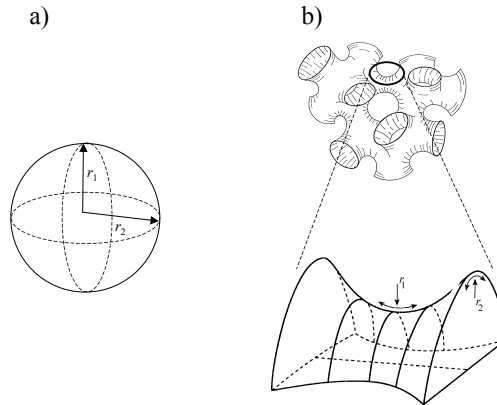


Figure 2-14: Principle curvature radii r_i for a spherical interface where both radii are equal a). Membrane in a sponge-like structure such as the bicontinuous phase b) (upper part taken from [87], lower part according to [107], taken from [108]).

The curvature is defined as negative when the amphiphilic film encloses the water and positive when it encloses the oil. The *mean curvature* H and the *Gauss curvature* K are defined by

$$H = \frac{1}{2} \cdot (c_1 + c_2) = \frac{1}{2} \cdot \left(\frac{1}{r_1} + \frac{1}{r_2} \right) \quad (10)$$

$$K = c_1 \cdot c_2 = \frac{1}{r_1} \cdot \frac{1}{r_2} \quad (11)$$

The relation between the spontaneous curvature of the amphiphilic film and the microstructures are shown in figure 2-15.

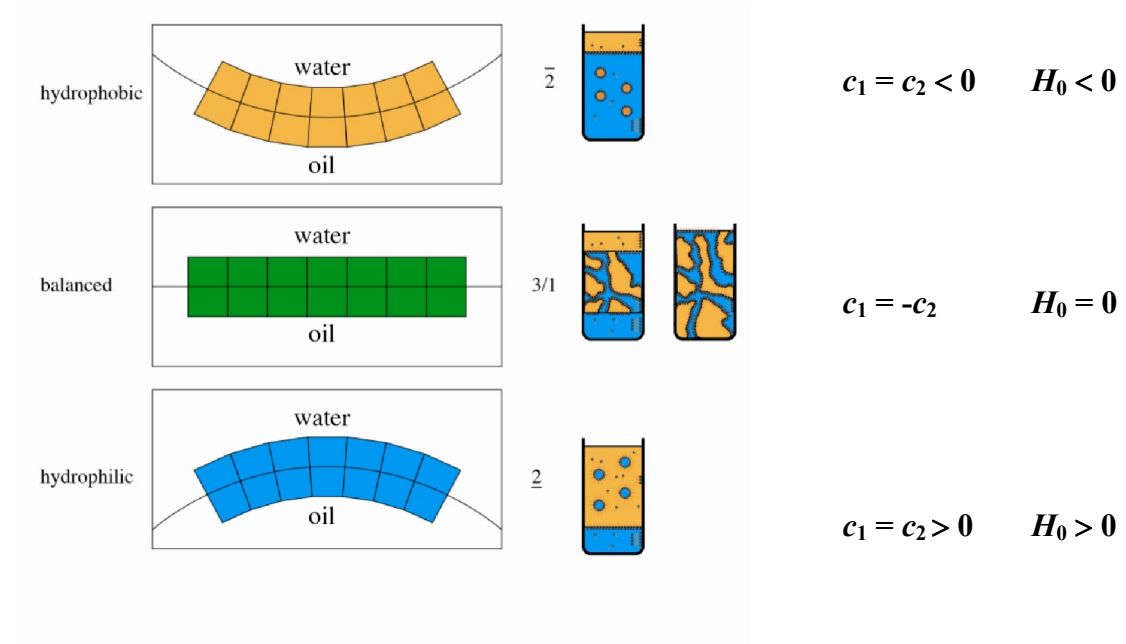


Figure 2-15: Schematic drawing of the correlation between spontaneous curvature H_0 and the structure, respectively, the phase behaviour in microemulsion systems (according to [109] , redrawn from [60]).

Microemulsions are described as an ensemble of flexible surfaces impacted by the bending rigidity κ [105]. The *Helfrich free energy* f is defined as

$$f = 2\kappa(H - H_0)^2 + \bar{\kappa}\kappa \quad (12)$$

while $\bar{\kappa}$ is the saddle-splay modulus of the membrane and H_0 the spontaneous curvature.

The curvature of the amphiphilic film depends on the relative volumes of the hydrophilic head group and the hydrophobic chain length of the surfactant. *Israelachvili et al.* describes the *molecular packing parameter* Π as the quotient of the relative volume v of the hydrophobic chain length l to the head-group area a_0 [110, 111]:

$$\Pi = \frac{v}{la_0} \quad (13)$$

A conical shape of the surfactant molecule is found for $\Pi < 1$, for $\Pi = 1$ a cylindrical one and a truncated conical for $\Pi > 1$. The packing parameter and the mean curvature have to be considered for the actual structure.

2.1.11 Compounds

Surfactants and additives used for microemulsified fuels are fully combustible and based on raw materials due to the depletion of fossil fuels.

Hydrophilic component A

Bidistilled water is used for laboratory examination, while distilled water is used for engine tests. Short chained alcohols like ethanol or *n*-propanol are added as antifreeze additives in order to decrease the freezing point. The mass fraction of alcohol ψ in the aqueous compound is given by equation (7).

In order to suppress the lamellar phase, the lyotropic salt NH_4NO_3 is applied in the aqueous phase of the fuel microemulsion. The mass fraction of salt ε in the aqueous compound is defined in equation (8).

Hydrophobic component B

Conventional diesel fuel is used as the hydrophobic component which fulfils EN 590. Diesel fuel is a mixture of aliphatic and aromatic middle distillates obtained by crude oil. Accordingly, diesel fuel specifications differ from various fuel grades and in different countries. The important properties, which are used to characterise diesel fuel, are: density, viscosity, fuel volatility, flash point, lubricity and cetane number. In order to fulfil the quality norm according to EN 590, different additives are added to the fuel. For example, anti-foaming agents (polysilane), detergents (amine, amide, poly-alkylamine) to protect against deposit and anti-corrosive agents (amphiphilic long-chained carboxylate) help to optimise the diesel fuel properties. Winter diesel fuels additionally contain agents to lower the cold filter plug point (CFPP).

Amphiphilic component C

Fully combustible, bio-derived and technical grade surfactants are applied in fuel microemulsions. Oleic acid, $\text{C}_{18}\text{H}_{34}\text{O}_2$, is a monounsaturated fatty acid (18:1; omega-9 fatty acid) which is found naturally in many plant sources.

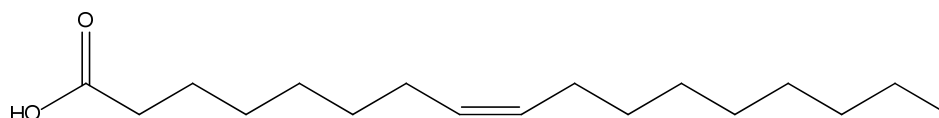


Figure 2-16: Molecular structure of oleic acid ($\text{C}_{18}\text{H}_{34}\text{O}_2$).

In this work ionic surfactants were produced *in situ* through a neutralisation reaction of oleic acid with monoethanolamine. In previous studies alternative bases as ammonia or sodium hydroxide showed an inapplicable property in terms of corrosivity and combustion [56]. Partially neutralised oleic acid positively influences the temperature invariant state [54].

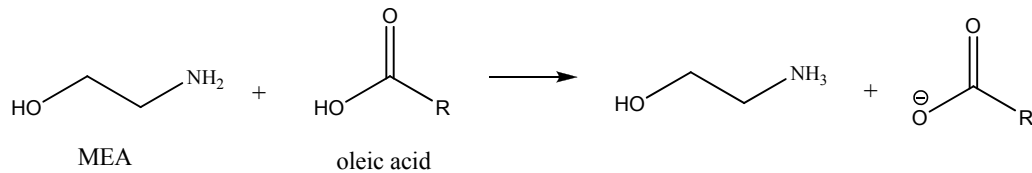


Figure 2-17: Neutralisation reaction of the acid group (of oleic acid) with monoethanolamine (MEA) in order to generate ionic surfactants.

The grade of neutralisation n is given as:

$$n = \frac{n_{\text{base}}}{n_{\text{oleic acid}}} \quad (14)$$

which is based on the molar ratio of the base n_{base} to $n_{\text{oleic acid}}$. With $n = 1$, an equimolar neutralisation of oleic acid is achieved.

Temperature invariance in microemulsion as fuels is essential. As described in chapter 2.1.6, the combination of non-ionic and ionic surfactant enhances the stability of the one-phase microemulsion over a wide temperature range. Oleic acid diethanolamide, $\text{C}_{22}\text{H}_{43}\text{NO}_3$, is applied as non-ionic surfactant in the surfactant blend and results from the catalysis-free condensation reaction of oleic acid with diethanolamide.

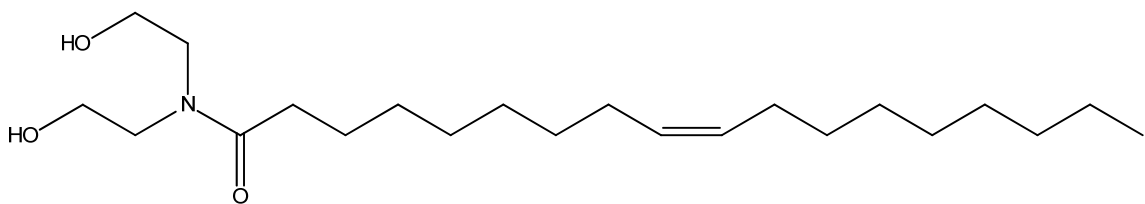


Figure 2-18: Molecular structure of oleic acid diethanolamide ($\text{C}_{22}\text{H}_{43}\text{NO}_3$).

In former studies [56, 60] oleic acid diethanolamide were used which contained an intolerable high amount of sodium due to its catalytic production. Consequently, an increased ash-content was observed during combustion. The improved production process without involving a metalliferous catalyst permitted the resumption of oleic acid diethanolamide.

All applied surfactants exhibit ash content less than 0.001 wt.%, which were determined after EN ISO 6245 from Intertek in Hamburg.

Amphiphilic triblock copolymer

In order to enhance the solubilisation efficiency of the pure surfactant, commercial available Pluronic[®] triblock copolymer of the type poly(ethylene-oxide)-co-poly(propylene-oxide)-poly(ethylene-oxide) (PEO_m-PPO_n-PEO_m, m,n = molar weight per block) was added with a mass fraction δ_{poly} given by equation (5).

Table 1: Pluronic[®] triblock copolymers and their chemical properties.

polymer	formula (monomer units)	M _w [g/mol]	EO [wt.%]
PE 6800	PEO ₇₃ -PPO ₂₈ -PEO ₇₃	8000	80
F 98	PEO ₁₁₈ -PPO ₄₅ -PEO ₁₁₈	13000	80

2.2 Emulsions

Emulsions are colloid dispersions of at least two immiscible liquids with a kinetic stability and appear macroscopically homogenous. Emulsions usually contain oil (o) and water (w), and are defined as water in oil (w/o; e.g. margarine) or oil in water (o/w; e.g. milk) emulsions.

Typical emulsions feature emulsion droplets between 1 to 10 µm, while their stability is disturbed by gravity forces. Breakdown processes like flocculation, creaming and coalescence can occur in emulsions and are shown in figure 2-19.

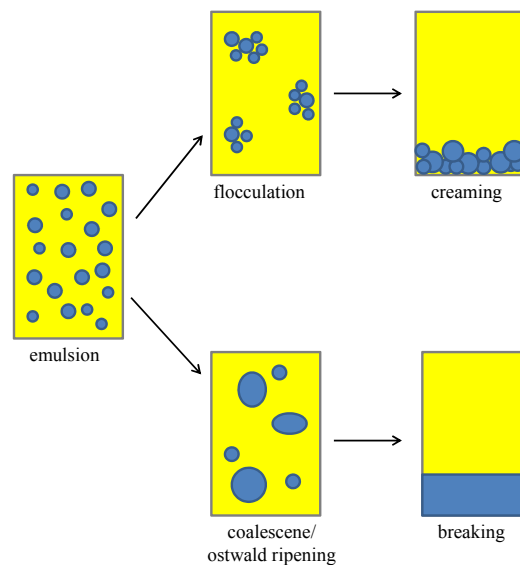


Figure 2-19: Schematic drawing of the breakdown processes in emulsions.

The main process is driven by coalescence/ostwald ripening, where dispersed droplets grow to bigger aggregates due to reduction of the interfacial tension by increasing the droplet volume.

In order to lower the interfacial tension and thereby suppress break down processes, a small amount of surfactant is added. *Brancroft's* rule suggests that the emulsion type (o/w or w/o) depends on the nature of the surfactant, while the phase in which the surfactant is more soluble, becomes the continuous phase [112]. After *Griffin* [88], the HLB-concept (hydrophilic-lipophilic balance) for non-ionic surfactants defines the surfactant characteristics which are given in numerical values of zero to 20,

$$HLB = 20x \left(1 - \frac{M_1}{M} \right) \quad (15)$$

where M_l is the molecular mass of the lipophilic portion of the molecule, and M is the molecular mass of the whole molecule. A HLB value of 0 correlates to a lipophilic molecule, a HLB value of 20 correlates to a completely hydrophilic molecule.

Table 2: HLB-values in relation to application and miscibility in water [113].

HLB-value	Application	miscibility in water
1.5 - 3	anti-foaming agent	insoluble
3 - 8	w/o-emulsions	whitish
7 - 9	microemulsions	
8 - 18	o/w-emulsions	whitish stable dispersion
13 - 15	washing active substances	clear
12 - 18	solubiliser	clear

2.2.1 Types of emulsions

Emulsions are divided into macro-, nano- and microemulsions by their domain sizes. Microemulsions were precisely described in chapter 2.1. Emulsion can appear transparent with droplet sizes between 10 to 200 nm, while an increased stability is observed. Those emulsions are called nanoemulsions [114, 37] or mini-emulsions [115]. Emulsions with droplet sizes ≥ 200 nm appear whitish; those macroemulsions differ in their thermodynamic stability from microemulsions. In general, emulsions appearance between translucent [116] and white [117] depends on their droplet sizes. The advantage of a nanoemulsion is a reduced amount of surfactant while still providing long time stability and small droplet sizes.

Table 3: Main difference of micro-, nano- and macroemulsions.

emulsion type	Size	stability	Formation
micro-	5 - 10 nm	thermodynamic	spontaneous
nano-	10 - 200 nm	kinetic	PIT, EIP
macro-	> 200 nm	low kinetic	shearing

2.2.2 Emulsification methods

In order to prepare a kinetically stable emulsion consisting of water, oil and surfactants, energy is required to expand the interface between water and oil. The *Gibbs free energy* ΔG of formation an emulsion is given as

$$\Delta G = \Delta A \sigma - T \Delta S \quad (16)$$

where ΔA is the change in interfacial area, σ is the interfacial tension and ΔS is the change of entropy. The interfacial tension σ is positive; consequently the energy to expand the interface is positive and has a high value (first term). Since the second term is small, the energy term cannot be compensated; therefore the *Gibbs free energy* ΔG becomes positive. Due to equation (16), the formation of emulsions is non-spontaneous and energy is necessary. A high-energy input can be achieved by high-shear stirring (ultra-high mixers) or high-pressure homogenisers leading to a break up of droplets into smaller droplets. The *Laplace pressure* p gives a better understanding of the formation of high-energy required emulsions and is defined as

$$p = \sigma \left(\frac{1}{r_1} + \frac{1}{r_2} \right) \quad (17)$$

where r_1 and r_2 are the radii of curvature of the drop. The equation is simplified for a spherical drop ($r_1 = r_2 = r$) to:

$$p = \frac{2\sigma}{r} \quad (18)$$

Consequently, the deformation of small droplets into smaller ones increases p . Due to a lower interfacial tension with increased surfactant content, the *Laplace pressure* p is reduced and therefore less stress (less shear rate) is needed to break up a drop [114].

To determine the droplet size distributions of the emulsions, dynamic light scattering techniques (DLS) are used. The technique details are reviewed in chapter 2.3.1.

Three methods for the preparation of a emulsions are presented in this sub-chapter. The high energy method using a high pressure homogeniser, the low energy method which includes the *Phase Inversion Temperature* (PIT) [37, 118-120] and *Emulsion Inversion Point* (EIP) [121-124] methods.

High energy method

In order to break up large droplets into smaller ones, high energy by using homogenisation, high pressure or shearing techniques are required. These procedures are generally efficient but low energy methods are favoured. The process intensity of making small droplets is ruled by the net power density ($\epsilon_{pd}(t)$) and is given as

$$p = \epsilon_{pd}(t) dt \quad (19)$$

where t is the emulsification time. The breakup of droplets (smaller mean droplet diameters) only occurs at high ϵ_{pd} values as *Schultz et. al* observed using different high-pressure dispersing systems [125].

Low energy method

Emulsion systems can be achieved by a low energy method with different approaches. The three different low energy emulsification techniques [126] are divided into: A stepwise addition of water to an oil surfactant-mixture (a); secondly, a stepwise addition of oil to a solution of the surfactant in water (b); and mixing all the compounds simultaneously (c). Due to the different techniques, various droplet sizes of the same emulsion system can be observed.

Phase Inversion Temperature (PIT) method

Due to the temperature dependence of the HLB value of the system, a transitional inversion can be induced by changing the temperature. Hence, the HLB-concept is not transferable to emulsion behaviours at higher temperatures. *Shinoda et al.* noticed a transitional phase inversion from o/w- to a w/o-microemulsion while increasing the temperature. The inversion at the critical temperature is the so called Phase Inversion Temperature (PIT) method [126, 127]. At the PIT, the interfacial tension σ and the droplet sizes reach their minimum, while the spontaneous curvature becomes zero. In order to understand this effect, figure 2-20 represents the temperature dependence of interfacial tensions in the system water - oil - non-ionic surfactant with a link to the phase prism (center). As discussed in chapter 2.1.1, the solubility of non-ionic surfactants in the aqueous phase depends on the temperature with a simultaneously change in interfacial tensions. At temperatures below T_l and above T_u , only the water/oil interfacial tensions σ^{ab} occurs, which refers to the interfacial tension between a

w/o (o/w)-microemulsion and its coexisting oil (water)-rich excess phase. The three-phase body, which is observed between T_l and T_u , exists with the interfacial tensions between the water-rich and surfactant-rich middle phase σ^{ac} and between the oil-rich and surfactant-rich phase σ^{bc} . *Sottmann et al.* studied the interfacial curves as function of the temperature shown in figure 2-20 (right) [38]. At T_l (the two phases) (a) and (c) are identical, the interfacial tension σ^{ac} starts from zero and increases monotonically with increasing temperature while the interfacial tension σ^{bc} decreases and vanishes at T_l due to the formation of two, identical phases (c) and (b).

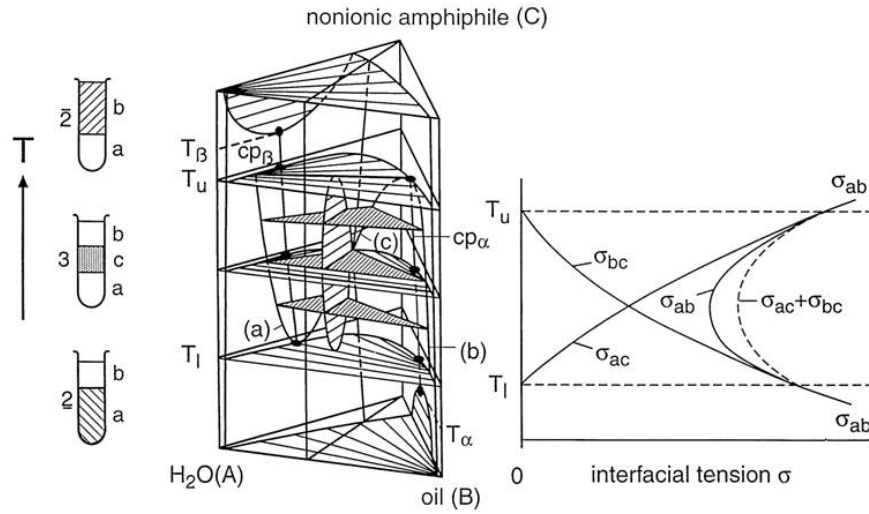


Figure 2-20: Schematic drawing of the phase behaviour (center) and the interfacial tensions (right) as function of the temperature in the system water - oil - non-ionic surfactant. At T_m the minimum of the water/oil interfacial tension σ^{ab} is obtained as a consequence of the phase behaviour (according to [38], taken from [86]).

This opposite trend in dependence of temperature results in a minimum in the sum of $\sigma^{ac} + \sigma^{bc}$. The stability of the water/oil interface is ensured when

$$\sigma^{ab} \leq \sigma^{ac} + \sigma^{bc} \quad (20)$$

is given.

The change of emulsion phase with increasing temperature [129] is shown in figure 2-21.

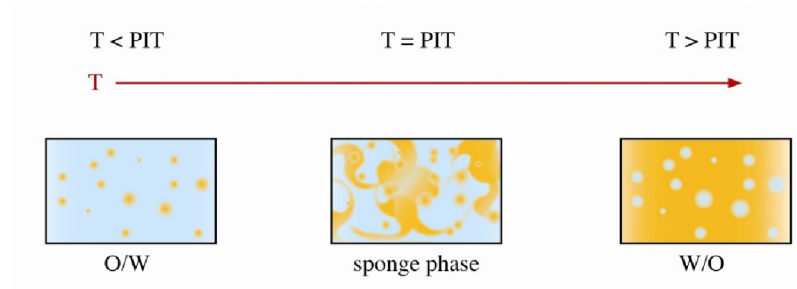


Figure 2-21: Change of structure of the system A-B-C (non-ionic system) with increasing temperature (redrawn and modified from [130]).

An oil-in-water (o/w)-microemulsion is found at low temperatures in a system A - B - C (non-ionic surfactant). With increasing temperature, at the Phase Inversion Temperature (PIT), the minimum of the water/oil interfacial tension σ^{ab} is observed. Above PIT, a water-in-oil (w/o)-microemulsions is formed.

Emulsion Inversion Point (EIP) method

A change of the spontaneous curvature is affected by changing the water volume fraction. The term emulsion inversion point (EIP) refers to the fact that water is successively added into oil due to formation of water droplets in the continuous oil phase. By increasing the water volume fraction, the spontaneous curvature changes and the w/o emulsion is inversed to an o/w emulsion. During the catastrophic phase inversion the area of ultra low interfacial tension is achieved, resulting in the formation of small droplets [121-124]. The process of the emulsion inversion point (EIP) method is illustrated in figure 2-22.

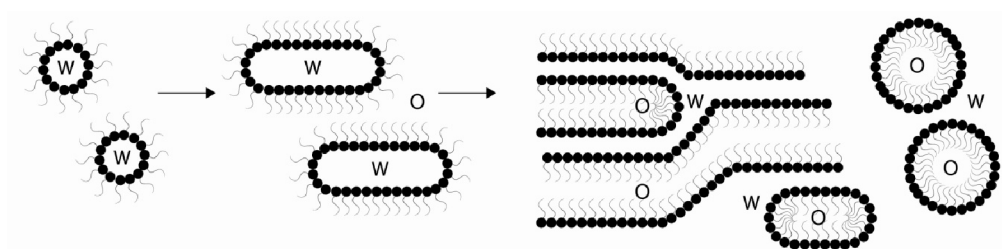


Figure 2-22: Change of the spontaneous curvature with increasing the water volume fraction. Water-in-oil droplets merge together and give bicontinuous structure that are finally converted into fine oil-in-water droplets (redrawn from [131]).

The water-in-oil droplets merge together and give bicontinuous or lamellar structures that are finally converted into fine oil-in-water droplets.

A schematic illustration of both methods (PIT, EIP) for the preparation of dispersed o/w nanoemulsions is shown in figure 2-23.

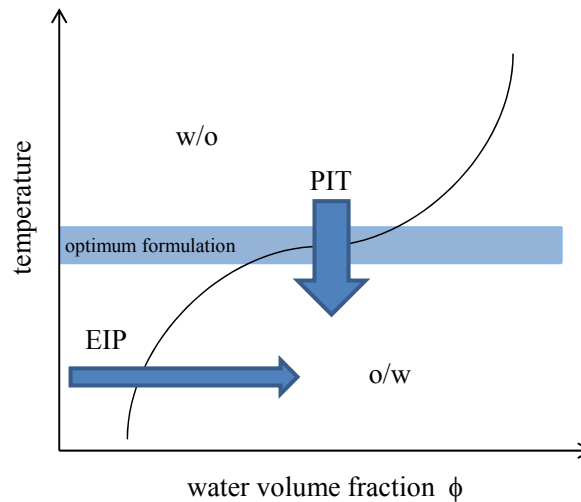


Figure 2-23: Schematic illustration of both methods (PIT, EIP) for the preparation of fine dispersed oil-in-water nanoemulsions. Within the optimum formulation zone, the interfacial tension is minimal. Both low energy emulsification methods utilise this ultralow interfacial tension to form finely dispersed droplets (redrawn from [131]).

2.2.3 Compounds

As described in chapter 2.1.11, only fully combustible and bio-derived surfactants are applied.

Hydrophilic component A

For the formulation and investigation of emulsions in the laboratory, bidistilled water is applied, while distilled water is used for engine experiments. In order to guarantee an anti-corrosive property of the water phase, an agent based on monoethylene glycol (Clariant® Antifrogen NTM) is added in the aqueous phase of the fuel emulsion. Additives based on quaternated amido amine ethoxy-late (Evonik® Rewoquat W 325 PGTM) and on polyethylene glycol (Lubrizol® Veg EsterTM) are applied as lubricant in order to decrease friction.

Hydrophobic component B

Conventional diesel fuel is used as hydrophobic component B. A detailed description is given in chapter 2.2.11.

Amphiphilic component C

“Green surfactants” based on sorbitol are used as amphiphilic component C. Sorbitan monooleate (SMO) is a non ionic fatty acid ester surfactant with a hydrophobic nature which is produced by the reaction of sorbitol with oleic acid.

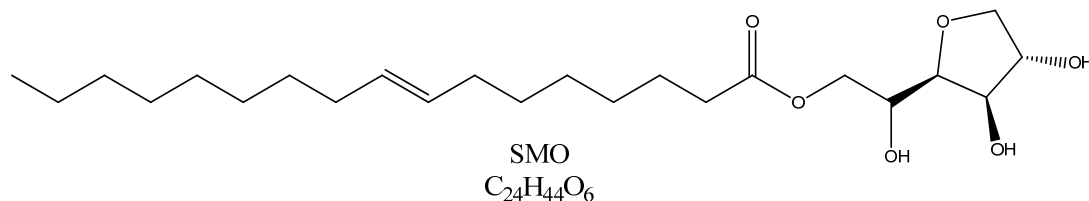


Figure 2-24: Molecular structure of sorbitan monooleate (SMO).

Furthermore, two polysorbates (Polysorbat 85 and Polysorbat 80) were used. Both polysorbates are a mixture of oleate esters of sorbitol and sorbitol anhydrides. Polysorbat 85 (Walloxen STO 200) and Polysorbat 80 (Merpoxen SMO 200QL) mainly differ in the degree of esterification and in its hydrophilicity. The first number marks the esterified fatty acid (here: 8 = oleic acid) while the second marks the type of esterification (here: 0 = monoester with 20 polyoxyethylene units; 5 = triester with 20 polyoxyethylene units). The polysorbates are produced through esterification of sorbitol with oleic acid, followed by a polyaddition of ethylene oxide.

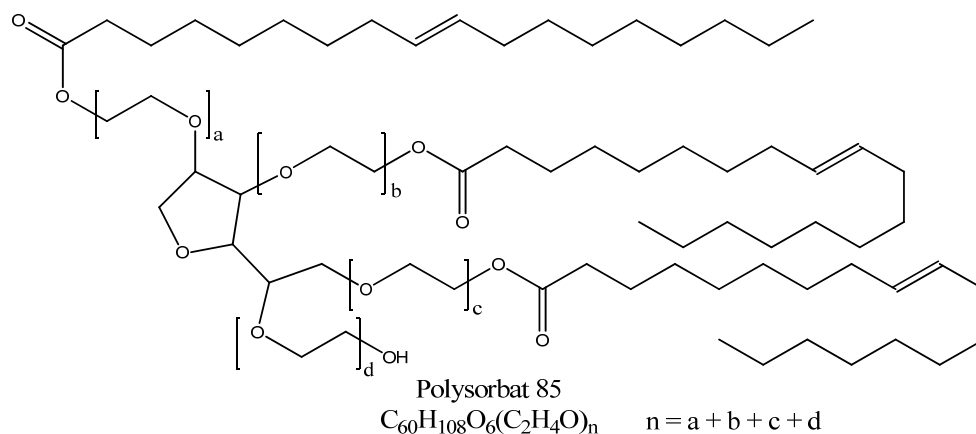


Figure 2-25: Molecular structure of polysorbat 85 (Walloxen STO 200).

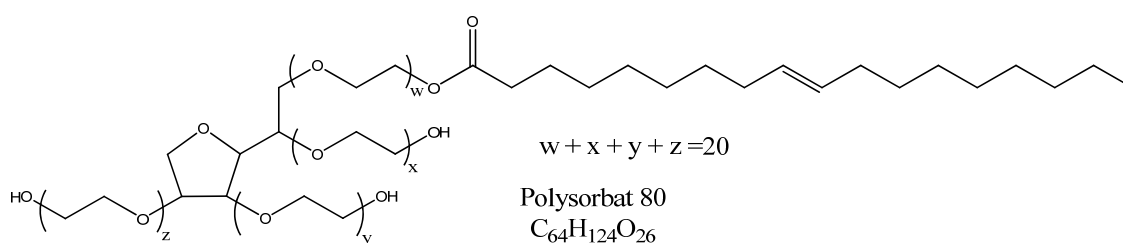


Figure 2-26: Molecular structure of polysorbat 80 (Merpoxen SMO 200QL).



In table 4 the applied surfactants with their chemical formula, HLB-value and ash content (measured by Intertek[®] Hamburg) are listed.

Table 4: Applied surfactants for water-in-oil emulsions and their chemical properties.

surfactant	Formula	HLB-value	ash-content [wt.%]
sorbitan monooleate	$C_{24}H_{44}O_6$	4.3	0.049
polyoxyethylene sorbitan trioleate (Walloxen STO 200)	$C_{62}H_{112}O_6(C_2H_4O)_n$	11	0.096
polyoxyethylene sorbitan monooleate (Merpoxen SMO 200QL)	$C_{64}H_{124}O_{26}$	15	0.099

All three surfactant feature suitable properties to formulate clean water-in-fuel emulsions.

2.3 Microstructure and formation kinetics

In this section, the fundamentals of the structural exploration techniques used in this work are introduced. Dynamic light scattering (DLS) and small angle neutron scattering (SANS) were applied. A stopped-flow setup was used to determine the formation kinetics of the microemulsified fuels.

2.3.1 Dynamic light scattering

Dynamic light scattering (DLS) is a method to size submicron particles by measuring their diffusion in emulsions and suspensions. The *Stokes-Einstein* equation relates the diffusion coefficient and the particle size which is valid for spherical particles and very low concentrations. Quasi-elastic light scattering (QELS) and Photon correlation spectroscopy (PCS) are synonyms for DLS. The time-resolved measurement of the scattered light intensity from a sample cell that contains the particle system in a solvent is the basic of the DLS-measurement principle. Due to thermal energies the particles undergo a *Brownian motion*, the intensity oscillates around an average value. Those fluctuations contain information about the diffusion coefficient of the particles depending on their sizes. The schematic shown in figure 2-27 shows the DLS set-up.

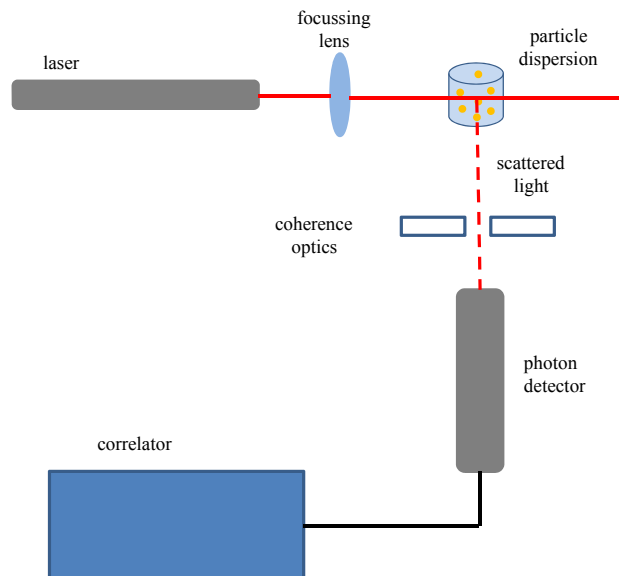


Figure 2-27: Schematic illustration of the dynamic light scattering set-up for the determination of the water domain sizes.

The sample was prepared in a cylindrical sample tube and is fixed in a thermostated toluene bath with $\Delta T \pm 0.05$ °C temperature stability. The instrument was equipped with a He/Ne laser ($\lambda = 633$ nm) as a light source. The detector collected the scattered light $I(q, t)$ from the particles under scattering angles at $30^\circ < \theta < 150^\circ$ and a photomultiplier was used as a detector to count the impinging photons. The photon count rate was taken as an equivalent to the intensity. A computer was used for the data output and handling.

A commercially available device (ALV, Langen, Germany. Type: ALV/SP-86#059 Laser Goniometer) is used for DLS experiments in this work. The temperature of the sample tube was measured with a high precision thermometer with a PT100 temperature sensor (Greisinger GMH 3710, $\Delta T \pm 0.05$ °C). For the evaluation of the results the program package BATCON [132] is used. In order to extract the time-field correlation function $g^{(1)}(q, \tau)$ and the distribution function $A(\Gamma)$ the program package CONTIN [133, 134] is used.

The scattered light is detected at a constant angle θ which is related to the scattering vector q . The scattering vector q is defined as:

$$q \equiv |\vec{q}| = \frac{4\pi}{\lambda} \sin \frac{\theta}{2} \quad (21)$$

where n is the refractive index of the medium and λ_0 is the wavelength of the incident beam in vacuum. Due to the *Brownian motion* a time dependant fluctuation of the scattered intensity $I(q, \tau)$ is observed. Those fluctuations are described with a second-order autocorrelation (For a more detailed description see e.g. [135]:

$$g^{(2)}(q, \tau) \equiv \frac{\langle I(q, 0) I(q, \tau) \rangle}{\langle I(q, t) \rangle^2}. \quad (22)$$

For the scattering data analysis the time-field correlation function is usually used:

$$g^{(1)}(q, \tau) \equiv \frac{\langle E(q, 0) E^*(q, \tau) \rangle}{\langle I(q, t) \rangle^2} \quad (23)$$

The *Siegert* equation relates the second-order autocorrelation function with the first-order autocorrelation function as:

$$g^{(2)}(q, \tau) = 1 + \beta (g^{(1)}(q, \tau))^2 \quad (24)$$

where the parameter β is the coherence factor and has typically values of $\beta = 0.9 - 1.0$.

The field correlation function for monodisperse particles of size x and translational diffusion coefficient D_t is a exponential decay function:

$$g^{(1)}(q, \tau) = \exp(-D_t q^2 \tau). \quad (25)$$

A connection between the particle size and the translational diffusion coefficient can be obtained from a force balance between the fluid friction and the thermodynamic osmotic force and is named *Stokes-Einstein* relation:

$$D = \frac{k_B T}{6 \pi \eta r_s} \quad (26)$$

where k_B is defined as *Boltzmann* constant, T as the temperature and η as the viscosity.

2.3.2 Small angle neutron scattering

Scattering techniques are widely applied to clarify the structure of inhomogeneous media. The incoming radiation beam interacts with the sample and delivers a scattering pattern due to a large difference in the scattering length of the different domains.

Radiation passes through a particle and is mainly transmitted without any interaction with the sample. A small part of the radiation might interact with the sample and is scattered at the scattering angle θ .

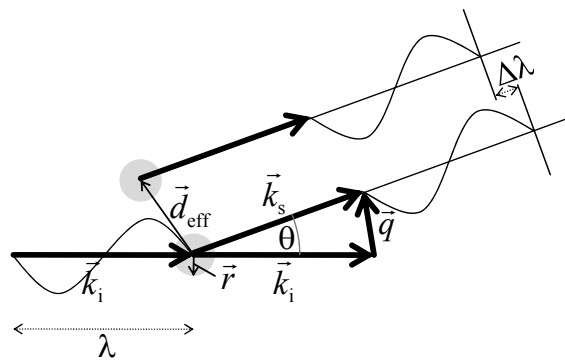


Figure 2-28: Schematic drawing of the scattering for a spherical droplet with the radius \vec{r} . The incident beam is scattered at an angle θ , which influences the absolute value q (taken from [69]).

As shown in figure 2.28, the incident neutron radiation \vec{k}_i is elastically scattered by scattering vector \vec{q}

$$\vec{q} = \vec{k}_s - \vec{k}_i, \quad (27)$$

into the scattering direction with the wave \vec{k}_s

$$|\vec{k}_i| = |\vec{k}_s| = \frac{2\pi}{\lambda}, \quad (28)$$

$$q \equiv |\vec{q}| = \frac{4\pi}{\lambda} \sin \frac{\theta}{2}. \quad (29)$$

If the scattering process is elastic, the absolute value of the wave vectors is equal: $k_i = k_s$ (equation 28). According to wave-particle dualism, the moment of the neutrons $\vec{p} = \hbar \vec{k}$ (with the Planck constant $\hbar = h / 2\pi$) are connected by the *de Broglie* relation:

$$\lambda = \frac{h}{\vec{p}} = \frac{h}{m_n |\vec{v}|}, \quad (30)$$

where m_n is the neutron rest mass and v the velocity.

Constructive interference, which depends on the internal structure of the particle, is described by the *Bragg* law

$$n\lambda = 2d \sin \frac{\theta}{2} \quad (31)$$

connecting the length scale d of the internal structure with the scattering pattern. By combining (29) and (31), the structural length scale d is related to the scattering vector q (for $n = 1$ for the first maximum of interference) is

$$d = \frac{2\pi}{q}. \quad (32)$$

A detailed description for the data treatment is given in chapter 6.2.

2.3.3 Formation kinetics

The formation kinetics of microemulsions is a rather neglected issue although it offers a fundamental understanding regarding the adsorption and self-aggregation of amphiphiles.

First investigations were performed on aqueous-solutions (H_2O - surfactant) while studying the formation kinetics of micelles in those systems [136, 1367]. *Anainsson* and *Wall* developed a theoretical model, describing the formation kinetics and mechanism of micelles in 1974 [138, 139]. Assuming the formation of micelles as an association (and dissociation) of monomers in unitary steps are then:



where A_s represents an aggregate containing s surfactant monomers, k^+ and k^- the rate constants for the association/dissociation reactions of one amphiphil ion to/from micelles. A_1 denoting surfactant monomer, while A_2 denoting the dimer etc. Introducing the relative deviation from equilibrium

$$\xi_s = (A_s - \overline{A_s}) / \overline{A_s} \quad (34)$$

while using the equilibrium relation

$$k_s^+ \cdot \overline{A_1} \cdot \overline{A_{s-1}} = k_s^- \cdot \overline{A_s} \quad (35)$$

thus a reaction flow in aggregation space can be written as

$$J_s = -k_s^- \cdot \overline{A_s} \cdot [\xi_s - \xi_{s-1} \cdot (1 + \xi_1) - \xi_1] \quad (36)$$

If ξ is so small that it can be neglected, this equation turns into the form

$$J_s = -k_s^- \cdot \overline{A_s} \cdot [\xi_s - \xi_{s-1} - \xi_1] \quad (37)$$

The deviation of the system from the equilibrium state can therefore be defined as

$$\frac{dA_s}{dt} = J_s - J_{s-1} \quad (38)$$

The existence of two relaxation processes related to the equilibrium state are divided into a fast process related to the formation of micelles from monomers, which can be expressed as a monoexponential process with a time constant τ_1 and a slow process (τ_2) which is attributed to the almost finished micelles passing through the intermediate state.

2.4 Combustion parameters

In this section, the basic characteristic engine and operation parameters will be explained for an improved understanding of the combustion test results.

Diesel engine

A diesel and a gasoline engine are internal combustion engines that convert chemical energy in fuel to mechanical energy in order to move the pistons, which are connected via connecting rail to the engine's crankshaft. The linear motion of the piston is changed via crankshaft into the rotary motion which is needed for the propel force of the vehicle's wheels. Combustion process of the diesel engines differs from the gasoline engines. Both processes release energy, when fuel reacts chemically with oxygen in the air and the combustion, in the form of series of small explosions, takes place. In diesel fuel engines a self-ignition starts the combustion, whereas gasoline engines work with induced ignition from a spark plug. Figure 2-29 shows a schematic diesel fuel ignition.

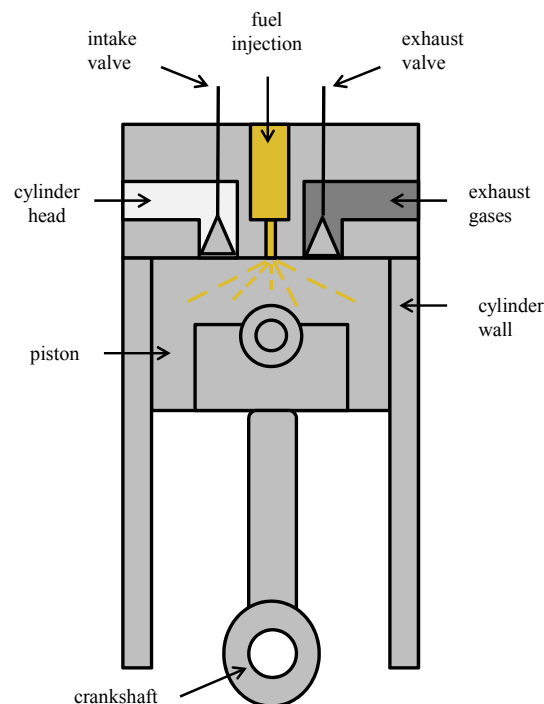
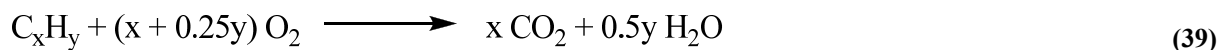


Figure 2-29: Schematic drawing of a diesel engine. Chemical energy in fuel is converted to mechanical energy in order to move the pistons. The four-stroke cycle is characteristic for a compression-ignition engine.

Diesel engines, also known as compression-ignition engines, utilise four strokes. At the first stroke the piston is pulled towards the crankshaft while the inlet valve is open, air is drawn into the combustion chamber. At the second stroke (compression stroke) both valves are closed and the piston is pulled towards the cylinder head. Near the top dead center (TDC) diesel fuel will be injected and ignites spontaneously due to heated air. At the power stroke (third stroke), the combustion releases heat and produces exhaust gases, driving the piston downward (bottom dead center; BDC). At the last stroke (exhaust stroke; fourth stroke), the exhaust valve is opened and gas is pushed by decline of the piston to TDC past the valve and exits the engine. The cycle begins again with the first stroke.

Fuel/Air mixtures

The ratio of fuel to air by volume is significant for complete oxidative combustion of the fuel. The basic combustion process equation for a hydrocarbon follows an oxidation represented as:



A non stoichiometric fuel/air ratio can lead to incomplete combustion and high exhaust gas emissions are produced. The stoichiometric fuel/air ratio L_{st} is defined as the stoichiometric air mass $m_{air,st}$ to the fuel mass m_F . The combustion air approximately contains 21 vol.% oxygen and has to be considered for the calculation of L_{st} , which is described as:

$$L_{st} = \frac{m_{air,st}}{m_F} \quad (40)$$

The fuel/air relation λ is defined as the ratio of the actual fuel/air mass ratio m_{air} to the stoichiometric fuel/air ratio $m_{air,st}$:

$$\lambda = \frac{m_{air}}{m_{air,st}} \quad (41)$$

A mixture with excess air ($\lambda > 1$) is called a fuel-lean mixture, a mixture with lack of air ($\lambda < 1$) is a fuel-rich mixture. A stoichiometric mixture is achieved at $\lambda = 1$.

Exhaust gas emissions can be minimised if optimal combustion is achieved. The amount of carbon monoxide (CO), non-combusted residua hydrocarbons (HC) and nitrogen oxides (NO_x) are connected with the fuel/air ratio λ , as shown in figure 2-30.

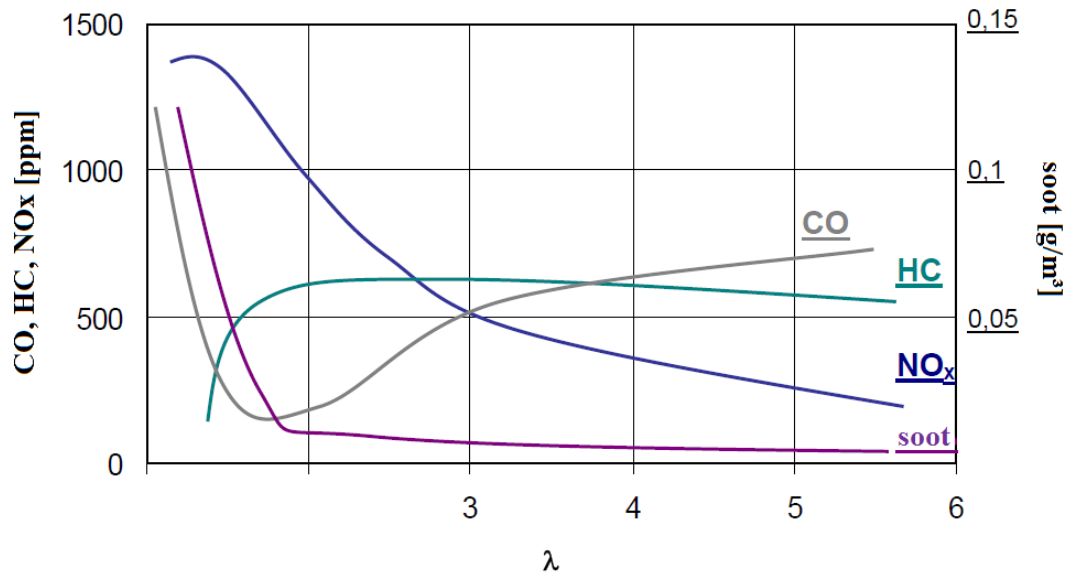


Figure 2-30: Overview of exhaust emissions (CO, HC, NO_x, soot) in dependence of the air/fuel-ratio λ (redrawn and modified from [140]).

Lower heating value (LHV)

The lower heating value (*LHV*) of a fuel is defined as the maximum amount of heat by combusting a specified quantity of fuel while condensation of water does not appear. The condensation enthalpy of water is not converted into heat and is therefore deducted from the heating value of the fuel. The sum of all reaction enthalpies of the compounds in the fuel denotes the heating value and can be expressed after *W. Boie* [141] as

$$LHV = 34.8c + 93.9h + 6.3n + 10.5s - 10.8o - 2.5w \quad (42)$$

where the co-efficients c , h , n , s , o , w are mass fractions of carbon, hydrogen, oxygen, sulfur, nitrogen and water containing in the fuel mixture.

Efficiency

Combustion in diesel engines operates like the constant pressure cycle. This idealised process has peak efficiencies around 60 % while the efficiency of the real process is given by about 40 %.

The four-stroke cycle begins with an isentropic (adiabatic) compression (1-2) as shown in figure 2-31. Subsequently, an atomised mist of diesel fuel is injected into the compressed air (at temperatures to allow ignition of the fuel mist) while expanding the gas at constant

pressure (2-3). Then, the gas expands isentropic (adiabatically) as a power stroke (3-4) and the exhaust valve is finally opened to release exhaust gas at constant volume.

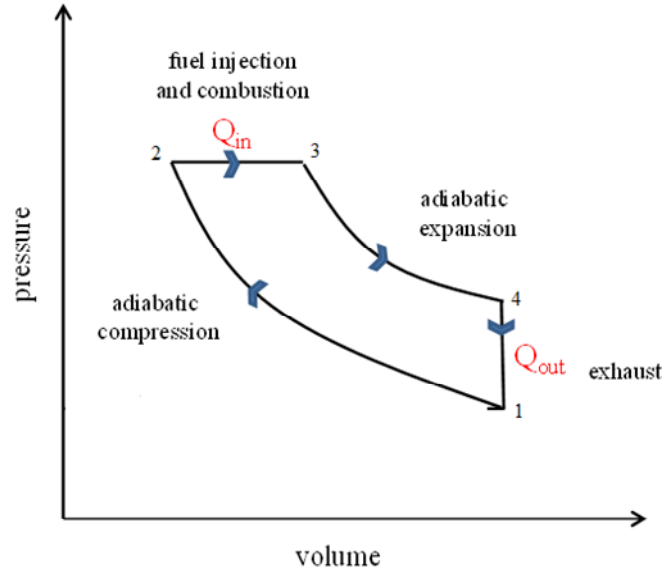


Figure 2-31: Schematic illustration of the diesel cycle. The four-stroke cycle begins with an adiabatic compression (1-2), followed by the fuel injection at constant pressure (2-3). Next, the piston expands adiabatically as a power stroke (3-4). Finally, exhaust gas is released at constant volume (4-1). (redrawn and modified).

The thermal efficiency η_{th} is defined as a percentage of heat energy that is transformed into work:

$$\eta_{th} = \frac{P_{th}}{\dot{Q}} \quad (43)$$

while P_{th} is the engine's power output and \dot{Q} is the heat transfer.

The efficiency η_e is defined as the ratio of the engine's power output P_e to the energy in the feeding fuel:

$$\eta_e = \frac{P_e}{\dot{m}_F \cdot LHV} \quad (44)$$

The energy input is related to the fuel mass flow \dot{m}_F and its lower heating value LHV . The fuel mass flow is given by

$$\dot{m}_F = \frac{d m_F}{d t} = \rho_F \frac{d V_F}{d t} \quad (45)$$

where V_F is the volume of fuel and ρ_F the density of fuel.

The engine's power output P_e results from the torque M at a given rotational speed n

$$P_e = M 2 \pi n \quad (46)$$

The brake specific fuel consumption b_e describes the energy input relative to the engine's power output:

$$b_e = \frac{\dot{m}_F}{P_e} = \frac{1}{\eta_e \cdot LHV} \quad (47)$$

2.4.1 Diesel injection

The physics of spray formation are highly complex. In order to calculate the temporal distribution of the liquid and the gas phase, numerical methods, like CFD, are used.

In this chapter the fundamentals of liquid sprays regimes, droplet formation and breakup-zones are presented.

Spray formation

In diesel engines the fuel atomisation process strongly influences combustion and exhaust emission [143]. In figure 2-32 the disintegration process of the fuel injection is shown. The liquid spray can be characterised by two regimes: the primary and the secondary breakup-zone. The first disintegration of the liquid into big droplets and ligaments near the nozzle is called the primary breakup-zone. The further breakup of droplets into smaller ones is called the secondary breakup-zone. Due to the velocity between liquid and gas, aerodynamic forces of the gas generate small droplets. For high pressure injection the effects of cavitation and turbulence may already occur inside the nozzle hole. High pressure is subjected to the liquid inside the holes, while at the inlet of holes the pressure rapidly decreases. The formation of cavitation structures occurs. These structures extend and leave the nozzle while collapsing [144, 145].

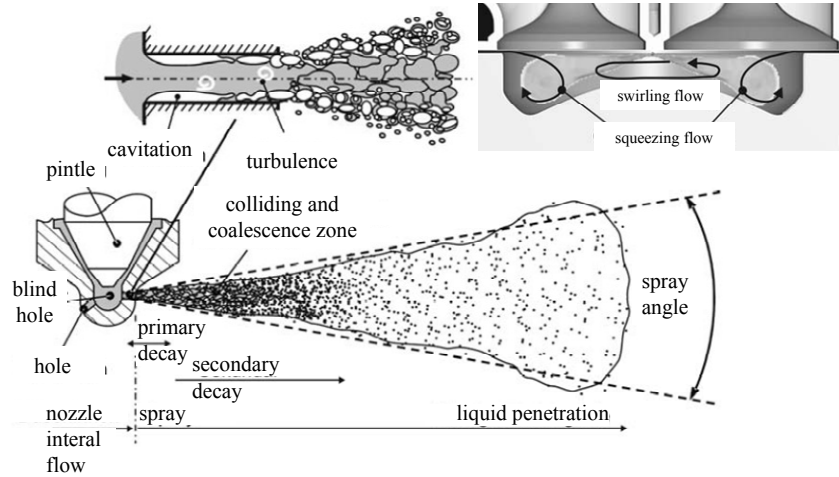


Figure 2-32: Schematic illustration of the spray formation (according to [146], adapted from [147]).

Breakup-zones

The disintegration of the liquid is divided into two mechanisms. The primary breakup-zone is identified by the droplet size and its breakup length. The secondary breakup-zone is also characterised by the size of the droplets. The physical properties of the fuel influence the droplet size and the breakup-length. The velocity between gas and liquid, as well as pressure and temperature during combustion, plays an important role in the characterisation of the two breakup-zones.

The most important and interesting mechanism is the primary breakup-zone. It determines the droplet sizes and the evaporation behaviour, which are the basics of the secondary breakup-zone.

Primary breakup-zone

The shape, structure and penetration length of the spray, as well as the droplet sizes are determined by the disintegration of the liquid phase. Those characteristics are strongly influenced by the physical properties of the liquid, like density, viscosity and surface tension. The primary breakup-zone is divided into four regimes: *Rayleigh*-, first and second wind-induced- and atomisation regime. To distinguish those regimes, the *Ohnesorge number* (Oh), the *Reynolds number* (Re) and the *Weber number* (We) are introduced [146]:

$$Oh = \frac{\eta_L}{\sqrt{\rho_L \sigma D_0}} = \frac{\sqrt{We}}{Re} \quad (48)$$

where the *Reynolds number* (Re) is defined as:



$$R_e = \frac{\rho_G D_0 \rho_L}{\eta_L} \quad (49)$$

The *Reynolds number* (R_e) predicts laminar or turbulent flow in different flow situations. Turbulent flow occurs at high *Reynold numbers*, while laminar flow occurs at low *Reynold numbers*. The *Reynolds number* is the ratio between inertial and viscous forces.

And the *Weber number* (We) is expressed as:

$$W_e = \frac{\rho_G D_0 v^2}{\sigma} \quad (50)$$

where σ is the surface tension, ρ_G is the density of the gas, ρ_L is the density of the liquid, η_L is the dynamic viscosity, v is the jet velocity and D_0 is the diameter of the nozzle. The *Weber number* is the ratio between inertial and surface tension forces, while the *Ohnesorge number* can then be seen as a ratio between viscous forces and surface tension forces.

Secondary breakup

Due to aerodynamic forces that are induced by the relative velocity between the droplets and the surrounding gas, the droplets are disrupted into smaller droplets.

The disintegration of droplets is based on instable growth of waves, which occur on the gas-liquid interface. With the *Weber number* (W_e) the processes at the secondary breakup can be identified:

$$W_e = \frac{\rho_G dv^2}{\sigma} \quad (51)$$

where the nozzle diameter D_0 is replaced with the droplet diameter d before breakup. The surface tension σ rises with a decreased droplet diameter. Consequently, the relative velocity between liquid and gas has to be higher to reach disintegration.

The different breakup regimes are approached by numerical simulations and schematically shown in figure 2-33.

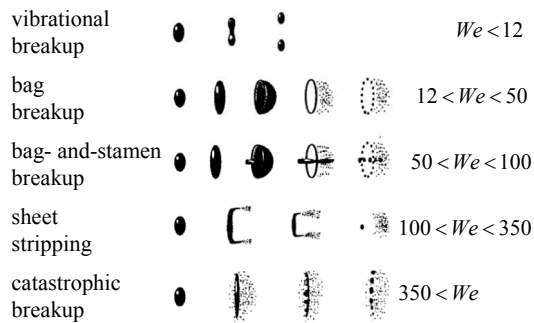


Figure 2-33: Schematic illustration of the secondary breakup regimes in dependence of the *Weber number* of droplets (according to [148], taken from [60]).

All breakup regimes in the engine occur at the same time. Most of the breakups take place close to the nozzle, where the *Weber number* is high. Due to lower relative velocities far from the nozzle, the breakup is less strong; the *Weber number* is lower.

2.4.2 Diesel spray atomisation

As the piston reaches the end of the compression stroke (top dead center), the fuel is injected into the combustion chamber. Usual diesel injectors have nozzle size diameters of approximately 200 μm , while the length of the nozzle hole is approximately 1 mm. The injection pressure amounts up to 2000 bar, thus the jet velocity reaches values of 500 m/s or more. These conditions atomise the liquid fuel into small droplets. Evaporation and mixing with the compressed air of the combustion chamber follow. Due to the high pressure and temperature above fuel's ignition point, spontaneous ignition occurs. The formation of a quasi-steady diesel jet is shown in figure 2-34.

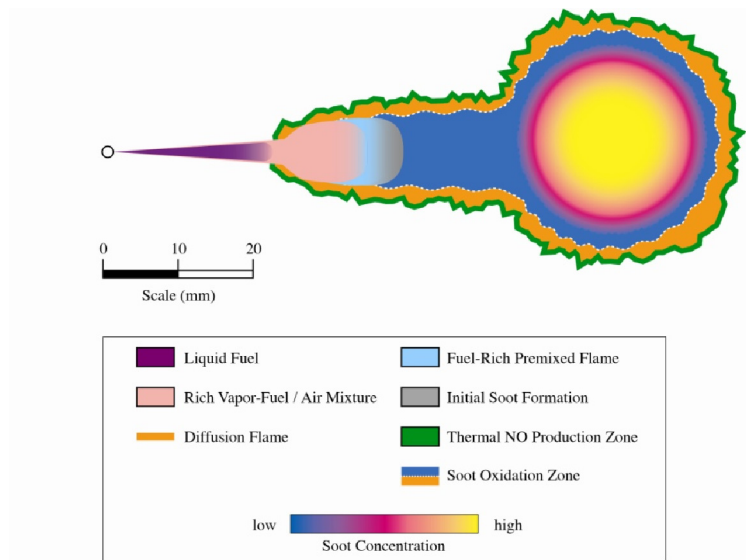


Figure 2-34: Schematic drawing of the diesel spray atomisation. Soot precursors and unburnt hydrocarbons are formed in the periphery of the premixed flame (redrawn and modified after [149]).

The fuel penetrates into the combustion chamber and evaporates due to high temperatures. The liquid length remains relatively constant until the end of injection. In the fuel-rich premixed reaction zone, which occurs beyond the liquid length, the rich premixed fuel and air are still heated till they react. The soot precursors, like C_2H_2 , C_2H_4 and unburnt hydrocarbons, are formed in the periphery of the premixed flame and are converted to soot particles. The soot particles grow in size through agglomeration, coagulation and surface growth while reaching the spray head. In the soot oxidation zone, the soot particles are all oxidised as they mix with the surrounding air at high temperatures [150].

2.4.3 Internal combustion emissions

In the previous chapter, the physical and thermodynamical properties of internal combustion engines were presented. The complex physical and chemical interactions during combustion and the pollutant formation are discussed in the present chapter.

The combustion of fuel results mainly in the emission of nitrogenoxides (NO_x), particulate mass (PM), unburnt hydrocarbons (HC) and carbon monoxides/dioxides (CO , CO_2). During injection, the temperature of the combustion chamber is approximately $440^\circ C$, thus enabling the droplets to evaporate rapidly. Due to diffusion of the fuel vapour with the gas phase in the combustion chamber, an ignitable mixture is formed. Finally, ignition and combustion occur [151]. The oxidation of the hydrocarbon chains in fuel follows the model given in figure 2-35, which is initiated by an attack of $\cdot H$ -, $\cdot O$ - or of $\cdot OH$ -radicals on a CH -bound. The resulting

alkyl-radical is degraded in a thermal reaction to an alkene and a shorter chained alkyl-radical. Those radical pyrolysis steps continue till relatively stable methyl- and ethyl-radicals are formed. The rate determining step in the reaction mechanism is the following oxidation of the methyl- and ethyl-radicals. Methyl-radicals mainly react with oxygen leading to the formation of formaldehyde which is then degraded to CO and $\cdot\text{H}$ due to a thermal H-abstraction. Additionally, recombination reactions occur in dependence of the stoichiometric composition of the fuel/air ratio.

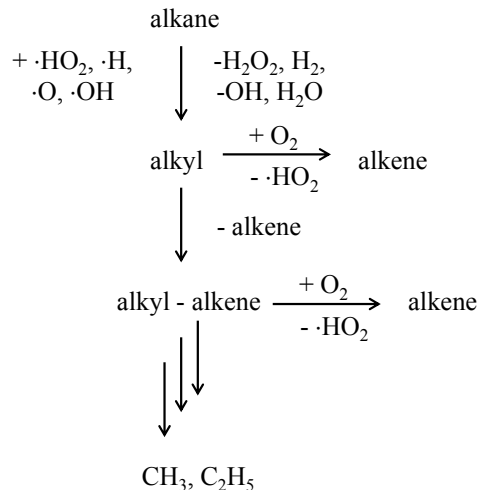


Figure 2-35: Schematic reaction mechanism for the radical pyrolysis of long chained aliphatic hydrocarbons under formation of CH_3 , C_2H_5 [151].

Unburnt hydrocarbons (HC)

Hydrocarbons are fragments of unburnt fuel molecules. The main reason for incomplete combustion is the flame quenching at cold cylinder walls. Due to high heat losses close to the cylinder walls, the laminar flame, which spreads near the cold wall, may be quenched. The ignition of the fuel is oppressed and unburnt fuel leaves the combustion chamber. Another reason is a fuel spray area, where the mixture composition is too rich to oxidise. Additionally, the geometry of the injection nozzle plays an important role in the emission of unburnt hydrocarbons. Due to the evaporation of unburnt fuel from the blind hole volume of the nozzle, an increased HC-formation and -emission occur [56].

Diesel Particulate matter

All non-gaseous emissions collected by a filter belong to particulate matter emissions. Particulate matter emissions consist of organic and inorganic particles; figure 2-36 shows an overview of those particles.

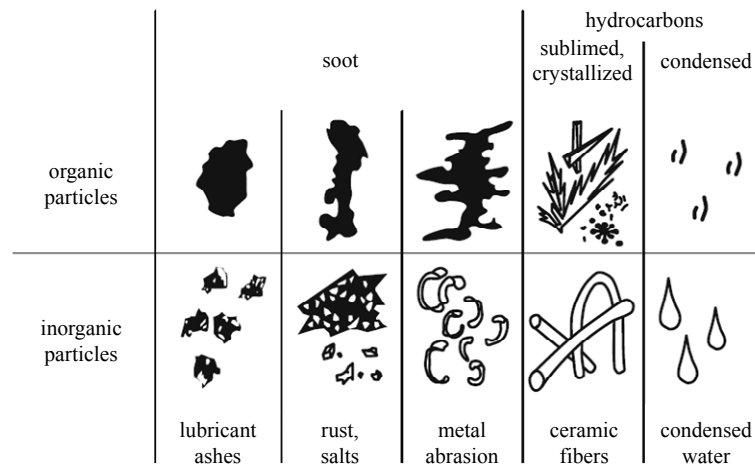


Figure 2-36: Partition of organic and inorganic particles and their subdivisions (according to [152], taken from [60]).

The organic particles are separated into soot particles and hydrocarbons. The hydrocarbons can occur in a crystallized or condensed form. The inorganic particles can contain rust and salts, as well as lubricant ashes and metal abrasion from mechanical friction. Ceramic fibers from combusted lubricants and condensed water are also collected in the filter. A particle analysis in soluble organic fraction (SOF), soluble inorganic fraction (SIOF) and insoluble fraction (ISF) is a standard to determine the particulate matter emissions.

Polycyclic aromatic hydrocarbons (PAHs)

Polycyclic aromatic hydrocarbons (PAHs) consist of a large group of organic compounds with two or more aromatic rings. Due to incomplete combustion, small hydrocarbon chains, C_1 (CH , CH_2) and C_2 (C_2H_2), are formed in the flame front. Those can form C_3H_3 molecules, which can compose ring structures through recombination [153] and rearrangement (figure 2-37).

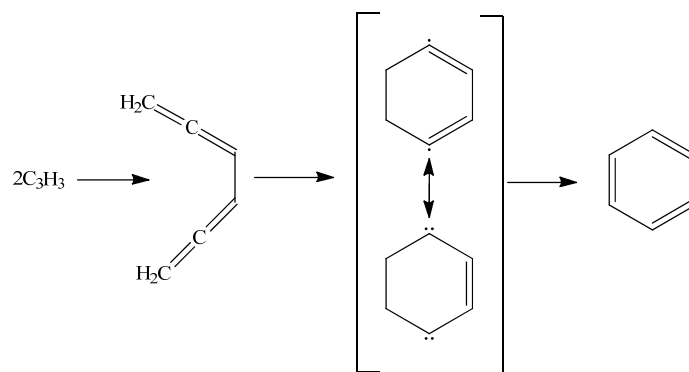


Figure 2-37: Schematic drawing of the ring structure formation (according to [150]).

Due to addition of acetylene to a phenyl-radical, a styrol-radical is formed which builds naphthalene after another addition of acetylene. The growth of these *polycyclic aromatic hydrocarbons* (PAHs) are the precursors of soot which are fine particles [154-156].

Soot consists of an insoluble carbon nucleus, where inorganic and organic bonds are adsorbed. The organically compounds feature a very high toxically potential with carcinogenic and mutagenic properties. The soot particles sizes can vary from ultra-fine until fine particles with a size range of 10 nm to 2 μm . The fine particles are respirable and therefore dangerous to health [157]. Due to nucleation, PAHs are agglomerated at a molecular mass between 500 and 2000 a.m.u. Based on van der Waals forces, the PAHs are kept together. The particle growth includes surface growth, coagulation and aggregation. The surface growth in a heterogeneous process continues through further addition of acetylene and aromatic, leading to an increased amount of soot but the number of particles remains unchanged. Within the following coagulation, where the particles collide and coalesce, the number of particles decreases without changing the total mass of soot. Aggregation of particles into chains and clusters (of approximately 50 nm) occur, when surface growth is finished. The soot-formation is schematically shown in figure 2-38.

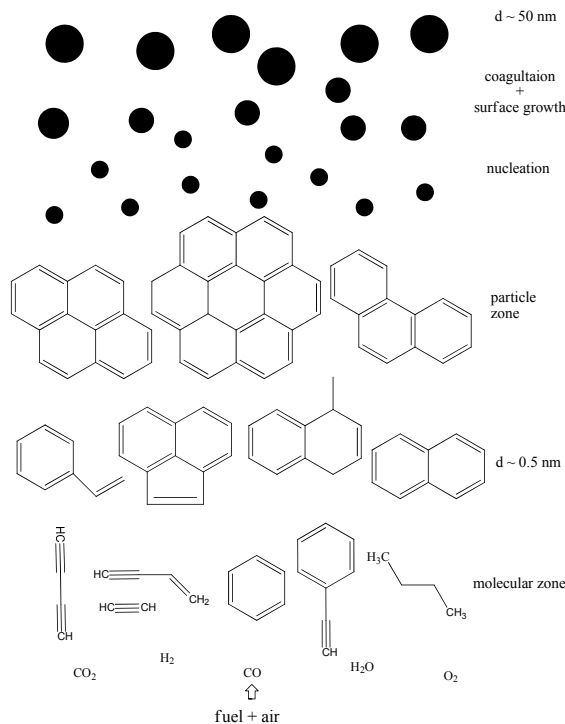


Figure 2-38: Schematic illustration of soot-formation (modified from [150]).

The soot formation is related to the combustion temperature and fuel/air ratio. Relatively low combustion temperatures and lack of air promote the soot formation, while decreasing the NO_x formation. This opposing trend is called *soot- NO_x trade-off*.

NO_x Formation

Nitrogen oxides NO_x formed in the combustion process is referred as a mixture of nitric oxide (NO) and nitrogen dioxide (NO_2). NO_x contribute to the formation of ozone and smog, which are known as human health hazard. Lung irritation is also connected to NO_x emissions.

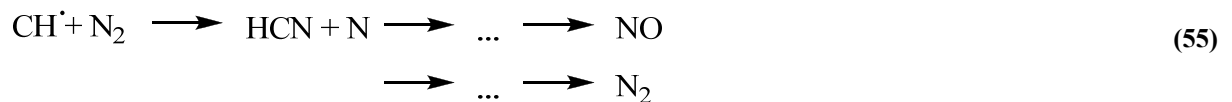
The atmospheric intake-air consisting of about 79 vol.% nitrogen is the major source for nitrogen. NO_x also includes other nitrogen oxides, like N_2O , NO_3 , N_2O_4 and N_2O_5 . In the combustion emissions these nitrogen oxides species are insignificant because they readily react to NO and NO_2 . NO_x emissions from fuel combustion consist over 90 % of NO and 10 % of NO_2 . The formation of NO can be explained by three different mechanisms; one is the *Zeldovich* mechanism, the other is the *Fenimore* mechanism and the final one is the N_2O intermediate mechanism [158].

The *Zeldovich* mechanism includes three elementary reactions:



Due to a high activation energy for the N_2 triple bond-decomposition, the first reaction only proceeds at high temperatures.

In the second mechanism, known as the *Fenimore* mechanism, *prompt* NO is quickly formed in the premixed laminar flame before thermal NO has been formed. Molecular nitrogen reacts with the hydrocarbon radical to hydrogen cyanide (HCN), which is an intermediate to NO formation:



Due to high pressures in the combustion chamber and short residence times of *prompt* NO, the formation is considered insignificant in combustion engines.

The third mechanism includes a N_2O -intermediate, which has to be stabilised through a third molecule (M). The formation of NO is important in fuel-lean and lower temperature conditions ($T < 1800 \text{ K}$).



Two moles of NO are formed per one mole of N_2O . The formation of NO through a N_2O -intermediate is not significant at higher flame temperatures than 1800 K.

Carbon monoxide

Carbon monoxide (CO) emissions from fuel combustion have toxicological effects on humans. The toxic gas is formed from incomplete combustion with lack of oxygen, while carbon dioxide (CO₂) yield from complete combustion. Due to the slow oxidation of carbon monoxide to carbon dioxide, carbon monoxide usually remains as pollutant.

2.4.4 Aftertreatment

In order to control and reduce the exhaust gas emissions during combustion, some aftertreatment systems have been developed.

Exhaus Gas Recirculation (EGR):

A way to reduce NO_x emissions is the exhaust gas recirculation. Inert exhaust gases (up to 40 %) are recirculated back into the intake air. This procedure causes a lower peak cylinder temperature and reduces the NO_x formation. Due to a lower availability of oxygen in the cylinder, the applied system shows a *trade-off* between NO_x and soot. At high EGR-rates, soot emissions increase.

Selective Catalytic Reduction (SCR):

In order to reduce the emission of nitrogen oxides, exhaust gas aftertreatment with a selective catalytic reduction (SCR) catalytic converter is used. Those SCR systems can convert up to 90 % of the nitrogen oxides produced during the combustion process. A schematic drawing of the SCR-system is shown in figure 2-39.

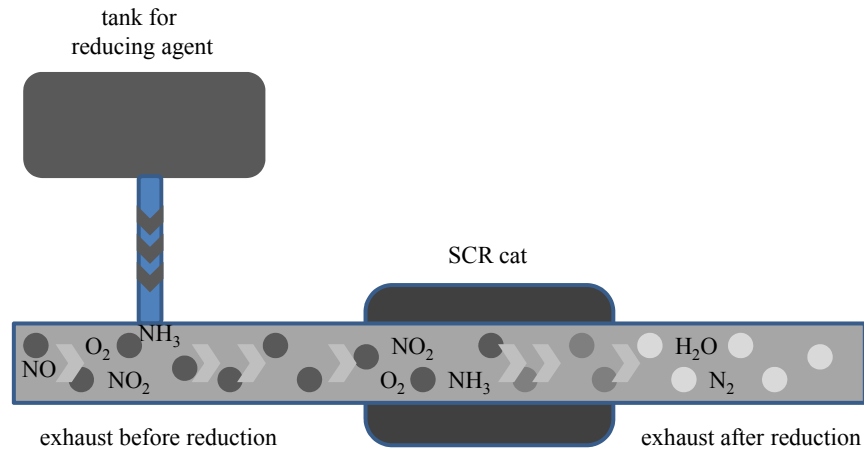
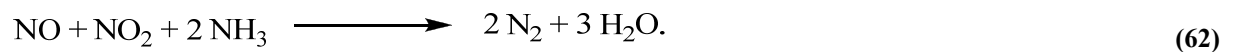
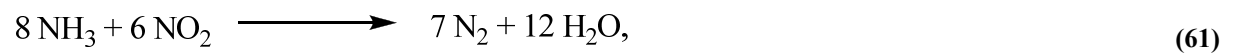
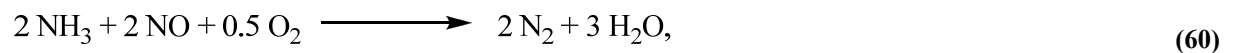
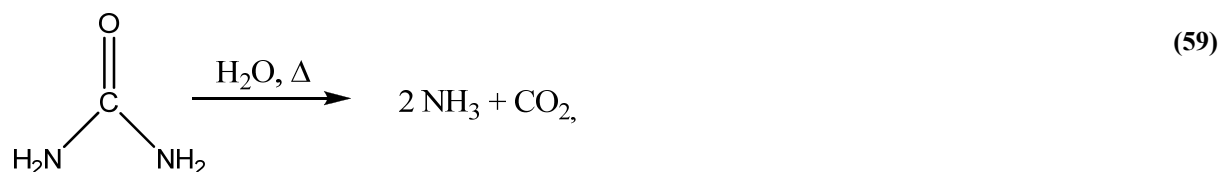


Figure 2-39: Schematic drawing of a selective catalytic reduction (SCR) system to reduce nitrogen oxides to nitrogen (redrawn from [159]).

Urea solutions were applied which release ammonia in a thermal hydrolysis reaction (equation 53). Ammonia reacts with NO_x to convert the pollutants into harmless nitrogen and water. The chemical reduction and its deployment are given in the following equations:



Diesel Particulate Filter (DPF):

Particulate matter is the result of unburnt fuel during the combustion process. Soot emissions can be reduced by using a diesel particulate filter (DPF). Exhaust gases enter an open channel of the filter. The semipermeable walls of the filter allow the gases to pass through, while the soot particles are collected in the DPF. The filter has a thin layer of catalyst than converts the particles to harmless carbon dioxide (CO_2).

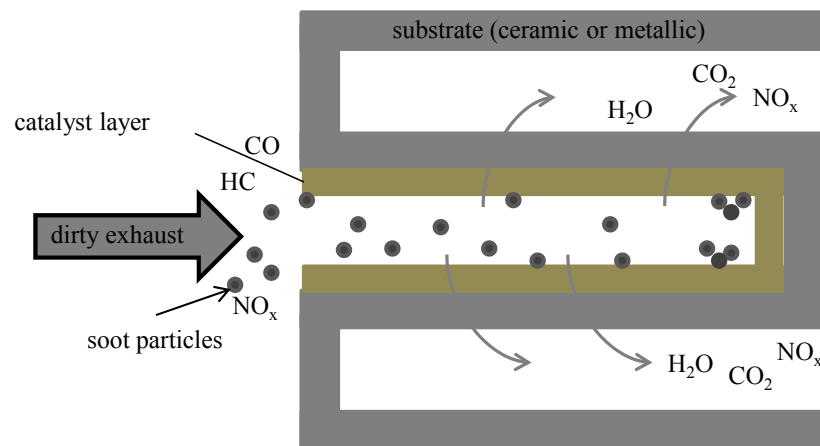


Figure 2-40: Schematic illustration of a diesel particulate filter. Catalyst layer converts soot particles to harmless carbon dioxide (redrawn from [160]).

Diesel Oxidation Catalyst (DOC):

A diesel oxidation catalyst is used to reduce the emissions of unburnt hydrocarbons and carbon monoxide. Those are oxidised over a catalytic surface of a ceramic monolith-core which is coated with platinum, rhodium or palladium. These oxidation reactions take place at relatively low temperatures of about $T = 300\text{ }^{\circ}\text{C}$. Due to lower activation energy, the oxidation of hydrocarbons and carbon monoxide to carbon dioxide and water occurs. Additionally, nitrogen oxide/dioxide is converted by a cerium-(IV)-oxide to harmless nitrogen.

All those aftertreatment-systems are complex, expensive and need an additional modification of the engine. Thus, water containing fuels offer a potential benefit mainly regarding soot- and NO_x -emissions, which were also proved in former studies [55,56, 60,61]. Combustion of water containing fuels avoids the *soot- NO_x -trade-off* and results in a reduction of soot and NO_x -emissions at the same time (figure 2-41).

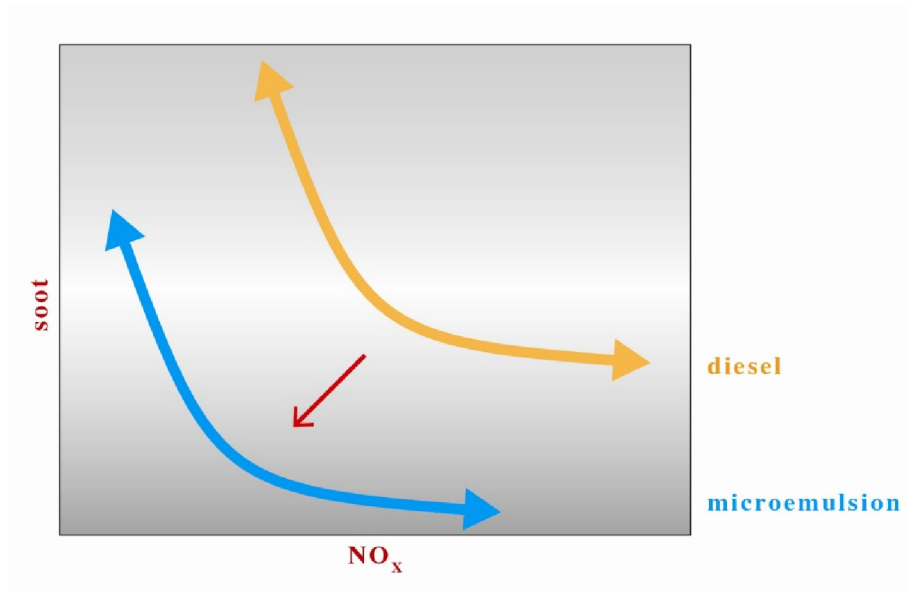


Figure 2-41: Schematic illustration of the *soot-NO_x-trade-off*. A simultaneous reduction of both emissions is very difficult as by rising the combustion temperature, the emission of soot declines while the emission of NO_x increases. In contrast, the emission of NO_x is reduced at the expense of an increased soot-formation at lower combustion temperatures (yellow line). A simultaneous reduction of both emissions is achieved applying water containing fuels (blue line).





3 WATER CONTAINING FUELS

This chapter contains on the one hand the systematic studies of water fuel microemulsions (section 3.1) and on the other hand the one of water fuel nanoemulsions (section 3.5). Accordingly, the analysis of water fuel microemulsions and nanoemulsions usually starts with the right choice of surfactants which consist of completely combustible, inexpensive, green compounds.

The water fuel microemulsions were systematically formulated, characterised and optimised in terms of their phase behaviour (sub-chapter 3.1.1 - 3.1.6). In section 3.2, crucial physical properties of four different water fuel microemulsions (with 0, 8, 16 and 24wt.% water) were determined in order to fulfil the norm according to EN 590. Furthermore, the structural analysis via dynamic light scattering (DLS) and small angle neutron scattering (SANS) are discussed in section 3.3. Formation kinetics of microemulsified fuels varying the water content and the temperature obtained via transmitted light in a stopped-flow system are summarised in section 3.4.

In order to formulate appropriate, low surfactant content water nanoemulsified fuels for load point dependent on injector-blending systems, the water phase has to exhibit an anti-corrosive and a highly lubricating property, which are presented in section 3.5.1. The results of the dynamic light scattering experiments revealing the hydrodynamic radii of water-in-fuel nanoemulsions are shown and discussed in sub-chapter 3.5.2. Various water fuel nanoemulsions with different HLB-values were studied to characterise the dependence of water droplet sizes on the HLB-value.

3.1 Water fuel microemulsions

This section contains the systematic results of the investigations of water containing fuels. Conventional diesel fuel is used as the hydrophobic component which fulfils EN 590. Diesel fuel is a mixture of aliphatic and aromatic middle distillates obtained by crude oil. Accordingly, diesel fuel specifications differ from various fuel grades and from different countries. The important properties which are used to characterise diesel fuel are: density, viscosity, fuel volatility, flash point, lubricity and cetane number. In order to fulfil the norm EN 590, different additives are added to the fuel. For example, anti-foaming agents (polysilane), detergents (amine, amide, poly-alkylamine) to protect against deposit and anti-

corrosive agents (amphiphilic long-chained carboxylate) help to optimise diesel fuel properties. Winter diesel fuel additionally contains agents to lower the cold filter plug point (CFPP).

The characterisation of microemulsions is based upon the determination of the phase behaviour. Former studies on water fuel microemulsions by *Bemert* [56] and *Wulff* [60] were based upon microemulsion systems with several components. Thereby, the initial system of this study was based on water/ammonium nitrate/ethanol as polar component, conventional diesel fuel as oil component and a blend of oleic acid/monoethanolamine/oleic acid diethanolamide as surfactant component.

Phase behaviour

Analysis of water fuel microemulsions usually starts with the determination of the phase behaviour by performing $T(\gamma)$ -sections through the phase prism. Temperature invariance of a water fuel microemulsion is the first essential condition for the use as fuels. The stability of the one-phase region within the entire temperature range has to be ensured. The temperature invariance has to cover a temperature range between -10 and 90 °C. By combining ionic and non-ionic surfactants a temperature invariance state can be achieved (see chapter 2.1.6). In order to reach an optimum load point dependent amount of water, the phase behaviour at different water-to-oil ratios α has to be studied. Due to financial aspects, the microemulsions should contain as less surfactant as possible, thus different parameters (n , δ , ε , ψ and α) were varied to optimise the phase behaviour.

3.1.1 Influence of n -variation on the phase behaviour

The initial system consists of: water/ammonium nitrate/ethanol - diesel fuel - oleic acid/monoethanolamine/oleic acid diethanolamide at $\alpha = 0.5$, $\delta_{(\text{ion})} = 0.7$, $\delta_{(\text{OD4})} = 0.3$, $\varepsilon = 0.004$, $\psi = 0.20$. The studies were started with a variation of the grade of neutralisation n .

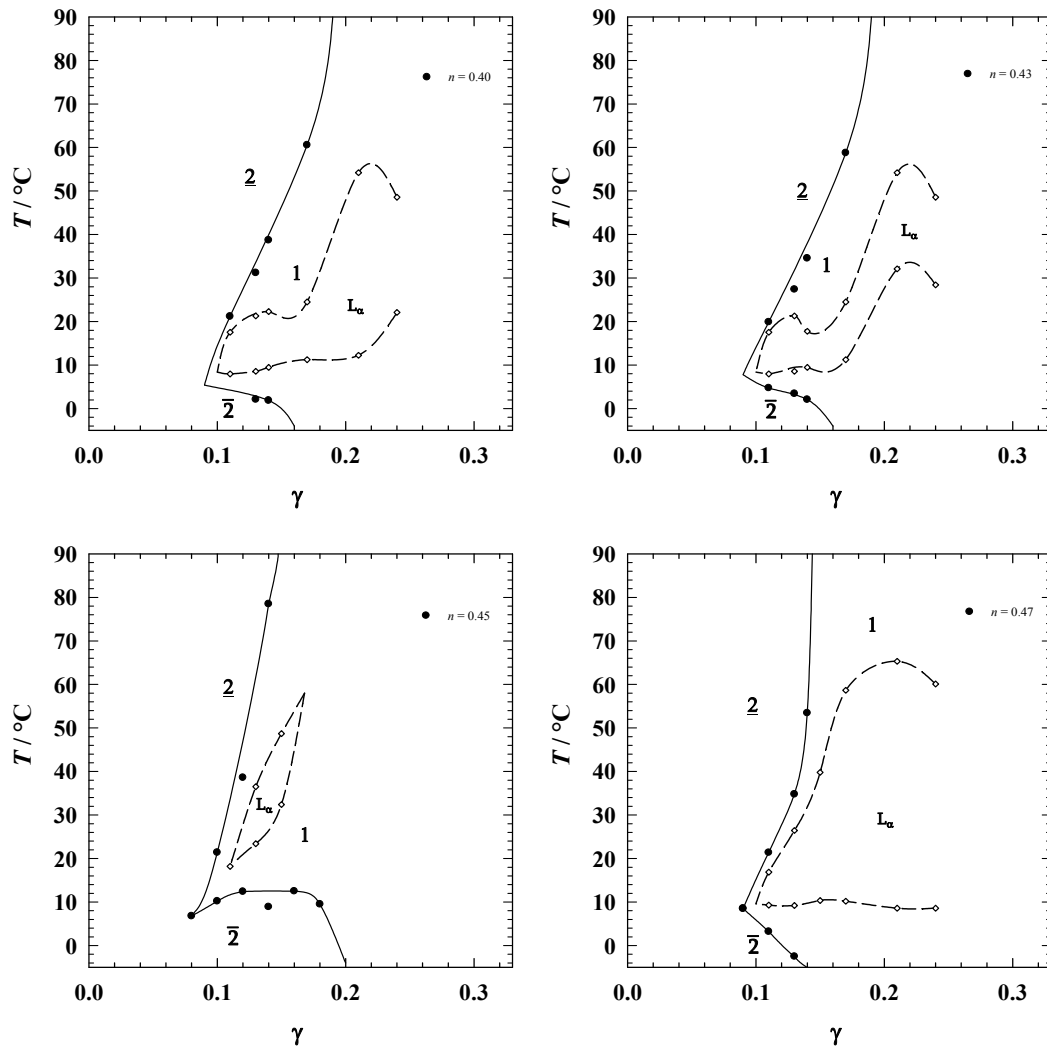


Figure 3-1: Phase diagram of the system water/ammonium nitrate/ethanol - diesel fuel - oleic acid/monoethanolamine/oleic acid diethanolamide at $\alpha = 0.5$, $\delta_{(\text{ion})} = 0.7$, $\delta_{(\text{OD4})} = 0.3$, $\varepsilon = 0.004$, $\psi = 0.20$ with various n ($n = 0.40$; 0.43 ; 0.45 ; 0.47). Ionic phase behaviour and a lamellar region in the one-phase region is observed. The X-point of the systems with $n = 0.40$, $n = 0.43$ and $n = 0.47$ are located at $\tilde{\gamma} = 0.090$, the X-point of $n = 0.45$ is located at $\tilde{\gamma} = 0.080$. The temperature invariance is achieved for $n = 0.45$ at a surfactant mass fraction of $\gamma_{\text{inv}} = 0.205$, the temperature invariant state for other n -values could not be determined due to the expansion of the lamellar phase.

In figure 3-1 the phase diagrams of the system water/ammonium nitrate/ethanol - diesel fuel - oleic acid/monoethanolamine/oleic acid diethanolamide at $\alpha = 0.5$, $\delta_{(\text{ion})} = 0.7$, $\delta_{(\text{OD4})} = 0.3$, $\varepsilon = 0.004$, $\psi = 0.20$ with $n = 0.40$ (top left), $n = 0.43$ (top right), $n = 0.45$ (bottom left) and $n = 0.47$ (bottom right) are presented. At low temperatures $\bar{2}$, a water-in-oil microemulsion phase coexisting with a water excess phase is found. On the contrary, at higher temperatures the state $\underline{2}$, an oil-in-water microemulsion phase coexisting with an oil excess phase is observed. Compared to non-ionic microemulsion systems, the phase behaviour is

inverted, which is characteristic for ionic microemulsions [59]. The X-points of the systems with $n = 0.40$, $n = 0.43$ and $n = 0.47$ are located at approximately $\tilde{\gamma} = 0.090$, while the X-point of the system with $n = 0.45$ is located at $\tilde{\gamma} = 0.080$ and $\tilde{T} = 6.70$ °C. No linear relation between the grade of neutralisation and surfactant concentration $\tilde{\gamma}$ is observed. The phase inversion temperature \tilde{T} slightly grows with increasing grade of neutralisation ($\Delta\tilde{T} = 3.23$ °C between $n = 0.40$ and $n = 0.47$), which corresponds to the evolution with increasing amount of the ionic surfactant in the surfactant mixture. All systems show a region of the coexisting lamellar phase (L_α) in the one-phase region. The lamellar phase features a significantly higher viscosity as well as a phase separation as function of time. Due to those facts, temperature invariance without a lamellar phase is favoured for use as fuels. The system with $n = 0.45$ shows a significant smaller region of the coexisting lamellar phase with a temperature invariant state achieved at a surfactant mass fraction $\gamma_{\text{inv}} = 0.205$. Due to an enlarged lamellar region, temperature invariance state could not be achieved for $n = 0.40$, $n = 0.43$ and $n = 0.47$.

Hence, the δ -variation is now based upon the optimised system water/ammonium nitrate/ethanol - diesel fuel - oleic acid/monoethanolamine/oleic acid diethanolamide at $\alpha = 0.5$, $\delta_{(\text{ion})} = 0.7$, $\delta_{(\text{OD4})} = 0.3$, $\varepsilon = 0.004$, $\psi = 0.20$ and $n = 0.45$.

3.1.2 Influence of δ -variation on the phase behaviour

Surfactants with bio-derived and completely combustible compounds are favoured. In order to increase the efficiency of the system water/ammonium nitrate/ethanol - diesel fuel - oleic acid/monoethanolamine/oleic acid diethanolamide at $\alpha = 0.5$, $\delta_{(\text{ion})} = 0.7$, $\delta_{(\text{OD4})} = 0.3$, $\varepsilon = 0.004$, $\psi = 0.20$, $n = 0.45$, a δ -variation was performed.

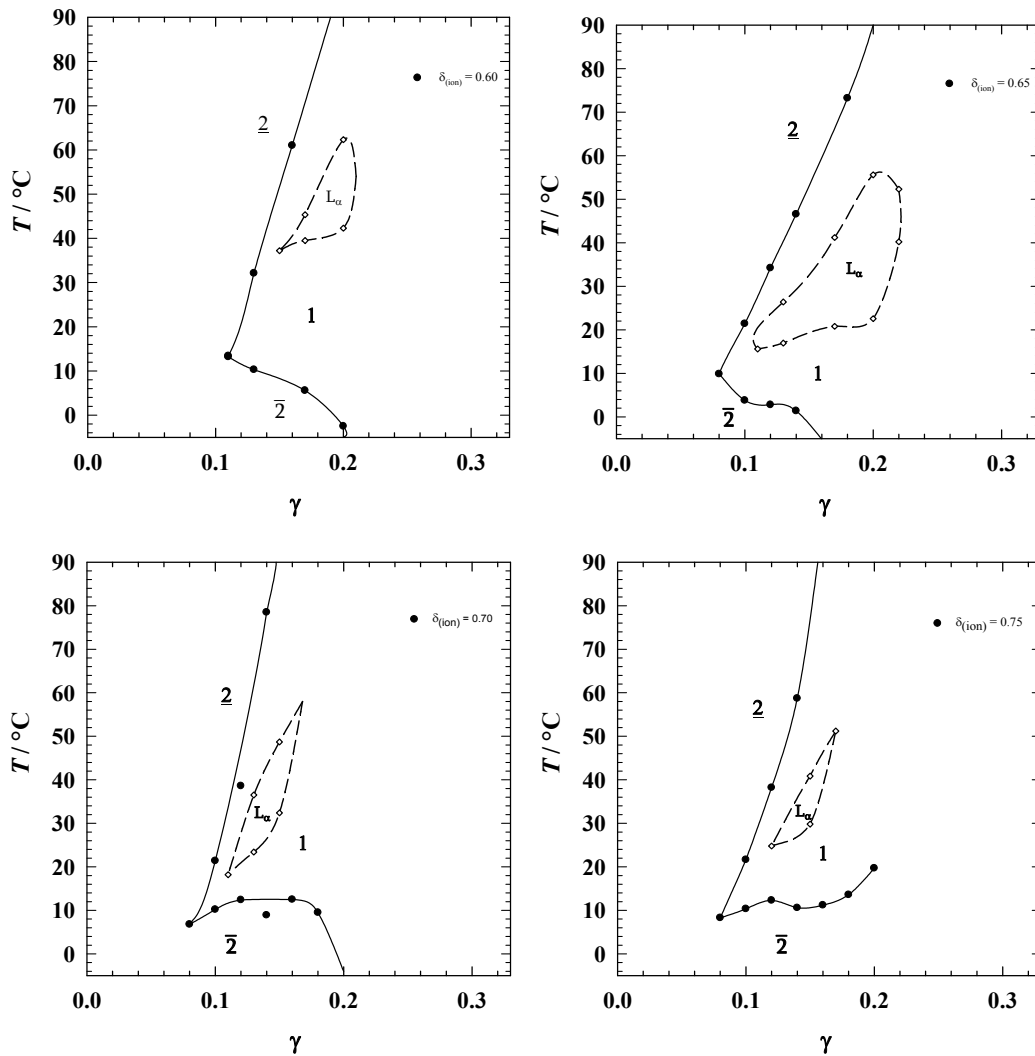


Figure 3-2: Phase diagram of the system water/ammonium nitrate/ethanol - diesel fuel - oleic acid/monoethanolamine/oleic acid diethanolamide at $\alpha = 0.5$, $\varepsilon = 0.004$, $\psi = 0.20$, $n = 0.45$ with various δ . Ionic phase behaviour and an *insular* lamellar region are observed. The X-point is located at approximately $\tilde{\gamma} = 0.08$ with \tilde{T} lower than 10°C for the systems with $\delta_{(ion)} = 0.65$, $\delta_{(ion)} = 0.70$ and $\delta_{(ion)} = 0.75$. Lower phase boundary is shifted to higher temperatures with increasing δ -values.

Figure 3-2 shows the phase behaviour of the system water/ammonium nitrate/ethanol - diesel fuel - oleic acid/monoethanolamine/oleic acid diethanolamide at $\alpha = 0.5$, $\varepsilon = 0.004$, $\psi = 0.20$, $n = 0.45$ varying the δ -value. As already described in figure 3-1, an ionic phase behaviour is observed. The X-points of the systems with $\delta_{(ion)} = 0.65$, $\delta_{(ion)} = 0.70$ and $\delta_{(ion)} = 0.75$ are approximately located at $\tilde{\gamma} = 0.08$ with \tilde{T} lower than 10°C . In all phase diagrams an *insular* area of lamellar phase is observed. Due to an increased viscosity and phase separation as function of time, lamellar regions cannot be used as fuels and should therefore be eliminated. The lower phase boundary is shifted to lower temperatures with

decreasing δ -values. A temperature invariant state is only achieved with the lowest δ -value ($\delta_{(\text{ion})} = 0.60$) at $\gamma_{\text{inv}} = 0.203$. An enhanced efficiency should be achieved at $\delta_{(\text{ion})} = 0.60$ varying further parameters in the multi-component system (ε - and ψ -variation). A smaller δ -value than $\delta_{(\text{ion})} = 0.60$ led to an expansion of the lamellar phase region. Deviations from the trend found by *Kahlweit* and *Strey* [59] which describe the trend of PIT as a function of the mass fraction for “classical” microemulsions (figure 2-9), are related to the present multi-component system with seven components and to the technical nature of the surfactants. The next variation (ε -variation) uses the system water/ammonium nitrate/ethanol - diesel fuel - oleic acid/monoethanolamine/oleic acid diethanolamide at $\alpha = 0.5$, $\delta_{(\text{ion})} = 0.6$, $\delta_{(\text{OD4})} = 0.4$, $\varepsilon = 0.004$, $\psi = 0.20$, $n = 0.45$ as basis in order to suppress the lamellar phase.

3.1.3 Influence of ε -variation on the phase behaviour

The influence of an electrolyte was already discussed in chapter 2.1.9. Like surfactants, the electrolyte has to be fully combustible and should only consist of carbon, nitrogen, oxygen and hydrogen. Phosphor and sulfur are not appropriate due to their further reaction to the correspondent oxoacids acids and its emission during combustion. Therefore, ammonium nitrate (NH_4NO_3 , lyotropic salt) is applied into the water fuel microemulsion. In order to eliminate the coexisting lamellar phase in the one-phase region, the influence of a ε -variation on the phase behaviour was determined.

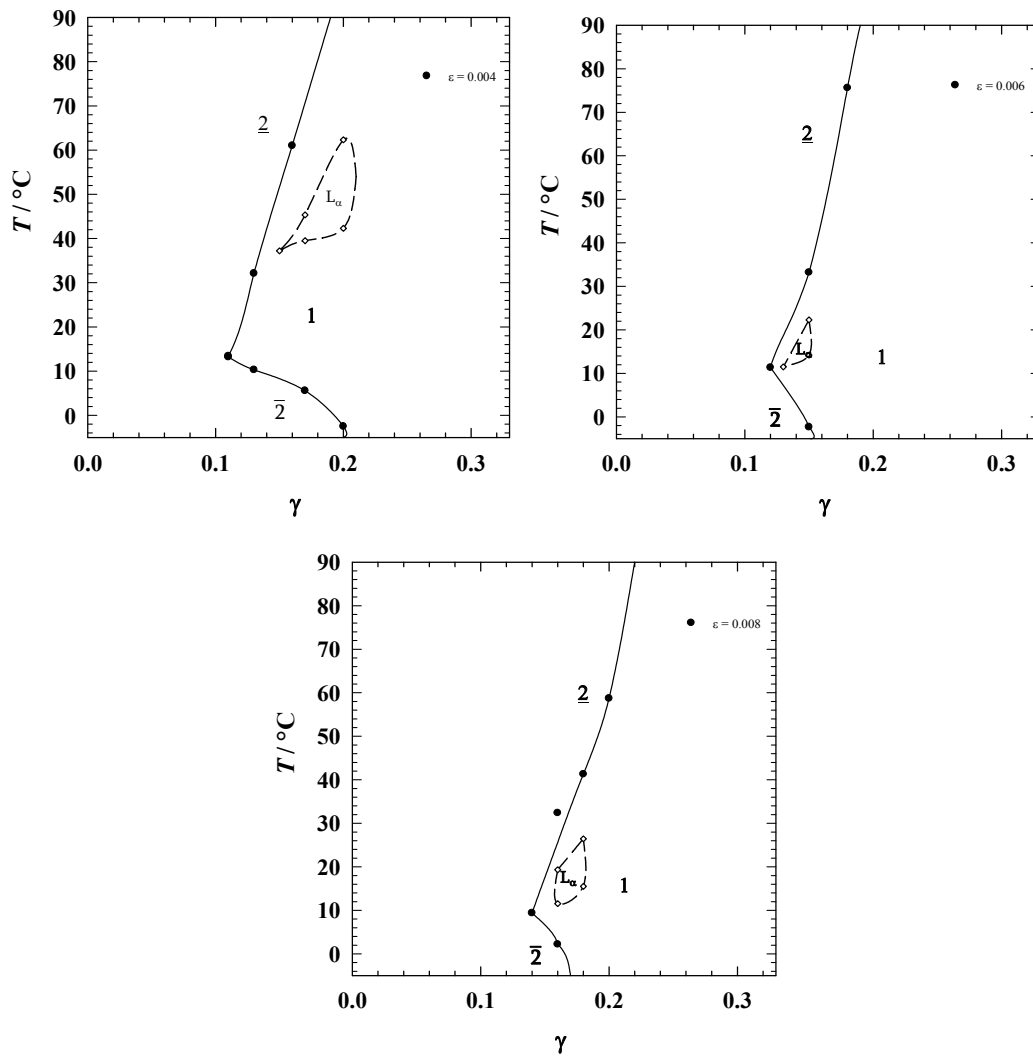


Figure 3-3: Phase diagram of the system water/ammonium nitrate/ethanol - diesel fuel - oleic acid/monoethanolamine/oleic acid diethanolamide at $\alpha = 0.5$, $\delta_{(\text{ion})} = 0.6$, $\delta_{(\text{OD4})} = 0.4$, $\psi = 0.20$, $n = 0.45$ with various ε . Again, ionic phase behaviour and *insular* lamellar region are observed. The temperature invariance of the optimised system with $\varepsilon = 0.006$ (due to a better splitting of the phase boundaries and a smaller lamellar region) is achieved at $\gamma_{\text{inv}} = 0.194$.

The effect of the electrolyte on the lamellar region size and on the *pseudo*-binary side system A - C is crucial regarding the temperature invariant state. Due to a wider spreading of the phase boundaries and a smaller lamellar phase region, the system with $\varepsilon = 0.006$ is regarded as the initial system for the next investigations. The X-point is located at $\tilde{\gamma} = 0.110$ and $\tilde{T} = 11.50^\circ\text{C}$. The smaller lamellar phase region can be explained with a changing curvature of the interface. The electrostatic interference between electrolyte cation and ionic surfactant anion can reduce the size of the electrical double layer (*Debye length*) and therefore influence the curvature of the amphiphilic film. Thus, the curvature of the interface increases

and simultaneously reduces the lamellar phase region. Additionally, the hydration of the electrolyte by water molecules causes a more polar A-component. Hence, the surfactant head group becomes more hydrophilic (lower miscibility gap between water and surfactant is reduced), and the phase inversion temperature \tilde{T} is shifted to lower temperatures [161].

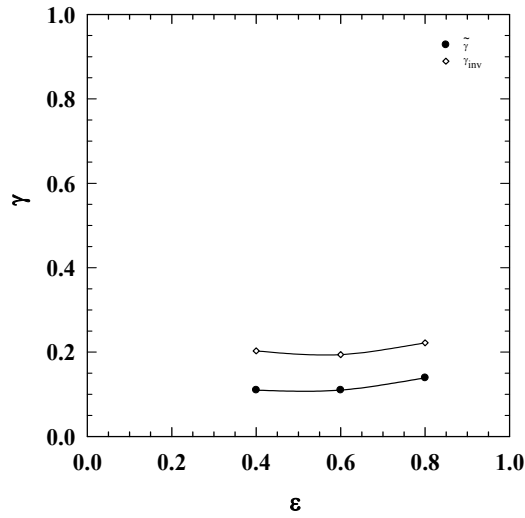


Figure 3-4: Efficiency $\tilde{\gamma}$ (full circles) and utilisable efficiency γ_{inv} (empty circles) in dependence of salt concentration ϵ in the system water/ammonium nitrate/ethanol - diesel fuel - oleic acid/monoethanolamine/oleic acid diethanolamide at $\alpha = 0.5$, $\delta_{(ion)} = 0.6$, $\delta_{(OD4)} = 0.3$, $\psi = 0.20$, $n = 0.45$. γ_{inv} value ranges from 0.194 - 0.223 with a minimum at $\epsilon = 0.006$.

The projection of $\tilde{\gamma}$ and the utilisable efficiency γ_{inv} on the $\gamma(\epsilon)$ plane is shown in figure 3-4. In this plot the γ_{inv} value ranges from 0.194 - 0.223 with a minimum at $\epsilon = 0.006$ due to an increased curvature of the amphiphilic film. In the system water/ammonium nitrate/ethanol - diesel fuel - oleic acid/monoethanolamine/oleic acid diethanolamide at $\alpha = 0.5$, $\delta_{(ion)} = 0.6$, $\delta_{(OD4)} = 0.4$, $\psi = 0.20$, $n = 0.45$ only ϵ -values between $0.004 < \epsilon < 0.008$ featured a measurable nature.

The highest solubilisation efficiency is achieved at $\epsilon = 0.006$ and thus, further studies of the phase behaviour are based upon the optimised system water/ammonium nitrate/ethanol - diesel fuel - oleic acid/monoethanolamine/oleic acid diethanolamide at $\alpha = 0.5$, $\delta_{(ion)} = 0.6$, $\delta_{(OD4)} = 0.3$, $\epsilon = 0.006$, $\psi = 0.20$, $n = 0.45$.

3.1.4 Influence of ψ -variation on the phase behaviour

Ethanol is added into the water phase to reduce the formation of liquid crystalline phases and to function as an antifreeze additive. A ψ -variation of the system water/ammonium nitrate/ethanol - diesel fuel - oleic acid/monoethanolamine/oleic acid diethanolamide at $\alpha = 0.5$, $\delta_{(\text{ion})} = 0.6$, $\delta_{(\text{OD4})} = 0.4$, $\varepsilon = 0.006$, $n = 0.45$ is shown in figure 3-5.

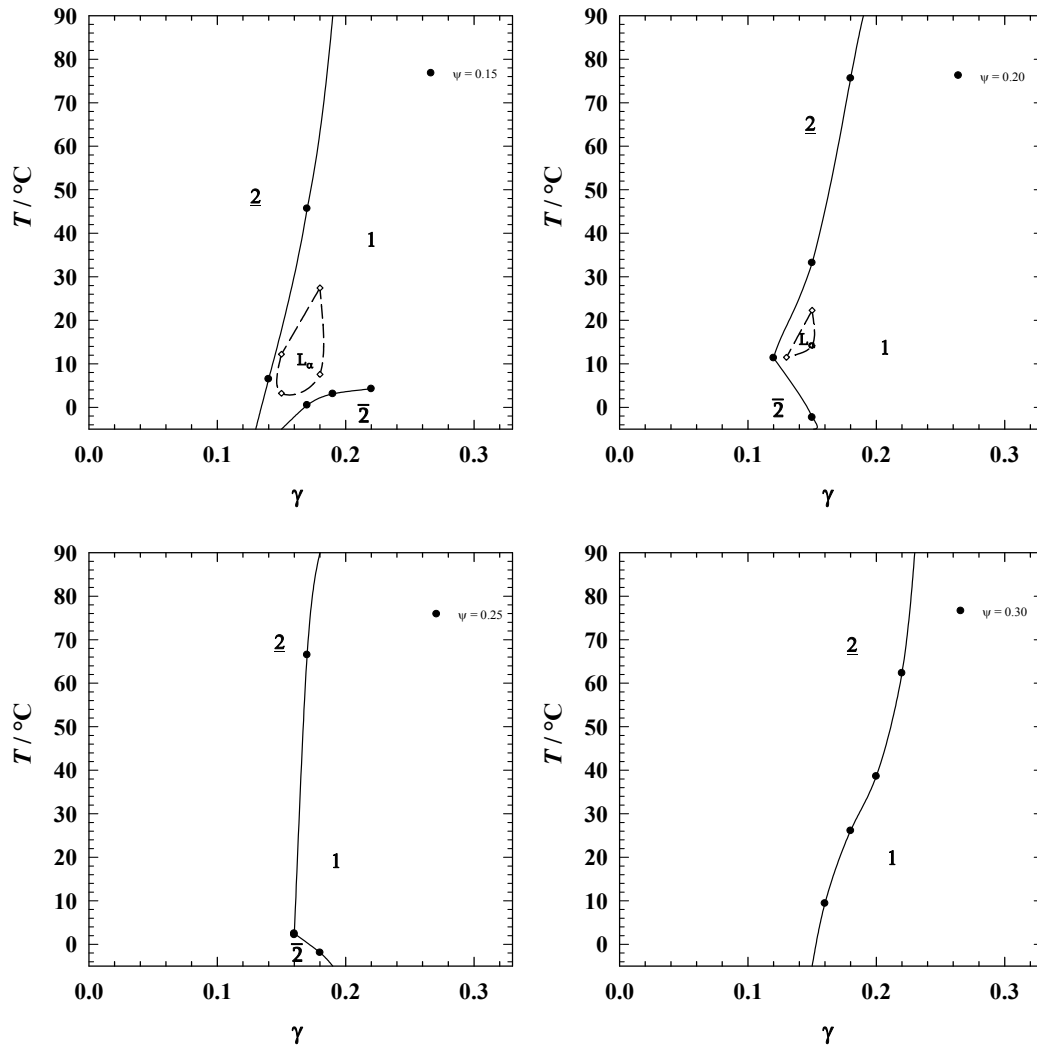


Figure 3-5: Phase diagram of the system water/ammonium nitrate/ethanol - diesel fuel - oleic acid/monoethanolamine/oleic acid diethanolamide at $\alpha = 0.5$, $\delta_{(\text{ion})} = 0.6$, $\delta_{(\text{OD4})} = 0.4$, $\varepsilon = 0.006$, $n = 0.45$ with various ψ . Ionic phase behaviour and a reduced expansion of the lamellar region is observed with increased alcohol concentration. At $\psi = 0.25$ a complete elimination of the lamellar phase with a X-point at $\tilde{\gamma} = 0.158$ and $\tilde{T} = 2.22^\circ\text{C}$ is achieved.

Due to the amphiphilic nature of ethanol, it inserts into the amphiphilic film and operates as an inefficient co-surfactant. The lower phase boundary is shifted to lower temperatures whereby the X-points of the systems with $\psi = 0.15$ and $\psi = 0.30$ cannot be approximated. The

$T(\gamma)$ -sections of the system with $\psi = 0.25$ and $\psi = 0.30$ show a complete elimination of the lamellar phase with a X-point for $\psi = 0.25$ at $\tilde{\gamma} = 0.158$ and $\tilde{T} = 2.22^\circ\text{C}$. In comparison with the previous investigated systems, the present system water/ammonium nitrate/ethanol - diesel fuel - oleic acid/monoethanolamine/oleic acid diethanolamide at $\alpha = 0.5$, $\delta_{(\text{ion})} = 0.6$, $\delta_{(\text{OD4})} = 0.4$, $\varepsilon = 0.006$, $\psi = 0.25$ and $n = 0.45$ shows the most suitable phase behaviour for the use of water fuel microemulsions as fuels. The temperature invariance is achieved at a surfactant mass fraction $\gamma_{\text{inv}} = 0.194$.

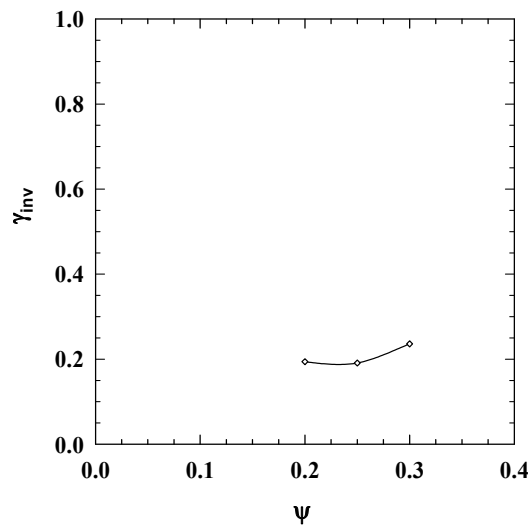


Figure 3-6: Projection of the utilisable efficiency γ_{inv} versus the mass fraction ψ . The utilisable efficiency γ_{inv} ranges from 0.194 - 0.236 with a minimum at $\psi = 0.25$.

The influence of the mass fraction ψ of ethanol in the aqueous compound on the utilisable efficiency γ_{inv} is shown in figure 3-6. As discussed in chapter 2.1.9, short-chained alcohols insert into the amphiphilic film and operate as an inefficient co-surfactant. Since an increased amount of ethanol in nonionic-systems causes a more hydrophilic behaviour, the ionic system becomes more hydrophobic and shift to lower temperatures. This effect is based upon an enhanced miscibility gap in the binary system A - C and a simultaneously reduced miscibility gap in the binary system C - B. Additionally, the formation of liquid crystalline phases is reduced by the destabilising effect of short-chained alcohols on the amphiphilic film. As shown in figure 3-6, the utilisable efficiency γ_{inv} ranges from 0.194 - 0.236 with a minimum at $\psi = 0.25$. Due to an increased viscosity and phase separation as function of time, lamellar phases are undesirable for use as fuels. Hence, the system with a complete elimination of the lamellar region ($\psi = 0.25$) shows the most appropriate phase behaviour.

3.1.5 Influence of α -variation on the phase behaviour

Previous investigations showed that potential benefits of water containing fuels are achieved applying 8-30 wt.% water [56, 60]. In order to analyse the influence of water in terms of combustion emissions, three different water contents (8, 16 and 24 wt.% water) of the optimised, “green” system water/ammonium nitrate/ethanol - diesel fuel - oleic acid/monoethanolamine/oleic acid diethanolamide at $\delta_{(\text{ion})} = 0.6$, $\delta_{(\text{OD4})} = 0.4$, $\varepsilon = 0.006$, $\psi = 0.25$ and $n = 0.45$ were chosen.

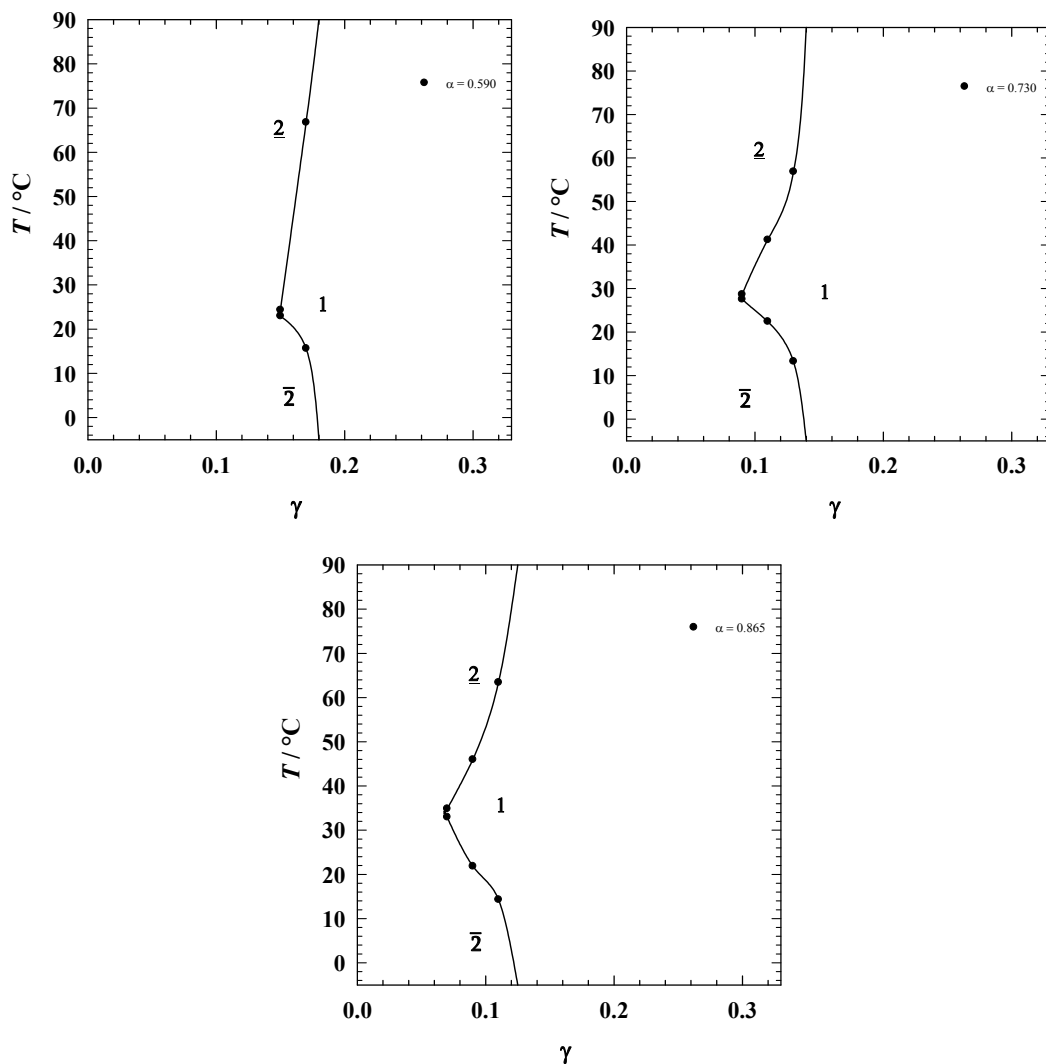


Figure 3-7: Phase diagram of the three, subsequently applied, optimised systems water/ammonium nitrate/ethanol - diesel fuel - oleic acid/monoethanolamine/oleic acid diethanolamide at $\delta_{(\text{ion})} = 0.6$, $\delta_{(\text{OD4})} = 0.4$, $\varepsilon = 0.006$, $\psi = 0.25$, $n = 0.45$ with various α . The X-points are shifted to lower surfactant mass fractions $\tilde{\gamma}$ and higher phase inversion temperatures \tilde{T} with increasing oil to water-plus-oil mass fraction α . Temperature invariant state is achieved at a maximum surfactant mass fraction $\gamma_{\text{inv}} = 0.184$ ($\alpha = 0.590$).

In figure 3-7 the α -variation of the system water/ammonium nitrate/ethanol - diesel fuel - oleic acid/monoethanolamine/oleic acid diethanolamide at $\delta_{(\text{ion})} = 0.6$, $\delta_{(\text{OD4})} = 0.4$, $\varepsilon = 0.006$, $\psi = 0.25$, $n = 0.45$ is shown. The investigation of the phase behaviour provides an overview in dependence on the oil-to-water ratio. The X-point of the system with $\alpha = 0.590$ is located at $\tilde{\gamma} = 0.149$ and $\tilde{T} = 23.56^\circ\text{C}$. With increasing oil content (α -values higher than $\alpha = 0.590$), the X-point is shifted to lower surfactant mass fractions ($\tilde{\gamma} = 0.067 / 0.089$) and higher temperatures ($\tilde{T} = 28.06 / 33.99^\circ\text{C}$) at $\alpha = 0.73 / 0.865$. In all three $T(\gamma)$ -sections, a lamellar phase region is not observed and a wide, temperature invariant one-phase region, which is an essential property for combustible fuel microemulsions, is achieved. The temperature invariant state is achieved at a surfactant mass fraction of $\gamma_{\text{inv}} = 0.129$ ($\alpha = 0.865$), $\gamma_{\text{inv}} = 0.144$ ($\alpha = 0.730$) and $\gamma_{\text{inv}} = 0.184$ ($\alpha = 0.590$). These are the systems used for the combustion experiments in chapter 4. Optimised systems were formulated in further investigations (chapter 3.1.6) but could not undergo combustion tests due to lack of time.

Trajectory of the middle phase

In order to study the general pattern of water fuel microemulsions, systematic studies of the phase behaviour were performed varying the oil-to-water ratio in the system water/ammonium nitrate/ethanol - diesel fuel - oleic acid/monoethanolamine/oleic acid diethanolamide at $\delta_{(\text{ion})} = 0.6$, $\delta_{(\text{OD4})} = 0.4$, $\varepsilon = 0.006$, $\psi = 0.25$ and $n = 0.45$. From the location of the X-points the trajectory of the middle phase was constructed. In the following figure the trajectory of the X-points as function of oil-to-water ratio is shown. In addition, the phase inversion temperature \tilde{T} in dependence on the oil-to-water ratio is discussed.

At the oil-rich- and water-rich side a decreased amount of surfactant is needed to achieve the temperature invariant state. Previous investigations have shown the same progress of the utilisable efficiency γ_{inv} depending on the α -value [60]. An identical trend is observed regarding the location of the X-points. A parabolic-shaped curve describes the efficiency $\tilde{\gamma}$ as function of the oil to water-plus-oil mass fraction α . The properties of the trajectory of the X-points of the water fuel microemulsion exhibit, except for slight deviations due to the technical nature of the surfactants, the characteristics which were described for “classical” microemulsions in literature [99].

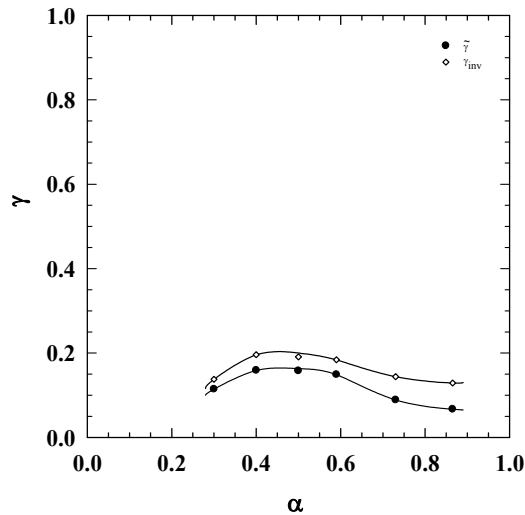


Figure 3-8: Projection of efficiency $\tilde{\gamma}$ (full circles) and utilisable efficiency $\tilde{\gamma}_{inv}$ (empty circles) as function of the oil to water-plus-oil mass fraction α . At $\alpha = 0.5$ an increased amount of surfactant is needed to achieve the temperature invariant state.

The phase inversion temperature \tilde{T} as function of oil to water-plus-oil fraction α (figure 3-9) shows an approximately sigmoidal progress, whereat a plateau at the oil-rich side is observed. The progression of the phase inversion temperature \tilde{T} in dependence of the oil to water-plus-oil fraction α follows, except for slight deviations at the water-rich side, the systematic trend known from classical and pure C_iE_j -systems discussed in chapter 2.1.8 [98, 99].

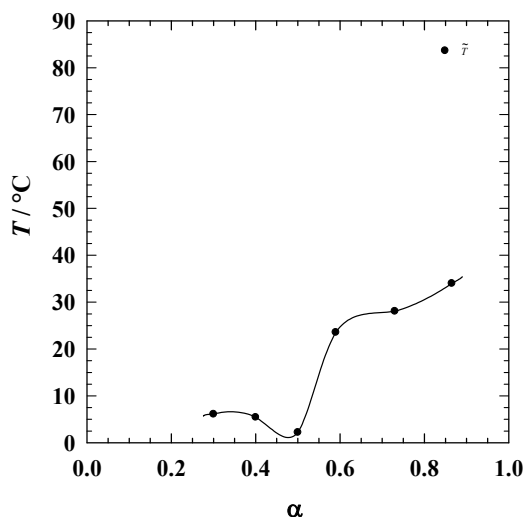


Figure 3-9: Projection of the phase inversion temperature \tilde{T} in dependence of the oil to water-plus-oil mass fraction α .

3.1.6 Optimised systems

In order to lower the surfactant mass fraction γ_{inv} , some components of the complete system could be replaced. Due to the fact, that the additives and surfactants should be completely combustible and produced from renewable raw materials, the choice of additives and surfactants was limited. An alternative alcohol to ethanol is *n*-propanol. A variation of the parameters (n , δ , ε , ψ) was examined and the most suitable system with *n*-propanol in the water phase is shown in figure 3-10.

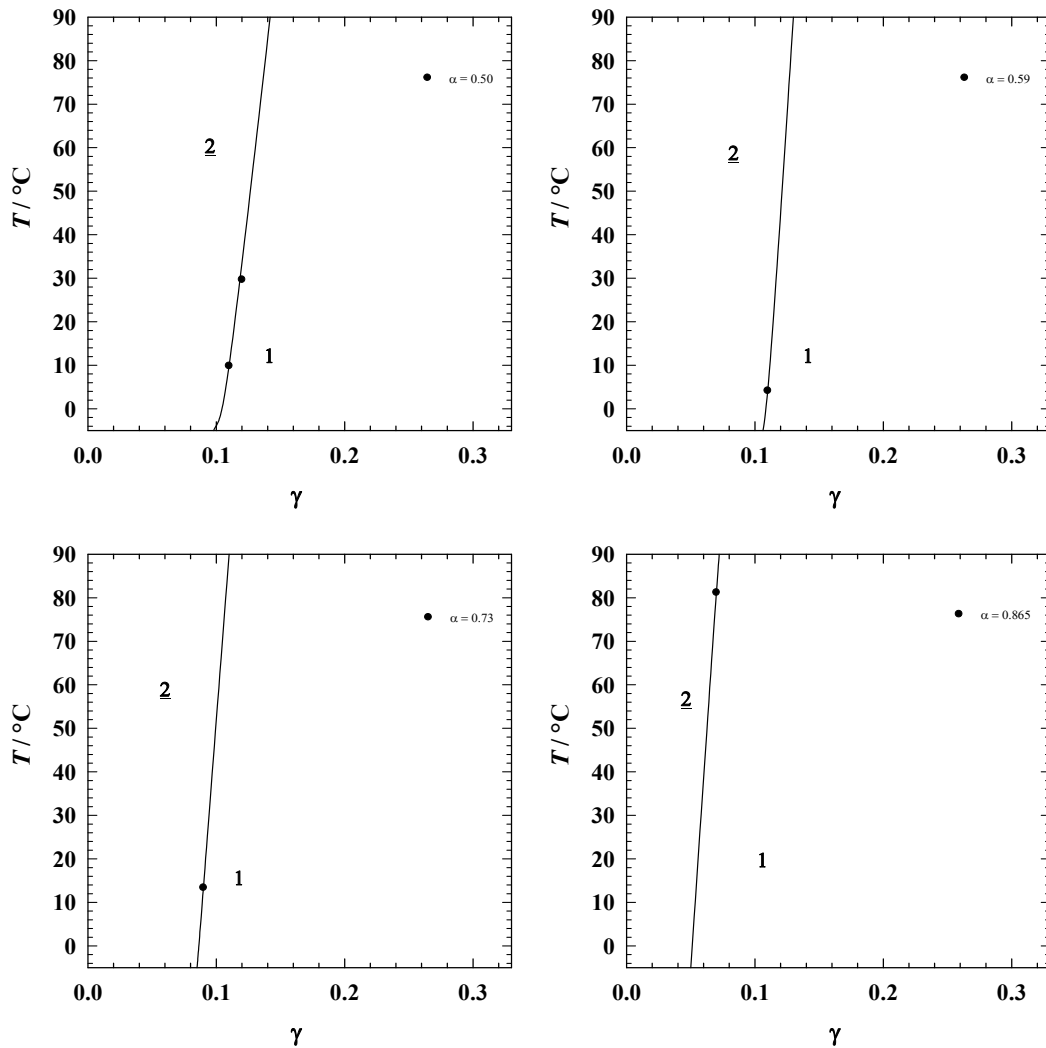


Figure 3-10: Phase diagram of the system water/ammonium nitrate/*n*-propanol - diesel fuel - oleic acid/monoethanolamine/oleic acid diethanolamide at $\delta_{(ion)} = 0.7$, $\delta_{(OD4)} = 0.3$, $\varepsilon = 0.008$, $\psi = 0.25$, $n = 0.43$ with various α . Ionic phase behaviour without a lamellar region is observed. Lower phase boundaries are shifted to lower temperatures ($< -5^\circ\text{C}$) and the steep upper phase boundaries separate the two-phase state from the one-phase state.

The system water/ammonium nitrate/*n*-propanol - diesel fuel - oleic acid/monoethanolamine/oleic acid diethanolamide at $\delta_{(ion)} = 0.7$, $\delta_{(OD4)} = 0.3$, $\varepsilon = 0.008$, $\psi = 0.25$

and $n = 0.43$ shows a significant change in terms of the phase behaviour compared to former systems with ethanol as additive. The lower phase boundary is shifted to lower temperatures and the X-point cannot be determined. Additionally, an abrupt upper phase boundary is observed which separates the two-phase state from the one-state phase.

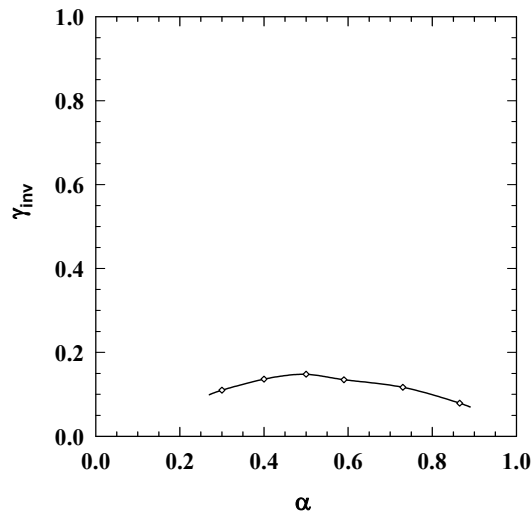


Figure 3-11: Projection of the utilisable efficiency γ_{inv} as function of the oil to water-plus-oil mass fraction α . An enhanced solubilisation utilisable efficiency γ_{inv} is achieved at the oil-rich site.

Figure 3-11 shows the trend of the utilisable efficiency γ_{inv} as function of the oil to water-plus-oil mass fraction α . A parabolic-shaped progress of γ_{inv} in dependence on the oil-to-water content is observed. At the oil-rich- and water-rich side a decreased amount of surfactant is needed to achieve the temperature invariant state. This property accords to the former studies observed for water fuel microemulsions shown in figure 3-9 and also examined by *Wulff* [60].

To sum up, a highly efficient microemulsion system is achieved by exchanging ethanol with *n*-propanol. The temperature invariant state is compared in the following table:

Table 5: Overview of the utilisable efficiency γ_{inv} for the system water/ammonium nitrate/ethanol - diesel fuel - oleic acid/monoethanolamine/oleic acid diethanolamide at $\delta_{(ion)} = 0.6$, $\delta_{(OD4)} = 0.4$, $\varepsilon = 0.006$, $\psi = 0.25$, $n = 0.45$ (middle) and for the optimised system water/ammonium nitrate/*n*-propanol - diesel fuel - oleic acid/monoethanolamine/oleic acid diethanolamide at $\delta_{(ion)} = 0.7$, $\delta_{(OD4)} = 0.3$, $\varepsilon = 0.008$, $\psi = 0.25$, $n = 0.43$ (right) for various α .

α	ethanol γ_{inv}	<i>n</i> -propanol γ_{inv}
0.500	0.214	0.148
0.590	0.184	0.135
0.730	0.144	0.117
0.865	0.129	0.079

As shown in table 5, the temperature invariant states with *n*-propanol as antifreeze additive are observed at remarkable lower surfactant mass fractions.

The influence of the alcohol on the physical parameters of the water fuel microemulsion has also been considered. Due to a lower vapour pressure of *n*-propanol (table 6) possible cavitation in the nozzle hole should be reduced. The density and the boiling point (among other parameters) play an important role in terms of evaporation behaviour. With increasing density, the jet angle decreases and might lead to incomplete combustion. Consequently, higher emissions are obtained [162]. The boiling point influences the penetration depth; with increasing boiling point, the penetration depth of the liquid phase increases and might cause a coating of fuel on the pistons surface leading to inefficient combustion [163].

Table 6: Overview of the main physical properties of ethanol and *n*-propanol.

alcohol	vapour pressure / hPa at 20 °C	Density / g/cm ³	boiling point / °C
ethanol	58	0.79	78
<i>n</i> -propanol	20	0.80	97

Another opportunity to optimise the former water fuel microemulsion systems is to add amphiphilic block copolymers as *e.g.* of the type poly(ethylene-oxide)-co-poly(propylene-oxide)-poly(ethylene-oxide) (PEO_m-PPO_n-PEO_m, *m*, *n* = molar weight per block) to enhance the solubilisation efficiency of the polymer-surfactant mixture. Preliminary experiments in my

diploma thesis showed an *efficiency boosting effect* in the system with H₂O - Diesel - C₁₀E₄ / F 98 at $\alpha = 0.50$ [164].

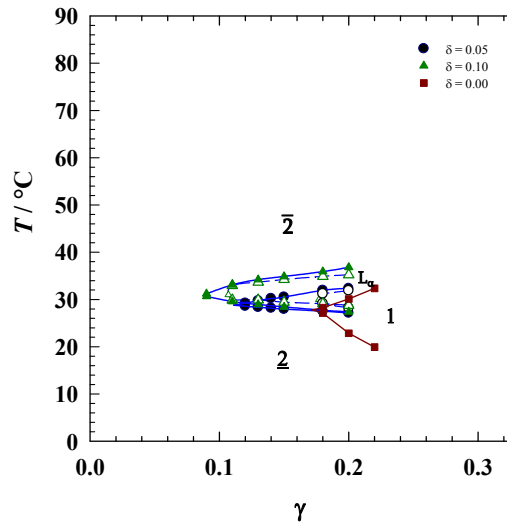


Figure 3-12: Phase behaviour of the system H₂O - Diesel - C₁₀E₄ / F 98 at $\alpha = 0.50$ for variable polymer mass fractions δ_{poly} . The phase boundaries are shifted to lower γ , while the phase inversion temperature remains approximately unchanged (taken from [164]).

The X-point with increasing δ -value is shifted to lower surfactant mass fractions $\tilde{\gamma}$ and higher temperatures \tilde{T} . Due to this effect, the triblock copolymer PEO₁₁₈PPO₄₅PEO₁₁₈ (F 98) is added to the optimised system water/ammonium nitrate/*n*-propanol - diesel fuel - oleic acid/monoethanolamine/oleic acid diethanolamide at $\alpha = 0.50$, $\delta_{(\text{ion})} = 0.7$, $\delta_{(\text{OD4})} = 0.3$, $\varepsilon = 0.008$, $\psi = 0.25$ and $n = 0.43$. Different mass fractions of the surfactant - triblock copolymer mixture ($\delta_{\text{poly}} = 0.05$, $\delta_{\text{poly}} = 0.10$, $\delta_{\text{poly}} = 0.15$) are examined and shown in figure 3-13.

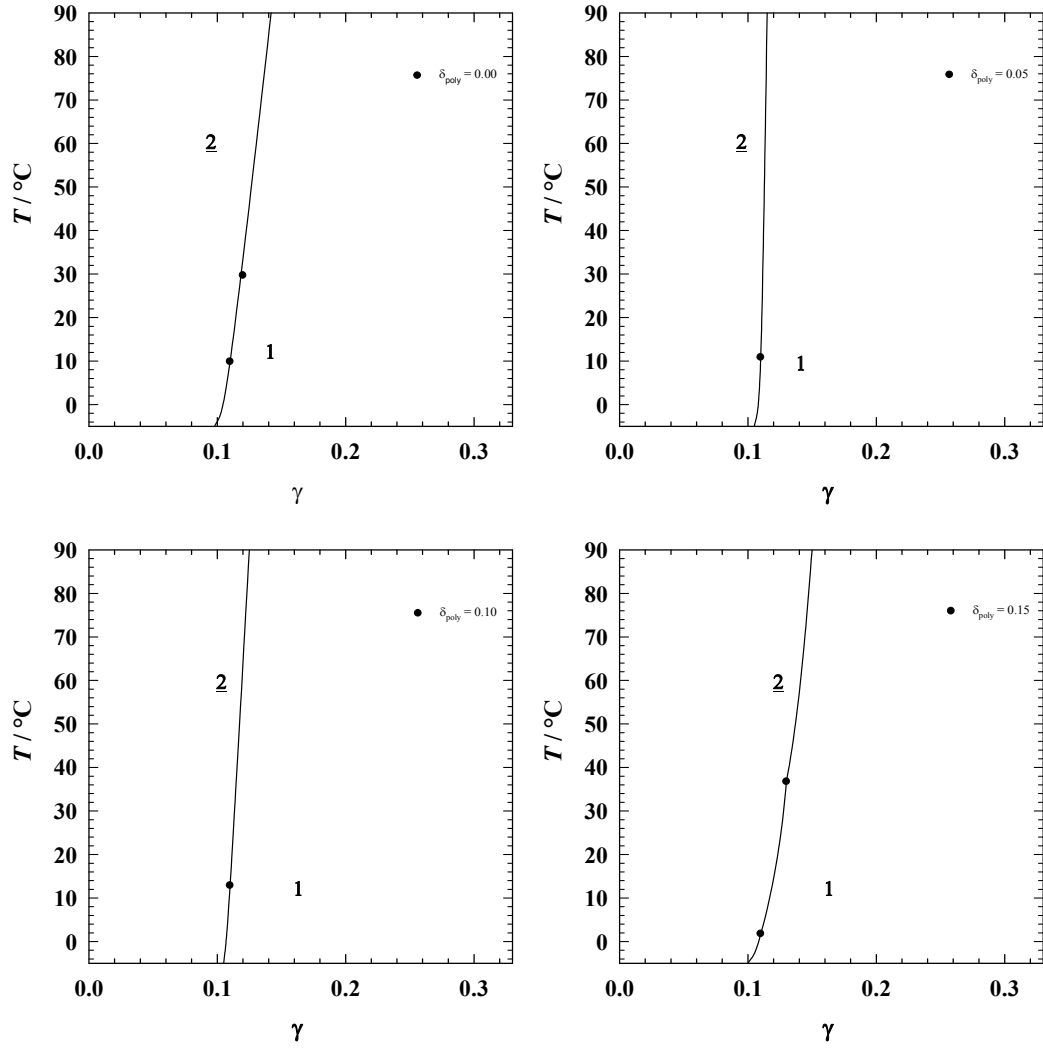


Figure 3-13: Phase diagram of the system water/ammonium nitrate/*n*-propanol - diesel fuel - oleic acid/monoethanolamine/oleic acid diethanolamide/F98 at $\alpha = 0.5$, $\delta_{(ion)} = 0.7$, $\delta_{(OD4)} = 0.3$, $\varepsilon = 0.008$, $\psi = 0.25$, $n = 0.43$ for variable polymer mass fractions δ_{poly} . Temperature invariant state is achieved at lower surfactant mass fractions ($\Delta\gamma_{inv} = 0.030$) at $\delta_{poly} = 0.05$.

While for the polymer-free microemulsion a temperature invariant state is found at $\gamma_{inv} = 0.148$, an enhanced solubilisation efficiency up to $\gamma_{inv} = 0.118$ is achieved at $\delta_{poly} = 0.05$. In comparison to the polymer-free system, the temperature invariant state is achieved at lower surfactant mass fractions ($\Delta\gamma_{inv} = 0.030$). The efficiency boosting effect can be explained by the adsorption of the amphiphilic triblock copolymer molecules to the amphiphilic film [165] while increasing the bending rigidity of the amphiphilic film, resulting in an enhanced solubilisation efficiency [166, 167]. Interestingly, the positive influence of the triblock copolymer decreases at $\delta_{poly} = 0.10$ and $\delta_{poly} = 0.15$. The X-point of the systems cannot be approximated, therefore the determination of the “*efficiency boost factor*” f_B (which is related to the location of the X-point) is not possible. The polymers were also added to the ethanol-

systems (figure 3-7) but no positive effect was observed. Due to the multicomponent system, a systematically optimisation and evaluation was intricate and extensive.

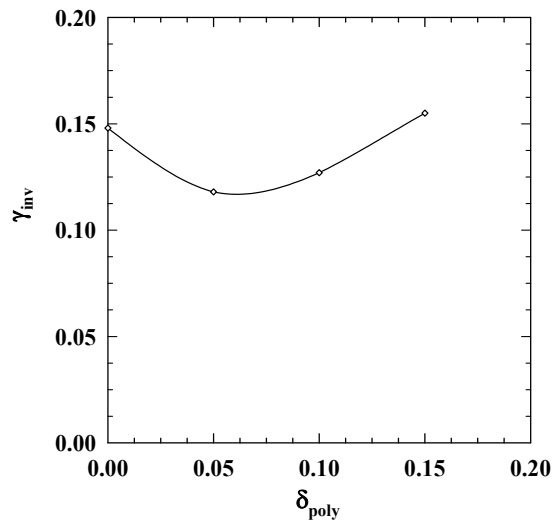


Figure 3-14: Plot of the utilisable efficiency γ_{inv} versus the polymer mass fraction δ_{poly} . At $\delta_{poly} = 0.05$ an enhanced solubilisation efficiency of the polymer-surfactant mixture compared to the solubilisation efficiency of the pure surfactant is achieved.

Figure 3-14 reveals the evolution of the utilisable efficiency γ_{inv} in dependence of the polymer mass fraction δ_{poly} . The amount of surfactant could be slightly minimised by adding a small amount of triblock copolymers PEO₁₁₈PPO₄₅PEO₁₁₈ (F 98) to the surfactant blend. Due to an enhanced solubilisation efficiency of the polymer-surfactant mixture compared to the solubilisation efficiency of the pure surfactant, the temperature invariant state with a minimum utilisable efficiency γ_{inv} value is achieved at $\delta_{poly} = 0.05$.

For the further investigations (chapter 3.2 - 3.4) and for the combustion experiments (chapter 4) the system water/ammonium nitrate/ethanol - diesel fuel - oleic acid/monoethanolamine/oleic acid diethanolamide at $\delta_{(ion)} = 0.6$, $\delta_{(OD4)} = 0.4$, $\varepsilon = 0.006$, $\psi = 0.25$ and $n = 0.45$ was consulted. Due to lack of time, the optimised systems with *n*-propanol could not undergo combustion tests. Therefore, a comparison and evaluation of the combustion tests between the system with ethanol and the system with *n*-propanol as antifreeze was not possible.



3.2 Physical properties

In order to use water fuel microemulsion as fuels, particular specifications according to EN 590 has to be fulfilled [168]. The following table gives the relevant norms for diesel fuel:

Table 7: Overview of the main specific values of diesel fuel after the standards in accordance with DIN EN 590.

specific value	Unit	DIN EN 590	influence on vehicle operation
density 15 °C	kg/cm ³	820 - 845	exhaust emission, consumption, performance
viscosity 40 °C	mm ² /s	2.0 - 4.5	vapourisation, lubrication
flash point	°C	> 55	security
ash content	wt. %	max. 0.01	residues in combustion chamber
lubricity 60 °C	µm	max. 460	abrasion

The suitability and efficiency of an engine depends amongst others upon crucial physical characteristics of the fuel. Fuel density and viscosity may have a marked effect on fuel injection, spray behaviour and abrasion. The aerosol formation and accordingly the atomisation quality, which are described by the *Ohnesorge number* (*Oh*), that includes the *Weber number* (*We*) and *Reynold number* (*Re*) (chapter 2.4.1), also depend on the physical properties of the fuel [169-172]. With increasing density, a smaller jet angle is observed [162] which affects the performance leading to increased exhaust emissions. An increased mean droplet diameter during injection is attributed to higher dynamic viscosity with a simultaneously increased penetration depth of the liquid phase [172-176]. *Rayleigh* analysed the liquid jet breakup, which was modified by *Weber* considering the viscosity and the density of the liquid [170]. Besides these parameters, the flash point plays an important role in terms of compression-ignition engines and risk classification. At a low flash point, an advanced ignition might be observed [177, 178], which also affects the security. The flash point is determined by the component with the lowest boiling point and the highest vapour pressure, which is ethanol (78 °C, 58 hPa) in the present water fuel microemulsions. In this sub-chapter, the crucial physical characteristics of water fuel microemulsions are determined. The investigations only include the water fuel microemulsions which are used for the combustion experiments in chapter 4. The system water/ammonium nitrate/ethanol - diesel fuel - oleic

acid/monoethanolamine/oleic acid diethanolamide at $\delta_{(\text{ion})} = 0.6$, $\delta_{(\text{OD4})} = 0.4$, $\varepsilon = 0.006$, $\psi = 0.25$ and $n = 0.45$ was integrated into the following matrix in figure 3-15:

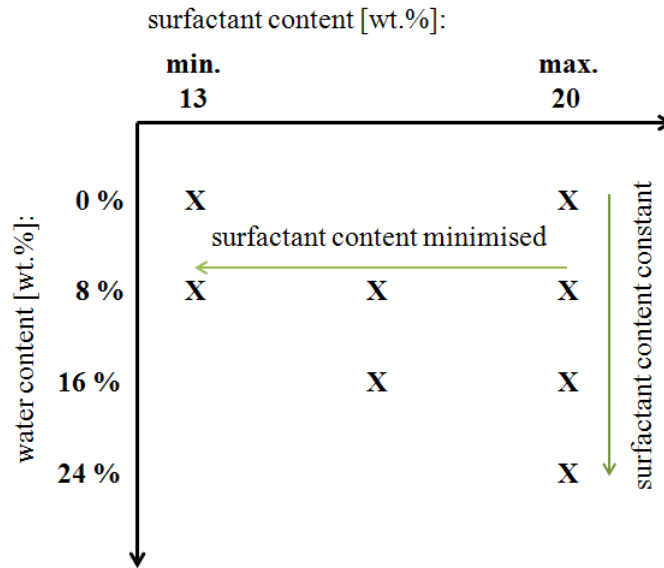


Figure 3-15: Matrix including water- and surfactant content [wt.%].

The water fuel microemulsions are defined as in the suggested matrix in figure 3-15. Hence, the influence of water and surfactant on the physical properties, structure, formation kinetics and combustion tests can be regarded separately. The microemulsions were formulated with a water content of 0 to 24 wt.% (in steps of 8 wt.%) with a constant surfactant content, which corresponds to the required surfactant content for the temperature invariant microemulsion with 24 wt.% water (20 wt.% surfactant). Thus, the influence of water can be analysed independent of the surfactant influence. In addition, microemulsion with 0 and 8 wt.% water with a minimal amount of surfactant (13 wt.%) are investigated. The influence of the surfactant is analysed with the microemulsion with 8 wt.% water at various surfactant contents of 13, 15 and 20 wt.%. Table 8 gives an overview and the nomenclature of the investigated water fuel microemulsion:

Table 8: Overview and the nomenclature of the studied systems with various water- and surfactant-contents [wt.%].

nomenclature	water content [wt.%]	surfactant content [wt.%]
DWME 2420	24	20
DWME 1620	16	20
DWME 0820	8	20
DWME 0020	0	20
DWME 1615	16	15
DWME 0815	8	15
DWME 0813	8	13
DWME 0013	0	13

Dynamic Viscosity

A *Haake* falling-ball viscometer was used for the viscosity measurements at a temperature range between 15 °C to 65 °C. The viscosity of the system water/ammonium nitrate/ethanol - diesel fuel - oleic acid/monoethanolamine/oleic acid diethanolamide at $\delta_{(\text{ion})} = 0.6$, $\delta_{(\text{OD4})} = 0.4$, $\varepsilon = 0.006$, $\psi = 0.25$, $n = 0.45$ with variable water contents was determined. The dynamic viscosity process is shown in figure 3-16.

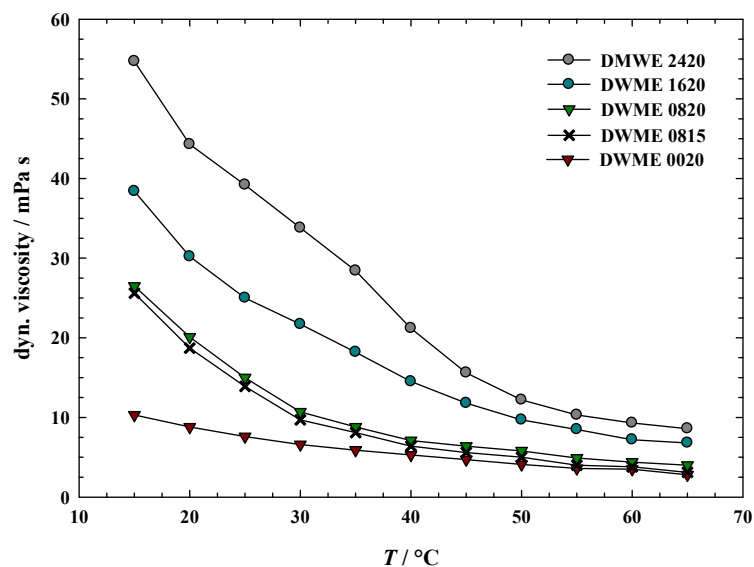


Figure 3-16: Dynamic viscosity in dependence of the temperature for several microemulsions. Dynamic viscosity increases with higher water content.

The rise in viscosity is referred to increased water content. Based on a strong viscosity change at higher temperatures, the viscosity plots of the various microemulsions approximate. Hence, the viscosity has to be considered for the utilisation of water fuel microemulsions as fuel. The increased dynamic viscosity at low temperatures plays an important role in terms of insertion of ‘finished’ water fuel microemulsions since the flow rate of the fuel pump has to be adjusted. The change of viscosity is attributed to the microscopical structure of the microemulsion which depends on the comprised components. With these investigations, the influence of the individual components of the complex systems should be identified. A slightly increase in viscosity is observed at higher surfactant contents comparing DWME 0820 and DWME 0815.

Kinematic viscosity

Additionally, the kinematic viscosity of the water fuel microemulsion with a water content of 0, 8, 16 and 24 wt.% is determined. In order to compare the viscosity of a microemulsion with a reduced surfactant content, the microemulsion DWME 0815 was added to the investigations.

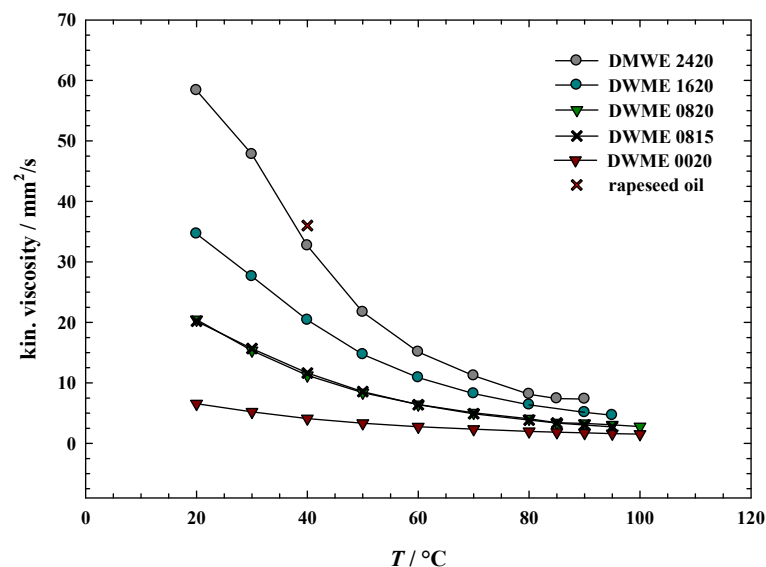


Figure 3-17: Kinematic viscosity as function of the temperature for several microemulsions. Increased kinematic viscosity is observed with increased water content [179].

In common with the further analysis shown in figure 3-17, an increased kinematic viscosity with increased water content is observed. The viscosity of DWME 2420 at 40 °C is at the

same level like rapeseed oil (max. 36 mm²/s at 40 °C) [DIN V 51605]. Furthermore, a steeper temperature profile with increased water content is obtained.

Density

The oscillating U-tube, Heraeus/Paar DMA 601W was used to determine the density of the formulated microemulsion system shown in figure 3-15 (matrix). Fuel density depends on temperature and influences the flow characteristics of fuel in the nozzle [180, 181]. The density value of diesel fuel according to EN 590 is around 820-846 kg/cm³ (40 °C) and thus below the density values of the microemulsions.

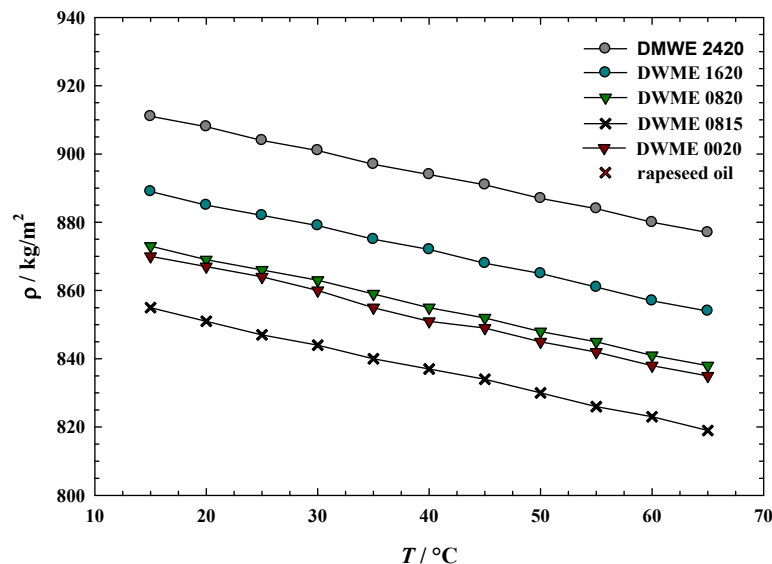


Figure 3-18: Density process in dependence of the temperature for several microemulsions. Density increases and shows equal temperature dependence with increased water content.

Expectedly, the density process (figure 3-18) features a linear trend. The density increases and shows equal temperature dependence with increased water content. As mentioned before, an increased density leads to a smaller jet angle [162] which can affect the performance resulting in an increase of exhaust emission. Those effects have to be considered while an adjustment of the fuel injection cannot be bypassed. Comparing DWME 0820 and DWME 0815, a slightly higher density is determined with a higher amount of surfactant in the microemulsified fuel.

High Frequency Reciprocating Rig (HFRR)

The HFRR method was used to determine the lubricity of the water fuel microemulsions. Diesel fuel injection pumps are lubricated by the fuel itself in order to provide wear protection. The HFRR values of the microemulsions were determined with different water and surfactant contents.

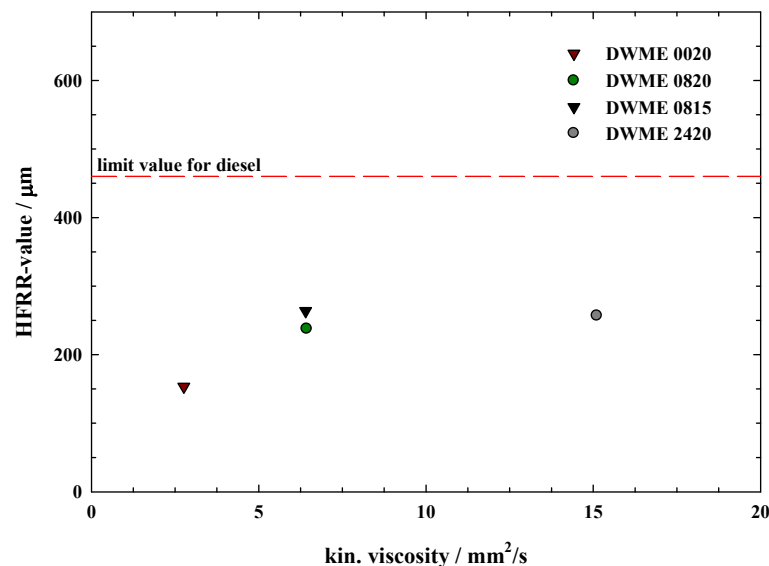


Figure 3-19: High frequency reciprocating rig (HFRR)-values in dependence of the kinematic viscosity for several microemulsions. A significant better lubrication ability is observed for all microemulsions (DWME 2420, 0820, 0020, 0815) compared to the lubrication ability of pure diesel fuel [179].

Figure 3-19 reveals the HFRR value of various water fuel microemulsions at their specific kinematic viscosity. The limiting value according to the specifications after EN 590 is marked with a red dashed line at 460 μm. All microemulsions (DWME 2420, 0820, 0020, 0815) indicate better lubrication ability than pure fuel; surfactant-blend contributes to the lubricating film. The microemulsion with the lowest surfactant content for 8 wt.% water (DWME 0815) shows a slight influence on the lubricity compared to the microemulsion with the maximum surfactant content of 20 wt.% for 8 wt.% water (DWME 0820); both HFRR values do not greatly change while varying the surfactant amount.

High pressure phase behaviour (at 300 bar)

In order to provide a one-phase microemulsion during the fuel injection process, the phase behaviour of DWME 2420 was determined at an increased pressure of 300 bar.

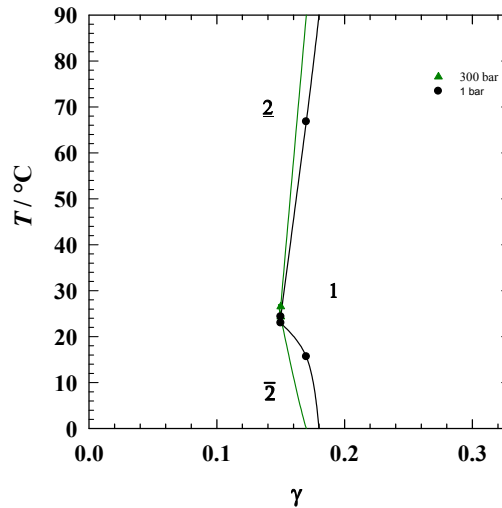


Figure 3-20: Phase behaviour of the system water/ammonium nitrate/ethanol - diesel fuel - oleic acid/monoethanolamine/oleic acid diethanolamide at $\alpha = 0.59$, $\delta_{(\text{ion})} = 0.6$, $\delta_{(\text{OD4})} = 0.4$, $\varepsilon = 0.006$, $\psi = 0.25$, $n = 0.45$ (DWME 2420) at 1 bar (black) and at 300 bar (green). A slight deviation of the phase behaviour at 300 bar is observed.

In figure 3-20 the phase behaviour of the system water/ ammonium nitrate/ethanol - diesel fuel - oleic acid/monoethanolamine/oleic acid diethanolamide at $\alpha = 0.59$, $\delta_{(\text{ion})} = 0.6$, $\delta_{(\text{OD4})} = 0.4$, $\varepsilon = 0.006$, $\psi = 0.25$, $n = 0.45$ (DWME 2420) at standard pressure (1 bar; black) and at increased pressure (300 bar; green) is presented. The phase behaviour at 300 bar shows a slight deviation compared to the phase behaviour at 1 bar (at atm pressure) which is in accordance to the described phase behaviour in literature [96, 192]. A stronger hydration of the hydrophobic head group with increased pressure leads to an increased volume of the head group as described in chapter 2.1.7. Hence, the distinctive curvature of the amphiphilic film encloses the oil whereby the change of curvature is compensated with an increased temperature. Marginally steeper phase boundaries are observed while increasing the pressure to 300 bar. The X-point is now located at $\tilde{\gamma} = 0.148$ and $\tilde{T} = 25.36^\circ\text{C}$. The evolution of the phase behaviour at increased pressure implies the warranty of a one-phase microemulsion during the injection process. A phase separation as function of pressure would feature a negative effect on fuel injection, spray behaviour, abrasion and corrosion.

Flash point

The flash point is the lowest temperature at which the fuel can form an ignitable mixture in air near the liquid's surface. Thus, ignition characteristics and risk classification of fuels are determined by the flash point. Like other physical parameters, the diesel engine and its complete injection- and incentive-system, have to consider the modified physical characteristics. The flash points of the eight microemulsion formulations and diesel fuel are listed in table 9.

Table 9: Overview of the flash point of the studied microemulsions.

microemulsion	flash point / °C
DWME 2420	~ 31
DWME 1620	~ 31
DWME 0820	~ 31
DWME 0020	~ 25
DWME 1615	~ 30
DWME 0815	~ 30
DWME 0813	~ 31
DWME 0013	~ 25
diesel fuel	~ 67

The flash point is strongly affected by the component with the lowest vapour pressure and boiling point, which is ethanol in the present water fuel microemulsion. Thereby, the flash point value ranges from 25 °C - 31 °C. At this low flash points, an advanced ignition might be observed [177, 178], which affects the security and do not fulfil the specifications after EN 590. In order to reach a required flash point value, the alcohol in the aqueous phase could be exchanged with *n*-propanol, which features a significant lower vapour pressure (20 hPa).

Lower heating value (LHV)

The lower heating value (*LHV*) of the water fuel microemulsion systems are determined by equation (42) and listed in table 10.

Table 10: Overview of the lower heat value *LHV* of the studied microemulsions.

microemulsion	lower heat value <i>LHV</i> / MJ/kg
DWME 2420	28.90
DWME 1620	33.17
DWME 0820	37.26
DWME 0020	41.14
DWME 1615	32.37
DWME 0815	37.40
DWME 0813	37.41
DWME 0013	41.56
diesel fuel	42.50

As expected, the microemulsion features a reduced lower heating value (*LHV*) than pure diesel fuel. Due to this effect, the spray hole diameter has to be adjusted to each microemulsion in order to provide an equal energy input per minute into the combustion chamber. Thus, a meaningful comparison between water fuel microemulsions and pure diesel fuel in terms of emissions is guaranteed.

Distillation range

The distillation characteristics of diesel fuel and five water containing fuel microemulsions (DWME 2420, DWME 1620, DWME 0820, DWME 0020 and DWME 0813) were determined according to ASTM D 86. The average volatility requirements of diesel fuel vary with engine speed and size. Fuels with a low volatility tend to reduce power output and fuel economy through poor atomisation due to an inadequate penetration depth in the nozzle. The distillation range should be as low as possible, without adversely influencing the flash point, heat content, burning quality or viscosity of the fuel. The temperature for evaporating 50 vol.% of the fuel, is known as the *mid-boiling point* and is usually taken as an indication of

the fuel distillation characteristics. A high *mid-boiling point* can adversely affect the smoke formation, produce objectionable odor and promote engine deposits. On the other hand, an excessively low *mid-boiling point* features a too low viscosity and heat content per unit volume [183].

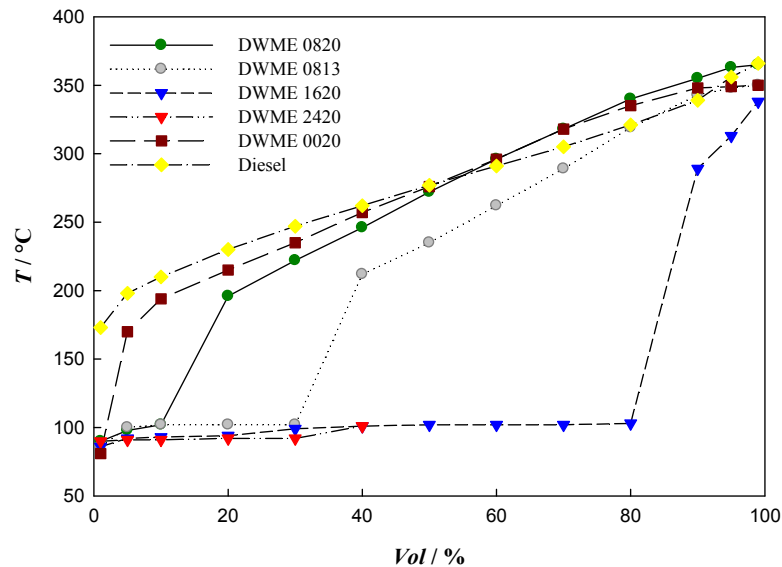


Figure 3-21: Projection of the temperature as function of the volume. The *mid-boiling point* (evaporating 50 vol.% of the fuel) of the microemulsions with a water content of > 16 wt.% features a very low value without the characteristic shape of the distillation curve of pure fuel [179].

As shown in figure 3-21, each fuel has a specific initial and final boiling point, as well as a characteristic shape of the distillation curves. The *mid-boiling point* of the microemulsions with a water content less than 16 wt.% shows a suitable value of approximately $T = 220 - 270$ °C. On the contrary, the microemulsions with a water content of 16 wt.% and more, (DWME 1620, DWME 2420) exhibit a very low *mid-boiling point* due to a lower heating value than the other investigated microemulsions. The insertion of water in fuel effect an abrupt rise at approximately $T = 100$ °C (due to the boiling point of water) in all microemulsions. The end-points of the studied fuels are all approximately located at the characteristic temperature for diesel fuel ($T \approx 350$ °C).

3.3 Microstructure

The structure of the formulated microemulsions is linked to the viscosity and can therefore influence the fuel injection and spray behaviour. An estimation of the size distribution of the water sphere in the oil continuous microemulsion is possible by using the dynamic light scattering method (DLS). As described in chapter 2.3.1, the hydrodynamic radii are determined and are the basis for the estimation of the structure size.

3.3.1 DLS-measurements

With a simultaneously consideration of the oil continuous phase and the location of the phase boundaries in the $T(\gamma)$ -section (figure 3-7), the size of the water sphere was approximately determined by assuming water swollen micelles. The hydrodynamic radii of eight microemulsion formulations (given in table 8) were investigated. First measurements were performed at $T = 20\text{ }^{\circ}\text{C}$.

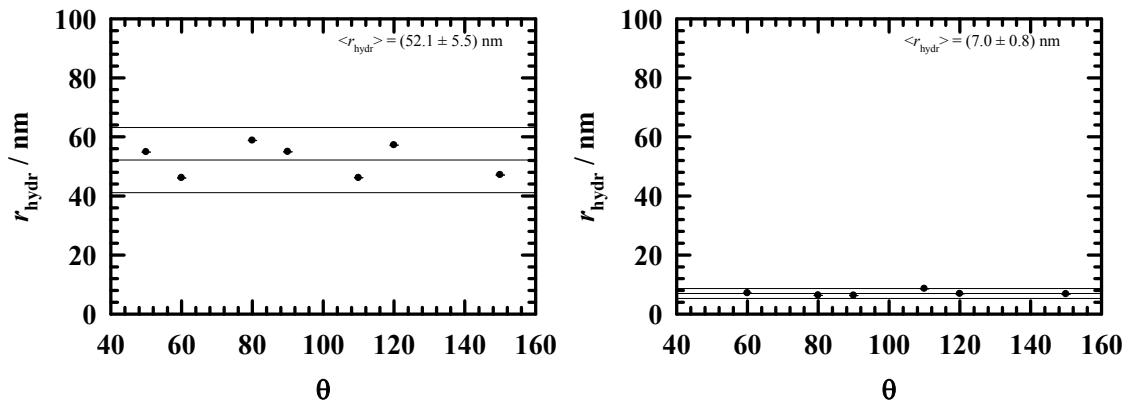


Figure 3-22: Hydrodynamic radii of water spheres in fuel (DWME 2420: left; DWME 1620: right) at various scattering angles θ . Larger radii are observed at a higher water content.

Figure 3-22 shows the hydrodynamic radii for the microemulsions DWME 2420 (left) and DWME 1620 (right). The size of water spheres of the microemulsion DWME 0820 and DWME 0020 cannot be determined due to very small radii. As expected, the size of water spheres of the microemulsion with higher water content features a higher value ($r_{\text{hydr}} = 52.1$) than the microemulsion with 16 wt.% water ($r_{\text{hydr}} = 7.0$).

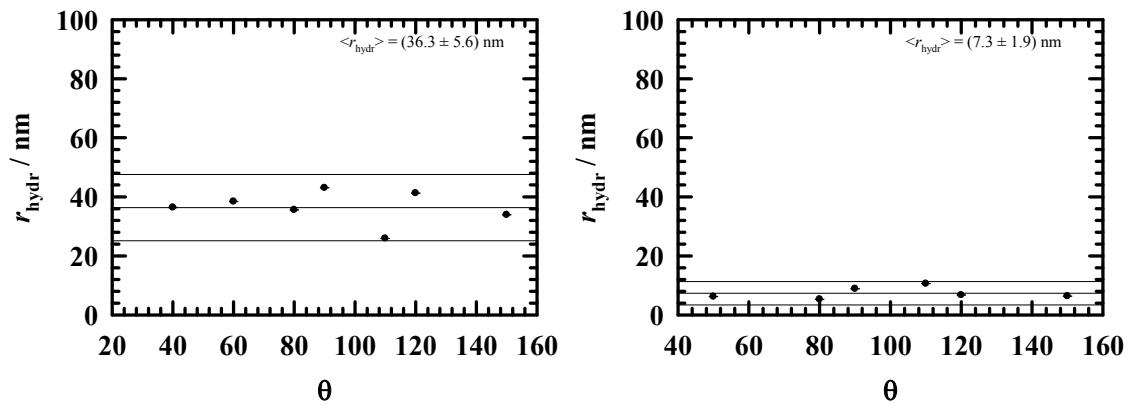


Figure 3-23: Hydrodynamic radii of water spheres in fuel (DWME 1615: left; DWME 0815: right) as function of the scattering angle θ .

In figure 3-23 the hydrodynamic radii is plotted against the angle. Enlarged water spheres are observed with decreasing surfactant content (compared to the former indeterminable small water spheres of DWME 1620 and 0820). This effect can be explained by the process of water swollen micelles in dependence of the surfactant mass fraction in the $T(\gamma)$ -section. Larger water swollen micelles are obtained with decreasing surfactant mass fraction due to a higher surface tension.

The investigations of the water sphere sizes are summarised in table 11.

Table 11: Overview of the mean hydrodynamic radii of the water-fuel microemulsions at various temperatures.

microemulsion	$r_{\text{hyd}} / \text{nm}$ at 20 °C	$r_{\text{hyd}} / \text{nm}$ at 40 °C	$r_{\text{hyd}} / \text{nm}$ at 60 °C
DWME 2420	52.6	7.6	-
DWME 1620	7.0	-	-
DWME 0820	-	-	3.3
DWME 0020	-	-	-
DWME 1615	36.3	33.6	3.8
DWME 0815	7.3	4.7	5.1
DWME 0813	7.5	6.3	4.4
DWME 0013	-	-	-

As listed in table 11, the dependence on water content shows enlarged water sphere sizes with increased water content as also observed for microemulsions with reduced surfactant concentrations, which are both related to the solubilisation efficiency.

The advantages of a homogeneous distribution of the water are clearly identified. On one hand, the peak temperature of the combustion is reduced by the phase transition and on the other hand, the radical formation from water and partly oxidised components lead to a better decomposition of the carbon chain [31]. Those phenomena are limited whereby the size distribution and the water sphere sizes represent fundamental parameters.

3.3.2 SANS-measurements

Small angle neutron scattering (SANS) was applied to clarify the structure of the microemulsions. The scattering data was analysed by using a polydisperse hard spheres model (form factor $P(q)$) with *Percus-Yevick* (structure factor $S(q)$) approximation for sphere-sphere interactions [184] (see chapter 6.2 for a detailed description). The model fit after *Teubner-Strey* for bicontinuous systems was neglected due to the assumption of water-swollen micelles at high temperatures [185]. In order to structurally characterise the newly formulated, temperature invariant water containing fuels, the microemulsions DWME 2420, 1620 and 0820 were investigated at an approximately injection temperature of $T = 80\text{ °C}$. The SANS measurements were performed at the experimental setup KWS-1 in Munich (see chapter 6.2 for a detailed description).

The first SANS measurement was performed at $T = 80\text{ °C}$ with the microemulsion DWME 2420 containing 24 wt.% water and 20 wt.% surfactant.

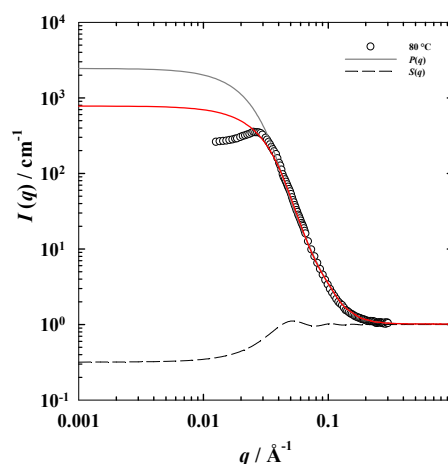


Figure 3-24: Neutron scattering data from DWME 2420 at $T = 80\text{ °C}$. The curve is fitted as polydisperse hard sphere $P(q)$ (solid line) and with the *Percus-Yevick* approximation for repulsive sphere-sphere interactions $S(q)$ (dashed line). The red curve represents the total fit $I(q) = P(q) \cdot S(q)$.

The experimental scattering intensities $I(q)$ are shown as a function of the scattering vector q in a double-logarithmic plot at $T = 80\text{ °C}$. As shown in figure 3-24, the scattering curve is characteristic for scattering spectra from spherical aggregates of a constant scattering intensity I_0 at low q -values and a q^{-4} -decay at higher ones. The scattering curve can accordingly be described as polydisperse hard spheres by the applied model.

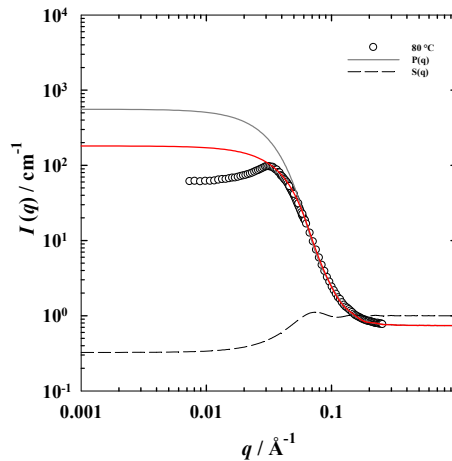


Figure 3-25: Neutron scattering data from DWME 1620 at $T = 80\text{ °C}$. The curve is fitted as polydisperse hard sphere $P(q)$ (solid line) and with the *Percus-Yevick* approximation for repulsive sphere-sphere interactions $S(q)$ (dashed line). The red curve represents the total fit $I(q) = P(q) \cdot S(q)$.

As previously described, the scattering curve with decreased water content (16 wt.%) also exhibits the same characteristic shape as observed in figure 3-24 for polydisperse hard spheres. The structure factor according to the *Percus-Yevick* approximation could not accurately describe the increased intensities at high q -values due to stronger inter-particle interaction than for DWME 2420.

Furthermore, SANS measurements were also performed for DWME 0820 in order to compare the change in structure for various water contents.

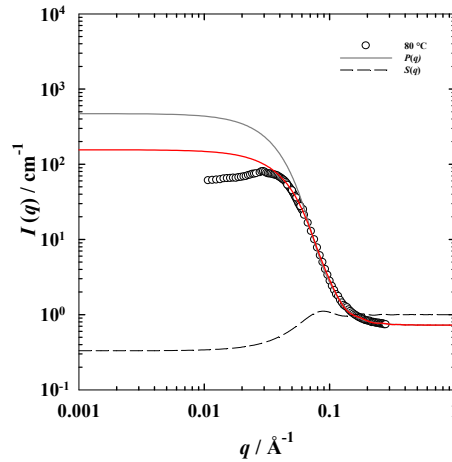


Figure 3-26: Neutron scattering data from DWME 0820 at $T = 80\text{ °C}$. The curve is fitted as polydisperse hard sphere $P(q)$ (solid line) and with the *Percus-Yevick* approximation for repulsive sphere-sphere interactions $S(q)$ (dashed line). The red curve represents the total fit $I(q) = P(q) \cdot S(q)$.

An appreciable peak at medium q -values is also observed in figure 3-26. Additionally, a slight shoulder on the q^{-4} -decay is observed for all scattering curves (DWME 2420, 1620 and 0820). As also obtained for DWME 1620, a stronger inter-particle interaction exists, which is expressed in a higher intensity at high q -values.

The comparison between all three systems shows a significant change in the number of density of scattering particles. As expected, the mean radius of the water-swollen micelles is enlarged with increasing water content which is related to the higher amount of water that has to be solubilised. The resulting fit parameters of the investigated systems are summarised in table 12 (for further fit parameters see chapter 7).

Table 12: Mean radius R_0 , polydispersity index σ_{rel} and volume fraction of the surfactant in the interface $\phi_{\text{c,i}}$.

DWME	$R_0 / \text{Å}$	σ_{rel}	$\phi_{\text{c,i}}$
2420	54	0.28	0.194
1620	39	0.22	0.192
0820	32	0.20	0.198

3.4 Stopped-flow measurement

Furthermore, the stopped flow equipment is used to study the formation kinetics of the water fuel microemulsion. After the setup and calibration of the stopped-flow system from Klemmer [186], the formation kinetics of water microemulsified fuels varying the water-content and the temperature were studied. Those investigations are essential in order to ensure the *in situ* formation of microemulsions during the on injector-blending of water- and diesel-phase (including surfactant-blend). The formation kinetics of water containing fuels has never been studied before and will be presented and discussed in this sub-chapter.

First, the formation kinetics of the system water/ammonium nitrate/ethanol - diesel fuel - oleic acid/monoethanolamine/oleic acid diethanolamide at $\delta_{(\text{ion})} = 0.6$, $\delta_{(\text{OD4})} = 0.4$, $\varepsilon = 0.006$, $\psi = 0.25$, $n = 0.45$ with 8 wt.%, 16 wt.% and 24 wt.% water (DWME 0820, DWME 1620, DWME 2420) at $T = 20\text{ }^{\circ}\text{C}$ will be determined. Additionally, the temperature influence on the formation kinetics of the system with 24 wt.% water (DWME 2420) will be presented and discussed in detail.

In figure 3-27 the transmission experiment for DWME 0820 (8 wt.% water) at $T = 20\text{ }^{\circ}\text{C}$ to determine the formation kinetics using a stopped-flow system is shown. Based on turbidity and scattering, the transmission measurements determines the time, when the mixture is completely transparent (microemulsion is formed). The transmission change is a monoexponential first-order relaxation process with a time constant of $\tau = 1.79 \pm 0.01\text{ s}$ for microemulsion with 8 wt.% water (DWME 0820) at $T = 20\text{ }^{\circ}\text{C}$.

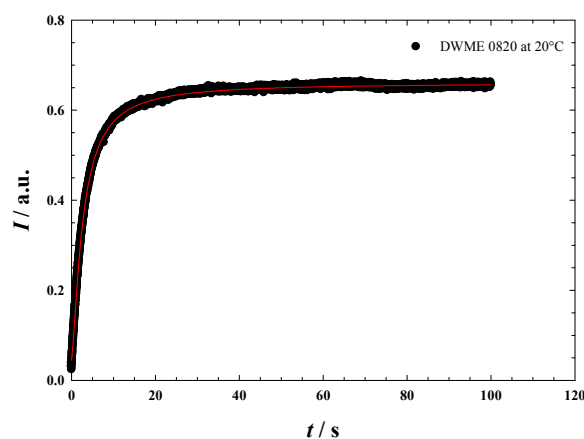


Figure 3-27: Transmission measurement of DWME 0820 at $T = 20\text{ }^{\circ}\text{C}$. The data can be described as a monoexponential function with a time constant of approximately $\tau = 1.79\text{ s}$. Red curve represents the monoexponential fit.

Transmission experiments were also performed for DWME 1620 (16 wt.% water) at $T = 20\text{ °C}$ in order to determine the effect of the water content on the formation kinetics (figure 3-28). The observed monoexponential process has a time constant of $\tau = 4.35 \pm 0.01\text{ s}$. Compared to the same experiments obtained with less water content (8 wt.%), the water / diesel fuel (including surfactant-blend)-mixture with 16 wt.% water features an extended solubilisation process of water and diesel fuel (including surfactant-blend) with an increased time constant.

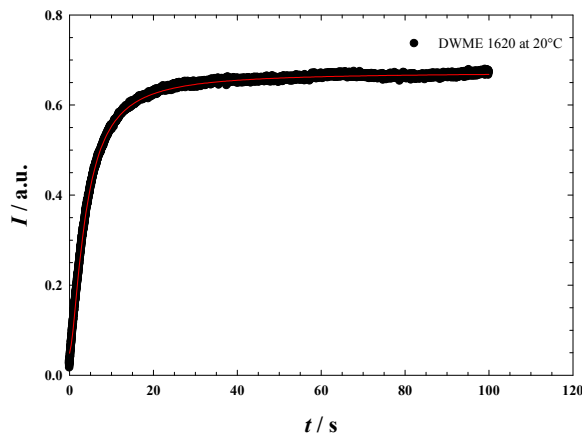


Figure 3-28: Transmission measurement of DWME 1620 at $T = 20\text{ °C}$. A time constant of approximately $\tau = 4.35\text{ s}$ is observed for the monoexponential relaxation process. Due to an extended clearing process of water and diesel fuel (including surfactant-blend), an increased time constant compared to DWME 0820 with a lower water content is obtained. Red curve represents the monoexponential fit.

As expected, the transmission change of the microemulsion with the largest amount of water (DWME 2420) features the highest time constant of $\tau = 7.60 \pm 0.02\text{ s}$ compared to the previous systems with lower water ratios (figure 3-27). This might be explained by the extended clearing process of the mixture while introducing 24 wt.% water into the diesel-phase (including surfactant-blend).

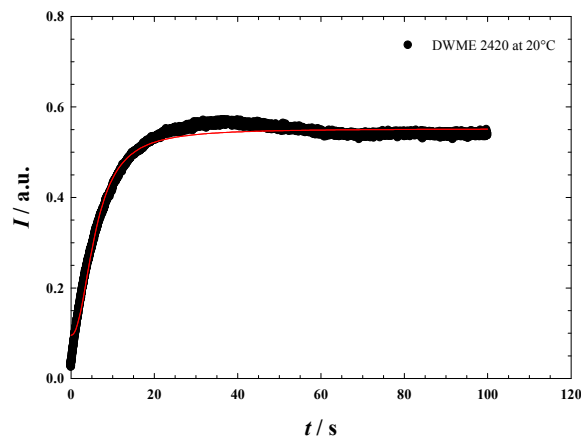


Figure 3-29: Transmission measurement of DWME 2420 at $T = 20\text{ }^{\circ}\text{C}$. An increased time constant of approximately $\tau = 7.60\text{ s}$ is observed compared to DWME 0820 due to an extended clearing process of water and diesel fuel (including surfactant-blend). Red curve represents the monoexponential fit.

The effect observed in the previous investigations while varying the water content of the system water/ammonium nitrate/ethanol - diesel fuel - oleic acid/monoethanolamine/oleic acid diethanolamide at $\delta_{(\text{ion})} = 0.6$, $\delta_{(\text{OD4})} = 0.4$, $\varepsilon = 0.006$, $\psi = 0.25$, $n = 0.45$ is summarised in the following figure.

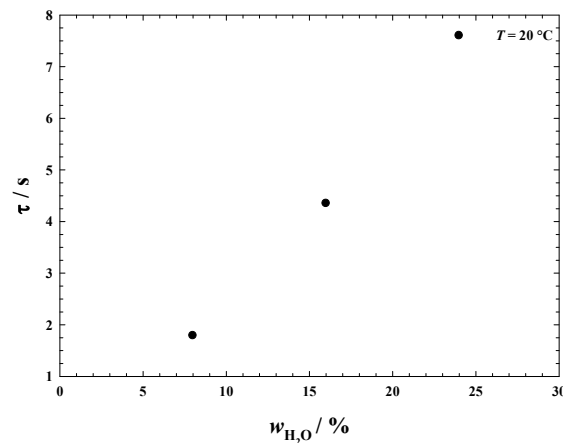


Figure 3-30: Time constant as a function of water content for three studied microemulsions (DWME 0820, DWME 1620, DWME 2420). An extended clearing process is observed at higher water ratios in the microemulsion system leading to a higher time constant.

As expected and explained above, an extended clearing process is observed at higher water ratios in the microemulsion system. The formation kinetics is slowed for the microemulsified fuel with 24 wt.% water.

In order to determine the influence of the temperature on the formation kinetics, the optical transmission of the sample with 24 wt.% water (DWME 2420) at $T = 60\text{ }^{\circ}\text{C}$ was also evaluated. As shown in figure 3-31, the resulting transmission graph exhibits a monoexponential function with a time constant of $\tau = 0.79 \pm 0.01\text{ s}$. In comparison to the time constant obtained at $T = 20\text{ }^{\circ}\text{C}$, an approximately 10 times faster microemulsion formation is achieved at $T = 60\text{ }^{\circ}\text{C}$.

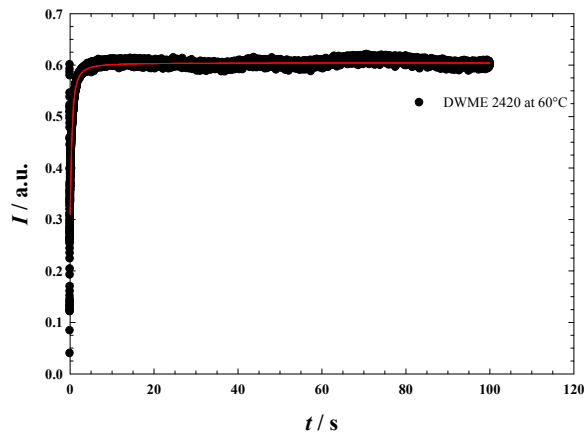


Figure 3-31: Transmission measurement of DWME 2420 at $T = 60\text{ }^{\circ}\text{C}$. A lower time constant of approximately $\tau = 0.79\text{ s}$ is observed compared to DWME 2420 at $T = 20\text{ }^{\circ}\text{C}$. Red curve represents the monoexponential fit.

In figure 3-32 the time constant and the dynamic viscosity of DWME 2420 are plotted against the temperature. The enhanced formation kinetics at higher temperatures is based upon a lower dynamic viscosity of the microemulsion at $T = 60\text{ }^{\circ}\text{C}$, resulting in a faster formation of the one-phase microemulsion.

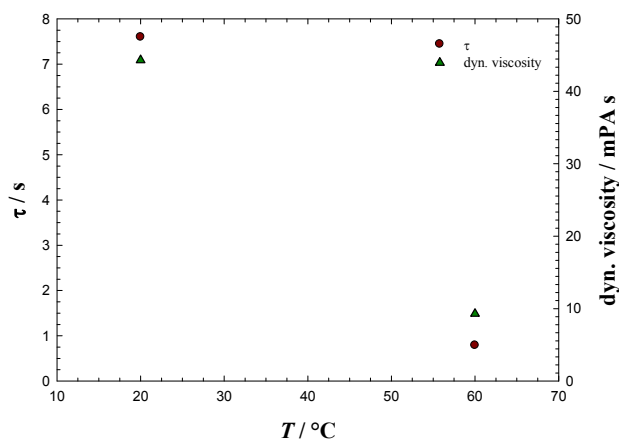


Figure 3-32: Time constant and dynamic viscosity of DWME 2420 as a function of temperature. Due to a lower dynamic viscosity of the microemulsion at $T = 60\text{ }^{\circ}\text{C}$, an enhanced formation kinetics with a lower time constant is observed.

Approaching the on injector-blending conditions, while pressure differences of $\Delta p = 100$ bar between water- and diesel fuel-rail exist, it can be assumed that the formation kinetics might be drastically enhanced compared to the results obtained using a stopped-flow setup with an approximately pressure difference of $\Delta p = 1$ bar between both pathways.

Conclusion

In order to introduce water into fuels to reduce exhaust emissions, an efficient, temperature invariant ($T = -10$ °C - 90 °C), ash-free microemulsion fuel of the type water/ammonium nitrate/ethanol - diesel fuel - oleic acid/monoethanolamine/oleic acid diethanolamide at $\delta_{(\text{ion})} = 0.6$, $\delta_{(\text{OD4})} = 0.4$, $\varepsilon = 0.006$, $\psi = 0.25$, $n = 0.45$ with various water contents was formulated (figure 3-7). A systematic phase behaviour study of this green multidimensional composition space (n , δ , ε , ψ) and the substitution of ethanol by n -propanol (figure 3-10) were studied to optimise the initial system. Additionally, crucial physical properties of the microemulsified fuels were determined regarding the general applicable requirements for diesel fuels according to DIN 590 and their influence on the spray behaviour. Detailed analysis revealed that these microemulsified fuels exhibit an enhanced lubricity (figure 3-19), very pronounced anti-corrosive properties and a very low ash content (< 0.001 wt.%) making them well suited for practice-oriented application. The structure of water-fuel microemulsions was examined by small angle neutron scattering (SANS) with a combination of dynamic light scattering (DLS) revealing homogeneously distributed, nano-scaled, water-swollen micelles and no lamellar phases.

Furthermore, the formation kinetics of microemulsified fuels, aiming for microemulsification milliseconds before injection, was recorded via transmitted light in a stopped-flow system varying the water content and temperature. It turned out that microemulsions form even faster approaching combustion conditions, because of high temperature and pressure conditions (figure 3-31).

3.5 Water fuel nanoemulsions

As mentioned in chapter 2.2, emulsions are colloid dispersion of at least two immiscible liquids with a kinetically stability. The main focus of this section was to formulate appropriate, economically more appealing, low surfactant content water-in-diesel nanoemulsion fuels with small droplet sizes by utilising the ultra-low interfacial tension during phase inversion and simultaneously low shear rates. Those nanoemulsified fuels should be applied for further combustion experiments, where load point dependent on injector-blending of water and diesel streams milliseconds before injection into the combustion chamber (chapter 4.1). In order to prevent corrosion and provide an adequate lubricity of the aqueous phase, various additives were analysed (chapter 3.5.1). In chapter 3.5.2 the influence of surfactant concentration and HLB-value on the stability of the formulated nanoemulsions was studied. The characterisation of nanoemulsions is based upon the determination of the water droplet sizes which are studied using dynamic light scattering (DLS).

3.5.1 Aqueous phase

The formulation of water-in-fuel nanoemulsions starts with the analysis of the aqueous phase. Due to a separate high pressure pump for the aqueous- and fuel-phase in the on injector-blending system, the aqueous phase has to fulfil certain properties. Hence, the influence of a lubricant and an anti-corrosion additive for the aqueous phase is studied.

3.5.1.1 Lubricity of the aqueous phase

Coefficient of traction of the aqueous phase is determined in a PCS Mini Traction Machine (measured by *Haensel*, Evonik). Traction is the force used to generate motion of a body on a tangential surface, which is expressed as the ratio of the maximum tractive force to the normal force. This correlation is termed as the coefficient of traction. A comparison of the coefficient of traction of pure water, of a 5 % aqueous solution of Lubrizol® Veg Ester™ and of a 0.25 % aqueous solution of Evonik® Rewoquat W 325 PG™ is shown in figure 3-33.

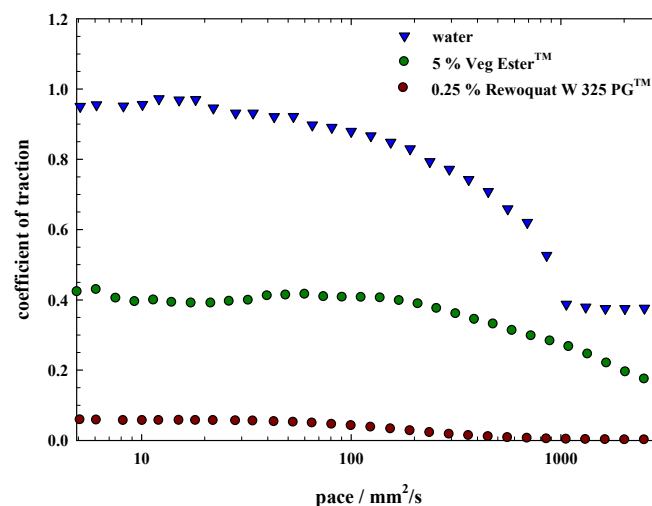


Figure 3-33: Coefficient of traction as function of the pace of pure water, 5 wt.% aqueous solution of Lubrizol® Veg Ester™ and 0.25 wt.% aqueous solution of Evonik® Rewoquat W 325 PG™. By adding lubricants into the aqueous phase, a significant reduction of the coefficient of traction is observed.

In figure 3-33 the coefficient of traction is plotted against the pace. Thereby, a 0.25 wt.% aqueous solution of Evonik® Rewoquat W 325 PG™ features the most efficient result due to a lowest coefficient of traction value starting at approximately 0.05. A decreased coefficient of traction than pure water is also observed with the 5 wt.% aqueous solution of Lubrizol® Veg Ester™. Compared to pure water, the addition of lubricants into the aqueous phase could significantly reduce the coefficient of traction up to 90 %. The aqueous phase added with Evonik® Rewoquat W 325 PG™ (0.25 wt.%) creates a lubrication film by absorption onto metal surfaces and thus providing wear protection. For further investigations, the lubricant Evonik® Rewoquat W 325 PG™ with a concentration of 0.25 wt.% in the aqueous phase was used.

3.5.1.2 Corrosion tests

One of the most important properties of the aqueous phase is the prevention of corrosion. The aim is to prevent corrosion during the delivery of the aqueous phase by the high pressure pump to the water rail. The standard corrosion tests according to DIN 51 360 (“Determination of anti-corrosive properties of water-based cooling lubricants” [187]) describes a simple laboratory method to determine anti-corrosive/corrosive properties.



Figure 3-34: Standard corrosion test according to DIN 51 360 from pure water. Strong corrosion is observed on the filter surface.

Figure 3-34 shows the first corrosion test result obtained from pure water. As expected, more than 5 % of the filter surface is discoloured and signifies strong corrosion with a corrosion grade of 4 (see chapter 6.2 for more information).

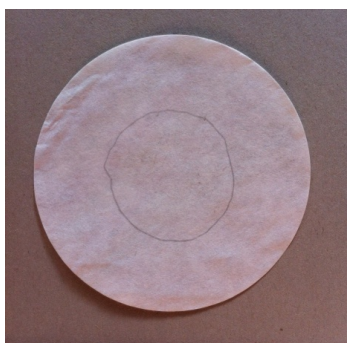


Figure 3-35: Corrosion test from pure anti-corrosive agent (Clariant® Antifrogen N™) features an unchanged filter surface.

In figure 3-35 the result of the corrosion test from pure additive (Clariant® Antifrogen N™) is presented. Expectedly, an unchanged filter surface is observed, which means that no corrosion occurs (corrosion grade: 0).

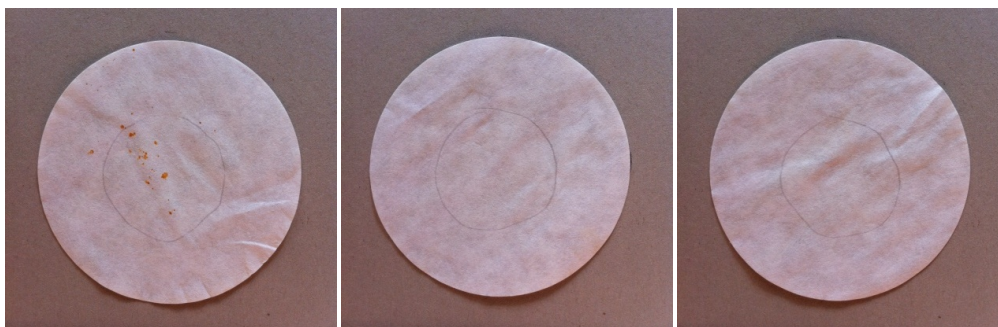


Figure 3-36: Corrosion tests from various aqueous phases including 0.25 wt.% lubricant and 1 wt.% (left), 5 wt.% (center) and 10 wt.% (right) of the anti-corrosive agent (Clariant® Antifrogen N™). Anti-corrosive properties are achieved by adding 5 wt.% and 10 wt.% of the anti-corrosive agent into the aqueous phase.

Figure 3-36 shows the corrosion test results from aqueous phases with various anti-corrosive agent concentrations. As presented in figure 3-33, the aqueous phase already includes 0.25 wt.% of the lubricity agent (Evonik® Rewoquat W 325 PG™). 1, 5 and 10 wt.% of the anti-corrosive agent (Clariant® Antifrogen N™) were added into the aqueous phase in order to prevent corrosion.

The corrosion tests from the aqueous phase including 0.25 wt.% lubricity agent and a minimum required amount of the anti-corrosive agent (5 wt.%) exhibited a non-corrosive property. A lower concentration of the lubricant (1 wt.%) did not prevent from corrosion anymore; light traces of corrosion are observed (corrosion grade: 1). For further investigations, the aqueous phase with 0.25 wt.% lubricant and 5 wt.% anti-corrosive agent was used.

3.5.2 Dynamic light scattering

In order to prove the potential benefits of water containing fuels, not only water microemulsified fuels were studied, but also water nanoemulsified fuels. As explained in chapter 2.2, the main difference between microemulsions and emulsions lies in their stability. By utilising the ultra-low interfacial tension during phase inversion water-in-diesel emulsions with small droplets and a simultaneously higher kinetic stability should be formulated. Efficient surfactants play an important role in the formation of emulsified fuels. By lowering the interfacial tension σ , the *Laplace pressure* p as described in equation (18) is reduced and less stress (shear rate) is then needed to break up a droplet into smaller ones. Depending on the choice of surfactants, HLB-value and emulsification method, different emulsions types including different droplet sizes and stabilities are accessible. The influence of the emulsion droplets sizes on exhaust emission were studied for water heavy fuel emulsions and showed that finer water dispersions lead to an enhanced reduction of coke emissions [188]. Thus, efficient and sustainable surfactants are needed to formulate emulsions with small water droplet sizes. Kinetically stable nanoemulsions possess emulsified droplets in the range of 10 - 200 nm, while bigger sized macroemulsions (> 200 nm) feature a very low stability. Therefore, suitable surfactants (sustainable, fully combustible and efficient) are required to formulate water-in-fuel nanoemulsions with small droplet sizes. In table 4 (chapter 2.2.3) the applied surfactants (with various HLB-values) for the formulation of nanoemulsified fuels are listed. In the studies of microemulsions, other surfactants were used which are inappropriate to formulate water-in-fuel nanoemulsions due to their inappropriate HLB-values. According

to table 2 in chapter 2.2, a HLB-value range of 3 - 8 is desirable in order to formulate low surfactant content water-in-oil nanoemulsions. Thereby, a combination of two efficient surfactants is needed to achieve an appropriate HLB-value.

To determine which surfactant is most suited to enhance the stability, the trend induced by various HLB-values has to be compared. In the following, the hydrodynamic radii of an water-fuel emulsion including additives (0.25 wt.% lubricant and 5 wt.% anti-corrosive agent) with a combination of sorbitan monooleate (HLB = 4.3) and polyoxyethylene sorbitan monooleate (HLB = 15) as surfactant blend (3 wt.%) at various HLB-values will be compared.

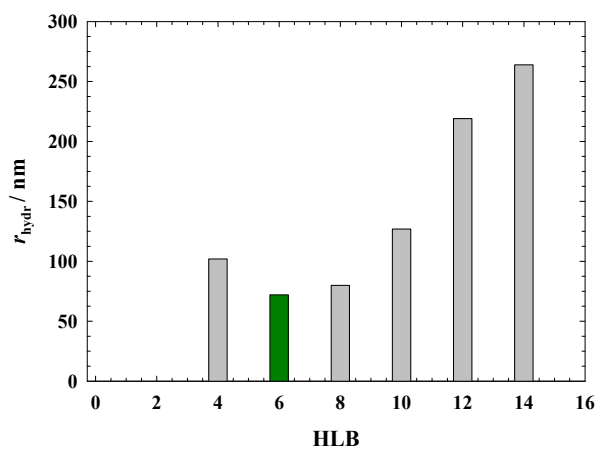


Figure 3-37: Mean hydrodynamic radii $\langle r_{hydr} \rangle$ depending on the HLB-value for the system water/anti-corrosive agent/lubricant - diesel fuel - sorbitan monooleate/polyoxyethylene sorbitan monooleate with 8 wt.% water and 3 wt.% surfactant blend at $T = 25^\circ\text{C}$. A minimum hydrodynamic radius is achieved at HLB = 6.

Figure 3-37 shows the trend of the hydrodynamic radii as a function of HLB-value for the system water/anti-corrosive agent/lubricant - diesel fuel - sorbitan monooleate/polyoxyethylene sorbitan monooleate with 8 wt.% water and 3 wt.% surfactant blend at $T = 25^\circ\text{C}$. A parabolic-shaped relation implies where the minimum mean hydrodynamic radius is obtained. Thus, the combination of sorbitan monooleate and polyoxyethylene sorbitan monooleate at a HLB-value of 6, leads to an enhanced stability (minimum mean hydrodynamic radius) due to a larger resulting interface. This effect is based upon utilising ultra-low interfacial tension during phase inversion at HLB = 6.

In figure 3-38 the determination of the hydrodynamic radii as function of time for the system water/anti-corrosive agent/lubricant - diesel fuel - sorbitan monooleate/polyoxyethylene sorbitan monooleate with 8 wt.% (left) and 16 wt.% water (right) and 3 wt.% surfactant blend

at $T = 25\text{ }^{\circ}\text{C}$ ($\text{HLB} = 6$) is presented. Both systems exhibit a mean hydrodynamic radius of $r_{\text{hydr}} < 120\text{ nm}$ over the entire time axis. Hence, it was verified that the newly formulated water-in-fuel emulsions by utilizing the ultra low interfacial tension can be described as water-in-fuel nanoemulsion with a higher kinetic stability than macroemulsions. Large droplets were torn into smaller ones due to a relatively low shear rate including the emulsification method (described in chapter 2.2.2) using a syringe and result in an enlarged interface. The present mean hydrodynamic radius for NE 08 (nanoemulsion with 8 wt.% water) is approximately $\langle r_{\text{hydr}} \rangle = 72 \pm 7\text{ nm}$ and $\langle r_{\text{hydr}} \rangle = 95 \pm 7\text{ nm}$ for NE 16 (nanoemulsion with 16 wt.% water).

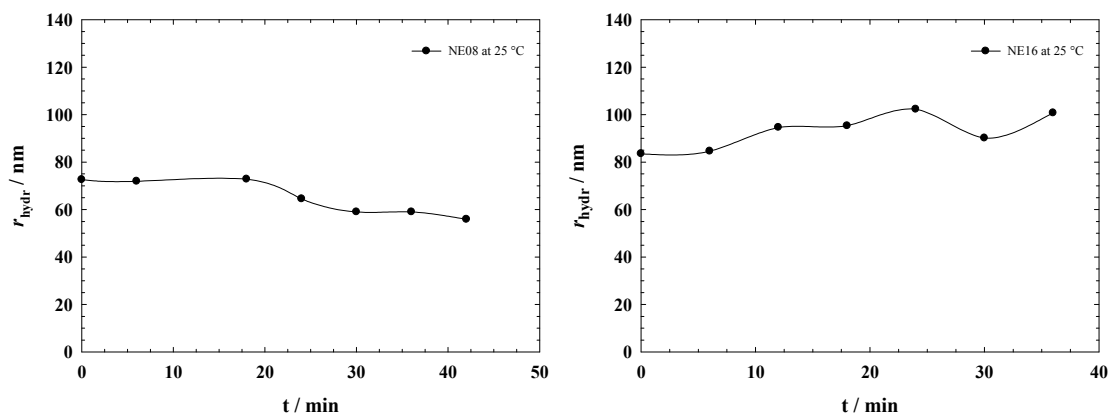


Figure 3-38: Hydrodynamic radius r_{hydr} as function of time for the system water/anti-corrosive agent/lubricant - diesel fuel - sorbitan monooleate/polyoxyethylene sorbitan monooleate with 8 wt.% (left) and 16 wt.% water (right) and 3 wt.% surfactant blend at $T = 25\text{ }^{\circ}\text{C}$ ($\text{HLB} = 6$). Hydrodynamic radii of $r_{\text{hydr}} < 120\text{ nm}$ are observed.

Following the trend in figure 3-39 it is obvious, that the stability of the formulated nanoemulsions is even provided three hours after preparation. The hydrodynamic radius of both systems was determined after three hours and features a hydrodynamic radius $r_{\text{hydr}} < 140\text{ nm}$ over the entire time axis. A mean hydrodynamic radius of $\langle r_{\text{hydr}} \rangle = 76 \pm 8\text{ nm}$ was obtained for NE 08, while the mean hydrodynamic radius for NE 16 was about $\langle r_{\text{hydr}} \rangle = 111 \pm 16\text{ nm}$. Due to the fact that the aqueous- and oil-phase are mixed milliseconds before injection into the combustion chamber (on injector-blending, chapter 4.1), a long-term stability in the water-fuel nanoemulsions is not necessary.

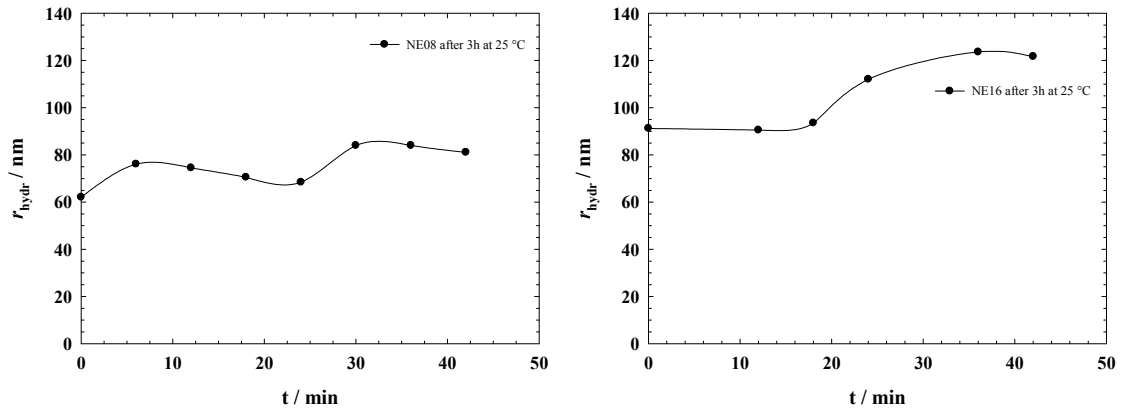


Figure 3-39: Repeated determination (three hours after preparation) of the hydrodynamic radius r_{hydr} in dependence of time in the system shown in figure 4-6. Kinetic stability including hydrodynamic radius $r_{hydr} < 140$ nm is even provided three hours after preparation.

In order to ensure small sizes of nanoemulsion droplets approaching combustion conditions (higher temperatures), the mean hydrodynamic radius of the formulated water-in-fuel nanoemulsions of the system water/anti-corrosive agent/lubricant - diesel fuel - sorbitan monooleate/ polyoxyethylene sorbitan monooleate with 8 wt.% (left) and 16 wt.% water (right) and 3 wt.% surfactant blend were determined at a higher temperature $T = 50$ °C (HLB = 6).

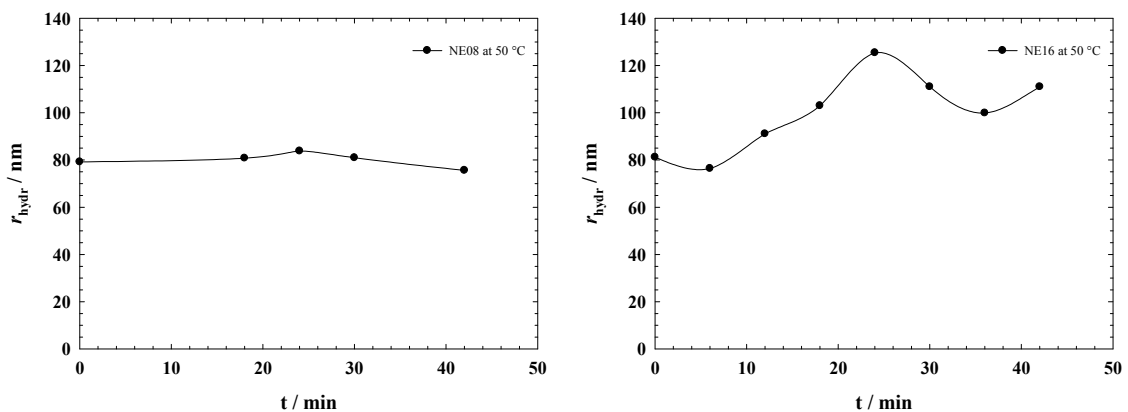


Figure 3-40: Hydrodynamic radius r_{hydr} as function of time in the system shown in figure 3-38 at $T = 50$ °C. Both systems feature fine water droplets with $r_{hydr} < 140$ nm.

Figure 3-40 shows the hydrodynamic radii of the formulated systems as a function of time at $T = 50$ °C. Since the values of the hydrodynamic radii in dependence of time follow the same trend shown in figure 3-38, the kinetic stability including fine water droplets ($r_{hydr} < 140$ nm) is maintained. A mean hydrodynamic radius of $\langle r_{hydr} \rangle = 80 \pm 3$ nm (NE 08) and $\langle r_{hydr} \rangle = 117 \pm 16$ nm (NE 16) was obtained and thus guarantees that enlarged water domains



due to breakdown processes (figure 2-19) will not be formed approaching combustion conditions.

Conclusion

In this section a newly, economically more appealing, low surfactant content water-in-diesel nanoemulsion fuels of the type water/anti-corrosive agent/lubricant - fuel - sorbitan monooleate/polyoxyethylene sorbitan monooleate with 3 wt.% surfactant for 8 wt.% and 16 wt.% water was successfully formulated by utilising the ultra-low interfacial tension during phase inversion and applied for further combustion experiments using the load point dependent on injector-blending system (chapter 4.3). First, a selection of lubricants was studied in order to provide an adequate lubricity of the aqueous phase. These measurements implied that the addition of 0.25 wt.% of Evonik® Rewoquat W 325 PGTM into the aqueous phase creates a lubrication film by absorption onto metal surfaces and thus providing wear protection (figure 3-33). Based on this result, anti-corrosive agents were investigated according to DIN 51 360. Standard corrosion tests proved that 5 wt.% of Clariant® Antifrogen NTM in the aqueous phase prevents from corrosion (figure 3-36). Finally, dynamic light scattering (DLS) was applied to determine the mean hydrodynamic radii in dependence of the HLB-value. A HLB-value of 6 yielded to smaller mean hydrodynamic radii ($r_{\text{hydr}} < 120$) and thus nanoemulsified fuels with 3 wt.% water were formulated (figure 3-38). Regarding the economic aspect (chapter 4.3), it was proven that the system water/anti-corrosive agent/lubricant - diesel fuel - sorbitan monooleate/polyoxyethylene sorbitan monooleate with 3 wt.% surfactant blend at HLB = 6 offers an appropriate water containing fuel with a reduced amount of surfactant compared to the formulated microemulsion systems in chapter 3.1. Due to the load point dependent on injector-blending of water (including anti-corrosive agent and lubricant) and diesel (including surfactant-blend) streams milliseconds before injection into the combustion chamber, a long-term stability of those formulated nanoemulsion fuels is not necessary. In contrary to pre-mixed microemulsions, which are unsuitable for load point dependent addition of water to the fuel, the newly formulated nanoemulsion fuel is appropriate using the load point dependent on injector-blending of water and diesel with a reduced amount of surfactant.

Now it is interesting to compare the combustion tests of microemulsions and nanoemulsions as alternative fuels in terms of exhaust gas emissions. If same potential benefits are obtained with nanoemulsified fuels, those would be then favoured from an economic perspective.



4 COMBUSTION RESULTS

In this chapter the main results obtained in combustion experiments using the formulated water fuel-microemulsions (chapter 3.1) and -nanoemulsions (chapter 3.5) are presented and discussed. In an interdisciplinary cooperation (FVV project; Forschungsvereinigung Verbrennungskraftmaschinen) with the *University of Applied Sciences in Trier* (HS Trier) and the *Rheinisch Westfälische Technische Hochschule Aachen* (RWTH; Lehrstuhl für Verbrennungskraftmaschinen VKA), a detailed examination of the influence of these formulated water containing fuels on the exhaust emissions and spray behaviour were performed.

4.1 On injector-blending

In contrary to pre-mixed microemulsions, the on injector-blending allows the generation of appropriate water/fuel-mixing ratios directly at the injector. Due to an optimal, for each operation point fitted water/fuel-mixing ratio (load point dependent), the addition of water to diesel fuel can be completely prevented during the warm-up phase (of ICE). This system was developed by the *University of Applied Sciences in Trier* within a research project in 2009. Compared to an on board-blending, the reaction time of the on injector-blending is reduced by a lower dead volume (volume of the mixing chamber of the on board-blending systems and volume of the fuel lines between mixing chamber and the main injectors) [33]. In figure 4-1 the schematic illustration of the on injector-blending system is shown.

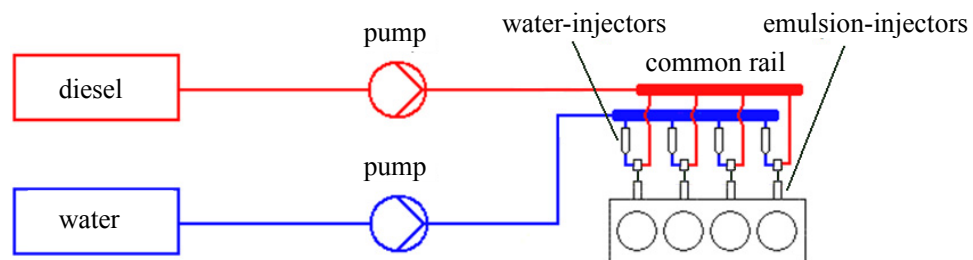


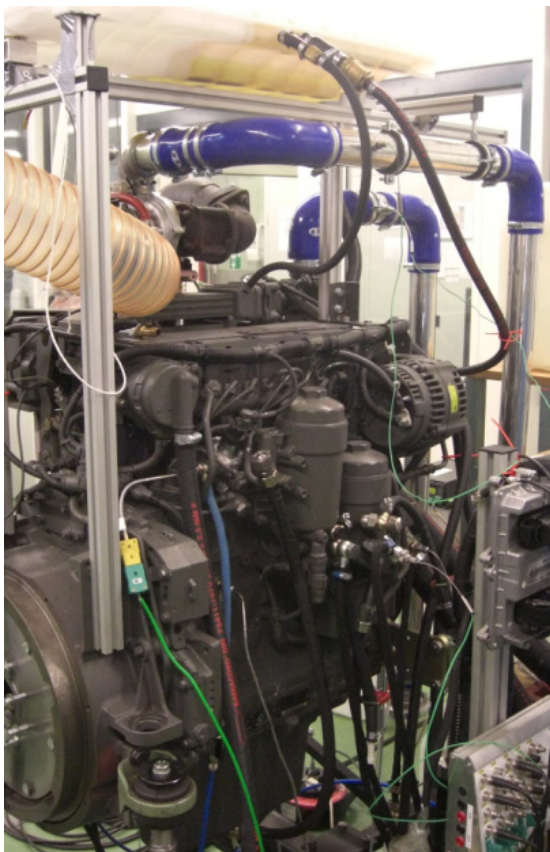
Figure 4-1: Schematic drawing of the on injector-blending (taken from [189] and modified). Two different high pressure pumps transmit water- and diesel-phase to the water- and diesel-rail.

On the contrary to the on board-blending, the water- and diesel-phase delivery to water- and diesel-rails is accomplished by two high pressure pumps. In order to avoid corrosion and to improve the lubricity of the water phase, an anti-corrosive additive and a lubricity agent were

added into the water phase (see chapter 3.5.1). The water from the water-rail reaches the mixing chamber through the water-injector, while diesel from the diesel-rail is directly forwarded into the mixing chamber. Due to a short mixing length, an efficient surfactant is needed to form a homogeneous mixture.

Test engine

In order to study exhaust emissions of water containing fuels in form of microemulsions and nanoemulsions (containing conventional EN 590 diesel fuel as polar component), combustion tests have been performed on a four-cylinder inline internal combustion engine (ICE) with common-rail injection (1400 bar), intercooling and cooled exhaust gas recirculation (EGR) manufactured by DEUTZ AG[®]. The test engine and its specifications are shown in figure 4-2.



specifications

engine displacement [ltr]:	4
bore/stroke [mm]:	101/126
brake mean effective pressure (BMEP) [bar]:	20.8
injection pressure [bar]:	1400
compression ratio:	18:1
max. power [kW]:	113
peak torque [Nm]:	657
certified to:	EPA Tier 3

Figure 4-2: Four-cylinder test engine with common-rail injection (left) and its specifications (right) manufactured by Deutz AG[®] (taken from [189]).

The combustion experiments were planned and supervised by Dipl.-Ing. (HS) M. Eng. *Heinrich Dörksen* (engineer of the *University of Applied Sciences in Trier*). The actual engine's setup, including the on injector-blending system, is presented in figure 4-3.

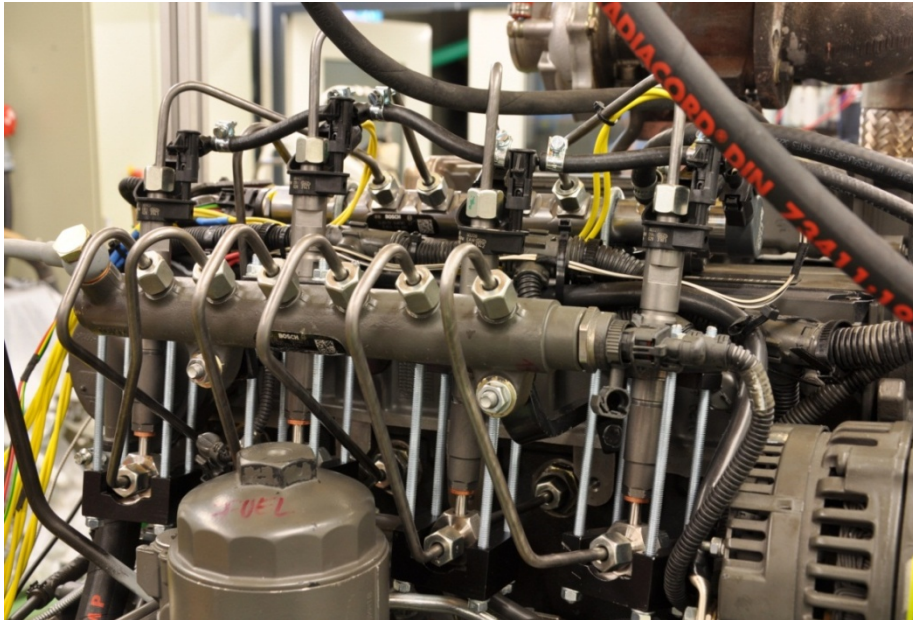


Figure 4-3: Engine's setup with additional on injector-blending system (taken from [189]).

Partial results presented and discussed in the following sub-section have been partly published on the *FFV-Herbsttagung* (Sep. 2012, Dortmund) [190] while further results will be published on the *FVV-Frühjahrstagung* (March 2014, Magdeburg) [191].

Selected engine states

In order to obtain results for typical operating conditions, two test series have been selected: the **B50**-point with a constant engine speed of $n = 1565 \text{ min}^{-1}$ and a brake mean effective pressure of $\text{BMEP} = 10 \text{ bar}$ and the **C100**-point with $n = 1853 \text{ min}^{-1}$ and $\text{BMEP} = 18 \text{ bar}$.

Exhaust gas and particulate matter measurements

The methods of analysis to determine the exhaust gas emissions and the exhaust particulates from internal combustion engines are listed in table 13.

Table 13: Overview of the methods of analysis to determine the exhaust gas emissions and the exhaust particulates from internal combustion engines.

substance	model	Method
CO, CO ₂	AVL AMA 4000	ND-IR spectroscopy
NO _x	AVL AMA 4000	UV spectroscopy
TOC	AVL AMA 4000	FID
particulate mass	AVL Smart Sampler SPC 472	Gravimetric (partial flow dilution)
opacity	AVL Opacimeter 439	optic (partial flow dilution)
Filter Smoke Number (FSN)	AVL Smoke Meter 415S	filter-type smoke meter
particle counter	AVL Particel Counter 489	light scattering

For the evaluation of the nitrogen oxide emissions, the emission values of nitrogen monoxide (NO) and nitrogen dioxide (NO₂) were summarised as NO_x-emissions. A detailed description of the measurements is composed in chapter 6.2.

4.2 Microemulsion combustions experiments

The results obtained in combustion experiments using the fuel microemulsions of the system water/ammonium nitrate/ethanol - diesel fuel - oleic acid/monoethanolamine/oleic acid diethanolamide at $\delta_{(\text{ion})} = 0.6$, $\delta_{(\text{OD4})} = 0.4$, $\varepsilon = 0.006$, $\psi = 0.25$, $n = 0.45$ with a water content of 0 - 24 wt.% (in steps of 8 wt.%) at a constant surfactant ratio are presented and discussed in this chapter. Exhaust emissions of the following combustion tests of water-fuel microemulsions were compared with the emissions of the reference sample of pure diesel-fuel (identical diesel fuel as used in the water microemulsions). The oleic phase contains the blend of surfactants (oleic acid, monoethanolamine and oleic acid diethanolamide), while the aqueous phase includes the additives (ethanol, ammonium nitrate, anti-corrosive agent and lubricant). Due to the trivial fact that water is not combustible, water containing fuels feature a reduced lower heating value (*LHV*) than pure diesel. Thus, the lower heating value of the

complete microemulsion was determined by equation (39) in order to provide an equal energy input per minute into the combustion chamber.

4.2.1 NO_x-emissions

The major source for nitrogen is the atmospheric intake-air consisting of about 79 vol.% nitrogen [158]. The mechanism for the formation of nitrogen oxides is described in detail in chapter 2.4.3. Nitrogen oxides NO_x formed in the combustion process are referred as a mixture of nitrogen monoxide, -dioxide and nitrous oxide. Nitrogen oxides are considered as hazardous to health and contribute, among other things, to the formation of acid rain [192]. In this section, the potential of the NO_x-emission reduction by application of microemulsified fuels is examined. An appropriate fuel microemulsion can be a beneficial alternative to the complex and expensive aftertreatments systems (chapter 2.4.4). Former combustion experiments have been performed by *Nawrath*, *Bemert* and *Wulff* which show a decrease of soot and NO_x-emissions by using temperature invariant microemulsions as fuel [53, 56, 60].

The NO_x-emissions from the internal combustion at operation point **B50** ($n = 1565 \text{ min}^{-1}$, BMEP = 10 bar) and **C100** ($n = 1853 \text{ min}^{-1}$, BMEP = 18 bar) are compared to NO_x-emissions of pure conventional diesel.

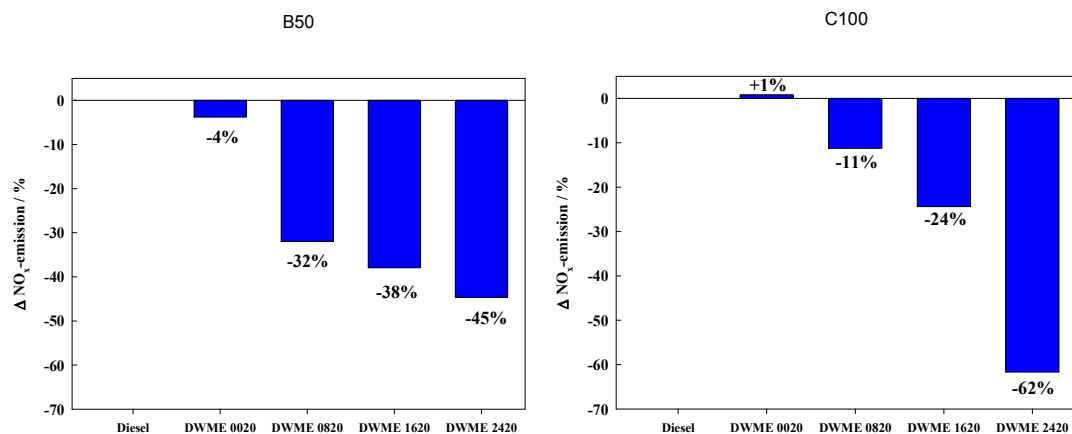


Figure 4-4: Bar chart of percental change of NO_x-emissions compared to pure diesel fuel at operating point B50 (left) and C100 (right). DWME 0020, DWME 0820, DWME 1620 and DWME 2420 mark the formulated microemulsions which were applied containing 0 wt.%, 8 wt.%, 16 wt.% and 24 wt.% water, each with 20 wt.% of the surfactant blend. A significant reduction of NO_x-emission up to 45 % and 62 % was obtained applying DWME 2420 at B50 and C100 compared to diesel fuel.

The percentage change of NO_x-emissions of the investigated microemulsions with various water contents (DWME 0020, DWME 0820, DWME 1620, DWME 2420) at operating point

B50 (left) and C100 (right) are shown in figure 4-4. As expected, the NO_x -emissions is nearly decreased proportional to the increased water content in the microemulsion. The effect is based upon the lowered combustion chamber temperature due to the endothermic water evaporation. Hence, the formation of the thermal *Zeldovich* NO is significantly reduced [158]. At operating point B50, the NO_x -emissions are reduced about 38 % for DMWE 1620 and 45 % for DWME 2420. This proves to be a significant higher decline than observed in previous investigations [53, 56, 60]. An enormous potential of NO_x -reduction (62 %) applying microemulsion-fuels was obtained for the microemulsion fuel containing 24 wt.% water at C100. At a higher load point (C100), higher reduction of NO_x -emissions is achieved.

4.2.2 Filter smoke number (FSN) and opacity

Combustion of diesel fuel results in a high amount of particulate matter and soot emissions. Both emissions are harmful to health [169]. Thus, the exhaust particulates also play an important role regarding the compliance with regulations for the limited exhaust emissions. The European emission standards regulate the emissions of nitrogen oxides (NO_x), total hydrocarbon (THC), carbon monoxide (CO) and particulate mass (PM) [7] and will become stricter in September 2014 (EURO 6). Diesel particulate filter are used since 1985 in order to reduce soot emissions. A detailed description of the functionality of a diesel particle filter is given in chapter 2.4.4. The measurements of the exhaust particulates are determined by two different methods. An official approved indication of the soot-emission represents the filter smoke number (FSN) which is based upon blackening on the filter surface caused by soot. The second method determines the optical permeability of the exhaust gas by using an opacimeter (for further details see chapter 6.2). Both methods specify approximate values and should be confirmed by measuring the particulate mass (chapter 4.2.3).

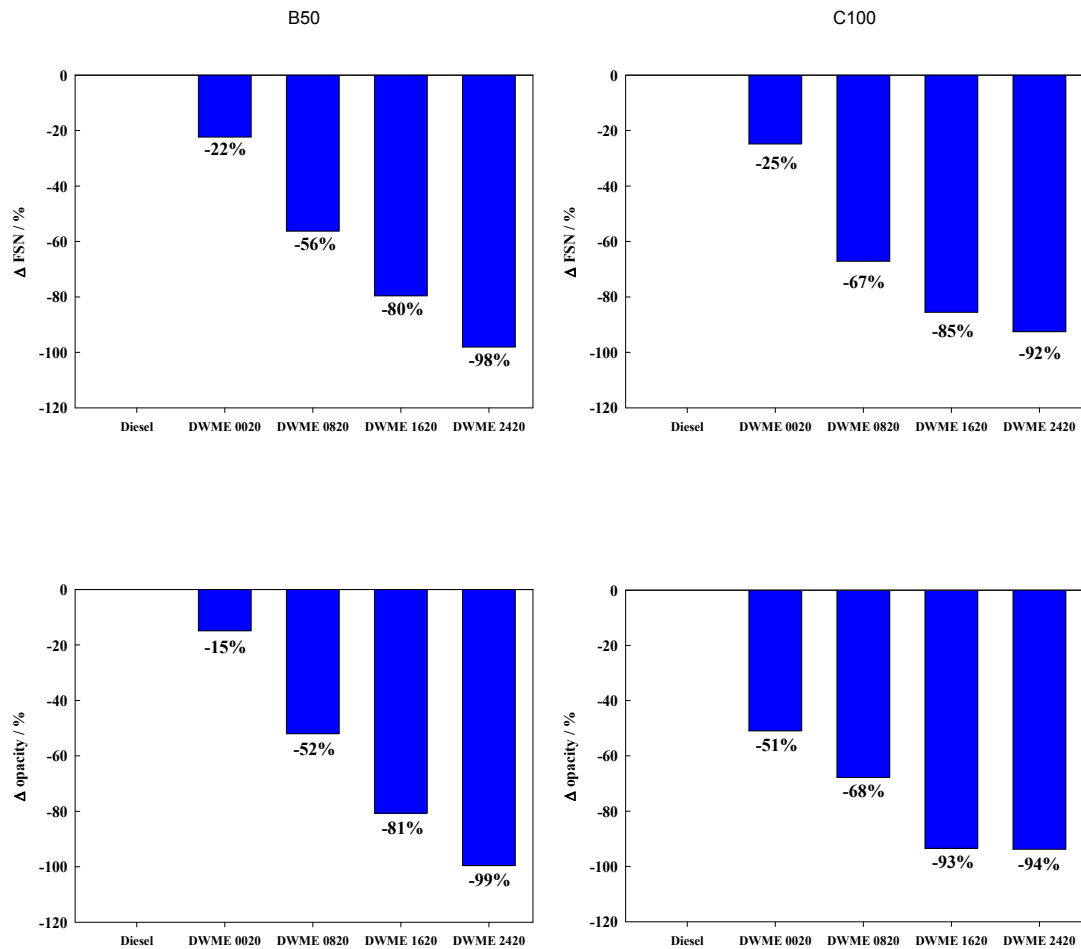


Figure 4-5: Percental change of filter smoke number (FSN; top) and opacity (bottom) at various water contents for operating point B50 (left) and C100 (right). A drastic reduction of FSN and opacity for both operating points is achieved. Combining both measuring methods, a reduction of soot-emissions over 92 % with water microemulsified fuels (DWME 2420) is observed compared to diesel fuel.

Figure 4-5 exhibits the percentage change of filter smoke number (top) and opacity (bottom) compared to pure diesel fuel. As expected, the use of microemulsions as fuel causes a significant reduction of exhaust gas turbidity, measured as smoke opacity and filter smoke number (FSN). The soot-emission at operating point B50 is reduced up to 98 % (FSN) and 99 % (opacity) for applying DWME 2420 compared to the emissions of pure diesel. For operating point C100, a reduction of soot-emissions up to 92 % (FSN) and 94 % (opacity) is also observed. Both methods feature comparable values and confirm a reduction of soot-emissions over 92 % with water containing fuels (DWME 2420). Analogous soot-reduction was achieved by *Nawrath*, *Bemert* and *Wulff* using water fuel microemulsions [53, 56, 60]. The addition of water has a significant influence on the internal combustion and thus on the various chemical processes during combustion. Water also changes the chemical properties of the diesel fuel, which affect the spray behaviour leading to a modified combustion process.

However, it is decisive that a certain proportion of water is splitted homogenous into radical species at temperatures of 2000-3000 K [193]. The hereby generated $\cdot\text{OH}$, $\cdot\text{O}$ and $\cdot\text{O}_2\text{H}$ -radicals accelerate the oxidation of the hydrocarbon chains, whereby a more efficient combustion is achieved [31]. An unexpected, significant reduction of the filter smoke number (FSN) and opacity is observed applying DWME 0020 with 0 wt.% water. The following gravimetric investigations of the soot-emissions should declare this effect.

4.2.3 Particulate mass

Gravimetric soot-emission investigations allow, contrary to the FSN- or opacity-method, determining the soot-reduction independent of the modified chemical composition of the soot, which might affect the blackening of the filter surface. Especially at readjusted combustion conditions, the soot-structure and composition can be altered without observing a change in weight of the soot. Hence, the blackening of the filter surface does not exhibit a representative declaration about the soot-emission whereby the combination of all three methods allows an optimum determination of the soot-emissions.

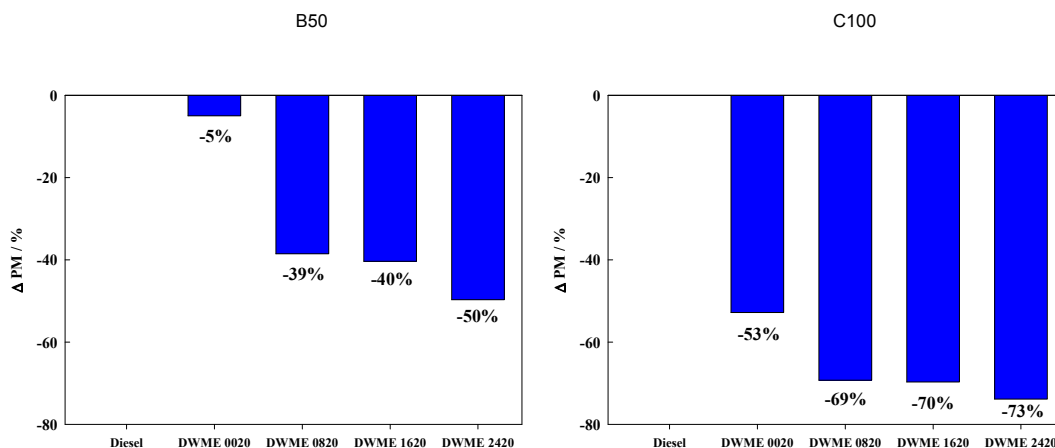


Figure 4-6: Percental change of particulate mass (PM) of microemulsion fuels (DWME 0020, DWME 0820, DWME 1620, DWME 2420) at B50 (left) and C100 (right). A drastic decline of PM up to 50 % (B50) and up to 73 % (C100) is obtained applying microemulsion with 24 wt.% water.

Figure 4-6 shows the percental change of particulate mass (PM) at different water contents compared to pure diesel fuel. The gravimetric determination of the particulate mass at B50 indicates a reduction up to 50 % with a maximum water content of 24 wt.%. The microemulsion DWME 0820 and DWME 1620 also cause a decline of the particulate mass up to 39 %. An enhanced effect is observed at higher loads with increasing water content; a maximum reduction up to 73 % is achieved applying DWME 2420. A reduction of the

particulate mass (PM) up to 53 % (C100) is obtained for DWME 0020 with 0 wt.% water and confirms the previous results shown in figure 4-5. Further investigations regarding the combustion temperature and spray behaviour should clarify the unexpected effect observed for the “microemulsion” with 0 wt.% water (DWME 0020).

As previously explained, the combination of all three methods (FSN, opacity, PM) provides a precise information about the actual soot-emission. In order to obtain an assessment of the correlation between all three methods used for the determination of exhaust particulates, the values of the methods are plotted in a 3D-diagram shown in figure 4-7.

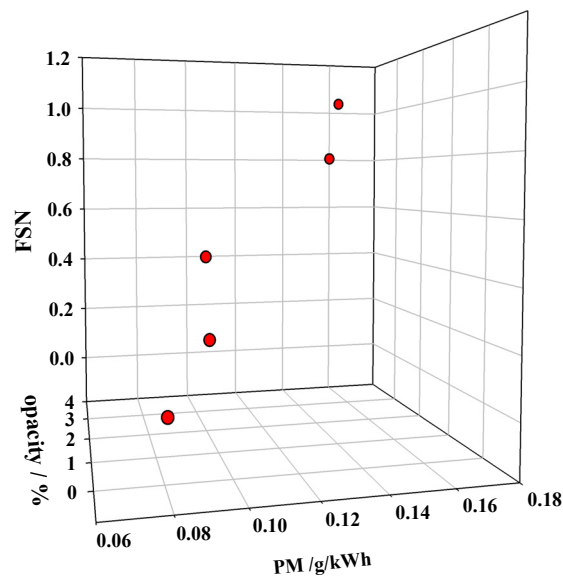


Figure 4-7: 3D-diagram showing the corresponding values of the applied methods (FSN, opacity, PM) to determine the soot-emission.

An approximately linear trend is observed between of all three methods and thus allows an estimation of the individual, unknown value if the values of the other two applied methods are known.

4.2.4 Number of particle

The number of particle plays an important role in terms of determining the mean diameter of soot particles. Their sizes can vary from ultra-fine to fine particles with a size range of 10 nm to 2 μm . Those alveolar, fine particles are harmful to human health and may cause cancer, asthma and cardiac problems [194]. Soot particles contribute to the global warming (first contributor: CO_2 ; second contributor: soot particles) and are involved in the increase of

regional temperatures and accelerate the melting of polar icecaps [195]. Thus, a reduced formation of soot and PAHs is essential.

The measurements of the number of particles do not include the work-intensive measuring technique to determine the particle size distribution. In former studies, water containing fuels drastically shift the diameter of soot particles to smaller values with an increased number of particles [56, 60, 61].

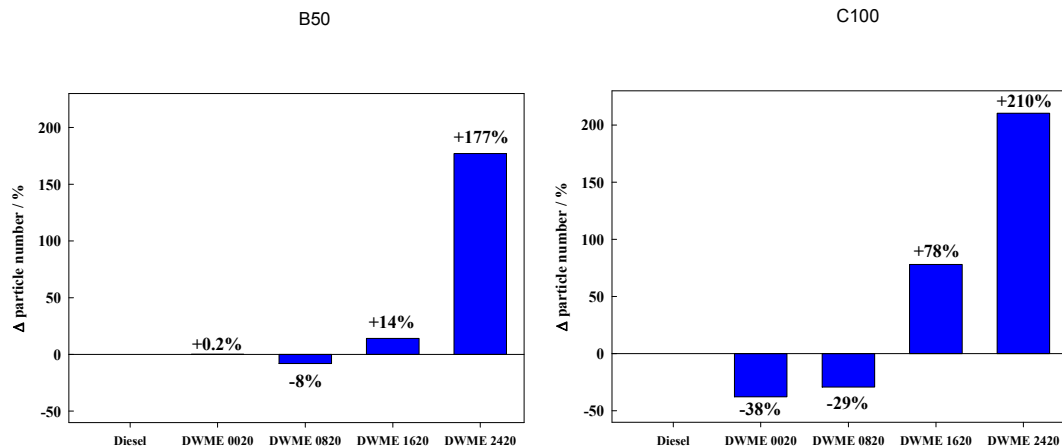


Figure 4-8: Percental change of the particle number of water-in-fuel microemulsions (DWME 0020, DWME 0820, DWME 1620, DWME 2420) at B50 (left) and C100 (right). A significant increase of the number of particles is observed applying water containing fuels.

In figure 4-8 the number of exhaust particles of different microemulsions is compared to the number of exhaust particles of pure diesel. As noted in the previous investigations [56, 60, 61], a significant increase of the particle number is obtained. Regarding the results for the absolute particulate mass, a reduction up to 73 % (DWME 2420; figure 4-6) is achieved. Due to that fact, it must be considered that the soot particle sizes are reduced. Few approaches for a plausible explanation can be proposed by the nucleation process. In conventional diesel-driven engines, soot-particles are formed which conduce as condensation nuclei for the emitted unburnt hydrocarbons. In case of operating with water microemulsions, less particulate mass are formed as shown in figure 4-6. Lack of condensation nuclei (which outer shell consists of unburnt hydrocarbons [196]) is thus observed. Consequently, a classical adsorption of hydrocarbons on the surface of carbon particles/inorganic residues does not take place but rather a homogenous nucleation of unburnt hydrocarbons [197, 198]. This implies that a change in particle composition can cause a misjudgment of the particle number and size.

4.2.5 Particulate matter composition

However, to clarify the composition of the particulate mass, an analysis of the composition was performed by the *VKA in Aachen* and the results are presented in the following figure.

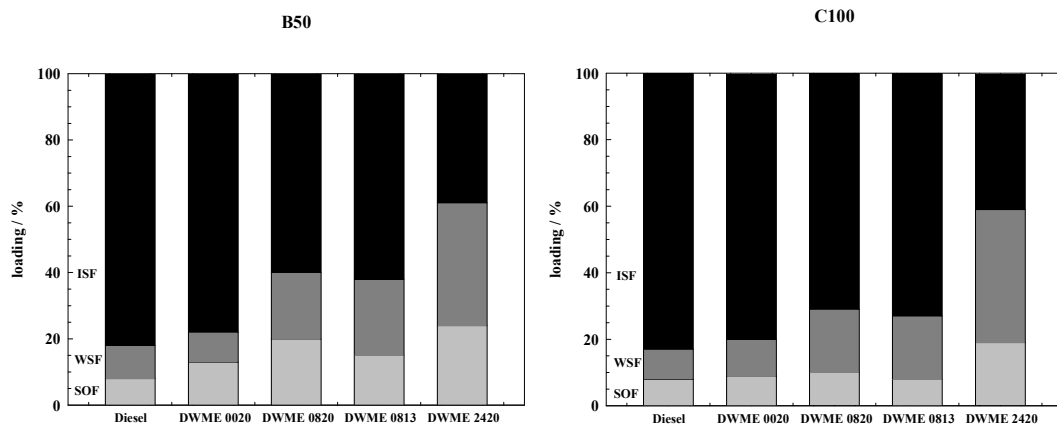


Figure 4-9: Percental composition of particulate mass (PM) at B50 (left) and C100 (right) for diesel fuel and microemulsion fuels (DWME 0020, DMWE 0820, DWME 0813, DWME 2420). Black: insoluble fraction (ISF), dark grey: water soluble fraction (WSF), grey: soluble organic fraction. The insolube fraction (ISF) is reduced with increasing water content at both operating points [179].

In figure 4-9 the percental composition of particulate mass emissions of diesel fuel, DWME 0020, DMWE 0820, DWME 0813 and DWME 2420 at both operating points is presented. By means of an extraction process (described in chapter 6.2), the collective particles were divided into insoluble fraction (ISF, black), water soluble fraction (WSF, dark grey) and soluble organic fraction (SOF, grey). Interestingly, a strong percental decrease of the insoluble fraction (ISF), which is mainly composed of black carbon and metal abrasion, is observed for microemulsified fuels compared to pure diesel. The percentage change of this insoluble fraction decreases from 82 % (83 %) for diesel fuel to 39 % (42 %) for DWME 2420 at B50 (C100). This result corresponds to a reduction by a factor of approximately 2 and confirms the results obtained in figure 4-6. Simultaneously, the percental emission of water soluble fraction (WSF) is increased from 10 % (9 %) for diesel fuel up to 37 % (40 %) for the microemulsion fuel with 24 wt.% water at B50 (C100). The percentage increase of the water soluble fraction (WSF; consisting of soluble salts as sulfate, nitrate, carbonate and their correspondent acids) can be explained by the addition of nitrogen containing surfactants which form soluble nitrates due to oxidation at high combustion temperatures. Furthermore, a slight increase of the soluble organic fraction (SOF; consisting of hydrocarbons from fuel, surfactant or engine oil) is observed applying water containing fuels. Those results correspond with the previous investigations from *Bemert and Wulff* [56, 60].

4.2.6 Unburnt hydrocarbons

Hydrocarbons (HC) result from recombination of radical degradation processes due to an incomplete combustion [199, 200]. The recombination of small products (e.g. C_2H_2) during combustion can lead to higher-ordered carbon-derivates which grow in a further recombination process to polycyclic aromatic hydrocarbons (PAHs). Due to agglomeration, these growing PAHs are the precursors of soot, as shown in 2-38. The formation of PAHs depends on the fuel and the combustion conditions while featuring carcinogenic and mutagenic properties [201]. Therefore, a detailed consideration on HC-emissions during combustion is followed.

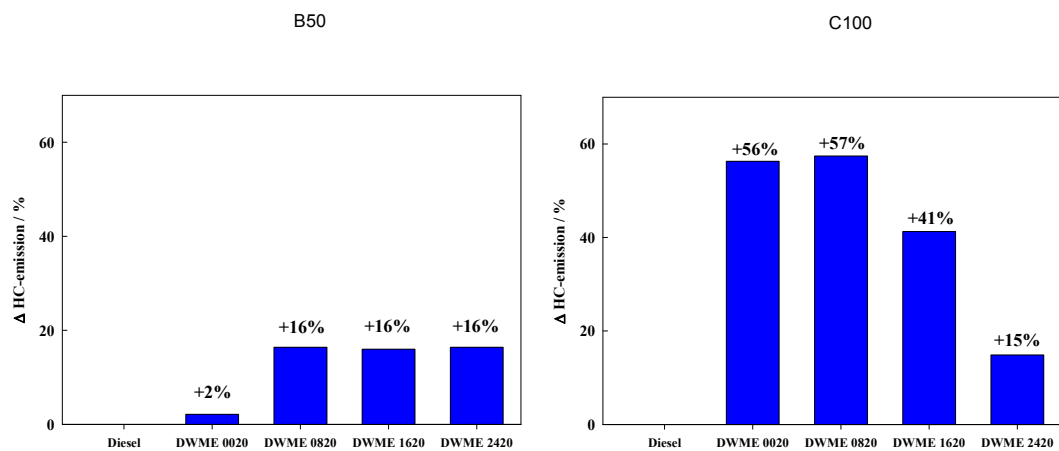


Figure 4-10: Percental change of unburnt hydrocarbons-emissions (HC) of microemulsion-fuels (DWME 0020, DWME 0820, DWME 1620, DWME 2420) at B50 (left) and C100 (right). An increase of HC-emissions is obtained for all water contents.

Figure 4-10 shows the percentage change of unburnt hydrocarbons-emissions in dependence of water content at operating point B50 (left) and C100 (right). An increase of HC-emission with water microemulsions is observed. One of the main reasons is the flame quenching at cold cylinder walls due to high turbulences at the flame front. Another reason is the higher penetration depth of the microemulsified fuels compared to pure diesel fuel as observed in figure 4-13, which suppresses the ignition of the fuel leading to unburnt fuel in the combustion chamber. Furthermore, the cooling of the reaction zone and the undesirable radical termination of the carbon chain reaction might also cause flame quenching [31].

4.2.7 Carbon monoxide and carbon dioxide

Carbon monoxide (CO) results from incomplete combustion with lack of oxygen, while carbon dioxide (CO₂) is formed from complete combustion after equation (39) in chapter 2.4. Carbon monoxide is a colourless, toxic gas that reduces the amount of oxygen in the blood cells if breathed in. Carbon dioxide is the first contributor for global warming. Therefore, a limited emission of CO and CO₂ during internal combustion was set in the European emission standards.

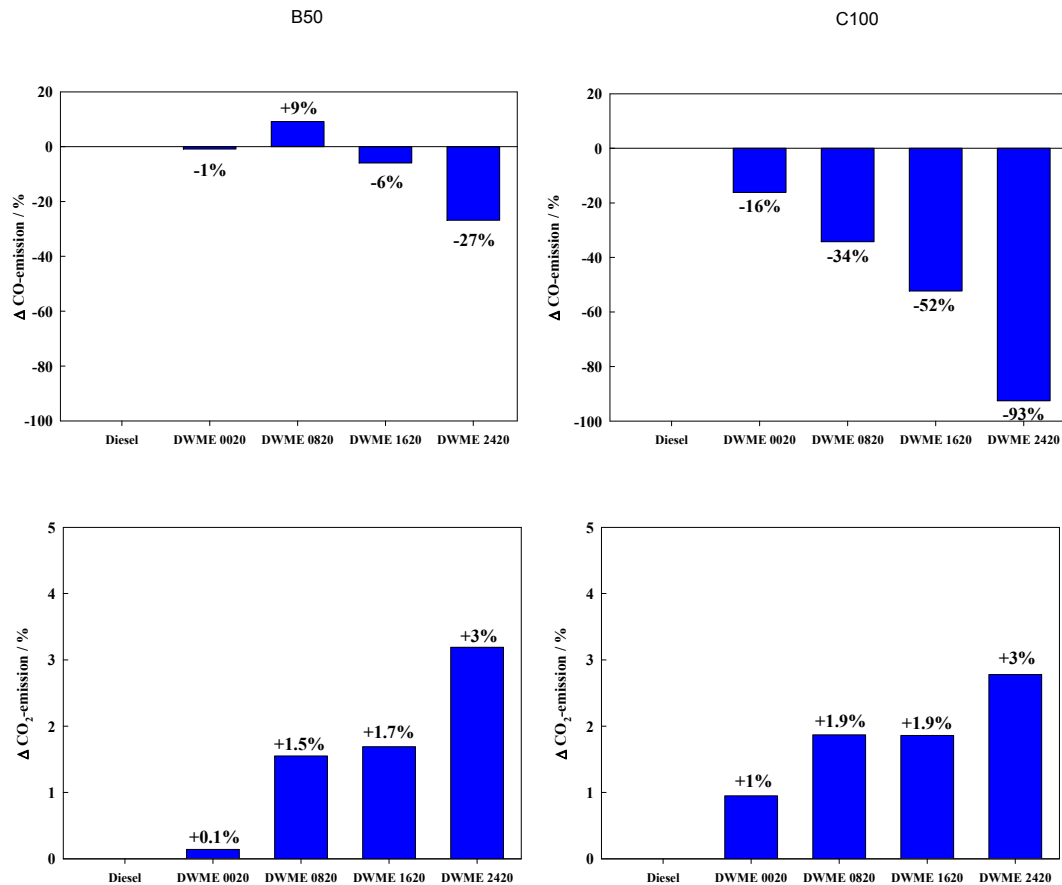


Figure 4-11: Percent change of CO- and CO₂-emissions of water-in-fuel microemulsions (DWME 0020, DWME 0820, DWME 1620, DWME 2420) at B50 (left) and C100 (right).

The percental change of CO- and CO₂-emissions at operating point B50 (left) and C100 (right) with various water contents are presented in figure 4-11. At B50, a slightly reduction of the CO-emissions are observed with DWME 1620 and DWME 2420 compared to the CO-emission of pure diesel. With the “microemulsion” containing 0 % water (DWME 0020), a constant emission is observed which implies that the surfactants do not influence the CO-emissions. At C100, an almost linear reduction of CO-emissions is noticed applying water containing fuels. In comparison with the results obtained at B50, the CO-emissions are

enhanced reduced with increased engine speed n and brake mean effective pressure BMEP at load point C100 which indicates that an efficient combustion was achieved.

The emissions of CO_2 , combined with the results of HC- and CO-emissions, allow a conclusion regarding complete or incomplete combustion. At both operating points, an increase of CO_2 -emissions and a decrease of CO-emissions with increased water content are observed. Due to equation (39) in chapter 2.4, an increased CO_2 -emission can be seen as an indication for a complete combustion of the water containing fuel. Due to the implementation of hydrocarbons to CO_2 , a direct correlation between CO_2 -emission and fuel consumption consists. The increased CO_2 -emissions are not equated with an increased fuel consumption since microemulsions feature a better energy balance with a significant reduction of soot-emissions (figure 4-6). At the beginning of the combustion, energy has to be expended in order to evaporate water (enthalpy of evaporation). The water vapour contributes to mechanical work which moves the piston. Furthermore, the formation of OH-radicals from water molecules accelerates the radical degradation of hydrocarbon chains of the fuel whereby energy is also released. With a homogenous distribution of the air/water-fuel mixture in the combustion chamber, all those processes proceed in an energetically more favourable way [151].

4.2.8 Spray behaviour

In the phase transformation, water containing fuels show the phenomena which are quantitatively different from that in the combustion of pure diesel. The evaporation of the water droplets in water containing fuels is frequently accompanied by the microexplosion which is not common to the combustion of pure diesel droplet. Due to volatility difference between the water and the fuel, this phenomenon might occur. From surrounding combustion gas and flame during combustion, the interior water becomes superheated as the microemulsion/nanoemulsion droplet is heated by radiative and convective heat transfer. As long as no phase transformation within the droplet occurs, the superheat of liquid which is in the thermodynamically metastable condition is maintained. Bubble nucleation occurs when the droplet temperature approaches the superheat limit leading to internal formation of vapour bubbles. The rapid evaporation consequently causes the disintegration of the superheated liquid. After the microexplosion of the primary droplet, a secondary atomisation is followed and produces a number of fine-sited secondary droplets which can evaporate very quickly. Consequently, the available period time for the pyrolytic reaction to proceed in the liquid phase is shortened and results in the suppression of the carbonaceous residue formation with a

simultaneously reduction of the flame temperature. Since high flame temperatures are a major source of thermal NO formation, the lowered flame temperature leads to a significant reduction of NO. Furthermore, the violent disintegration leads to fine secondary droplets and simultaneously an enhanced fuel/air mixture is observed. Improved combustion efficiency is therefore achieved while also suppressing the formation of NO_x, soot and unburnt hydrocarbons [39]. This phenomenon is schematically shown in figure 4-12.

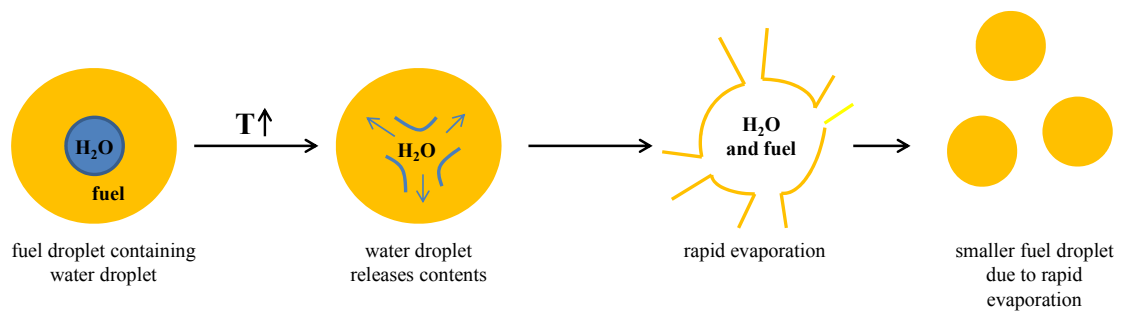


Figure 4-12: Schematic illustration of the microexplosion process. Water droplets inside the fuel cause a rapid evaporation which leads to smaller fuel droplets (microexplosion occurs)(redrawn and modified after [202]).

The size distribution of the dispersed water droplets has an important influence on the microexplosion rate. Smaller scaled size distribution of the dispersed water droplets with a simultaneously higher number density of water droplets lead to an early evaporation and a slower temperature increase in water containing fuels. Thus, the microexplosion will not occur and, consequently, a reduction of NO_x, soot and unburnt hydrocarbon-emissions will not be achieved [39, 56].

During the project, the evaporation- and ignition behaviour of microemulsified fuels (DWME 0820, DWME 0813, DWME 1620, DWME 2420) were studied in an optical accessible high pressure chamber by means of shadowgraphy and OH^{*}-chemiluminescence by the *Rheinisch Westfälische Technische Hochschule Aachen* (RWTH; Lehrstuhl für Verbrennungskraftmaschinen VKA). The results are shown in the following figure.

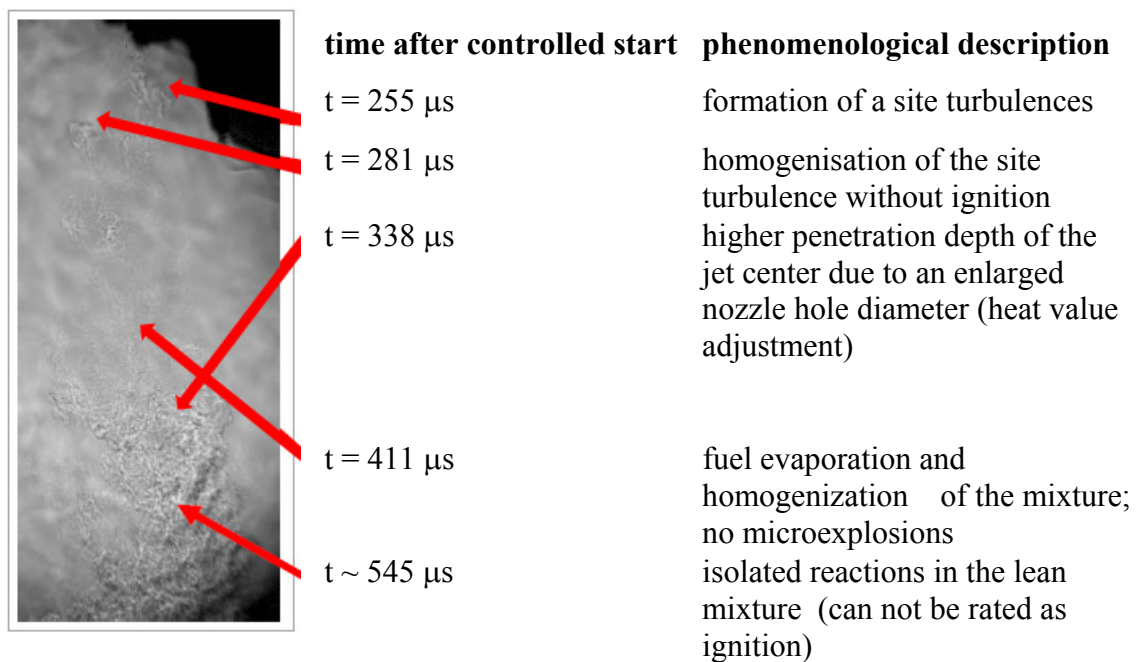
DWME 2420, A25

Figure 4-13: Optical investigations of the spray behaviour of DWME 2420 at A25. Microexplosions and ignition are not observed. Higher penetration depth due to an enlarged nozzle hole diameter (taken and modified from [179]).

In figure 4-13 the evaporation- and ignition behaviour of water-in-fuel microemulsion DWME 2420 at A25 is shown. No ignition and consequently no microexplosions are observed. Due to an enlarged nozzle hole diameter (heat value adjustment) a higher penetration depth of the jet center is recognised. Thus, a fuel-coating on the piston could not be prevented which led to a suppression of the fuel ignition.

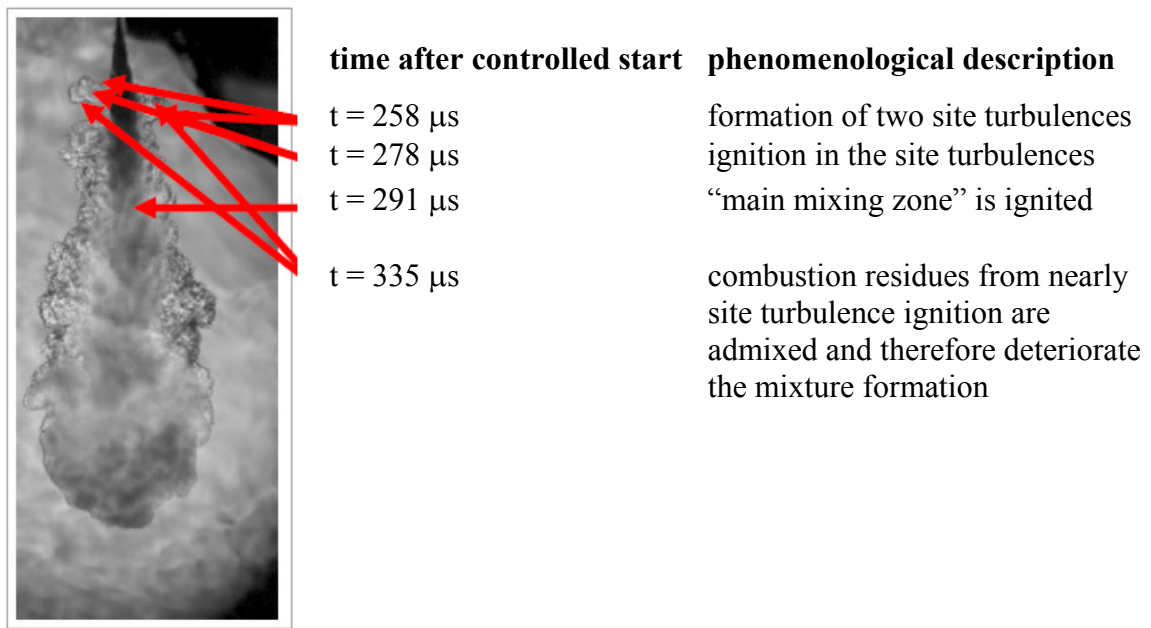
DWME 0820, B50

Figure 4-14: Optical investigations of the spray behaviour of DWME 0820 at B50. Ignition in the site turbulences and in the “main mixing zone” (taken and modified from [179]).

Figure 4-14 presents the evaporation- and ignition behaviour of DWME 0820 at B50. An ignition in the site turbulences and in the “main mixing zone” is observed while the combustion residues from the early site turbulence ignition are admixed and thus deteriorating the mixture formation. As well as shown in figure 4-13, no microexplosions are observed. Due to a small-scaled initial droplet of the microemulsion, an early evaporation of the water in the microemulsion droplets takes place and hence the phenomenon of microexplosions can not occur.

Further investigations were performed for DWME 0820, DMWE 0813 and DWME 1620 at operating points A25, B50 and C100. The core information implied that no identification of microexplosions was obtained and that increased water content led to a higher penetration depth for all three loads due to a higher viscosity [172-174]. While at operating point A25 the piston was coated with fuel due to an enlarged penetration depth, no fuel-coating was observed at higher loads (B50, C100). An increased penetration depth, projection surface and taper angle of the liquid phase are observed with increasing water content due to a higher viscosity [172-174] and density [162] (chapter 3.2). Thus, B50 and C100 offer appropriate conditions for microemulsified fuels in order to avoid fuel-coating on the piston and guarantee efficient ignition. Those results correspond with former optical studies of spray development

of microemulsion fuels in which droplets of the water containing fuels penetrate further than droplets of pure diesel fuel due to a relatively low volatility of the water [35].

Conclusion

In order to summarise this section, several striking results have to be remarked. At both operating points (B50, C100), the soot- and NO_x -emission can be drastically minimised using microemulsified fuels of the type water/ammonium nitrate/ethanol - diesel fuel - oleic acid/monoethanolamine/oleic acid diethanolamide at $\delta_{(\text{ion})} = 0.6$, $\delta_{(\text{OD4})} = 0.4$, $\varepsilon = 0.006$, $\psi = 0.25$, $n = 0.45$. The latent potential of reducing the soot-emission up to 73 % (figure 4-6) while also decreasing the NO_x -emission up to 62 % (figure 4-4) has been proved (DWME 2420; C100). The percentage composition of particulate mass showed a strong percentage decrease of the insoluble fraction (ISF) which is mainly composed of soot and metal abrasion (figure 4-9). Thus, the reduction by a factor of approximately 2 confirmed the previous results obtained for the gravimetric measurements of the particulate mass (figure 4-6). Furthermore, optical investigations of the evaporation- and ignition behaviour showed an increased penetration depth, projection surface and taper angle of the liquid phase due to a higher viscosity and density with increased water content. The phenomenon of microexplosions by applying water containing fuels could not be confirmed (figure 4-13, figure 4-14).

Hence, the main potential benefits of microemulsified fuels have been proved and further improvement suggestions could therefore be proposed.

4.3 Nanoemulsion combustion experiments

In this chapter, the results obtained in combustion experiments using the nanoemulsion fuel of the system water/*n*-propanol - diesel fuel - sorbitan monooleate/polyoxyethylene sorbitan monooleate at HLB = 6 are presented and discussed. The combustion tests were performed at a constant surfactant content of 3 wt.% with a water content of 0, 8 and 16 wt.%. An identical setup (chapter 4.1) and same measuring methods (table 13) have been applied. As well as in microemulsions combustion experiments, the oleic phase includes the blend of surfactant (sorbitan monooleate/polyoxyethylene sorbitan monooleate), while the aqueous phase contains the additives (*n*-propanol, ammonium nitrate, anti-corrosive and lubricity agent). As described in chapter 2.2.1, the thermodynamic stability of microemulsions is the main difference between the kinetic stable nanoemulsions. Another difference is the domain sizes, where droplet sizes of about 10 - 200 nm for nanoemulsions are observed. *Park et al.* [203] studied the combustion characteristics of emulsified diesel also regarding the so called microexplosions (described in chapter 4.2.8). For a group of droplets, microexplosions near the tip of the spray were observed. This effect is based on explosion of superheated water in the droplet, while the sizes of the microexplosions range from barely identifiable small ones to those with diameters of a few millimeters [204]. Consequently, the mixing of the fuel with the surrounding air is enhanced and an efficient combustion can take place. Contrary, microexplosions are not observed in microemulsions as shown and discussed in chapter 4.2.8. The appearance of microexplosions is mainly driven by the radius of the water droplets and its rapid evaporation [205]. Due to smaller-scaled water domains, the water content in the microemulsion-droplets is reduced faster than in emulsion-droplets. Therefore, a much slower temperature-increase of the microemulsion-droplets can take place without any microexplosions [56]. This effect of microexplosions has not yet been characterised completely and further studies should help determining the specific conditions for the formation of microexplosions.

4.3.1 NO_x-emissions

In this section, the NO_x-emission of pure diesel is compared with the NO_x-emissions of nanoemulsions with various water contents. To simplify, the nomenclature of nanoemulsions is defined as follows: “NE” stands for nanoemulsion and the number for the present water content (wt.%). As described in chapter 4.2.2, the European mission standards define a limit

for exhaust gases and include, among other things, a limited value for NO_x -emissions caused by using commercial vehicles.

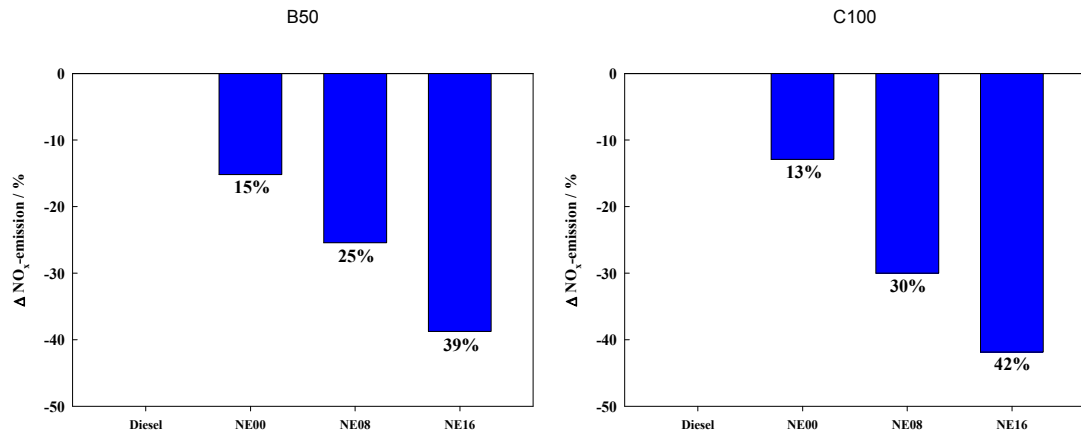


Figure 4-15: Percental change of NO_x -emission of water-in-fuel nanoemulsions (NE 00, NE 08, NE 16) compared to pure diesel fuel at operating point B50 (left) and C100 (right). NE 00, NE 08 and NE 16 mark the nanoemulsions which were applied containing 0 wt.%, 8 wt.% and 16 wt.% water with 3 wt.% surfactant blend. Drastic reduction up to 38 % (B50) and 42 % (C100) for NE 16 is obtained.

In figure 4-15 the NO_x -emission at different operating point B50 (left) and C100 (right) are shown. All values refer to the emission of pure conventional diesel fuel and are expressed as a percentage change. Analogous to the results obtained for microemulsions, the decrease in NO_x -emissions is explained by the reduction of the combustion temperature caused by the presence of water in the mixture [205]. The NO_x -emissions decrease nearly proportional to the increased water content in the nanoemulsion. A significant NO_x -reduction is observed by using water-in-oil nanoemulsions up to 25 % for NE 8 and 38 % for NE 16 at load point B50. At higher engine speeds (C100), slightly higher reductions of NO_x -emissions (up to 42 %) are achieved. Surprisingly, a reduction up to 15 % is also achieved applying NE 00 with 0 wt.% water. An explanation might be based upon the changed physical properties while adding 3 wt.% of the surfactant-blend and water into the diesel fuel. Density and kinematical viscosity are increased (as the trend shown in chapter 3.2) which affect the spray behaviour. The jet angle will decrease [162] while the mean droplet diameter and the penetration depth will increase [172-174]. How far those properties positively influence the combustion leading to a reduction of NO_x -emissions, are a complex interaction and need to be investigated more closely.

4.3.2 Filter smoke number (FSN) and opacity

Both the global and the local effects of the emissions on the environment are of concern for the use of water containing fuels for vehicles. Two different examination methods, also used in chapter 4.2.2, are applied in order to determine the soot-emission.

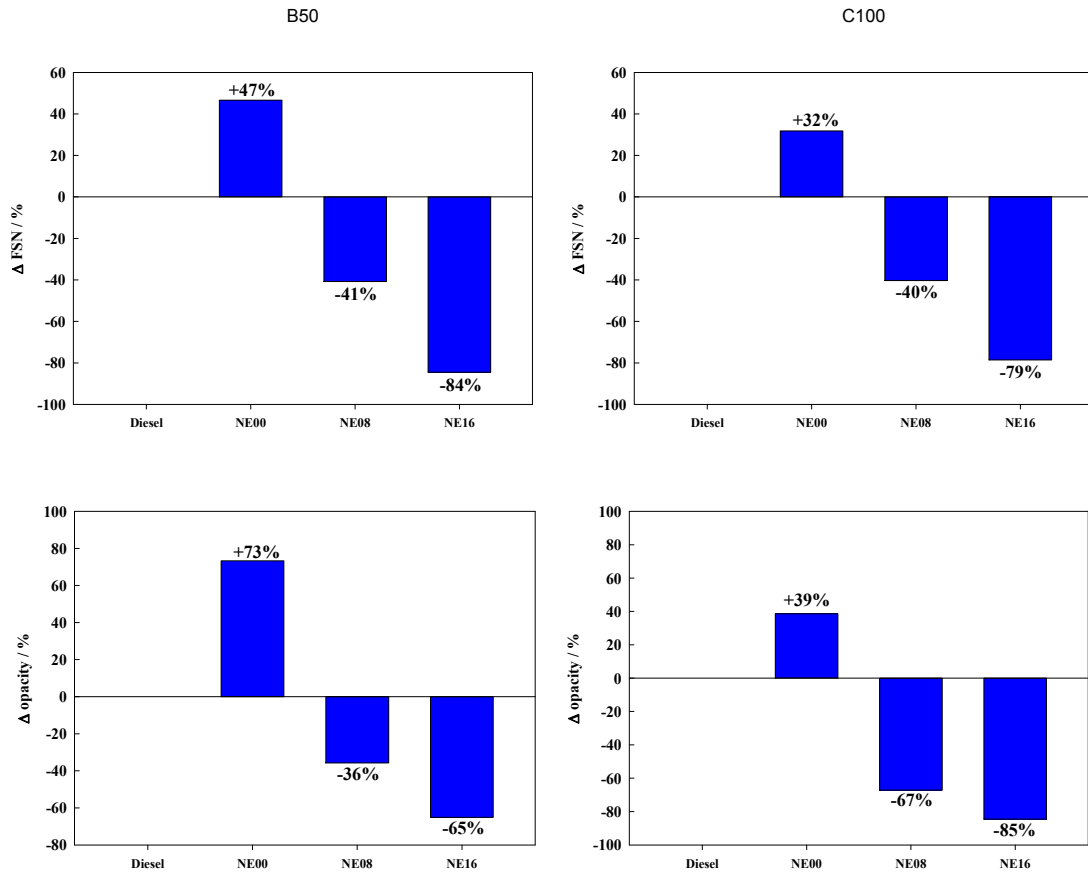


Figure 4-16: Percent change of filter smoke number (FSN; top) and opacity (bottom) of water nanoemulsified fuels (NE 00, NE 08, NE 16) at operating point B50 (left) and C100 (right). Water containing fuels lead to a drastic reduction of FSN (up to 79 %) and opacity (up to 85 %) at C100 for NE 16.

In figure 4-16 the percent change of filter smoke number (top) and opacity (bottom) with different water contents compared to pure diesel fuel are presented. As expected and as also observed, a significant decrease in soot-emissions is achieved applying water nanoemulsified fuels. At operating point B50, the soot-emission is reduced up to 84 % (FSN) and 65 % (opacity) for applying NE 16 compared to the emission of pure diesel. Approximately the same results are obtained at C100; a decrease in soot-emission up to 79 % (FSN) and 85 % (opacity) for the nanoemulsion with 16 wt.% water. Compared to the previous investigation from *Bemert* [56], who observed an increase of soot-emissions using macroemulsions, a more efficient water-in-oil nanoemulsion was formulated in this study. The reduction of soot-

emissions is attributed to an improved atomisation caused by the rapid evaporation of the water drops [205] and to the formation of hydroxyl radicals by water dissociation while enhancing the oxidation of soot. The improved atomisation might be based upon microexplosions, due to differences in the volatility of water and diesel [206]. Regarding the soot-emission of NE 00, containing zero water content, an incline of FSN and opacity is observed. The main reason might be the changed chemical composition of soot causing a changed blackening (independent form the soot-mass) on the filter surface. Mainly, the modified combustion conditions can influence the soot-structure and -composition, whereby a changed blackening is observed although the soot-mass remains the same. Therefore, a gravimetric investigation the soot-emissions should be considered to allow an optimum determination of the soot-emissions. Another reason for the soot-emission incline for NE 00 might be the changed physical properties leading to inefficient combustion.

Furthermore, the oil insoluble surfactant, polyoxyethylene sorbitan monooleate (Tween 80; HLB = 15), in the diesel - surfactant mixture might cause an inhomogenous mixture which is less appropriate as fuel.

4.3.3 Unburnt hydrocarbons

Incomplete combustion leads to unburnt hydrocarbons (HC), which are the precursors of soot. A detailed description of the formation and recombination process of unburnt hydrocarbons is reviewed in chapter 2.4.3.

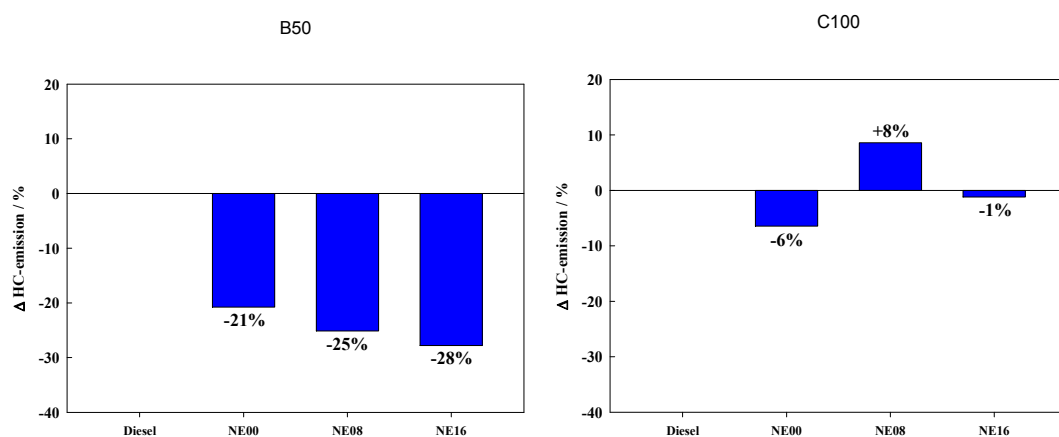


Figure 4-17: Percental change of unburnt hydrocarbons-emissions (HC) of water-in-fuel nanoemulsions (NE 00, NE 08, NE 16) at B50 (left) and C100 (right). HC-emissions are drastically reduced applying nanoemulsion-fuels at B50, whereas the HC-emissions at C100 show an unsteady trend.

Figure 4-17 shows the percental change of HC-emission in dependence of water content at operating point B50 (left) and C100 (right) compared to pure diesel fuel. At operating point

B50 the HC-emissions are reduced about 25 % for NE 08 and 28 % for NE 16. This proves that an efficient combustion with water-in-oil nanoemulsions took place. An even reduced HC-emission with 0 wt.% water is observed. Due to that fact, it may be assumed that the blend of surfactant, consisting of saccharoidal surfactants, did not adversely affect the combustion. With an increased engine speed and higher load at C100, a contrary result is obtained by applying water-in-oil nanoemulsion as fuel. As mentioned in chapter 4.2.6, the flame quenching leads to an incomplete combustion and a simultaneously increase of HC-emission.

4.3.4 Carbon monoxide and carbon dioxide

For a complete oxidative combustion of the fuel, a specific ratio of fuel to air by volume (as described in chapter 2.4) has to be guaranteed. The carbon is oxidised to carbon monoxide / carbon dioxide, while hydrogen oxides to water. An incomplete oxidation may occur when the fuel/air-ratio is fat; consequently carbon monoxide is formed instead of carbon dioxide.

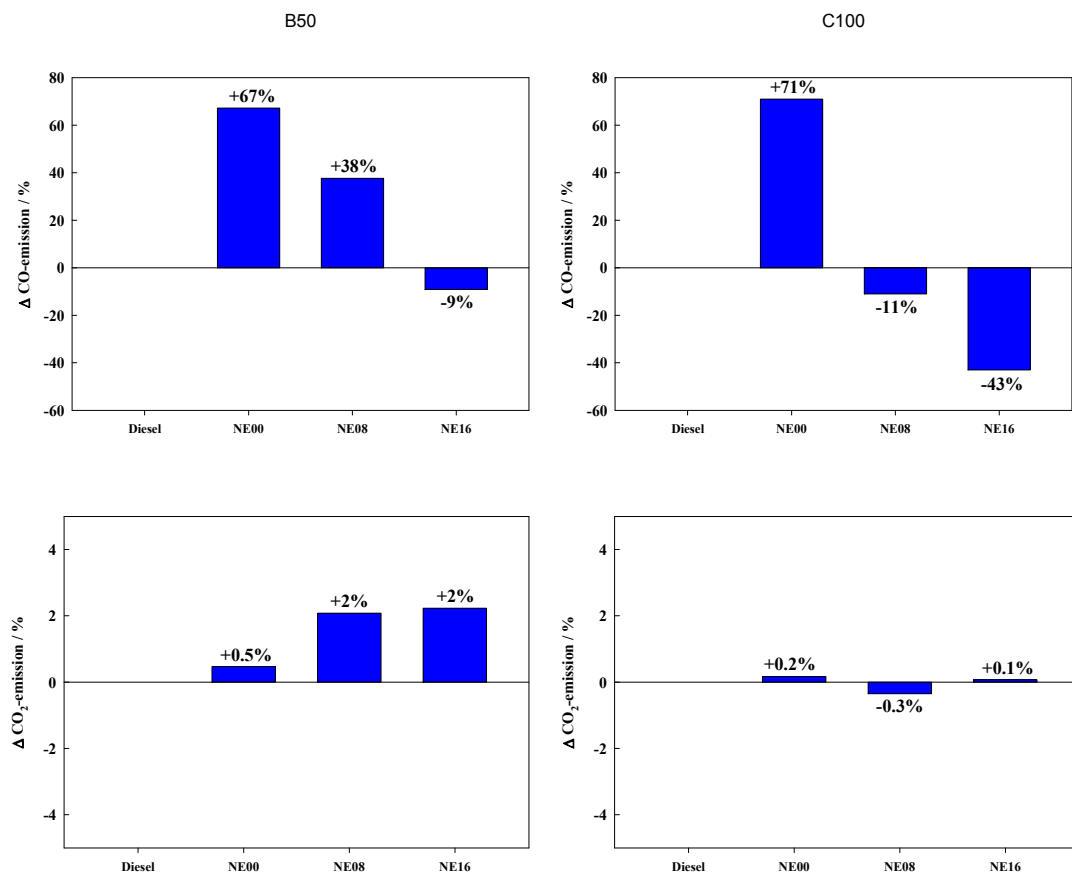


Figure 4-18: Percental change of CO- (top) and CO₂-emissions (bottom) at B50 (left) and C100 (right) of nanoemulsified fuels (NE 00, NE 08, NE 16). No apparent trend is observed for both emissions by applying water containing fuels.

In figure 4-18 the carbon monoxide- (top) and carbon dioxide-emissions (bottom) of water-in-fuel nanoemulsions at different operating points are presented. Contrary to the results obtained with the microemulsion with zero water content (DWME 0020; chapter 4.2.7), NE 00 shows an increase of CO-emissions at both operating points. This effect might be explained by the inhomogeneous mixture of fuel and surfactant for NE 00 with an inappropriate fuel/air-ratio. An increase of CO-emissions indicates an incomplete combustion of the fuel due to lower combustion temperature. A significant decline of CO-emission at C100 up to 43 % (NE 16) and 11 % (NE 08) is observed which implies that a complete combustion took place. With an increased rotational speed (C100), a higher engine's power output (equation (46), chapter 2.4) is achieved. The engine speed is also correlated with the injection point (SOI). Thus, an improved injection point might result in a reduction of CO-emission.

The CO₂-emissions at both operating points do not show a significant difference compared to the CO₂-emissions of pure diesel. As described in chapter 4.2.7, the phase transition of water containing fuels requires a higher thermal energy and has to be considered for the evaluation of CO₂-emissions.

4.3.5 Scanning electron microscope (SEM)

As obtained in chapter 4.3.2, a significant reduction of soot-emission with water-in-fuel nanoemulsions and a simultaneous increase of the particle number were observed at C100. This implies a reduction of the particle diameter. For an improved evaluation of the soot-emissions, the filter samples of the combustion experiments were collected and examined under a scanning electron microscope (SEM). The soot-structure and -size should confirm or refute the assumption that smaller particles are generated applying water containing fuels.

The filter-samples of the pure diesel differ from the ones of the water-in-fuel nanoemulsions based on different measuring methods. The filter-samples of pure diesel were taken from the partial flow dilution for the gravimetric soot determination, in contrast nanoemulsion filter-samples were taken from the smokemeter. Therefore, the structure and permeability of the two blank filters are analysed and have to be considered in the comparison of the soot-structure and -size between pure diesel and water-in-diesel nanoemulsions.

In the following figure 4-19, the blank filter [Pallflex[®], EMFAB[™] TX40HI20-WW; Smart Sampler for gravimetric soot determination] using SEM is shown. Those filters were used during combustion tests with pure diesel.

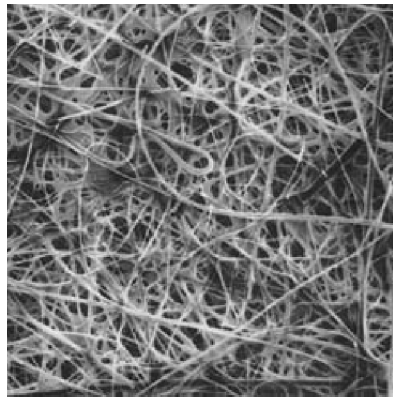
Pallflex® blank filter

Figure 4-19: Scanning electron microscopy (SEM) picture of the blank filter [Pallflex®, EMFAB™ TX40HI20-WW]. Filter consists of pure borosilicate glass microfibers which are reinforced with woven glass cloth bonded with polytetrafluoroethylene (PTFE) (taken from [207]).

The collection efficiency, according to the manufacturer, has a value of 99.9 % for 0.3 μm large particles. It may be assumed that particles with an even smaller primary particle diameter are collected due to agglomeration and adsorption in the filter. The Pallflex® filters consist of pure borosilicate glass microfibers which are reinforced with woven glass cloth bonded with polytetrafluoroethylene (PTFE) [207].

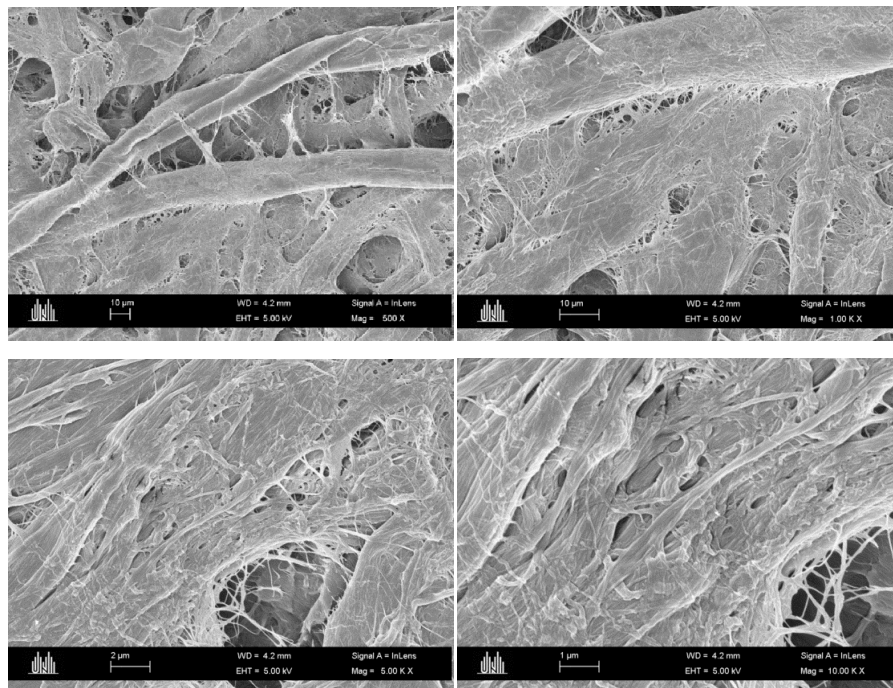
597 LA blank filter

Figure 4-20: Scanning electron microscopy (SEM) picture of the blank filter [filter paper 597 LA] for four various resolutions.

In figure 4-20 the blank filter [filter paper 597 LA; FSN-determination] for four various resolutions using SEM is presented. According to the manufacturer, the collection efficiency is 97 % for 0.3 μm large particles. Those filters were used for the collection of particles while applying nanoemulsions.

Soot particles mainly consist of black carbon (BC; elemental carbon) and a large variety of hydrocarbons or PAHs, forming the volatile fraction of the particles [208]. *Park et al.* studied the agglomerates of exhaust soot and observed that the primary particles had an average diameter of 31.0 nm [203]. *Ishiguro et. al* examined the microstructure by using electron microscopy, leading to the first observation of the inner core and outer shell of soot particles [209]. The inner core is made of several fine particles (as salt or metal oxides from additives and abrasion [210]) and several carbon layers with distorted structure. The outer shell consists of microcrystallines with periodic orientation of planar graphene layers [209] whereby the outermost layer is mainly composed of unburnt, aromatic and oxygenated hydrocarbons [211]. Small spherules of approximately 4 nm coalesce together to form the inner core of 8 - 15 nm. Due to gas phase surface growth, an outer shell of 4 - 12 nm is formed [212]. The majority of particles do not feature a core-shell structure due to inhomogeneous graphene segments. Therefore, a highly reactive soot is formed which is prone to oxidation. The outer shell may completely oxidise during expansion and particles will then be smaller [198]. Due to this fact, the chemical composition of the outer shell and the size are the main reasons for the hazardous property of soot-particles.

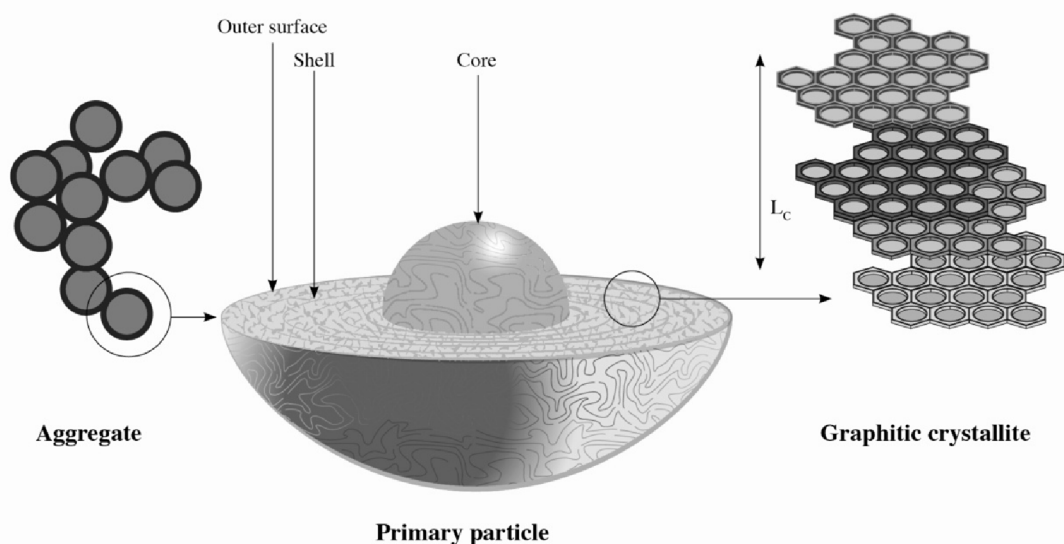


Figure 4-21: Schematic drawing of a diesel primary particle. Inner core consists of several fine particles and several carbon layers with distorted structure. Outer shell is made of microcrystallines with periodic orientation of planar graphene layers and unburnt hydrocarbons form the outermost layer [209, 211](redrawn and modified from [212]).

The filter samples of the exhaust emission at operating point B50 (top) and C100 (bottom) of water containing fuel are shown in figure 4-22.

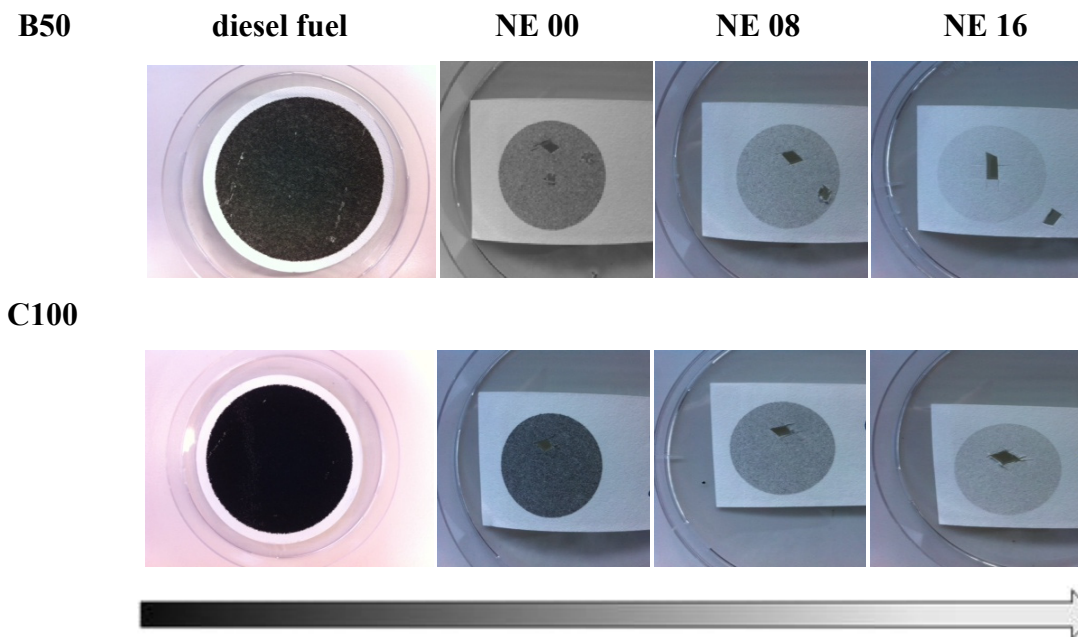


Figure 4-22: Filter samples at B50 (top) and C100 (bottom) of pure fuel (left) and nanoemulsion fuels (NE 00, NE 08, NE 16). Discolouring of the filter paper ranges from black (diesel) to light grey (NE 16).

Starting from the left, the filter sample of pure diesel is presented. The further pictures are sorted by increased water content. Due to a changed filter colouring (from “black” particles to “light grey” particles), depending on the water content, an investigation of the soot-agglomeration and size distribution under SEM is essential. The filter sample of pure diesel shows a strong blackening while the filter sample of water containing fuels exhibit a weaker blackening. The discolouration clearly shows that the evaluation of soot-emission using the FSN-method or the opacity is not sufficient enough. The FSN is determined by diffuse reflection of the blackened filter. Thus, the relative radiance factor, which is defined by the reflectometer value of the sample, does not correspond to the actual soot mass due to a change in absorption of “black” particles to “grey” particles. Furthermore, the opacity is measured at a wavelength of $\lambda = 550 - 570 \text{ nm}$ whereas “white” non-absorbent particles (e.g. sulfate surrounded by water or particulate reaction products as condensed hydrocarbons) cause a measuring effect due to light scattering. Consequently, a gravimetric measurement of the particulate mass, combined with the other two methods, would provide a descriptive determination of the soot-emissions.

The following figure shows the filter samples (at operating point B50) under SEM with various resolutions [500x, 1000x, 5000x and 10000x] in order to investigate the soot-structure and size distribution.

B50, diesel

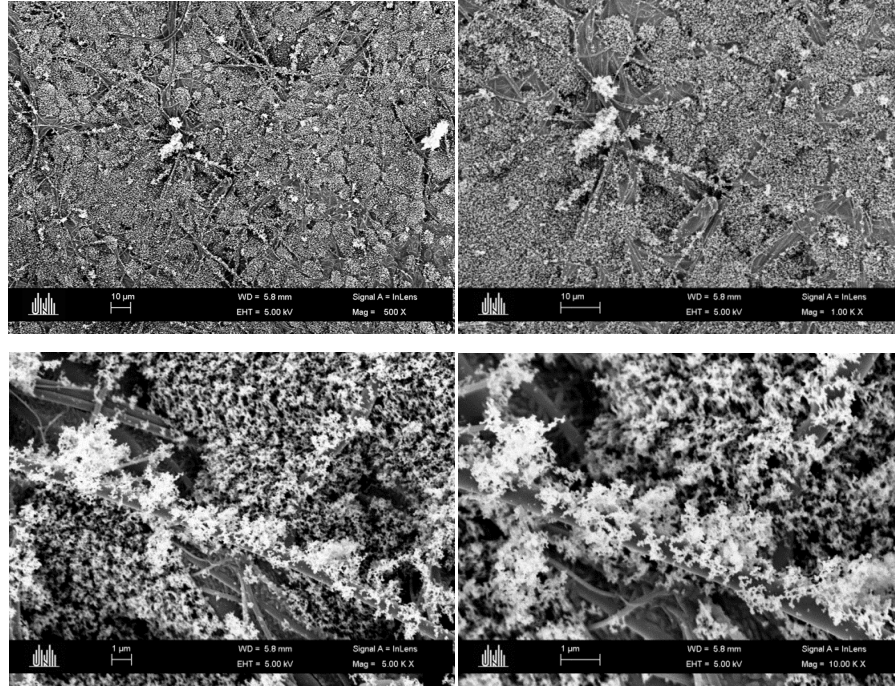


Figure 4-23: Scanning electron microscopy (SEM) picture of filter sample of pure diesel at various resolutions at B50. Filter is strongly occupied with agglomerated particles. Mean diameter of primary particles is approximately $d = 34$ nm.

In figure 4-23, the filter sample of pure diesel at B50 with various resolutions [500x (left, top; subimage 1), 1000x (right, top; subimage 2), 5000x (left, bottom; subimage 3), 10000x (right, bottom; subimage 4) which were also used for the further SEM pictures] under a scanning electron microscope is shown. A strong occupancy of the particles on the filter is recognisable in subimage 1. Subimage 4 exhibits a homogeneous distribution of the agglomerated particles. A precise determination of the soot-sizes was impeded by the strong soot deposit; the mean diameter of the primary particle has a value of approximately $d = 34$ nm.

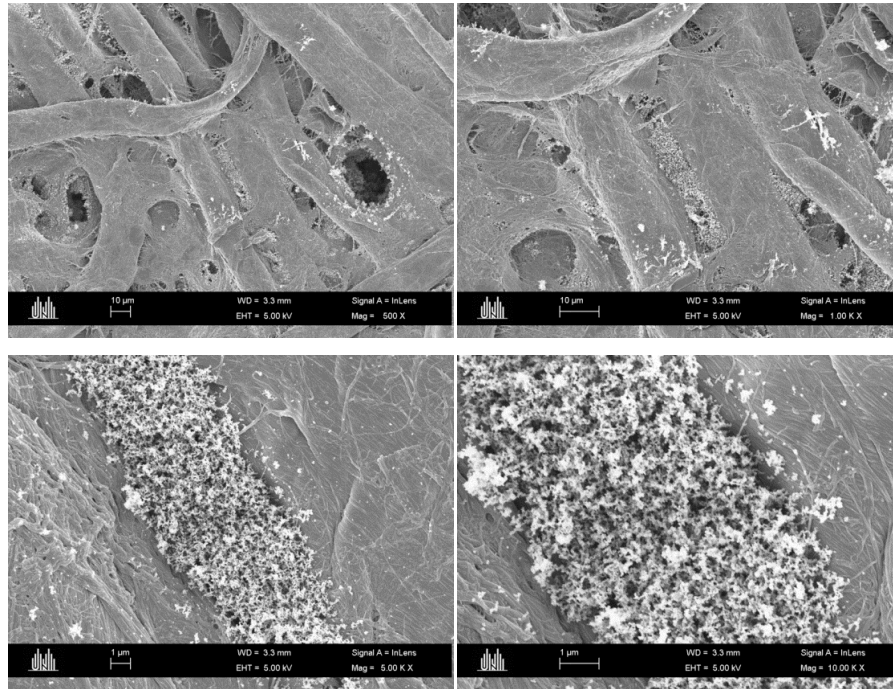
B50, NE 00

Figure 4-24: Filter sample of water-in-fuel nanoemulsion (NE 00) under scanning electron microscopy (SEM) at various resolutions at B50. Filter surface is less occupied compared with the filter sample in figure 4-25. Primary particles feature a mean diameter-size of approximately $d = 38$ nm.

Figure 4-24 presents the filter sample of the mixture with zero percent water and 3 wt.% surfactant (NE 00). Compared with the SEM-images of pure diesel, the surface of the filter is interestingly rarely occupied (subimage 1) although an increased $\Delta\text{FSN} = +47\%$ compared to pure diesel fuel was observed (figure 4.16). At particulate positions, an accumulation of agglomerated primary particles is observed (subimage 2). The present primary particles feature a larger mean diameter-size ($d = 38$ nm) than the particles from pure diesel ($d = 34$ nm).

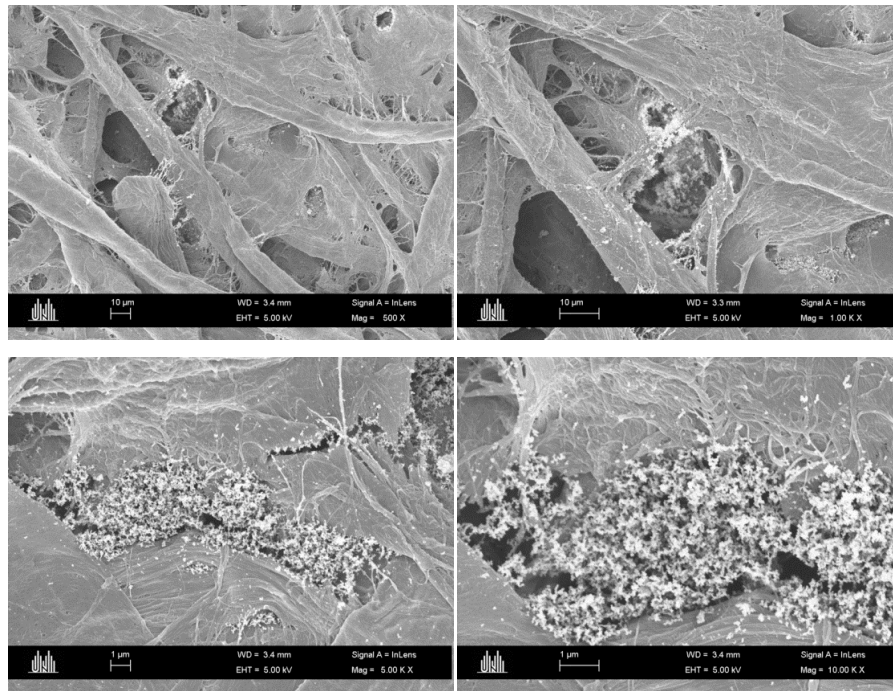
B50, NE 08

Figure 4-25: Scanning electron microscopy (SEM) picture of filter sample of nanoemulsion-fuel (NE 08) at various resolutions at B50. Agglomerated particles with a mean primary particles size of $d = 42$ nm are rarely presented.

In figure 4-25 the filter sample of NE 08 at B50 under SEM is shown. As expected, the coverage of the particles on the filter surface is less pronounced compared to the occupation of pure diesel fuel (figure 4-23); only at few locations agglomerated particles are observable. Surprisingly, those agglomerated particles seem to deposit inside the filter cloth although larger diameter-sizes ($d = 42$ nm) are noticed. Based on this result, a cross-section through the filter samples should help to determine the penetration depth of particles from pure diesel (figure 4-27) compared to the one from NE 08 (figure 4-28).

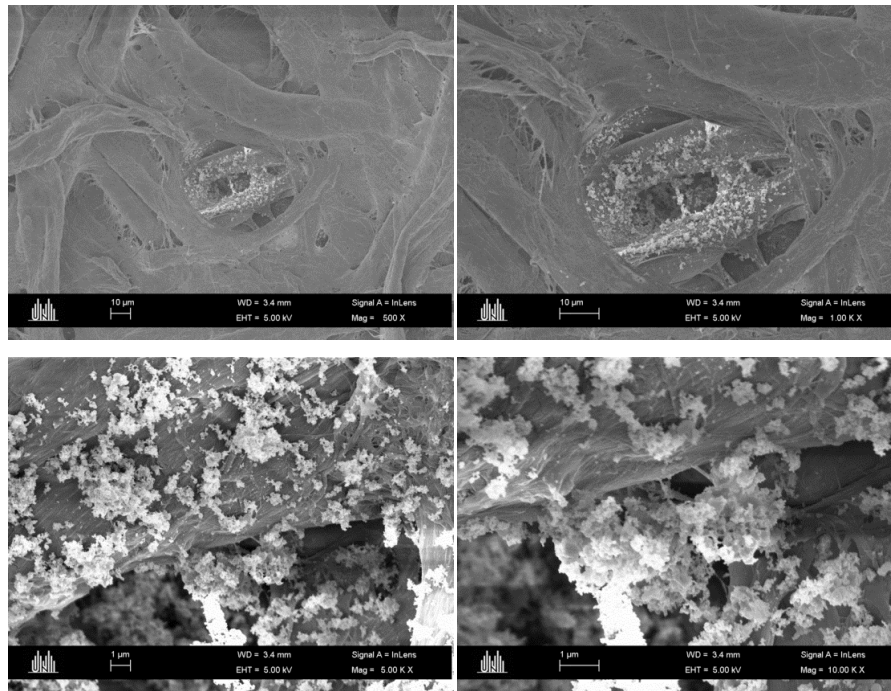
B50, NE 16

Figure 4-26: Filter sample of water-in-fuel nanoemulsion (NE 16) under scanning electron microscopy (SEM) at various resolutions at B50. Filter surface is rarely occupied; agglomerated particles with a mean diameter size of $d = 54$ nm are observed inside the filter cloth.

Following the trend in figure 4-26 it is obvious, that very few particles occupy the filter surface. Fewer particles with a diameter of $d = 54$ nm are discovered which might agglomerate merely inside the filter cloth.

Same investigations of the filter samples at operating point C100 under SEM were carried out. A similar trend was observed by increasing the water content in the fuel. The results obtained in the SEM images are summarised in the following table 14.

Table 14: Overview of the mean particle size diameters d at B50 and C100 for diesel and nanoemulsion-fuels (NE 00, NE 08, NE 16).

fuel	filter occupation	B50 d / nm	C100 d / nm
NE 00	++	38	26
NE 08	+	42	30
NE 16	+	54	38

For a complete evaluation of the soot-emissions, a gravimetric measurement of the soot mass is essential. As observed in chapter 4.2.3 (microemulsions), a drastic reduction of soot-mass should be also assumed by applying water-in-oil nanoemulsions. Therefore, a simultaneously, significant incline of the implies smaller particles. In previous investigations [56, 60, 61] the same effect was observed. In contrast to those results, fortunately larger particles are formed at both operating points (table 14) which are less hazardous than finer particles in terms of mortality and respiratory [213]. Finer particles are more respirable and lead to a higher carcinogenic property than bigger particles.

In order to determine the penetration depth of the particles, the cross-section through the filter-samples were performed and analysed in detail under the SEM.

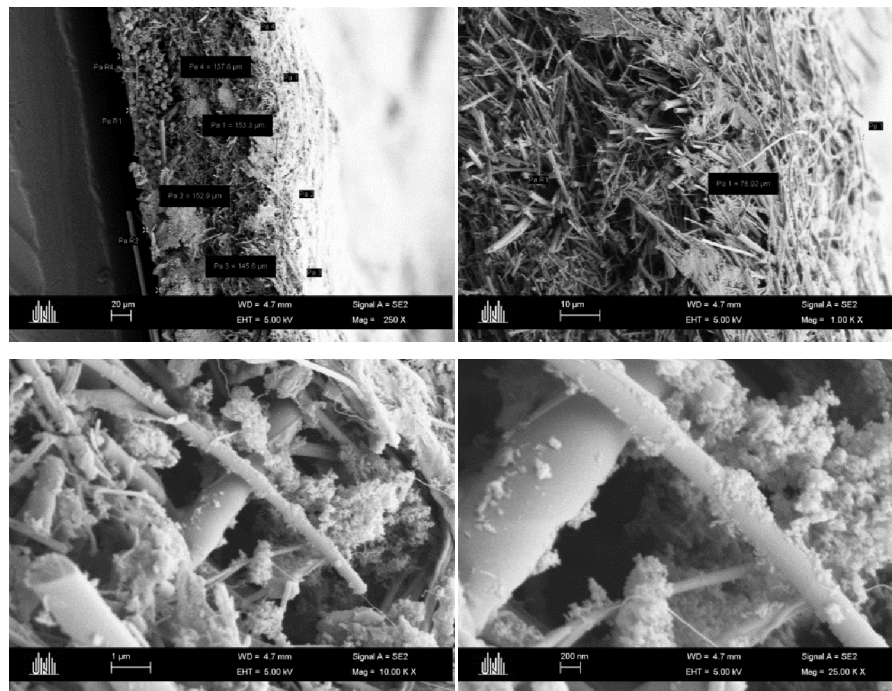
B50, pure diesel

Figure 4-27: Cross-section through the filter sample (filter surface points to the right) of pure diesel under scanning electron microscopy (SEM) at B50. Particles penetrate approximately up to half the thickness of the filter ($l = 78 \mu\text{m}$; subimage 2).

As observed and determined in subimage 1, the filter used for the diesel combustion experiments [Pallflex[®], EMFAB[™] TX40HI20-WW] exhibit a thickness of approximately $d_{\text{filter}} = 150 \mu\text{m}$. The filter consists of pure borosilicate glass microfibers which are reinforced with woven glass cloth bonded with polytetrafluoroethylene (PTFE) [207].

Subimage 3 and 4 both show an enlarged view of the area from the agglomerated particles, which are the furthest from the filter surface, respectively, which penetrate the furthest into the filter cloth. The particles penetrate approximately up to half the thickness of the filter ($l = 78 \mu\text{m}$), additional particles with a higher penetration depth were not observed (subimage 2). This implies that almost all particles were collected by the filter which is completely occupied with the agglomerated particles on its surface.

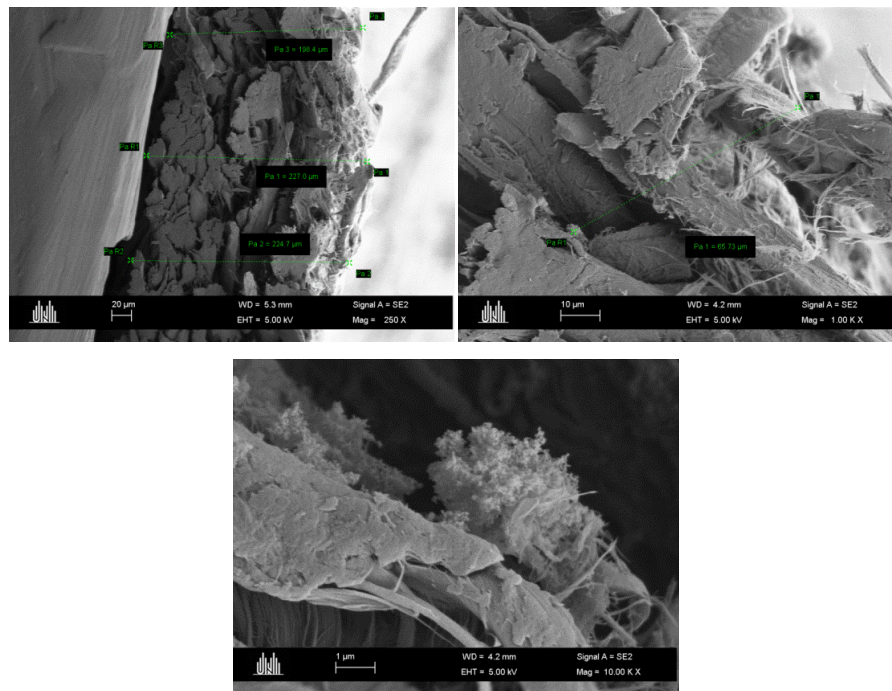
B50, NE 8

Figure 4-28: Cross-section through the filter sample (filter surface points to the right) of nanoemulsion-fuel (NE 08) under scanning electron microscopy (SEM) at B50. Agglomerated particles extend approximately up to one third of the filter thickness ($l = 65 \mu\text{m}$; subimage 2).

The cross-section of the filter [filter paper 597 LA] used for the combustion experiments while applying water-in-fuel nanoemulsions are shown in figure 4-30. Subimage 1 indicates the thickness of the filter with an approximately value of $d_{\text{filter}} = 220 \mu\text{m}$. The particles which penetrate the furthest are shown enlarged in subimage 2 and 3. The agglomerated particles extend approximately up to one third of the filter thickness ($l = 65 \mu\text{m}$), a higher penetration depth of a particle was not observed (subimage 2). Hence, the particles are mainly located in the front area of the filter and do not diffuse through the filter.

Conclusion

The positive effects applying nanoemulsified fuels of the type water/*n*-propanol - diesel fuel - sorbitan monooleate/polyoxyethylene sorbitan monooleate at HLB = 6 with 3 wt.% surfactant were confirmed in this section. Drastic reduction of NO_x -emissions up to 42 % (figure 4-15) was achieved using water-in-fuel nanoemulsions (NE 16; C100). Additionally, soot-emissions were reduced up to 85 % (opacity; figure 4-16); both results clarify the benefits of a water containing fuel in order to reduce the exhaust pollutant emissions. As expected, scanning electron microscopy (SEM) pictures proved that the filter sample surfaces are less occupied (figure 4-25, figure 4-26) and that larger mean particle size diameters d (table 14) are obtained applying water containing fuels.

4.4 Comparison of microemulsions and nanoemulsions

In order to evaluate the potential benefits of water containing fuels, both methods (microemulsified- and nanoemulsified fuels) to introduce water into fuels are compared in terms of exhaust gas emissions in this section. As mentioned before, microemulsions and nanoemulsions differ mainly in their thermodynamic stability and surfactant concentration. However, both systems have shown a significant reduction of exhaust pollutant emissions which were presented and discussed in chapter 4.2 and 4.3.

4.4.1 NO_x-emissions

First, NO_x-emissions applying nanoemulsified- (dark green) and microemulsified fuels (dark blue) with a water content of 0, 8 and 16 wt.% at load point B50 (left) and C100 (right) are compared (figure 4-29).

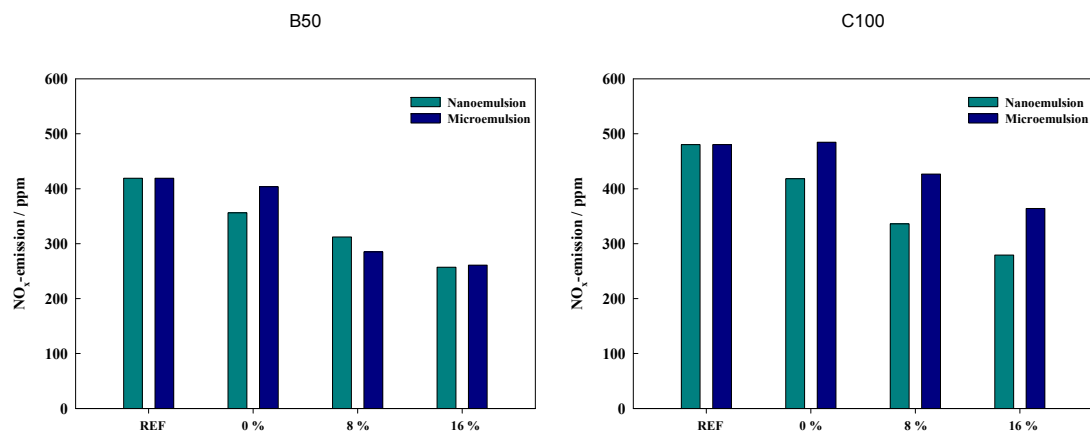


Figure 4-29: Comparison of NO_x-emissions applying nanoemulsion-(dark green) and microemulsion-fuels (dark blue) at B50 (left) and C100 (right). A drastic reduction of NO_x-emissions is observed using water containing fuels. At C100, an enhanced reduction of NO_x-emissions is achieved applying nanoemulsified fuels compared to microemulsified fuels.

In both systems a drastic reduction of NO_x-emissions is achieved at B50 as well as at C100. An enhanced reduction of NO_x-emissions up to 23 % (16 wt.% water; C100) is observed for nanoemulsified fuels compared to microemulsion fuels at C100. One reason might be that the surfactant-blend (sorbitan monooleate/polyoxyethylene sorbitan monooleate) in the nanoemulsions is nitrogen-free and does not additionally contribute to the NO_x-emissions, whereas the surfactant-blend (oleic acid/monoethanolamine/oleic acid diethanolamide) used for microemulsion fuels contains nitrogen. Additionally, larger-scaled water domains (< 120 nm for nanoemulsion fuels) might cause microexplosions, which did not occur for

microemulsion fuels (figure 4-13) leading to an enhanced reduction of the combustion chamber temperature compared and a simultaneously reduced formation of the thermal *Zeldovich* NO.

4.4.2 Filter smoke number (FSN) and opacity

The comparison of the FSN (top) and opacity (bottom) applying nanoemulsions and microemulsion as fuels at B50 (left) and C100 (right) are presented in figure 4-30.

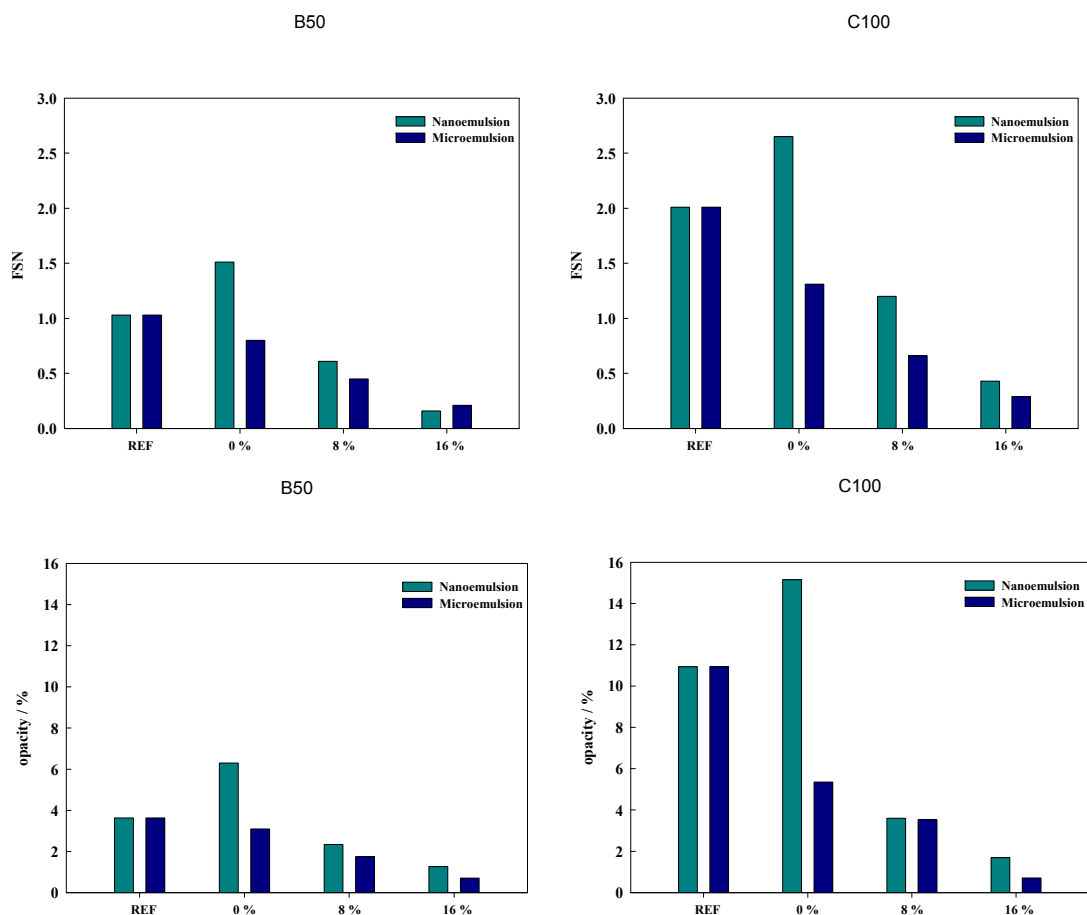


Figure 4-30: Comparison of FSN (top) and opacity (bottom) for nanoemulsions (dark green) and microemulsions (dark blue) as fuels at B50 (left) and C100 (right). For microemulsions an enhanced reduction is observed for both examination methods compared to nanoemulsions as fuels. Surfactant concentration may lead to a falsified determination of the soot-emissions due to an investigation based upon filter blackening.

The FSN and the opacity methods are based upon the blackening of the filter, which can be influenced by the chemical composition of the soot. Furthermore, the chemical composition of the soot depends on the fuel composition which differs from each other in this case due to a different surfactant-blend and composition. More surfactant (20 wt.%) is needed to formulate

thermodynamic stable microemulsions and might therefore lead to a less blackening of the filter. Due to a lower surfactant concentration, as required for kinetic stable nanoemulsions (3 wt.%), the blackening of the filter is not influenced as in the case of microemulsions. Consequently, the blackening of the filter might not exhibit a representative explanation about the soot-emission and has to be confirmed using additionally a gravimetric determination of exhaust particulates to allow an optimum determination of the soot-emissions. Unfortunately, a gravimetric determination of exhaust particulates applying water nanoemulsified fuels has not been performed and a comparison of soot-emission between both methods introducing water into fuels (as microemulsions or nanoemulsions) cannot be drawn. However, the scanning electron microscopy (SEM) pictures of filter samples of nanoemulsion-fuels (chapter 4.3.5) has revealed a reduction of the soot-particles and confirms the positive benefits of water containing fuels in form of nanoemulsion fuels.

Conclusion

An interesting result comparing both methods (microemulsified- and nanoemulsified fuels) to introduce water into fuel in terms of exhaust emissions was obtained in this section. Regarding the comparison of NO_x-emissions of nano- and microemulsified fuels, a surprisingly, enhanced reduction applying nanoemulsified fuels (figure 4-29) was achieved. This result led to the assumption that the nitrogen-free surfactant blend of the nanoemulsion fuel (sorbitan monooleate/polyoxyethylene sorbitan monooleate) does not additionally contribute to the NO_x-emissions, while the nitrogen containing surfactant blend of the microemulsion (oleic acid/monoethanolamine/oleic acid diethanolamide) further contribute to the formation of the harmful NO_x. Based on these results, nitrogen containing surfactants should be avoided in the future in order to achieve an enhanced reduction of NO_x-emissions using water containing fuels.

Nanoemulsified fuels offer benefits over microemulsion fuels in terms of surfactant concentration (3 wt.% respectively 20 wt.%) while achieving even more remarkable positive effects as microemulsified fuels regarding exhaust emissions. As mentioned in chapter 4.2.8, the size distribution of the dispersed water droplets has an important influence on the microexplosion rate. Those nanoemulsions feature larger-scaled dispersed water droplets (< 120 nm) with a lower number density of water droplets in a fuel droplet during combustion, which might lead, in contrary to microemulsified fuels (figure 4-13), to the formation of microexplosions. This phenomenon of microexplosions reduces the flame



temperature leading to a simultaneous suppression of thermal NO formation. Additionally, the violent disintegration causes fine secondary droplets which enhance the fuel/air mixture leading to an improved combustion efficiency while also suppressing the formation of soot and unburnt hydrocarbons [30]. Due to a smaller-scaled size distribution of the dispersed water droplets generated by microemulsions with a simultaneously higher number density of water droplets in a fuel droplet, an early evaporation and a slower temperature increase of the water in the microemulsion droplets takes place which suppresses the phenomenon of microexplosions [56]. Optical studies of the spray behaviour of nanoemulsified fuels should be carried out in order to confirm or refute this assumption.

5 SUMMARY

Due to growing environmental awareness, alternative fuels should be completely green. Hence, the first goal of this thesis was to formulate inexpensive, fully combustible microemulsions using “green” surfactants and additives as alternative fuel. The potential benefits of newly formulated water containing fuels regarding exhaust gas emissions and spray behaviour were studied in an interdisciplinary cooperation (FVV-project) with the *University of Applied Sciences in Trier* and the *Rheinisch-Westfälische Technische Hochschule Aachen*.

A systematic phase behaviour study of the multidimensional composition space ($n, \delta, \varepsilon, \psi$) yielded an efficient, temperature invariant ($T = -10\text{ °C} - 90\text{ °C}$) microemulsions fuel of the type water/ammonium nitrate/ethanol - diesel fuel - oleic acid/monoethanolamine/oleic acid diethanolamide at $\delta_{(\text{ion})} = 0.6$, $\delta_{(\text{OD4})} = 0.4$, $\varepsilon = 0.006$, $\psi = 0.25$, $n = 0.45$ capable of accommodating variable water contents (figure 3-7).

Not only do these fuels feature an ionic phase behaviour independent of the water content, but even more astonishingly they do so with a complete suppression of the lamellar phase (figure 3-7), which is remarkable for such efficient systems. Here, small angle neutron scattering (SANS) with a combination of dynamic light scattering (DLS) revealed homogeneously distributed, nano-scaled, water-swollen micelles and no lamellar phases.

After successful formulation, crucial physical properties of the microemulsified fuels were determined regarding the generally applicable requirements for diesel fuels according to DIN 590 and their influence on the spray behaviour. Detailed analysis revealed that these microemulsified fuels exhibit an enhanced lubricity (figure 3-19), very pronounced anti-corrosive properties and a very low ash content ($< 0.001\text{ wt.}\%$) making them well suited for practice-oriented application. Additionally, the distillation curve of water containing fuel microemulsions with a water content of less than 16 wt.% resembled a shape which is characteristic for diesel fuel (figure 3-21) and prove in accordance with the temperature dependent density (figure 3-18) and viscosity (figure 3-16) measurements, that these fuels behave just like common diesel fuel.

Regarding the microemulsification approaching injection conditions, the formation kinetics of these systems were recorded varying the temperature and water content in an ultra-fast stopped-flow system. Transmission measurements indicate that the microemulsion with 24 wt.% at $T = 60\text{ °C}$ is formed within 0.8 s (figure 3-31) while revealing a strong increase in formation speed for higher temperatures that seems to correlate with the systems viscosity.

The second goal of this work was the formulation and characterisation of economically more appealing nanoemulsified fuels in order to achieve an additional reduction of the surfactant content. For the application of water nanoemulsified fuels using the load point dependent on injector-blending technology, the aqueous phase has to match anti-corrosive and lubricity requirements. Hence, the influence of adequate lubricants and anti-corrosion additives for the aqueous phase was studied first. Traction coefficient measurements implied that the addition of 0.25 wt.% of Evonik® Rewoquat W 325 PG™ into the aqueous phase creates a lubrication film thereby providing better wear protection than *e.g.* adding 5 wt.% Lubrizol® Veg Ester™ (figure 3-33). Based on this result, anti-corrosion agents were also investigated according to DIN 51 360. Standard corrosion tests with variable anti-corrosive agent concentrations proved that of 5 wt.% of Clariant® Antifrogen N™ in the aqueous phase is best suited to prevent corrosion (figure 3-36). By utilising the ultra-low interfacial tension during phase inversion water-in-diesel nanoemulsions of the type water/anti-corrosion agent/lubricant - diesel fuel - sorbitan monooleate/polyoxyethylene sorbitan monooleate with 3 wt.% surfactant for 8 wt.% and 16 wt.% water were successfully formulated and applied for further combustion experiments using the on injector-blending system, in which the addition of water into fuel milliseconds before injection into the combustion chamber is possible (chapter 4.3). Here, dynamic light scattering (DLS) was applied to determine the hydrodynamic radii in dependence of the HLB-value of water-in-fuel emulsions using fully combustible, sustainable sugar surfactant-blends. A HLB-value of 6 resulted the smallest hydrodynamic radii ($r_{\text{hydr}} < 120 \text{ nm}$) due to its correlation with the phase inversion temperature of the system being at about room temperature thereby generating nanoemulsified fuels with as little as 3 wt.% surfactant (figure 3-38).

Finally, in industrial combustion tests the positive influence of water containing fuels was proven leading to a drastic reduction of soot up to 98 % (figure 4-5; FSN) as well as nitrogen oxide emissions up to 62 % (figure 4-4). A further analysis of the composition of particulate matter showed a strong percentage decrease of the insoluble fraction (ISF) which is mainly composed of soot and metal abrasion (figure 4-9). Thus, the reduction by a factor of approximately 2 confirmed the results obtained for the gravimetric measurements of the particulate mass (figure 4-6). Moreover, optical investigations of the evaporation and ignition behaviour showed an increased penetration depth, projection surface and taper angle of the liquid phase with increased water content (due to a higher viscosity and density). The phenomenon of microexplosions by applying water containing fuels could not be verified (figure 4-13, figure 4-14) using microemulsified fuels. As expected, scanning electron

microscopy pictures proved that the filter sample surfaces are less occupied (figure 4-25, figure 4-26) and that larger mean particle size diameters d (table 14) are obtained applying water containing fuels.

An interesting result, comparing both NO_x -emissions applying microemulsified- and nanoemulsified fuels (figure 4-29) was observed showing a surprising reduction up to 23 % while applying nanoemulsified fuels with a nitrogen-free surfactant-blend. This result led to the assumption that nitrogen-containing surfactants, which were used in the surfactant-blend of microemulsion fuels, further contribute to the formation of harmful NO_x . Another assumption, regarding the enhanced reduction of NO_x -emissions for nanoemulsified fuels, refers to the phenomenon of microexplosions which were not observed for microemulsified fuels (figure 4-13). Larger-scaled water domains (< 120 nm for nanoemulsion fuels) may cause microexplosions, leading to an enhanced reduction of the combustion chamber temperature with a simultaneously suppression of NO_x -formation.

Hence, the feasibility of applying water containing fuels in form of microemulsion or nanoemulsion has been successfully substantiated and discussed in this thesis. Remarkably, water-in-fuel nanoemulsions offer economical and ecological benefits over microemulsion fuels in terms of surfactant concentrations (3 wt.% respectively 20 wt.%) while also achieving approximately same or enhanced positive effects as microemulsified fuels regarding exhaust emissions.





6 EXPERIMENTAL SECTION

6.1 Chemicals

substance	chemical formula	produce/ provider	<i>M</i> / g/mol	purity
ammonium nitrate	NH ₄ NO ₃	WALL CHEMIE	80.04	≥ 99.00 %
Antifrogen	~ C ₂ H ₆ O ₂ + additives	Clariant	~ 62.07	technical
deuteriumoxid	D ₂ O	Euriso-top	20.03	99.97 %
diesel fuel (winter)	n. a.	Aral	n. a.	technical
ethanol	C ₂ H ₆ O	Merck	46.07	≥ 99.50 %
F 98	PEO ₁₁₈ -PPO ₄₅ - PEO ₁₁₈	Pluronic	~ 13000	technical
<i>n</i> -propanol	C ₃ H ₈ O	Sigma- Aldrich	60.09	≥ 99.50 %
monoethanolamine	C ₂ H ₇ ON	WALL CHEMIE	61.08	technical
oleic acid	C ₁₈ H ₃₄ O ₂	WALL CHEMIE	282.46	Technical
PE 6800	PEO ₇₃ -PPO ₂₈ - PEO ₇₃	Pluronic	~ 8000	Technical
polyoxyethylene sorbitan monooleate (Merpoxen SMO 200QL)	C ₆₄ H ₁₂₄ O ₂₆	WALL CHEMIE	1309.66	Technical
polyoxyethylene sorbitan trioleate (Walloxen STO 200)	C ₆₂ H ₁₁₂ O ₆ (C ₂ H ₄ O) _n	WALL CHEMIE	n.a.	Technical
Rewoquat W 325 PG	n.a.	Evonik	n.a.	Technical
sorbitan monooleate (SMO)	C ₂₄ H ₆₄ O ₆	WALL CHEMIE	448.76	Technical
Wallamid OD-4	C ₂₂ H ₄₃ NO ₃	WALL CHEMIE	369.58	Technical
Water	H ₂ O	-	18.02	Bidistilled
Water	H ₂ O	-	18.02	Demineralized

6.2 Measuring methods

Phase behaviour

Analysis of complex fluids usually starts with the determination of the phase behaviour. The water-in-oil microemulsion samples were prepared by weight. The water-in-fuel microemulsions were formulated by adding water to binary oil-surfactant mixtures.

The number and the type of phases were determined visually in an experimental setup which is shown in figure 6-1.

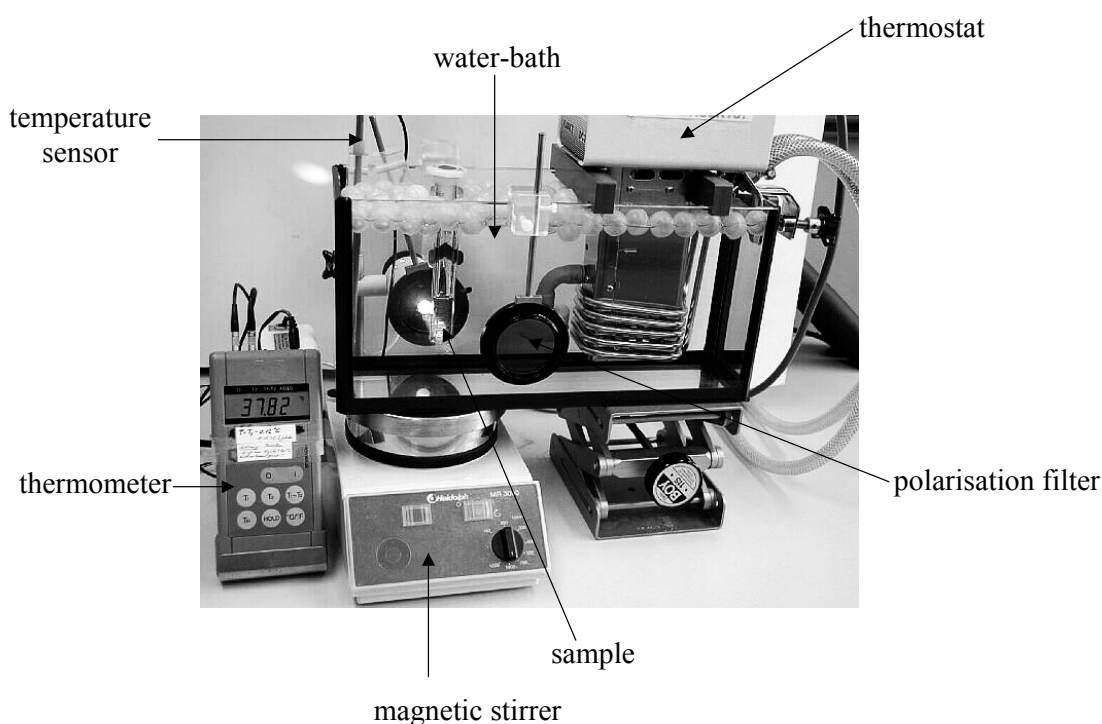


Figure 6-1: Experimental setup for the determination of the phase behaviour of microemulsions (taken from [60]; for details see text).

The single components are weighed into a 15 cm³ test tube equipped with a magnetic stir bar. The test tubes were placed in a de-ionised water-bath. The temperature of the water was adjusted with a thermostat which is hung in the water bath (Haake DC30) and controlled with a digital thermometer. The temperature was controlled with a precision of ± 0.05 °C. For the measurements of the phase boundaries below 4 °C an extra bath filled with glycol/water was cooled by a Lauda RE 320 cryostate. The samples were stirred at a temperature in the two-phase state to avoid memory effects or pathway dependences in the determination of the phase boundaries and after reaching the assumed temperature of the one-phase state the phase boundaries were visually determined after the sample was kept for two minutes without

stirring. To recognize birefringence, which is observed for samples with an anisotropic microstructure like lamellar structures, polarization filters were used.

Emulsification method

Water-in-fuel emulsions were formulated by adding diesel fuel including sorbitan monooleate using a syringe into the aqueous phase (including additives and polyoxyethylene sorbitan monooleate) at $T = 25\text{ }^{\circ}\text{C}$. The aqueous phase is weighed into a 15 cm^3 test tube equipped with a magnetic stir bar which is placed in the equipment as described above. High shear rates were created using a syringe to add the oil phase into the test tube containing the aqueous phase. Hydrodynamic radii of the samples were determined by dynamic light scattering (DLS).

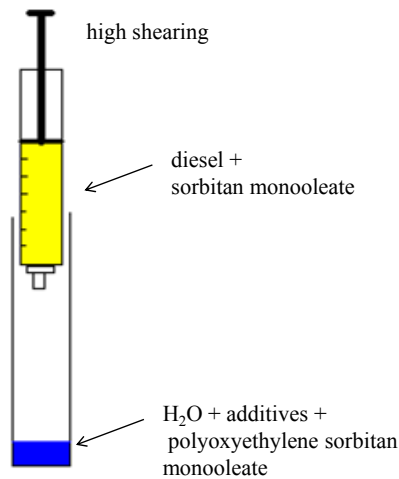


Figure 6-2: Schematic drawing of the emulsification method (for details see text).

Scanning Electron Microscopy (SEM)

The SEM is a microscope that forms an image by using electrons instead of light and has a resolution down to 1 nm. At the top of the microscope a beam of electrons is produced by an electron gun. The electron beam passes vertical through the microscope which is held under vacuum. The beam is focused and accelerated down toward the sample while passing through electromagnetic fields and lenses. The electrons interact with atoms in the sample and eject electrons and X-rays from the sample. Those X-rays and backscattered electrons are collected by the secondary electron detector and convert them into signals. The detected signals contain

information about the sample's surface topography and composition. In figure 6-3 the schematic representation of a SEM set-up is shown.

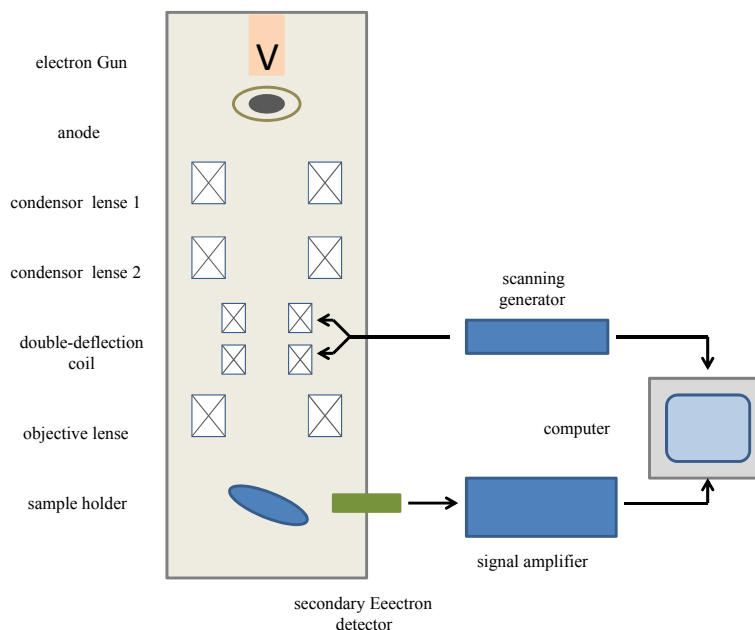


Figure 6-3: Schematic experimental setup of the scanning electron microscope (SEM; see text for details).

For the preparation of the soot-filter samples, a piece was cut out and fixed with a conductive silver lacquer on the sample holder. The filter samples were covered with a thin silver coating to ensure an interaction with the electron beam. The SEM is used to reveal information about size and texture of the agglomerated soot-particles on the sample-filter.

Stopped-Flow measurements

The kinetic measurements were performed using a BioLogic[®] SFM3000 stopped-flow base unit with a BioLogic[®] MPS 70/4 to regulate the flow. The temperature of the stopped-flow unit and its detection was adjusted with a Haake AC200, which is attached to a Haake G50 by ThermoScientific. The individual phases (water including antifreeze; diesel fuel including surfactant-blend) were prepared with a precision of $\Delta m = 0.005$ g and then filled into the reservoirs of the stopped-flow base unit using two separate 10 ml gas tight syringes (HamiltonTM). Solutions had to be gas- and bubble-free during the filling of the reservoirs, in order to prevent disturbances in the measurements while passing through the detection volume. To ensure this condition, the solutions were repeatedly inserted and extracted from the reservoir. Experimental parameters were set in the control software while also considering the sample's viscosity. Flow rate (8 ml/s), sample volume, mixing ratio and the required

temperature in the mixing chamber were adjusted. The formation kinetics was studied using a stopped-flow unit with a standard light scattering and transmission setup shown in figure 6-4.

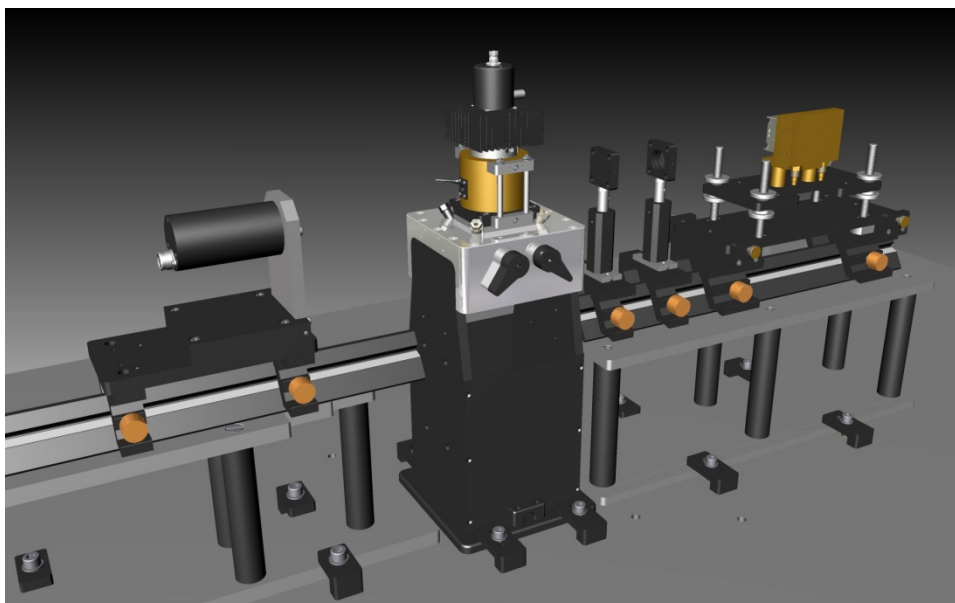


Figure 6-4: Overview of the complete experimental setup using light scattering. From right to left: laser, lenses, pinholes, stopped-flow unit (central) and transmission detection (taken from [186]).

The combination of syringes and a high efficient, static mixer (*Berger Ball Mixer*) of the stopped-flow unit enables the precise and fast blending of liquid components at a desired ratio with a short dead-time ($t_{\text{dead}} = 2.8 \pm 0.2$) ms determined by *Klemmer* [186].

Small angle neutron scattering (SANS)

The microstructure of microemulsions is accessible by small angle neutron scattering (SANS). The research reactor *FRM II* in Munich was applied as neutron source which is operated with highly enriched ^{235}U uranium fuel rods. The generated fast neutrons were moderated in heavy water (D_2O) and then decelerated in liquid deuterium D_2 to a *de Broglie*-wavelength of 3 - 40 Å. Afterwards, the neutron beam were mono-chromatised to wavelengths of 4.5 Å or 12 Å using a ^{58}Ni -coated neutron guide collimator. Both aperture (one close to the sample and the other at the end of the collimator) adjust the incident intensity I_0 . The 60 x 60 cm neutron detector was located at a variable distance of 4 to 20 m inside the detector tube. Different q -ranges were accessible at certain positions. The primary neutron beam was absorbed by a cadmium beam stop located in front of the detector.

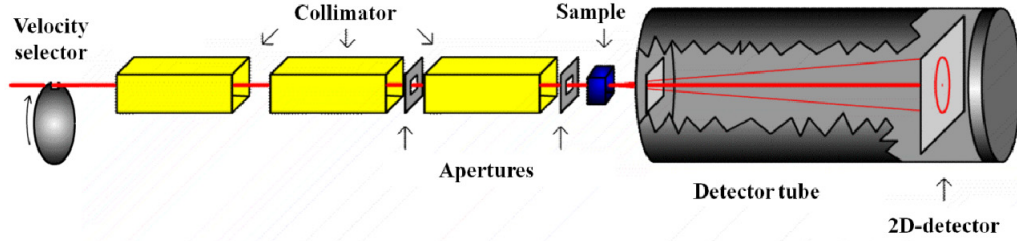


Figure 6-5: Schematic experimental setup of KWS-1 (*FRM II* in Munich). Collimator length was 4 to 20 m (taken from (60)).

Raw data treatment

Due to a various distance of sample to detector the received raw data are radially averaged (I_{Sa}) in order to get uniform intensity range. A calibration using a standard with known absolute scattering intensity is applied to obtain the absolute intensity. The experimentally obtained scattering intensity I_{sa} and I_{std} are corrected by the intensity scattered from the empty cell of sample (I_{EC}) and standard sample ($I_{\text{EC, std}}$), and the environmental background intensity I_{BG} . With transmission of the sample (T_{Sa}) and the calibration standard (T_{std}), this procedure leads to the absolute intensity of the sample $I(q)$ given by

$$I(q) = \frac{I_{\text{Sa}} - I_{\text{BG}} - \frac{T_{\text{Sa}}}{I_{\text{EC}}} (I_{\text{EC}} - I_{\text{BG}})}{I_{\text{St}} - I_{\text{BG}} - \frac{T_{\text{Sa}}}{I_{\text{EC, std}}} (I_{\text{EC, std}} - I_{\text{BG}})} \frac{T_{\text{std}}}{T_{\text{Sa}}} \frac{d_{\text{std}}}{d_{\text{Sa}}} \frac{d\Sigma}{d\Omega} (St). \quad (63)$$

The scattering curve of microemulsions often exhibits a single, broad maximum of scattering intensity with a q^{-4} -decay which is caused by an abrupt change of the scattering length density at the interface [214]. *Teubner* and *Strey* [215] developed a phenomenological, mathematical description for scattering bicontinuous systems written as

$$I(q) = \frac{8\pi c_2 \langle \eta^2 \rangle / \xi_{\text{TS}}}{a_2 + c_1 q^2 + c_2 q^4}. \quad (64)$$

The correlation length ξ_{TS} and the periodicity d_{TS} are accessible from the parameters a_2 , c_1 and c_2 :

$$d_{\text{TS}} = 2\pi \left(\frac{1}{2} \left(\frac{a_2}{c_2} \right)^{0.5} - \left(\frac{c_1}{4c_2} \right) \right)^{-0.5}, \quad (65)$$

$$\xi_{TS} = \left(\frac{1}{2} \left(\frac{a_2}{c_2} \right)^{0.5} + \left(\frac{c_1}{4c_1} \right) \right)^{-0.5}. \quad (66)$$

The length scale ξ of one domain pertains at an oil to water ratio of $\phi = 0.5$ [216] is

$$\xi = \frac{d_{TS}}{2}. \quad (67)$$

The amphiphilicity factor f_a describes the degree of order in bicontinuous microemulsions [217]:

$$f_a = \frac{c_1}{\sqrt{4a_2c_2}}. \quad (68)$$

An amphiphilicity factor in the range of $f_a = -0.7$ to $f_a = -0.9$ is obtained for well structured bicontinuous microemulsions [218]. At $c_1 = 0$, the *Lifshitz*-line is crossed and the structure peak vanishes when f_a increases further.

The adjustment of the data was performed by equation

$$I(q) = \frac{1}{a_2 + c_1q^2 + c_2q^4} + b. \quad (69)$$

where b describes the contribution of the incoherent background scattering for high q -values.

Deviations from the ideal course of scattering intensity could be observed in microemulsions with a high structural density (e.g. for microemulsion droplets), thus resulting in a weak peak of the second order [216]. The influence of the interference of neutrons scattered from different particles is taken into account by the structure factor $S(q)$. The microemulsion droplet-structure can be formed spherical, elongated or cylindrical. The evaluation of the scattering intensities is based upon the assumption of spherical water-in-oil micelles. The scattering intensity $I(q)$ for spherical particles is written as [219]:

$$\frac{d\sigma(q)}{d\Omega} = n \cdot P(q) \cdot S(q), \quad (70)$$

where n is the number density, $P(q)$ - the form factor, which describes the scattering of each particle and $S(q)$ - the structure factor, which describes the interference of neutrons scattered from different particles.

The scattering length density ρ_k of the individual components k is directly correlated to the contrast of the neutron scattering [220]

$$\rho_k = N_A \frac{\rho_k^0}{M_k} \sum_i b_i, \quad (71)$$

where N_A is the *Avogadro* constant, ρ_k^0 the macroscopical density, M_k the molecular mass of the component k and b_i the scattering length of each atom of the type i in the component k . For a mixture of several components the scattering length density ρ_m is written as

$$\rho_m = \sum_k \phi_k \rho_k, \quad (72)$$

with ϕ_k as volume fraction. The scattering length densities of ρ_{oil} , ρ_{core} (water) and ρ_{film} (surfactant) differs by several orders of magnitude in the investigated samples. The model, which considers the differences of the dispersed phase (water/antifreeze), the surfactant film (ionic/non-ionic surfactant) and the oil phase (diesel fuel) is applied for the evaluation of the scattering curves. As mentioned before, homogenous spherical particles with a diffuse interface and a radius R after *Rayleigh* are assumed [221]. The contribution of the surfactant film is defined after a model, which describes the amphiphilic film as diffuse interface using the radial density distribution after *Gauss* [218]. For the adjustment of the scatter data, the form factor was described as

$$P(q) = [A_{\text{cs}}(q)]^2 = \Delta \rho_{\text{film}}^2 \cdot V_{\text{film}}^2 \cdot A_{\text{film}}^2(q) + \Delta \rho_{\text{core}}^2 \cdot V_{\text{core}}^2 \cdot A_{\text{core}}^2(q) + 2 \cdot \Delta \rho_{\text{film}} \cdot V_{\text{film}} \cdot \Delta \rho_{\text{core}} \cdot V_{\text{core}} \cdot A_{\text{film}}(q) \cdot A_{\text{core}}(q). \quad (73)$$

A is amplitude of the surfactant film (A_{film}) or of the droplet (A_{core}). The contribution of the surfactant film-scattering is calculated as

$$\left. \frac{d\sigma(q)}{d\Omega} \right|_{\text{film}} = \phi_{\text{c,i}} \cdot \left(\frac{v_s}{a_s} \right) \cdot \frac{4\pi}{q^2 \cdot (R_0^2 + \sigma^2)} \cdot \Delta \rho_{\text{film}}^2 \cdot \exp\left\{ -\frac{q^2 \cdot t^2}{2} \right\} \cdot (f_1 + f_2 + f_3 + f_4), \quad (74)$$

$$\begin{aligned} f_1 &= \frac{1}{2} q^2 t^4 \{ 1 + \cos(2qR_0) \exp\{-2q^2 \sigma^2\} \} \\ f_2 &= q t^2 \{ R_0 \sin(2qR_0) + 2q \sigma^2 \cos(2qR_0) \} \exp\{-2q^2 \sigma^2\} \\ f_3 &= \frac{1}{2} R_0^2 \{ 1 - \cos(2qR_0) \exp\{-2q^2 \sigma^2\} \} \\ f_4 &= \frac{\sigma^2}{2} \left\{ 1 + 4qR_0 \sin(2qR_0) \exp\{-2q^2 \sigma^2\} + \cos(2qR_0) \{ 4q^2 \sigma^2 - 1 \} \right\} \exp\{-2q^2 \sigma^2\} \end{aligned} \quad (75)$$

R_0 is the radius of the microemulsion droplet, t the shell thickness of the surfactant film and σ the standard deviation of the particle size distribution. The volume of the surfactant

molecules was derived from the data for alkylpolyglycolether [218]. The scattering of droplets is describes as

$$\left. \frac{d\sigma(q)}{d\Omega} \right|_{\text{core}} = \phi_{\text{c,i}} \cdot \left(\frac{v_s}{a_s} \right)^{-1} \cdot \frac{4\pi}{q^6 \cdot (R_0^2 + \sigma^2)} \cdot \Delta\rho_{\text{core}}^2 \cdot (g_1 + g_2 + g_3), \quad (76)$$

$$\begin{aligned} g_1 &= \frac{1}{2} \{1 - \cos(2qR_0) \exp(-2q^2\sigma^2)\} \\ g_2 &= (-q) \cdot \{R_0 \sin(2qR_0) + 2q\sigma^2 \cos(2qR_0)\} \exp(-2q^2\sigma^2) \\ g_3 &= \frac{1}{2} q^2 \{(-4q\sigma^2 R_0 \sin(qR_0) \exp(-2q^2\sigma^2) + R_0^2 + \sigma^2 + \\ &R_0^2 \cos(2qR_0) \exp(-2q^2\sigma^2) + \sigma^2 \cos(2qR_0) \{1 - 4q^2\sigma^2\} \exp(-2q^2\sigma^2)\} \}. \end{aligned} \quad (77)$$

$$\left. \frac{d\sigma(q)}{d\Omega} \right|_{\text{cf}} = \phi_{\text{c,i}} \cdot \frac{8\pi}{q^4 \cdot (R_0^2 + \sigma^2)} \cdot \Delta\rho_{\text{film}} \cdot \Delta\rho_{\text{core}} \cdot \exp\{-q^2 \cdot t^2\} \cdot (h_1 + h_2 + h_3), \quad (78)$$

$$\begin{aligned} h_1 &= \frac{R_0}{2} \{1 - \cos(2qR_0) \exp(-2q^2\sigma^2)\} \\ h_2 &= q \cdot \sin(2qR_0) \exp(-2q^2\sigma^2) \left\{ \sigma^2 + \sigma^2 \left\{ 2q^2\sigma^2 - \frac{1}{2} \right\} - \frac{R_0^2}{2} \right\} \\ h_3 &= q^2 \{ (t^2 \sin(2qR_0) \exp(-2q^2\sigma^2) \left\{ \frac{1}{2q} + q\sigma^2 \right\} - \frac{R_0 t^2}{2} \right. \\ &\quad \left. - R_0 \cos(2qR_0) \left\{ \frac{t^2}{2} + 2\sigma^2 \right\} \exp(-2q^2\sigma^2) \} \}. \end{aligned} \quad (79)$$

The structure factor for repulsive hard-sphere interactions of monodisperse droplets with a diameter of $d_{\text{HS}} = 2 \cdot (R_0 + t)$ is calculated using *Percus-Yevick* with $x = q \cdot d_{\text{HS}}$.

$$S(q) = \frac{1}{1 - n \cdot c(q)}, \quad (80)$$

$$n \cdot c(q) = \frac{1}{x^3} \cdot \left\{ \begin{aligned} & A(\sin x - x \cdot \cos x) + B \left[\left(\frac{2}{x^2} - 1 \right) \cdot x \cdot \cos x \right] \\ & + B \left(2 \cdot \sin x - \frac{2}{x} \right) - \frac{A \cdot \phi_{\text{disp}}}{2} \cdot \frac{24}{x^3} \\ & - \frac{A \cdot \phi_{\text{disp}}}{2} \cdot \left[4 \left(1 - \frac{6}{x^2} \right) \sin x - \left(1 - \frac{12}{x^2} + \frac{24}{x^4} \right) \cdot x \cdot \cos x \right] \end{aligned} \right\}, \quad (81)$$

$$A = -24 \cdot \phi_{\text{disp}} \cdot \frac{(1 + 2\phi_{\text{disp}})^2}{(1 - \phi_{\text{disp}})^4} \quad (82)$$

$$B = 36 \cdot \phi_{\text{disp}}^2 \cdot \frac{(2 + \phi_{\text{disp}})^2}{(1 - \phi_{\text{disp}})^4}. \quad (83)$$

The structure factor is not determined in this investigation, therefore the assumption of ideal solutions without any interactions is used.

The simplification still provides the estimation of form and size of the dispersed phase in the investigated microemulsions. With the combination of dynamic light scattering (DLS) a more precise evaluation of the structure-size is possible.

Viscosity

The viscosity is the quantity that describes a fluid's resistance to flow and is related to the lubricity of the liquid. Due to its influence on combustion and spray behaviour, the viscosity of diesel fuel is one of the characteristic physical parameters required by the quality norm EN 590.

A *Haake* falling-ball viscometer was used to determine the viscosity at a temperature range between 15 °C to 65 °C. A spherical ball was added in a 0.5 ml *Hamilton* syringe which was filled bubble-free with the liquid to examine. The syringe was inserted towards the viscometer at a certain angle to avoid uncontrolled contact with the syringe wall. The computer regulated measurement equipment consists of a light sensor which is connected with the thermostat. The light sensor determines the falling time of the ball. The viscosity is given by:

$$\eta = K(\rho_k - \rho_L)t \quad (84)$$

where t is the falling time of the ball, K the characteristic constant for the particular sphere ball (which is determined for each ball with water - glycerin mixtures), ρ_k the density of the calibration substance and ρ_l the density of the liquid. Several balls of different diameters were available to cover certain viscosity ranges. By dividing the dynamic viscosity by the density of the liquid, the kinematic viscosity ν was calculated.

Density

The oscillating U-tube, Heraeus/Paar DMA 601W was used to determine the density. The liquid was filled into the measuring cell which has an oscillation capacity. The glass-tube was electronically excited into undamped oscillation. The natural frequency of the cell depends on the liquid's mass. The period τ had a resolution higher than 0.0005 g/cm^3 and is related to the density of the liquid in the oscillator:

$$\rho = A\tau^{-2} - B \quad (85)$$

where A and B are the device constants.

Pressure cell

The phase behaviour at 300 bar was studied in a high-pressure view-cell shown in figure 6-6.

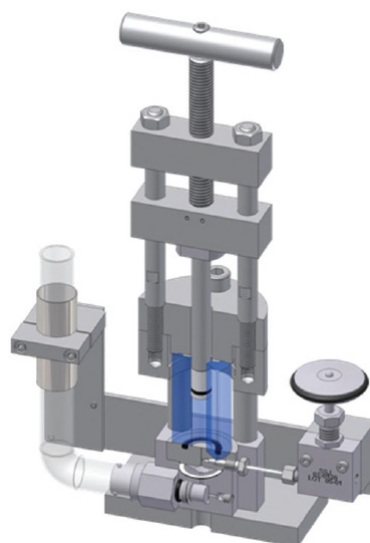


Figure 6-6: Schematic drawing of the pressure cell to determine the phase behaviour at pressures up to $p = 500 \pm 5 \text{ bar}$ (taken from [222]; details see text).

The sapphire cylinder ($h = 50 \text{ mm}$, $\varnothing_{\text{outside}} = 40 \text{ mm}$, $\varnothing_{\text{inside}} = 10 \text{ mm}$) allows the optical characterisation of the phases with a sample volume of about 3 ml. Pressures up to $p = 500 \pm 5 \text{ bar}$ can be achieved by turning down a piston into the sapphire cylinder. A miniature pressure transducer (Type 81530, Burster, Germany), which was placed in a casing at the bottom of the sample cell, determined the pressure. The homogenisation of the sample was provided by a magnetic stirring bar. In order to determine the phase boundaries as a function of the temperature, the whole pressure cell was placed into the thermostated water bath (figure 6-1).

High Frequency Reciprocating Rig (HFRR)

The HFRR-value is a measured value for the lubricity of fuels or lubricants. A moveable, computer-controlled steel ball was placed on a fixed platform which was located in a liquid bath of the liquid to be examined. The vibration height, -frequency and the load weight were variable. The lubricity was evaluated through light microscopy measurements of the abrasion indentation on the platform.

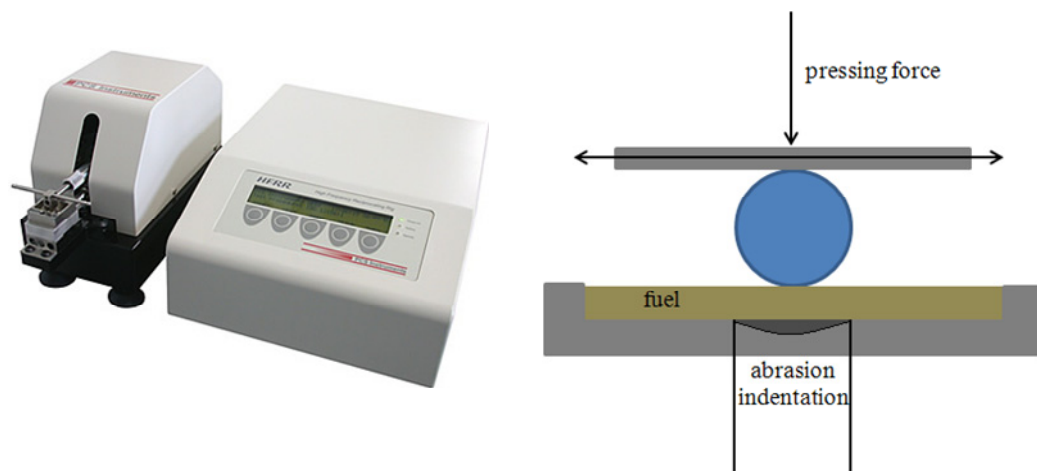


Figure 6-7: Experimental setup (PCS instruments) for the determination of the lubricity of fuels (right; taken from [223]) and schematic drawing of its functioning according to ASTM D 6079 (left; redrawn and modified from [224]).

Traction Coefficient

Traction coefficient of the water phase was determined in a PCS Instruments Mini Traction Machine (MTM). The MTM is a computer-controlled instrument to measure the frictional properties of lubricated and unlubricated contacts. The liquid was coated on a 46 mm

diameter steel disk. A steel ball was loaded against the surface of the disk to create a rolling/sliding contact. Both ball and disk were moved separately to measure the frictional force by a force transducer.

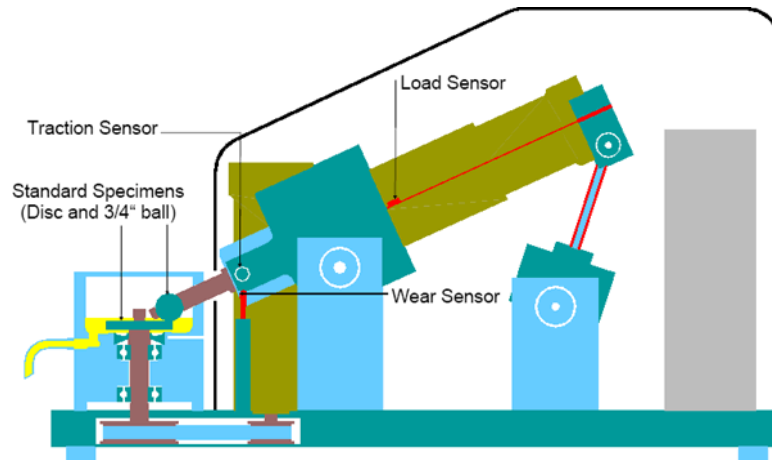


Figure 6-8: Schematic experimental setup of PCS Instruments Mini Traction Machine (MTM) (taken from [225], for details see text).

Corrosion Tests

The laboratory test method according to DIN 51 360 [226] was used to specify the corrosion protective properties of different cooling lubricants.

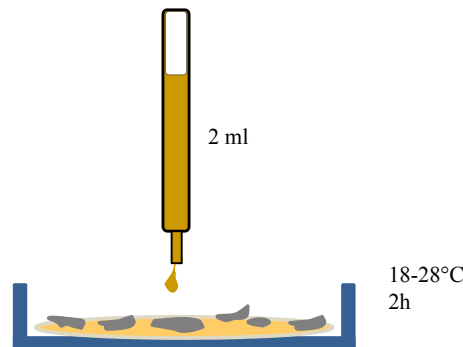


Figure 6-9: Schematic drawing of the experimental setup to specify corrosion properties according to DIN 51 360 (for details see text).

2 g of cast iron chips were placed on a marked region on the filter circle in a petri dish. The chips were equally coated with 2 ml of water and cooling lubricant mixtures. The petri dish was covered for two hours at a temperature between 18 °C and 28 °C while protecting from

sunlight or draught. Finally, the chips were removed by adding water and cleaned five seconds in acetone. The filter was dried at room temperature between 18 °C and 28 °C.

Corrosion stains are evaluated regarding their size and quality, finally divided into corrosion grades from zero to four (table 15).

Table 15: Overview of corrosion grades from zero to four according to DIN 51 360.

corrosion grade	relevance	description (filter surface)
0	no corrosion	Unchanged
1	traces of corrosion	at the most three corrosion stains with a diameter of < 1 mm
2	light corrosion	not more than 1 % of the surface is discoloured, but more and bigger corrosion stains than at corrosion grade 1 are observed
3	moderate corrosion	1 - 5 % of the surface is discoloured
4	strong corrosion	5 % < of the surface is discoloured

Exhaust gas measurements (CO-, CO₂-, HC- and NO_x-emissions)

Exhaust gas emissions were determined with the ALV AMA 4000 measurement systems. Non-Dispersive Infra-Red (NDIR) detectors were used to measure the concentration of CO and CO₂. The technique is based on absorption at the specific rotational vibration rotation spectrum bands of non-elemental gases in the middle of infrared range between 2 and 12 µm. Due to a bipolar moment of the gas molecules, an interaction with infrared radiation occurs.

The engine exhaust hydrocarbons were measured with the Flame Ionisation Detector (FID) method. Exhaust gas was introduced into a hydrogen flame inside the FID. Total organic carbons (TOC) produce ions during the burning process in the hydrogen flame and were detected using a metal collector. The ionisation current across the collector is proportional to the rate of ionisation which depends on the concentration of total organic carbons (TOC).

Chemiluminescence detectors (CLD) determine the concentration of nitrogen oxides (NO_x) in the exhaust gas. The measuring principle of the CLD is based on the emission of light from exited NO₂ molecules returning to a lower energy state (LUMO). A photomultiplier counted

the photons, which are proportional to the amount of NO in the sample. The NO₂ molecules were generated from the reaction of NO with ozon (O₃) and had to be converted back to NO, in order to determine the NO_x concentration in the exhaust gas. The CLD analyser determined the concentrations of NO or of NO_x, while the NO₂ concentration was derived as their difference in concentrations.

Exhaust particulates

A partial flow dilution system (AVL Smart Sampler SPC 472) is used for gravimetric sampling of exhaust particulates from internal combustion engines.

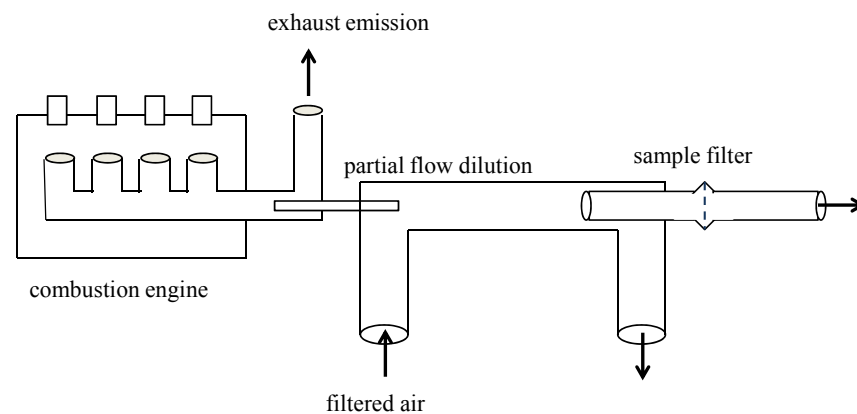


Figure 6-10: Schematic experimental setup of the partial flow dilution tunnel for gravimetric determination of exhaust particulates (for details see text, redrawn from [227]).

A partial flow from the engine's raw exhaust was diluted with a measured, constant flow of filtered air and then collected on a dedicated filter as shown in figure 6-10.

Opacity measurements

A dynamic partial-flow measuring instrument (ALV Opacimeter 439) was used for the continuous measurements of exhaust gas opacity.

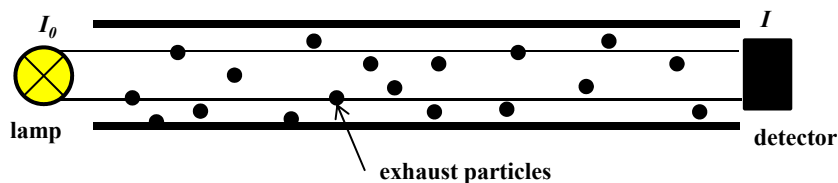


Figure 6-11: Schematic experimental setup of ALV Opacimeter 439 to determine the opacity (see text for details, redrawn from [228]).

Exhaust gas was homogenously filled in a measuring chamber (with a non-reflecting surface) of defined length. The opacity of the exhaust gas was calculated from the loss of light intensity between a light source and a receiver. The calculation is based on the *Lambert-Beert* law given as:

$$T = \frac{I}{I_0} \quad (86)$$

where I and I_0 are the intensity of the transmitted and the incident light.

Smoke Meter

The soot content in the exhaust of diesel engine was measured with a filter-type smoke meter (AVL Smoke Meter 415S). From the exhaust pipe a defined flow rate was sampled through a clean filter in the analyser. Blackening on the filter was caused by the filtered soot and was detected by a photoelectric measuring head and resulted in the Filter Smoke Number (FSN) which is normalized on a linear scale from 0 to 10.

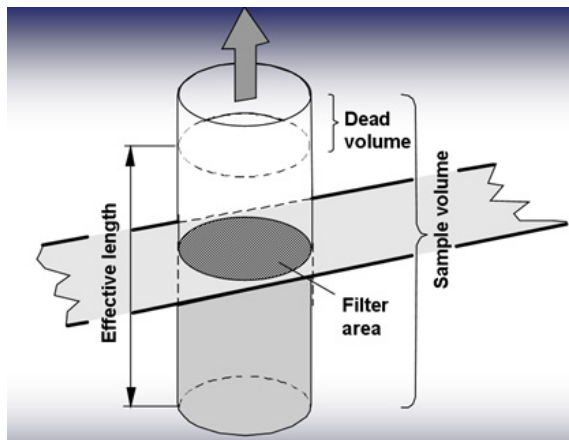


Figure 6-12: Schematic experimental setup of AVL Smoke Meter 415S to measure the soot content in the exhaust of diesel engine (taken from [229], see text for details).

Particle Counter

The non-volatile particle number concentrations of the exhaust gas were measured using the AVL Particle Counter 489. The sample was diluted at 150 °C and then transported to an evaporate tube, where the remaining volatile components were transferred into the gaseous

phase. Finally, the particles were detected after a second dilution and counted using the light-scattering method.

Particle analysis

The collected particles on the filter paper were analysed using an extraction process. The soluble organic fraction (SOF) on the filter was eluted with dichloromethane and the amount was then determined with the mass difference of the filter. In a further step, the extraction residue was examined with isopropanol and water. The concentration of the water soluble fraction (WSF), which integrates soluble salts as sulfate, nitrate, carbonate, acetate and their correspondent acids, could be then determined. The insoluble fraction (ISF) now consists of soot, metals or metal oxides (shown in figure 6-13).

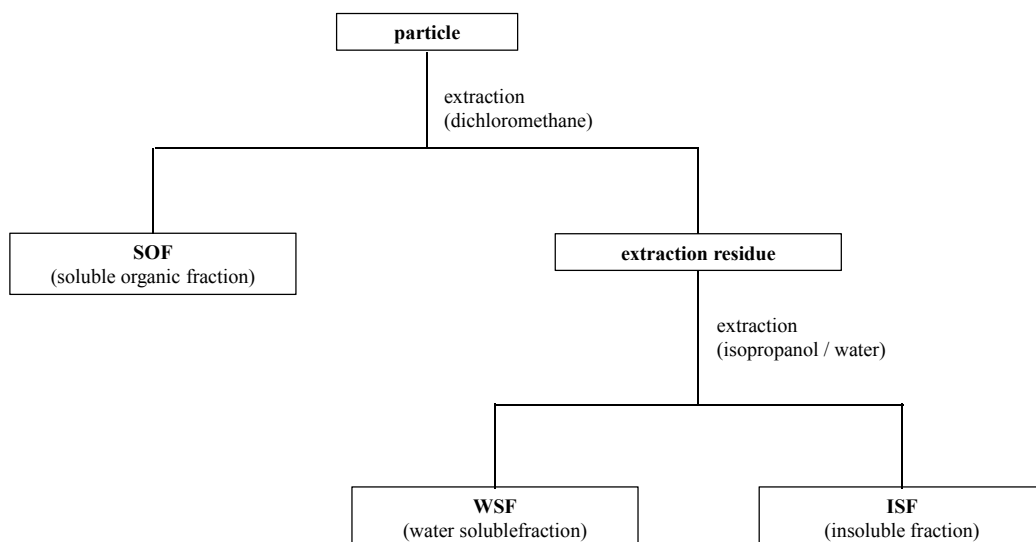


Figure 6-13: Analysis of the collected particles divided into soluble organic fraction (SOF), soluble inorganic fraction (SIOF) and insoluble fraction (ISF) (redrawn and modified from [56]).

High pressure chamber

Penetration depth and -area, fuel-mixture generation (microexplosions) and ignition processes were determined using an optical accessible high pressure chamber equipped with a setup for shadowgraph images which were located and performed by engineers at the *Rheinisch Westfälische Technische Hochschule Aachen* (RWTH; Lehrstuhl für Verbrennungskraftmaschinen VKA).

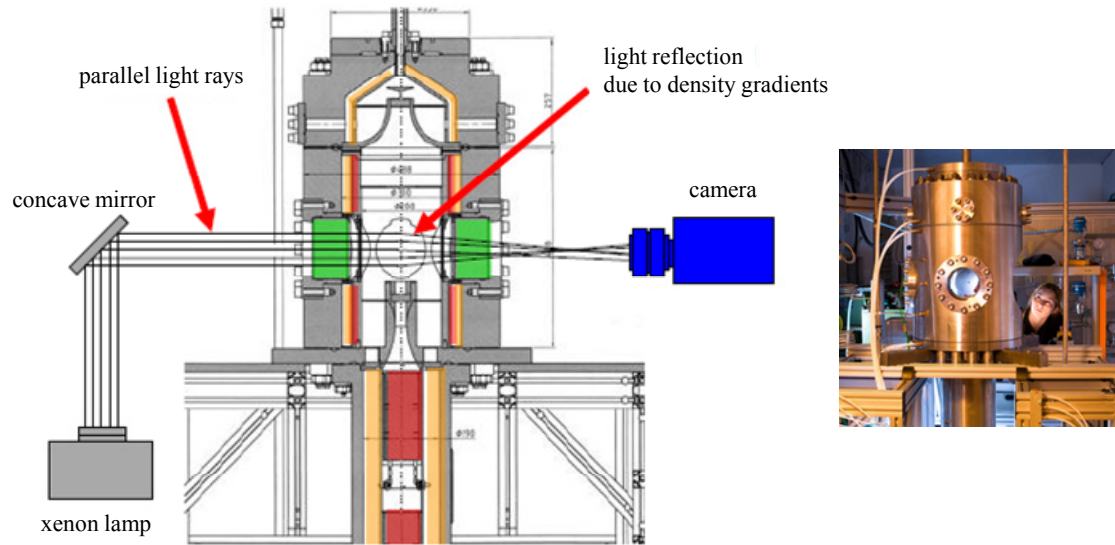


Figure 6-14: Schematic experimental setup of the high pressure chamber equipped with a setup for shadowgraph images (left: taken from [230] and modified; right: taken from [231]).

The shadowgraph technique allows the optical rendering of fluid flow patterns due to different indices of refraction in the flow. Images were recorded by means of a high time-resolved camera with 30.000 images per second.



7 APPENDIX

7.1 X-points and utilisable efficiency

7.1.1 Diesel fuel microemulsion

Table 16: X-points and utilisable efficiency of the system water/ammonium nitrate/ethanol - diesel fuel - oleic acid/monoethanolamine/oleic acid diethanolamide at $\alpha = 0.5$, $\delta_{(\text{ion})} = 0.7$, $\delta_{(\text{OD4})} = 0.3$, $\varepsilon = 0.004$, $\psi = 0.20$ with various n ($n = 0.40; 0.43; 0.45; 0.47$).

n	$\tilde{\gamma}$	$\tilde{T} / ^\circ\text{C}$	γ_{inv}
0.40	0.090	5.45	n.a.
0.43	0.089	7.79	n.a.
0.45	0.080	6.88	0.205
0.47	0.089	8.50	n.a.

Table 17: X-points and utilisable efficiency of the system water/ammonium nitrate/ethanol - diesel fuel - oleic acid/monoethanolamine/oleic acid diethanolamide at $\alpha = 0.5$, $\varepsilon = 0.004$, $\psi = 0.20$, $n = 0.45$ with $\varepsilon = 0.004$, $\psi = 0.20$ various $\delta_{(\text{ion})}$ ($\delta_{(\text{ion})} = 0.60; 0.65; 0.70; 0.75$).

δ	$\tilde{\gamma}$	$\tilde{T} / ^\circ\text{C}$	γ_{inv}
0.60	0.110	13.36	0.203
0.65	0.080	9.76	0.223
0.70	0.080	6.88	0.205
0.75	0.079	8.50	n.a.



Table 18: X-points and utilisable efficiency of the system water/ammonium nitrate/ethanol - diesel fuel - oleic acid/monoethanolamine/oleic acid diethanolamide at $\alpha = 0.5$, $\delta_{(\text{ion})} = 0.6$, $\delta_{(\text{OD4})} = 0.4$, $\psi = 0.20$, $n = 0.45$ with various ε ($\varepsilon = 0.004$; 0.006 ; 0.008).

ε	$\tilde{\gamma}$	$\tilde{T} / ^\circ\text{C}$	γ_{inv}
0.004	0.110	13.36	0.203
0.006	0.110	11.50	0.194
0.008	0.139	9.39	0.222

Table 19: X-points and utilisable efficiency of the system water/ammonium nitrate/ethanol - diesel fuel - oleic acid/monoethanolamine/oleic acid diethanolamide at $\alpha = 0.5$, $\delta_{(\text{ion})} = 0.6$, $\delta_{(\text{OD4})} = 0.4$, $\varepsilon = 0.006$, $n = 0.45$ with various ψ ($\psi = 0.15$; 0.20 ; 0.25 ; 0.30).

ψ	$\tilde{\gamma}$	$\tilde{T} / ^\circ\text{C}$	γ_{inv}
0.15	n.a.	n.a.	n.a.
0.20	0.110	11.50	0.194
0.25	0.158	2.22	0.191
0.30	n.a.	n.a.	0.236

Table 20: X-points and utilisable efficiency of the system water/ammonium nitrate/ethanol - diesel fuel - oleic acid/monoethanolamine/oleic acid diethanolamide at $\delta_{(\text{ion})} = 0.6$, $\delta_{(\text{OD4})} = 0.4$, $\varepsilon = 0.006$, $\psi = 0.25$, $n = 0.45$ with various α ($\alpha = 0.300$; 0.400 ; 0.500 ; 0.590 ; 0.730 ; 0.865).

α	$\tilde{\gamma}$	$\tilde{T} / ^\circ\text{C}$	γ_{inv}
0.300	0.115	6.12	0.138
0.400	0.159	5.45	0.196
0.500	0.158	2.22	0.191
0.590	0.149	23.56	0.184
0.730	0.089	28.06	0.144
0.865	0.067	33.99	0.129

Table 21: X-points and utilisable efficiency of the system water/ammonium nitrate/*n*-propanol - diesel fuel - oleic acid/monoethanolamine/oleic acid diethanolamide at $\delta_{\text{ion}} = 0.7$, $\delta_{\text{OD4}} = 0.3$, $\varepsilon = 0.008$, $\psi = 0.25$, $n = 0.43$ with various α ($\alpha = 0.300$; 0.400; 0.500; 0.590; 0.730; 0.865).

α	$\tilde{\gamma}$	$\tilde{T} / ^\circ\text{C}$	γ_{inv}
0.300	n.a.	n.a.	0.110
0.400	n.a.	n.a.	0.136
0.500	n.a.	n.a.	0.148
0.590	n.a.	n.a.	0.135
0.730	n.a.	n.a.	0.117
0.865	n.a.	n.a.	0.079

Table 22: X-points and utilisable efficiency of the system water/ammonium nitrate/*n*-propanol - diesel fuel - oleic acid/monoethanolamine/oleic acid diethanolamide at $\alpha = 0.5$, $\varepsilon = 0.008$, $\psi = 0.25$, $n = 0.43$ with various δ_{poly} ($\delta_{\text{poly}} = 0.00$; 0.05; 0.10; 0.15).

δ_{poly}	$\tilde{\gamma}$	$\tilde{T} / ^\circ\text{C}$	γ_{inv}
0.00	n.a.	n.a.	0.148
0.05	n.a.	n.a.	0.118
0.10	n.a.	n.a.	0.127
0.15	n.a.	n.a.	0.155



7.2 Physical properties

Table 23: Kinematic viscosity [mm²/s] of DWME 0020, DWME 0820, DWME 0815, DWME 1620, DWME 2420 at various temperatures.

<i>T</i> / °C	DWME 2420	DWME 1620	DWME 0820	DWME 0815	DWME 0020
0					
20	58.36	34.65	20.48	6.54	20.19
30	47.79	27.60	15.34	5.21	15.68
40	32.68	20.39	11.23	4.11	11.63
50	21.69	14.72	8.38	3.33	8.57
60	15.11	10.88	6.43	2.76	6.40
70	11.19	8.22	5.06	2.35	4.90
80	8.13	6.37	4.07	1.99	3.85
85	7.39		3.41	1.85	3.37
90	7.33	5.12	3.33	1.73	3.06
95		4.65	3.08	1.62	2.72
100			2.79	1.53	

Table 24: HFRR-value and viscosity of DWME 0020, DWME 0820, DWME 0815, DWME 2420 [measured by VKA Aachen].

	HFRR-value	viscosity / mm ² /s
DWME0020	153	2.76
DWME0820	238	6.43
DWME0815	264	6.40
DWME2420	257	15.11

7.3 DLS-measurements

Table 25: Mean hydrodynamic radii [nm] at $T = 25\text{ °C}$ for different HLB-values.

HLB	mean $r_{\text{hydr}} / \text{nm}$ $T = 25\text{ °C}$
4	102.2
6	72.4
8	80.6
10	127.9
12	219.6
14	264.7

Table 26: Dynamic light scattering (DLS) measurements of NE 08.

t / s	$r_{\text{hydr}} / \text{nm}$ $T = 25\text{ °C}$	$r_{\text{hydr}} / \text{nm}$ $T = 50\text{ °C}$	$r_{\text{hydr}} / \text{nm}$ after 3 h ($T = 25\text{ °C}$)
0	72.6	79.2	62.1
6	71.9	n.a.	76.1
12	n.a.	n.a.	74.5
18	72.8	80.8	70.5
24	64.5	83.8	68.4
30	59.0	81.0	84.0
36	59.0	n.a.	84.0
42	55.9	75.6	81.1



Table 27: Dynamic light scattering (DLS) measurements of NE 16.

t / s	$r_{\text{hydr}} / \text{nm}$ $T = 25 \text{ }^{\circ}\text{C}$	$r_{\text{hydr}} / \text{nm}$ $T = 50 \text{ }^{\circ}\text{C}$	$r_{\text{hydr}} / \text{nm}$ after 3 h ($T = 25 \text{ }^{\circ}\text{C}$)
0	83.5	81.2	91.2
6	84.6	76.4	n.a.
12	94.6	91.1	90.5
18	95.3	103.0	93.5
24	102.3	125.4	112.0
30	90.1	11.0	n.a.
36	100.7	99.9	123.6
42	n.a.	111.0	121.7



7.4 Combustion measurements

Table 28: Exhaust emissions of diesel fuels, DWME 0020, DWME 0820, DWME 1620, DWME 2420 at B50.

	Particle Mio# / ccm	FSN	opacity / %	HC / ppm	NO_x / ppm	COhigh / ppm	CO₂ vol.%	PM / g/kWh
Diesel	38.021	1.03	3.634	16.490	419.574	0.007	6.994	0.161
DWME0020	38.078	0.80	3.089	16.858	403.637	0.007	7.004	0.153
DWME0820	34.948	0.45	1.744	19.729	285.125	0.008	7.102	0.099
DWME1620	44.256	0.21	0.703	19.633	260.805	0.007	7.110	0.096
DWME2420	10.529	0.02	0.016	19.727	232.161	0.005	7.221	0.081

Table 29: Exhaust emissions of diesel fuels, DWME 0020, DWME 0820, DWME 1620, DWME 2420 at C100.

	Particle Mio# / ccm	FSN	opacity / %	HC / ppm	NO_x / ppm	COhigh / ppm	CO₂ vol.%	PM / g/kWh
Diesel	58.987	2.01	10.939	8.666	480.22	0.027	10.514	0.231
DWME0020	36.654	1.31	5.351	19.872	484.42	0.022	10.658	0.109
DWME0820	41.734	0.66	3.529	20.245	426.64	0.017	10.711	0.071
DWME1620	105.262	0.29	0.712	14.387	363.77	0.013	10.698	0.070
DWME2420	183.114	0.15	0.676	10.131	184.75	0.009	10.867	0.062

**Table 30: Exhaust emissions of diesel fuel, NE 00, NE 08, NE 16, NE 24 with 3 wt.% surfactant-blend at B50.**

	Particle Mio# / ccm	FSN	opacity / %	HC / ppm	NO_x / ppm	COhigh / vol.%	CO₂ / vol.%	b_e / g/kW h
Diesel	38.021	1.03	3.633	16.490	419.57	0.007	6.994	348.09
NE 00	0.949	1.51	6.297	13.064	355.87	0.011	7.027	321.16
NE 08	0.663	0.61	2.335	12.344	312.87	0.009	7.140	304.19
NE 16	0.788	0.16	1.268	11.905	257.02	0.006	7.151	291.85

Table 31: Exhaust emissions of diesel fuel, NE 00, NE 08, NE 16, NE 24 with 3 wt.% surfactant-blend at C100.

	Particle Mio# / ccm	FSN	opacity / %	HC / ppm	NO_x / ppm	COhigh / vol.%	CO₂ / vol.%	b_e / g/kWh
Diesel	58.987	2.01	10.939	8.666	480.22	0.027	10.514	310.47
NE 00	120.554	2.65	15.163	8.107	418.26	0.046	10.532	293.80
NE 08	99.640	1.20	3.597	9.410	336.09	0.024	10.477	270.95
NE 16	135.366	0.43	1.696	8.561	279.12	0.015	10.590	261.31

Table 32: Filter loading [mg/kWh] of SOF, WSF, ISF for diesel fuel, NE 00, NE 08, NE 16, NE 24 with 3 wt.% surfactant-blend at B50.

	SOF / mg/kWh	WSF / mg/kWh	ISF / mg/kWh
Diesel	2.96	3.86	31.75
DWME0020	4.38	3.07	26.46
DWME0820	2.32	2.39	7.04
DWME0815	1.15	1.78	4.75
DWME2420	1.51	2.31	2.44

Table 33: Filter loading [mg/kWh] of SOF, WSF, ISF for diesel fuel, NE 00, NE 08, NE 16, NE 24 with 3 wt.% surfactant-blend at C100.

	SOF / mg/kWh	WSF / mg/kWh	ISF / mg/kWh
Diesel	5.52	5.98	54.17
DWME0020	5.02	5.84	42.97
DWME0820	2.32	4.39	16.53
DWME0815	1.84	4.15	15.97
DWME2420	2.78	5.92	6.26



7.5 Corrosion-test



Figure 7-1: Corrosion test according to DIN 51 360 of DWME 2420 features an unchanged filter surface.

7.6 Scanning electron microscopy

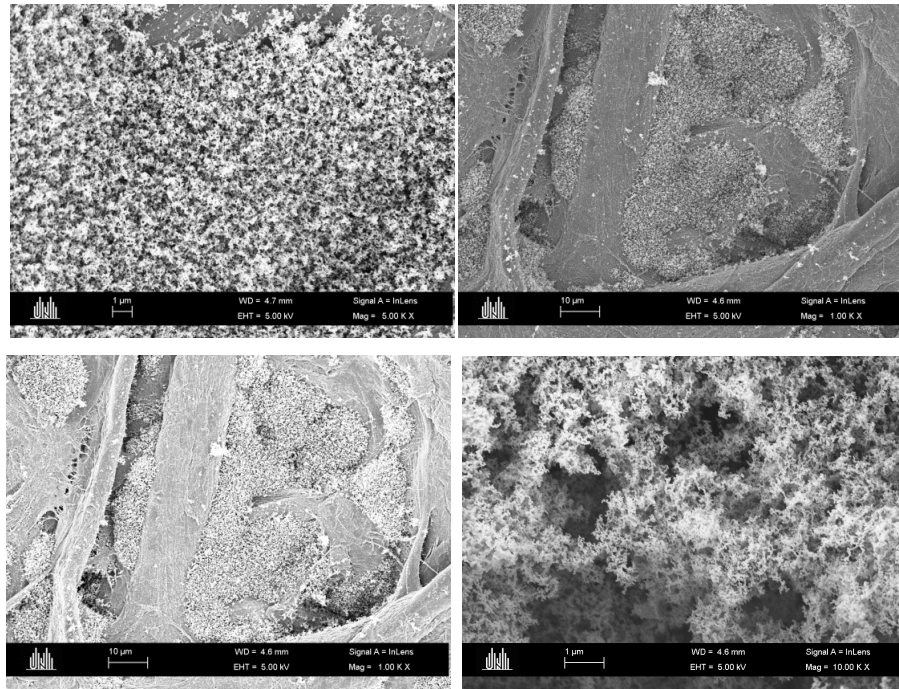


Figure 7-2: Scanning electron microscopy (SEM) picture of filter sample of nanoemulsion-fuel (NE 00) at various resolutions at C100. Filter surface is less occupied compared to the filter sample of pure diesel fuel. Primary particles feature a mean diameter-size of approximately $d = 26$ nm.

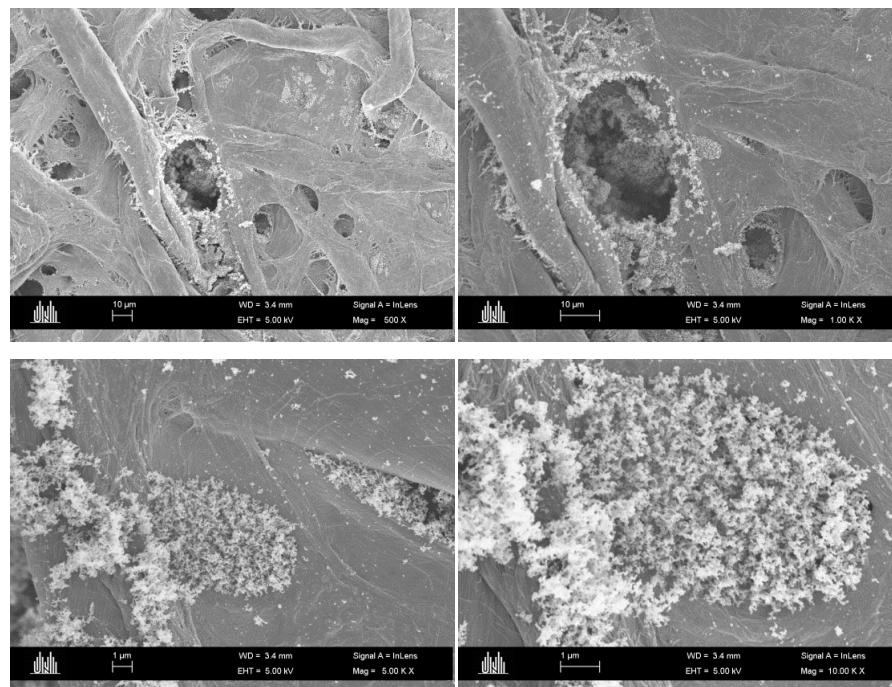


Figure 7-3: Scanning electron microscopy (SEM) picture of filter sample of nanoemulsion-fuel (NE 08) at various resolutions at C100. Agglomerated particles with a mean diameter-size of approximately are rarely presented.

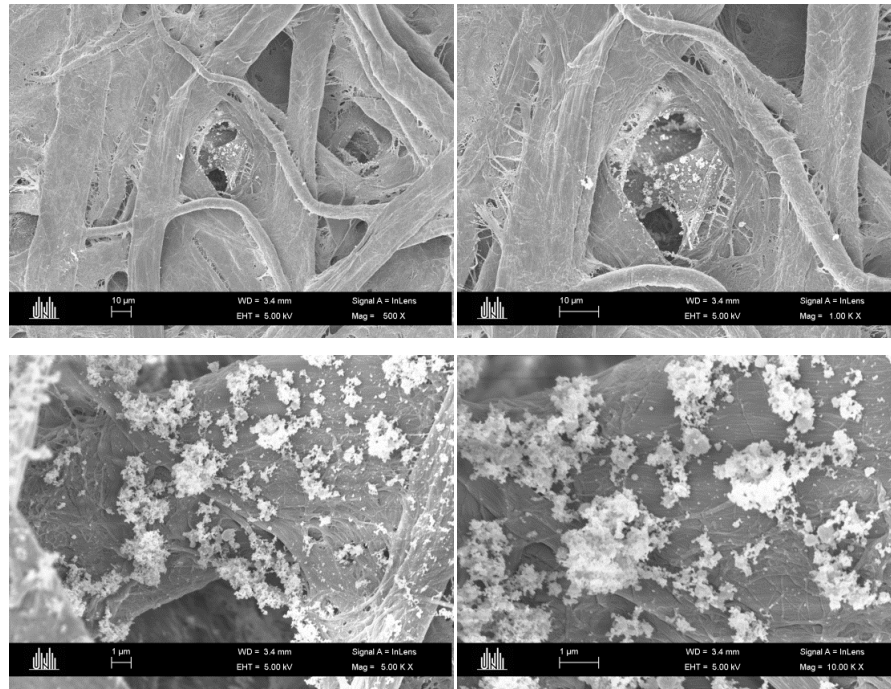


Figure 7-4: Scanning electron microscopy (SEM) picture of filter sample of nanoemulsion-fuel (NE 08) at various resolutions at C100. Filter surface is rarely occupied; agglomerated particles with a mean diameter size of $d = 38$ nm are observed.

7.7 Abbreviations and Symbols

Latin symbols

A	Interfacial area
	device parameter
	Amplitude of a relaxation process
a_0	head-group area
$A(\Gamma)$	distribution function of the inverse relaxation times Γ for all radii
B	device parameter
b	scattering length nucleus
b_e	brake specific fuel consumption
c	speed of light in vacuum
c_i	Curvature
c_1	order parameter
c_2	order parameter
d	Diameter
	self-diffusion coefficient
d_{TS}	Periodicity
F	Helfrich free energy
$F(x)$	auxiliary function
G	Gibbs free energy
$g^{(1)}$	time-field correlation function
$g^{(2)}$	normalised time - intensity correlation function
\hbar	$= h/2\pi$
H	mean curvature
H_0	spontaneous curvature
I	Intensity
I_{abs}	absolute intensity
I_{BG}	scattering intensity of the environmental background
I_{EC}	scattering intensities of the empty cell
$I_{\text{EC, std}}$	scattering intensities of the calibration standard
I_{Sa}	experimental scattering intensity of the sample
I_{std}	experimental scattering intensity of the calibration standard
$I_{\text{TS}}(q)$	intensity according to the <i>Teuber-Strey</i> formula
I_s	scattered intensity
I_0	incident intensity [neutrons/area and time]
K	Constant
k	kinetic rate constant
\vec{k}	wave vector
k_B	<i>Boltzmann</i> constant
\vec{k}_i	incident wave vector
\vec{k}_s	scattered wave vector



K	Gaussian curvature
l	length of hydrophobic chain
L_{st}	stoichiometric air-to-fuel ratio
n	grade of neutralization
	molar amount
	engine speed
	number density
n_{base}	molar amount of base (ethanolamine)
$n_{\text{oleic acid}}$	molar amount of oleic acid
N	number of particles
N	Load
m	Mass
M	Torque
m_{A}	mass of total hydrophoic phase
m_{air}	air mass
$m_{\text{air,st}}$	stoichiometric air mass
m_{alcohol}	mass of alcohol
m_{X}	mass of component X
Oh	Ohnesorge number
P	Moment
$P(q)$	form factor
\vec{q}	scattering vector
r	Radius
Re	Reynolds number
r_{S}	<i>solvodynamic</i> radius
S	Entropy
$S(q)$	structure factor
T	Time
T	Temperature
T_{l}	lower temperature of the three-phase region
T_{m}	mean temperature of the three-phase region
T_{u}	upper temperature of the three-phase region
T_{Sa}	transmission of the sample
T_{std}	transmission of the calibration standard
T_{α}	critical temperature
T_{β}	critical temperature
\tilde{T}	phase inversion tempterature
ν	cinematic viscosity
V_{X}	volume of component X
We	Weber number
w_{A}	mass fraction of component A
w_{B}	mass fraction of component A
w_{X}	mass fraction of component X

Greek symbols

α	oil to water-plus-oil mass fraction
β	device parameter
γ	surfactant mass fraction
γ_{inv}	surfactant amount reaching temperature invariance
γ_0	critical surfactant concentration
$\tilde{\gamma}$	surfactant concentration related to the X-point
Γ	inverse relaxation time
δ	chemical shift
	cosurfactant mass fraction adverted to total surfactant mass
	ionic mass fraction in a mixture of non-ionic and ionic surfactant
δ^*	critical ionic surfactant ratio
$\Delta\rho$	difference in scattering length density of solution and particle
ε	mass concentration in an aqueous solution of salt
η	dynamic viscosity
η	Efficiency
θ	scattering angle
κ	bending rigidity
$\overline{\kappa}$	saddle splay modulus
	over-stoichiometric air surplus / air-to-fuel ratio
	Wavelength
ξ	domain size
ξ_{TS}	correlation length
Π	molecular packing parameter
ρ	density
ρ_b	density of the ball
ρ_{core}	scattering length density of a structures core
ρ_F	density of fuel
ρ_{film}	scattering length density of a structures surfactant film
ρ_L	density of liquid
ρ_k	scattering length density of the component k
σ	Polydispersity
$d\sigma$	differential cross section of the scattering specimen [area]
τ	time interval between two pulses; period of time
ϕ	oil to water-plus-oil volume fraction
	volume fraction
ϕ_A	volume fraction of component A
ϕ_B	volume fraction of component B
ϕ_C	surfactant volume fraction
ψ	alcohol mass fraction relative to total water phase
$d\Omega$	spherical segment



Abbreviations

A	hydrophilic, lipophobic component
B	hydrophobic, lipophilic component
BASF	Badische Anilin- und Soda- Fabrik
BMEP	Brake mean effective pressure
BtL	bio mass to liquid (fuel)
C	amphiphilic compound
C _i E _j	<i>n</i> -i-alkyl j-polyglycol ether
cl _α	critical curve
cl _β	critical curve
CO	carbon monoxide
cp _α	critical point
cp _β	critical point
DPF	Diesel Particulate Filter
DLS	dynamic light scattering
DOC	diesel oxygenation catalyst
DWME	Diesel-Water Microemulsion
<i>e.g.</i>	<i>exempli gratia; lat.:</i> for example
EGR	engine gas recirculation
EIP	Emulsion Inversion Point
EN	European norm
<i>et al.</i>	<i>et alii; lat.:</i> and others
FAME	fatty acid methyl ester
FSN	filter smoke number
GtL	gas-to-liquid
HC	hydro carbons
HFRR	High Frequency Reciprocating Rig
HLB	hydrophilic lipophilic balance
ICE	Internal Combustion Engine
<i>i.e.</i>	<i>id est; lat.:</i> this is, this means
ISF	insoluble fraction
KWS	Kleinwinkelstreuungsanlage
<i>LHV</i>	Lower heating value
L ₃	bilayered sponge-like structure
L _α	lamellar phases
n.a.	not available
NE	Nanoemulsion
NO _x	nitrogen oxides
ME	Microemulsion
MEA	Monoethanolamine
o/w	oil-in-water
PAH	polycyclic aromatic hydrocarbon
PIT	Phase Inversion Temperature
ppm	parts per million

SANS	small angle neutron scattering
SCR	selective catalytic reduction
SEM	scanning electron microscope/microscopy
SMO	sorbitan monooleat
SOF	soluble organic fraction
THC	Total hydrocarbon
w/o	water-in-oil
WSF	Water soluble fraction
1	one-phase microemulsion; one-phase region
2	two-phase state
<u>2</u>	o/w microemulsion phase coexisting with oil excess phase
$\bar{2}$	w/o microemulsion phase coexisting with water excess phase
3	microemulsion phase coexisting with water and oil excess phases
wt%	weight percentage
vol%	volume percentage
PM	particulate matter

7.8 Literature

- [1] R. Diesel, Patent: Arbeitsverfahren und Ausführungsart für Verbrennungskraftmaschinen, Nr. 67207, **1892**.
- [2] J. Lewtas, *Air pollution combustion emissions: characterization of causative agents and mechanisms associated with cancer, reproductive, and cardiovascular effects*, Mutat Res.; 636 (1-3):95-133, **2007**.
- [3] A. Sydbom, A. Blomberg, S. Parnia, N. Stenfors, T. Sandström, SE Dahlén, *Health effects of diesel exhaust emissions*, Eur Respir J.; 17 (4):733-46, **2001**.
- [4] W.K.C. Morgan, R.B. Reger, D.M. Tucker, *Health effects of diesel emissions*, Ann. Occup. Hyg.; 41, (6): 643-658, **1997**.
- [5] V. Ramanathan, G. Carmichael, *Global and regional climate changes due to black carbon*, Nature Geoscience (1): 221-227, **2008**.
- [6] D.G. Streets, S. Gupta, S.T. Waldhoff, M.Q. Wang, T.C. Bond, B. Yiyun, *Black carbon emissions in China*, Atmospheric Environment (35), 4281-4296, **2001**.
- [7] Verordnung (EG) Nr. 715/2007, Europäisches Parlament, europa.eu, **2014**.
- [8] M. King Hubbert, *Drilling and Production Practice: Nuclear Energy and the Fossil Fuels*, American Petroleum Institute, New York, **1956**.
- [9] A.A. Bartlett, *An analysis of U.S. and world oil production patterns using Hubbert-style curves*, Math. Geology; 32, (1): 1.17, **2000**.
- [10] S. H. Mohr, G. Evans, *Peak Oil: Testing Hubbert's Curve via Theoretical Modeling*, Nat. Resour. Res.; 17, (1): 1-11, **2008**.
- [11] S. Mohr, G.M. Evans, *Long term prediction of unconventional oil production*, Energy Policy; 38, (1); 265–276, **2010**.
- [12] U. Bardi, *Peak oil: The four stages of a new idea*, Energy 34 (3): 323–326, **2009**.
- [13] Europäische Gemeinschaft, *Anpassung der Richtlinie 80/1268/EWG über Kohlendioxidemissionen und Kraftstoffverbrauch von Kraftfahrzeugen an den technischen Fortschritt*, Europäische Gemeinschaft, **1999**.
- [14] Deutsches Institut für Normung, *Kraftstoffe für Kraftfahrzeuge - Dieselkraftstoff - Anforderungen und Prüfverfahren*, **2010**.
- [15] A. Kowalewicz, M. Wojtyniak, *Alternative fuels and their application to combustion engines*, Proceedings of the Institution of Mechanical Engineers Part D Journal of Automobile Engineering; 219(1):103-125, **2005**.
- [16] R. W. R. Zwart, H. Boerrigter, A. van Drift, *The impact of biomass pretreatment on the feasibility of overseas biomass conversion to Fischer-Tropsch products*, Energy Fuels; 20 (5): 2192, **2006**.
- [17] A. Koltermann, *Second Generation Bioethanol: Challenges and Perspectives*, Journal of Biotechnology; 150: 553, **2010**.
- [18] P. Harrop, R. Das, *Electric Vehicle Forecasts, Trends and Opportunities 2014-2024*, Hybrid and pure electric vehicles for land, water and air, **2014**.

- [19] A. A. Pesaran, *Battery thermal models for hybrid vehicle simulations*, Journal of Power Sources; 110 (2): 377–382, **2002**.
- [20] A. De Risi, D. F. Manieri and D. Laforgia, *A Theoretical Investigation on the Effects of Combustion Chamber Geometry and Engine Speed on Soot and NOx Emissions*, Università degli Studi di Lecce, Dipartimento di Ingegneria dell'Innovazione, Italy.
- [21] Y. İċingür, D. Altıparmak, *Effect of fuel cetane number and injection pressure on a DI Diesel engine performance and emissions*, Elsevier; 44 (3): 389-397, **2003**.
- [22] B. D'Alleva, W. Lovell, *Relation of Exhaust Gas Composition to Air-Fuel Ratio*, SAE Technical Paper 360106, **1936**.
- [23] H. Tschöke, *Diesel- und Benzindirekteinspritzung V: Spraybildung, Simulation, Applikation*, Messtechnik, ISBN 978-3-8169-2867-5, **2009**.
- [24] C.O. Schmalzing, *Theoretische und experimentelle Untersuchung zum Strahlausbreitungs- und Verdampfungsverhalten aktueller Diesel-Einspritzsysteme*, **2001**.
- [25] R. L. McCormick, J. D. Ross, M. S. Graboski, *Effect of Several Oxygenates on Regulated Emissions from Heavy-Duty Diesel Engines*, Environ. Sci. Technol.; 31: 1144-1150, **1997**.
- [26] K. Tsurutani, Y. Takei, Y. Fujimoto, J. Matsudaira, *The Effects of Fuel Properties and Oxygenates on Diesel Exhaust Emissions*, SAE Technical Paper 952349, **1995**.
- [27] N. Ladommatos, M. Parsi, A. Knowles, *The effect of fuel cetane improver on diesel pollutant emissions*, Fuel; 75 (1); 8–14, **1996**.
- [28] K. E. Nord, D. Haupt, *Reducing the Emission of Particles from a Diesel Engine by Adding an Oxygenate to the Fuel*, Environ. Sci. Technol.; 39: 6260-6265, **2005**.
- [29] VDB - Verband der Deutschen Biokraftstoffindustrie eV, <http://biokraftstoffverband.de/index.php/start.html>, **2013**.
- [30] T. Kadota, H. Yamasaki, *Recent advances in the combustion of water fuel emulsion*, Progress in Energie and Combustion Science; 28 : 385-404, **2002**.
- [31] J. Warnatz, U. Maas, R. W. Dibble, *Verbrennung*, Berlin: Springer, 3. Auflage, ISBN 3540421289 **2001**.
- [32] C. Simon, R. Pauls, *Einfluß der geschichteten Wassereinspritzung auf das Abgas- und Verbrauchsverhalten eines Dieselmotors mit Direkteinspritzung*, MTZ, **2004**.
- [33] H. Dörksen, Ch. Simon, *Entwicklung einer neuen Betriebsart von Dieselmotoren mit Diesel-Wasser-Mikroemulsionen*, AiF/BMBF-Forschungsprojekt, **2009**.
- [34] C. Simon, H. Dörksen, R. Strey, K. Wormuth, S. Maleknia, vorraussichtliche Patentanmeldung: “In injector-blending”, **2014**.
- [35] R. Ochoterena, A. Lif, M. Nydén, S. Andersson, I. Denbratt, *Optical studies of spray development and combustion of water-in-diesel emulsion and microemulsion fuels*, Fuel 89; 122–132, **2010**.
- [36] D. Morales, J. M. Gutiérrez, M. J. García-Celma, Y. C. Solans, *A Study of the Relation between Bicontinuous Microemulsions and Oil/Water Nano-emulsion Formation*, Langmuir; 19 (18); 7196–7200, **2003**.
- [37] K. Shinoda, H.J. Saito, Journal of Colloid and Interface Science (30), 258, **1969**.



- [38] T. Sottmann, R. Strey, *Microemulsions*, in Fundamentals of Interface and Colloid Science; V, J. Lyklema, Academic Press, London, **2005**.
- [39] T. Kadota, H. Tanaka, D. Segawa, S. Nakaya, H. Yamasaki, *Microexplosion of an emulsion droplet during Leidenfrost burning*, Proceedings of the Combustion Institute; 31(2):2 125-2131, **2007**.
- [40] A. Lif, M. Stark, M. Nyden, K. Holmberg, *Fuel emulsions and microemulsions based on Fischer-Tropsch diesel*, Colloids and Surfaces A: Physicochemical and Engineering Aspects; 354 (1–3): 91–98, **2010**.
- [40] A.M.K. Jr. A. Rothrock, A. W. Jones, NACA Report No. 756, **1943**.
- [41] I. Cornet, W. E. Nero, *Emulsified Fuels*, Compression Ignition Engines, 2133-2141, **1955**.
- [42] A. I. Feuerman, A. I., *Gasoline-water emulsion*, Patent Nr.: US4158551(US19750544145 19750127), **1979**.
- [43] A. Velji, E. Eichel, W. Remmels, F. Haug, *Dieselmotoren erfüllen mit Wassereinspritzung zukuenftige NOx - und Russgrenzwerte*, MTZ 57, Nr. 7/8, **1996**.
- [44] U. Mathis et al., *Influence of Diesel Engine Combustion Parameters on Primary Soot Particle Diameter*, 1887-1892, **2005**.
- [45] F. Barnaud, P. Schmelzle, P. Schulz, *Aquazole™: An Original Emulsified Water-Diesel Fuel for Heavy-Duty Applications*, SAE Technical Paper, **2000**.
- [46] F. McCoy, G. Eckert, *Process of Preparing Novel Microemulsions*, US3876391, **1975**.
- [47] A. Schwab, *Diesel Fuel-Aqueous Alcohol Microemulsion*, US4451265, **1984**.
- [48] A. Schwab, E. Pryde, *Microemulsions from vegetable oil and aqueous alcohol with trialkylamine surfactant as alternative fuel for diesel engines*, Patent Nr.: US4451267, **1984**.
- [49] A. Schwab, E. Pryde, *Microemulsions from vegetable oil and aqueous alcohol with 1-butanol surfactant as alternative fuel for diesel engines*, Patent Nr.: US4526586, **1985**.
- [50] A. Schwab, E. Pryde, *Microemulsions from vegetable oil and lower alcohol with octanol surfactant as alternative fuel for diesel engines*, Patent Nr.: US4557734, **1985**.
- [51] E. A. Hazbun, S. G. Schon, R. A. Grey, *Microemulsion fuel system*, Patent Nr.: US4744796, **1988**.
- [52] M. W. David, *Water-in-Oil Microemulsions*, **2007**.
- [53] A. Nawrath, *Schadstoffarme und Effiziente Verbrennung von Kraftstoffen in Form von Mikroemulsionen*, Cuviller Verlag, Göttingen: Köln, **2007**.
- [54] K. Rottländer, *Dissertaion: Mikroemulsionen mit ionischen Tensiden als alternative Kraftstoffe*, **2007**.
- [55] A. Nawrath, T. Sottmann, R. Strey, *Mikroemulsionen und deren Verwendung als Kraftstoff*, DE10334897A1, **2003**.
- [56] L. Bemert, *Microemulsionen als alternative Kraftstoffe*, Köln: cuvillier Verlag Göttingen. ISBN: 978-3-86955-054-1, **2008**.
- [57] Lif A, Holmberg K, *Water-in-diesel emulsionsand related systems*, Adv Colloid Interface Sci.;123-126:231-9, **2006**.



- [58] A. Lif, M. Skoglundh, S. Gjirja, I. Denbratt, *Reduction of Soot Emissions from a Direct Injection Diesel Engine using Water-in-Diesel Emulsion and Microemulsion Fuels*, SAE Technical Paper 2007-01-1076, **2007**.
- [59] A. Lif, *Water-in-diesel emulsion and microemulsion fuels -The effect of water on emission levels*, Licentiatuppsatser vid Institutionen för kemi- och bioteknik, Chalmers tekniska högskola, ISSN 1652-943X, **2008**.
- [60] P. Wulff, *On the Phase Behavior, Structure and Emissions of Water-Fuel Microemulsions*, Köln: cuvillier Verlag Göttingen. ISBN: 978-3-86955-890-5, **2011**.
- [61] L. Menger, *Optimierung von wasserhaltigen Kraftstoffen und deren Emissionsbewertung unter realitätsnahen Bedingungen*, Köln: Verlag Dr. Hut München. ISBN: 978-3-8439-1330-0, **2013**.
- [62] *Rheinbahn testet neuen Kraftstoff-Mit Wasser-Diesel gut fahren*, <http://www.rp-online.de/nrw/staedte/duesseldorf/mit-wasser-diesel-gut-fahren-aid-1.1111331>, **2014**.
- [63] Fuel Water Emulsion, <http://de.mandieselturbo-greentechnology.com/0000509/Technologien/Sekund%C3%A4re-Ma%C3%9Fnahmen/Fuel-Water-Emulsion.html>, **2014**.
- [64] Fuel Emulsions International, <http://www.fuelemulsions.com/>, **2014**.
- [65] Emulsion Fuel System Technology, <http://www.nonoxltd.com/>, **2014**.
- [66] M. Kahlweit, R. Strey, *Phase-Behavior of Ternary-Systems of the Type H₂O-Oil-Nonionic Amphiphile (Microemulsions)*, Angew. Chem. Int. Ed., 24 (8): 654, **1985**.
- [67] R. Strey, *Microemulsion microstructure and interfacial curvature*, Colloid & Polymer Science; 272: 1005-1019, **1994**.
- [68] J. H. Schulman, T.P. Hoar, *Transparent water-in-oil dispersion: the oleophobic hydro-micelle*, Nature Reviews Microbiology; 152 (2); **1943**.
- [69] P. A. Winsor, *Solvent properties of amphiphilic compounds*, Butterworth Scientific Publications; **1954**.
- [70] D. Oc. Shah, R. S. Schechter, *Improved oil recovery by surfactant and polymer flooding*, American Institute of Chemical Engineers, Academic Press, ISBN: 0126417504, **1977**.
- [71] M. J. Lawrence, G. D. Rees, *Microemulsion-based media as novel drug delivery systems*, Advanced Drug Delivery Reviews 45: 89–121, **2000**.
- [72] A. Kogan, N. Garti, *Microemulsions as transdermal drug delivery vehicles*, Advances in Colloid and Interface Science 123-126, 369-385, **2006**.
- [73] E. E. Linn, M. P. West, *Water-in-oil microemulsions for cosmetic uses*, Patent US 4797272 A, **1989**.
- [74] T.F. Tadros, *Future developments in cosmetic formulations*, International Journal of Cosmetic Science, 14 (3): 93–111, **1992**.
- [75] N. Azemar, C. Solans, H. Kunieda, *The Role of Microemulsions, Detergency Processes*, Marcel Dekker Inc.; 66: 375-378, **1997**.
- [76] M.-J. Schwuger, K. Stickdorn, R. Schomaecker, *Microemulsions in Technical Processes*, Chem. Rev.; 95 (4): 849–864, **1995**.
- [77] A. Müller, *Preparation of Polymer Nano-Foams: Templates, Challenges and Kinetics*, Köln, Disseratation, **2013**.



- [78] E. Barni, P. Savarino, G. Viscardi, R. Carpignano, G. Di Modica, *Microemulsions and their potential application in dyeing processes*, Journal of Dispersion Science and Technology; 12 (3-4): 257-271, **1991**.
- [79] J. Flanagan, H. Singh, *Microemulsions: A Potential Delivery System for Bioactives in Food*, Critical Reviews in Food Science and Nutrition, 46: 221–237, **2006**.
- [80] F. Chen, Y. Wang, F. Zheng, Y. Wu, W. Liang, *Studies on cloud point of agrochemical microemulsions*, Colloids and Surfaces A: Physicochemical and Engineering Aspects; 175 (1–2): 257-262, **2000**.
- [81] B. H. Robinson, T. F. Towey, S. Zourab, A.J.W.G. Visser, A. van Hoek, *Characterisation of cadmium sulphide colloids in reverse micelles*, Colloids and Surfaces; 61: 175–188, **1991**.
- [82] A.P. Full, E. W. Kaler, J. Arellano, J. E. Puig, *Microemulsion Polymerization of Styrene: The Effect of Salt and Structure*, Macromolecules; 29 (8): 2764–2775, **1996**.
- [83] R. A. Mackay, S. A. Myers, L. Bodalbhai, A. Brajter-Toth, *Microemulsion structure and its effect on electrochemical reactions*, Anal. Chem.; 62 (10): 1084–1090, **1990**.
- [84] H. Saito, K. Shinoda, *The solubilization of hydrocarbons in aqueous solutions of nonionic surfactants*, J. Colloid & Interface Sci., 24 (10), **1967**.
- [85] M. Kahlweit, R. Strey and G. Busse, *Microemulsions - a Qualitative Thermodynamic Approach*, J. Phys. Chem., 94 (10), 3881, **1990**.
- [86] A. Klemmer, unpublished dissertation at the University of Cologne, **2014**.
- [87] R. Strey, W. Jahn, G. Porte, P. Bassereau, *Freeze-Fracture Electron-Microscopy of Dilute Lamellar and Anomalous Isotropic (L3) Phases*, Langmuir, 6 (11): 1635, **1990**.
- [88] W. C. Griffin, *Classification of Surface Active Agents by HLB*, J. Soc. Cosmet. Chem. 1: 311-326, **1949**.
- [89] S. Burauer, T. Sachert, T. Sottmann, R. Strey, *On microemulsion phase behavior and the monomeric solubility of surfactant*, Physical Chemistry Chemical Physics, 1(18): 4299-4306, **1999**.
- [90] S. Schetzberg, *Progress and first milestones in formulating food-grade microemulsions*, **2009**.
- [91] M. Kahlweit, R. Strey, P. Firman, D. Haase, J. Jen, R. Schomacker, *General Patterns of the Phase-Behavior of Mixtures of H₂O, Nonpolar-Solvents, Amphiphiles, and Electrolytes*, I. Langmuir, 4 (3), 499, **1988**.
- [92] B. Jakobs, T. Sottmann, R. Strey, J. Allgaier, L. Willner, D. Richter, *Amphiphilic Block Copolymers as Efficiency Boosters for Microemulsions*, Langmuir 15, 6707, **1999**.
- [93] H. Endo, J. Allgaier, G. Gompper, B. Jakobs, M. Monkenbusch, D. Richter, T. Sottmann, R. Strey, *Membrane decoration by amphiphilic block copolymers in bicontinuous microemulsions*, Phys. Rev. Lett., 85 (1), 102, **2000**.
- [94] B. Jakobs, T. Sottmann, R. Strey, *Efficiency boosting with amphiphilic block copolymers - a new approach to microemulsion formulation*, Tenside Surfact. Det., 37 (6), **2000**.
- [95] M. Kahlweit, R. Strey, *Phase behavior of Quinary Systems - Tracing the 3-Phase Body*, Journal of Physical Chemistry, 91 (6): 1553-1557, **1987**.



- [96] L. Bemert, H. Doerksen, C. Simon, R. Strey, *A method for in-situ production of water fuel mixtures in internal combustion engines*, DE102009048223 A1, **2011**.
- [97] L.G.A. Kramer, Überkritische CO₂-Mikroemulsionen als Vorstufen für Nanoschäume - Darstellung, Charakterisierung und Nanostruktur, Universität zu Köln, Dissertation, URN: urn:nbn:de:hbz:38-24319, **2008**.
- [98] T. Sottmann, R. Strey, *Evidence of corresponding states in ternary microemulsions of water - alkane - C₁₂E₆*, Journal of Physics-Condensed Matter, 8 (25A), A39, **1996**.
- [99] T. Sottmann, R. Strey, *Microemulsions*, in Fundamentals of Interface and Colloid Science; V, J. Lyklema, Academic Press, London, **2005**.
- [100] M. Kahlweit, R. Strey, G. Busse, *Effect of Alcohols on the Phase-Behavior of Microemulsions*, Journal of Physical Chemistry, 95(13): 5344-5352, **1991**.
- [101] R. Strey, M. Jonstromer, *Role of Medium-Chain Alcohols in the Interfacial Films Of Nonionic Microemulsions*, Journal of Physical Chemistry, 96 (11): 4537-4542, **1992**.
- [102] M. H. G. M. Penders, R. Strey, *Phase-Behavior of the Quaternary System H₂O/n-Octane/C(8)E(5)/n-Octanol - Role of the Alcohol in Microemulsions*, Journal of Physical Chemistry, 99 (25): 10313-10318, **1995**.
- [103] S. Mugra, M. M., B. W. Ninham, *Hofmeister Effects in cationic microemulsion*, Current Opinion in Colloid and Interface Science, (9): 102-106, **2004**.
- [104] P. Firman, D. Haase, J. Jen, M. Kahlweit, R. Strey, *On the Effect of Electrolytes on the Mutual Solubility between H₂O and Nonionic Amphiphiles*, Langmuir 1 (6): 718-714, **1985**.
- [105] W. Helfrich, *Elastic Properties of Lipid Bilayers - Theory and Possible Experiments*, Zeitschrift für Naturforschung C-a Journal of Biosciences, C28(11-1): 693-703, **1973**.
- [106] O. Y. Zhongcan, W. Helfrich, *Bending Energy of Vesicle Membranes - General Expressions for the 1st, 2nd, and 3rd Variation of the Shape Energy and Applications to Spheres and Cylinders*, Physical Review A, 39(10): 5280-5288, **1989**.
- [107] D. F. Evans, H. Wennerstrom, *The Colloidal Domain*, VCH Publishers, New York, **1994**.
- [108] T. Foster, *Microemulsions as compartmentalised reaction media: structural characterisation of water-in-oil microemulsions*, Cuvillier Verlag Göttingen, Köln, ISBN 978-3-86727-115-8, **2007**.
- [109] T. Sottmann, R. Strey, *Microemulsions*, in *Fundamentals of Interface and Colloid Science*, Volume V, J. Lyklema, Academic Press, London, **2005**.
- [110] J. N. Israelachvili, D. J. Mitchell, *A model for the packing of lipids in bilayer membranes*, Biochim. Biophys. Acta, 389 (1): 13, **1975**.
- [111] J. N. Israelachvili, D. J. Mitchell, B.W. Ninham, *Theory of self-assembly of hydrocarbon amphiphiles into micelles and bilayers*, Chem. Soc., Faraday Trans. 2 (72): 1525-1568, **1976**.
- [112] W. D. Bancroft, *The Theory of Emulsification*, The Journal of Physical Chemistry, ACS Publications, **1913**.
- [113] H.-D. Dörfler, *Grenzflächen- und Kolloidchemie*, VCH, Weinheim: 198, **1994**.
- [114] C. Solans, J. ESquena, A. M. Forgiarini, N. Ulson, D. Morales, P. Izquierdo, N. Azemar, M.J. Garcia-Celma, *Nanoemulsions: Formation, properties and Application*,

- in Absorption and Aggregation of Surfactants in Solution*, 109: 525-554, Marcel Dekker, New York, **2003**.
- [115] M. El-Aasser, C. Lack, J. Vanderhoff, F. Fowkes, *The Miniemulsification Process - Different Form of Spontaneous Emulsification*, Colloid Surf. 29; 103, **1988**.
- [116] C. Solans, P. Izquierdo, J. Nolla, N. Azemar, M.J. Garcia-Celma, *Nano-emulsions*, Curr. Opin. Colloid Interface Sci.; 10:102–110, **2005**.
- [117] S. Hoeller, A. Sperger, C. Valenta, *Lecithin based nanoemulsions: A comparative study of the influence of non-ionic surfactants and the cationic phytosphingosine on physicochemical behaviour and skin permeation*, Int. J. Pharm., 370:181–186, **2009**.
- [118] K. Shinoda, H.J. Saito, Colloid Interface Sci. 30: 258, **1969**.
- [119] T. Engels, W. Förster, W. von Rybinski, *The influence of coemulsifier type on the stability of water-in-oil emulsions*, Colloid Surf. A 99 141, **1995**.
- [120] F. Shambil, World Patent WO 89/11907.
- [121] J.L. Salager, *Encyclopedia of Emulsion Technology*, 3, Marcel Dekker, New York; **1988**.
- [122] J.L. Salager, L. Marquez, I. Mira, A. Pena, E. Tyrode, N.B. Zambrano, *Principles of Emulsion Formulation, Engineering Absorption and Aggregation of Surfactants in Solution*; 109(24): 501-524, Marcel Dekker, New York; **2003**.
- [123] B.W. Brooks, H.N. Richmond, M. Zerfa, *Phase Inversion and Drop Formation in Agitated Liquid-Liquid Dispersions in the Presence of Nonionic Surfactants*, in Modern Aspects of Emulsion Science, Cambridge: 175–204; **1998**.
- [124] F. Bouchama, G.A. van Aken, A.J.E. Autin, G.J.M. Koper, *On the mechanism of catastrophic phase inversion in emulsions*, Colloid Surf. A 231(11); **2003**.
- [125] S. Schultz, G. Wagner, K. Urban, J. Ulrich, *High-Pressure Homogenization as a Process for Emulsion Formation*, Chem. Eng. Technol. 27 (4): 361-368, **2004**.
- [126] A. Forgiarini, J. Esquena, J. Gonzalez, C. Solans, *Studies of the relation between phase behavior and emulsification methods with nanoemulsion formation*, Prog. Colloid Polym. Sci. 115:36-39, **2000**.
- [127] K. Shinoda, H. Saito, *The Stability of O/W Type Emulsions as Functions of Temperature and the HLB of Emulsifiers: The Emulsification by PIT- method*, J. Colloid Interface Sci. 30(2): 258-263, **1969**.
- [128] K. Shinoda, H. Saito, *The effect of temperature on the phase equilibria and the types of dispersions of ternary system composed of water, cyclohexane and nonionic surfactant*, J. Colloid Interface Sci. 26:70-71, **1968**.
- [129] K. Shinoda, S. Friberg, *Emulsion and Solubilization*, Journal of Chemical Technology and Biotechnology, 42 (3): 243-244, **1986**.
- [130] P. Heunemann, *Fundamental Research and Functionalisation of Nanoemulsions in respect to Low-Energy Formation Processes*, **2012**.
- [131] P. Fernandez, V. Andre, J. Rieger, A. Kühnle, *Nano-emulsion formation by emulsion phase inversion*, Colloids and Surface A: Physiochem. Eng. Aspects 251: 53-58, **2004**.
- [132] Top, A., BATCON 3. 3/95.
- [133] CONTIN (PCS-1 PACK) VERSION 2DP MAR, **1984**.



- [134] S. W. Provencher, P. Stepanek, *Global analysis of dynamic light scattering autocorrelation functions*, Part. Part. Syst. Char., 13 (5): 291; **1996**.
- [135] P. Pusey, P. Lindner, T. Zemb, *Dynamic Light Scattering, in Neutrons, X-Rays and Light: Scattering Methods Applied to Soft Matter*, Elsevier North-Holland: Amsterdam, ISBN 13: 978-0-444-51122-5, **2002**.
- [136] R. Strey, M. Kahlweit, Kinetics of nucleation in aqueous-solutions investigated with stopped-flow apparatus, Abstracts of Papers of the American Chemical Society, 175 (MAR): 136, **1978**.
- [137] M. Kahlweit, M. Teubner, On the kinetics of micellization in aqueous-solutions, Advances in Colloid and Interface Science, 13 (1-2): 1-64, **1980**.
- [138] E.A.G. Aniansson, S.N. Wall, Kinetics of step-wise micelle association, The Journal of Physical Chemistry, 78(10): 1024-1030, **1974**.
- [139] E.A.G. Aniansson, et al., Theory of the kinetics of micellar equilibria and quantitative interpretation of chemical relaxation studies of micellar solutions of ionic surfactant, The Journal of Physical Chemistry, 80(9): 905-922, **1976**.
- [140] Mollenhauer, Tschöke, *Handbuch Dieselmotoren*, Springer-Verlag Berlin ISBN: 978-3-540-72164-2 ; Neuausgabe **2007**.
- [141] W. Boie, *Vom Brennstoff zum Rauchgas*, Leipzig, Germany, Teubner; **1957**.
- [142] R. Nave, *The Diesel Engine*, HyperPhysics Thermodynamics, hyperphysics.phy-astr.gsu.edu, **2014**.
- [143] T. Su, C. Chang, R. Reitz, P. Farrell, *Effects of Injection Pressure and Nozzle Geometry on Spray SMD and D.I. Emissions*, SAE Technical Paper 952360; **1995**.
- [144] J. Bode, *Zum Kavitationseinfluss auf den Zerfall von Flüssigstrahlen*, Ph.D. Thesis, Max-Planck-Institut für Strömungsforschung, Göttingen; **1991**.
- [145] H. Chaves, M. Knapp, A. Kubitzek, F. Obermeier, *Experimental Study of Cavitation in the Nozzle Hole of Diesel Injectors Using Transparent Nozzles*, SAE Technical Paper 950290; **1995**.
- [146] C. Baumgarten, *Mixture Formation in Internal Combustion Engines*, Heat and Mass Transfers in Sprays, Springer, Berlin, ISBN 3540308350, **2006**.
- [147] G. P. Merker, C. Schwarz, *Grundlagen Verbrennungsmotoren Simulation der Gemischbildung, Verbrennung, Schadstoffbildung und Aufladung*, Vieweg+Teubner, Wiesbaden, ISBN 978-3-8348-0740-3, **2009**.
- [148] M. Pilch, C. A. Erdman, *Use of breakup time data and velocity history data to predict the maximum size of stable fragments for acceleration-induced breakup of a liquid drop*, Int. J. Multiphase Flow; 13 (6), 741; **1987**.
- [149] C. Argachoy, A. P. Pimenta, *Phenomenological model of particulate matter emission from direct injection diesel engines*, Journal of the Brazilian Society of Mechanical Sciences and Engineering, Print version ISSN 1678-5878; **2005**.
- [150] U. Maas, J. Warnatz, R.W. Dibble, *Verbrennung: Physikalisch-Chemische Grundlagen, Modellierungen und Simulation, Experimente, Schadstoffentstehung*; 3., Berlin: Springer, Berlin. ISBN: 3540421289; **2006**.
- [151] J. Warnatz, U. Maas, R. W. Dibble, *Verbrennung*; Berlin: Springer, **2001**.



- [152] C. B. Kweon, *Detailed Chemical Composition and Particle Size Assessment of Diesel Engine Exhaust*, SAE Powertrain & Fluid Systems Conference & Exhibition Technical Papers, San Diego, CA, USA; **2002**.
- [153] U. Alkemade, K. H. Homann, *Formation of C₆H₆ Isomers by Recombination of Propynyl in the System Sodium Vapor Propynylhalide*, Zeitschrift Fur Physikalische Chemie Neue Folge; 161: 19-34; **1989**.
- [154] M. Frenklach, D. Clary, *Aspects of Autocatalytic Reaction-Kinetics*, Industrial & Engineering Chemistry Fundamentals, 22 (4): 433-436; **1983**.
- [155] P. Brookes, M. R. Osborn, *Mutation in mammalian cells by stereoisomers of anti-benzo [a]pyrene-diolepoxide in relation to the extent and nature of the DNA reaction products*, Carinogenesis, 10; **1982**.
- [156] L. I. Pietrasanta, B. L. Smith, M. C. Macleod, *A novel approach for analyzing the structure of DNA modified by benzo[alpha]pyrene diol epoxide at single-molecule resolution*, Chemical Research in Toxicology, 13 (5): 351-355, **2000**.
- [157] J. E. A. Schneider, *Aerosolmassenspektrometrie - Messung verkehrsbedingter Partikelemissionen*, Max-Planck-Institut für Chemie, Mainz, Tätigkeitsbericht; **2006**.
- [158] Ya. B. Zeldovich, *The oxidation of nitrogen in combustion and explosions*, Acta Physicochimica URSS; 21: 577-628; **1946**.
- [159] H. Sinzenich, K. Wehler, R. Müller, *Selective Catalytic Reduction: Exhaust aftertreatment for reducing nitrogen oxide emissions*, http://www.mtu-online.com/fileadmin/fm-dam/mtu-global/technical-info/whitepapers/3100691_MTU_General_WhitePaper_SCR_2014.pdf, **2014**.
- [160] *The Technology of Emission Reduction*, <http://www.aerinox-inc.com/technology/>.
- [161] M. Kahlweit, R. Strey, D. Haase, *Phase-Behavior of Multicomponent Systems Water-Oil-Amphiphile-Electrolyte*, J. Phys. Chem. B, 89 (1), 163, **1985**.
- [162] Hiroyasu H., Arai M., *Empirical Equations for the Sauter Mean Diameter of a Diesel Spray*, SAE Paper 890464, **1989**.
- [163] Siebers D.L., *Liquid-Phase Fuel Penetration in Diesel Sprays*, SAE Paper 980809, **1998**.
- [164] S. Maleknia, *"Efficiency boosting" in einer Wasser-Diesel-Mikroemulsion*, **2010**.
- [165] H. Endo, M. Mihailescu, M. Monkenbusch, J. Allgaier, G. Gompper, D. Richter, B. Jakobs, T. Sottmann, R. Strey, I. Grillo, *Effect of amphiphilic block copolymers on the structure and phase behavior of oil - water - surfactant mixtures*, J. Chem. Phys., 115 (1), 580, **2001**.
- [166] G. Gompper, D. Richter and R. Strey, *Amphiphilic block copolymers in oil-water-surfactant mixtures: efficiency boosting, structure, phase behaviour and mechanism*, Journal of Physics-Condensed Matter, 13 (41), 9055, **2001**.
- [167] G. Gompper, H. Endo, M. Mihailescu, J. Allgaier, M. Monkenbusch, D. Richter, B. Jakobs, T. Sottmann, R. Strey, *Measuring bending rigidity and spatial renormalization in bicontinuous microemulsions*, Europhys. Lett., 56 (5), 683, **2001**.
- [168] EN 590, http://friedel.mivi-solutions.de/main/bsh_friedel_din_en_590_diesel_kraftstoff.pdf, **2014**.



- [169] R. V. Basshuysen, F. Schäfer, *Handbuch Verbrennungsmotoren Grundlagen Komponenten, Systeme, Perspektiven*, Wiesbaden: Vieweg Verlag. ISBN: 3834802271, **2002**.
- [170] C. Weber, *Zum Zerfall eines Flüssigkeitsstrahles*, ZAMM, 11: 136-154; **1931**.
- [171] C. Pfeifer, *Experimentelle Untersuchungen von Einflussfaktoren auf die Selbstzündung von gasförmigen und flüssigen Brennstoffen*, Karlsruhe. ISBN: 18699669, **2010**.
- [172] A. N. Astachow, G. Fitzky, G. Krüger, C. Köster, *Untersuchung der Zerstäubung von, Schwerölen bei Variation der Einspritzbedingungen*, FVV Forschungsbericht, **1996**.
- [173] A. N. Astachow, G. Fitzky, G. Krüger, *Experimentelle Untersuchungen zur Zerstäubung von Dieselkraftstoff und Schweröl*, FVV Forschungsbericht, Nr. 483, **1994**.
- [174] H. Hiroyasu, *Measurement of Spray Characteristics and Fuel Vapor Concentration in a Diesel Spray*, Mechanical Engineering Department, University of Hiroshima.
- [175] M. E. Tat, H. V. Gerpen, *The Kinematic Viscosity of Biodiesel and Its Blends with Diesel Fuel*, American Society for Testing Materials, 76(12): 1511-1513; **1999**.
- [176] A. Ghurri, J. D. Kim, H. G. Kim, J. Y. Jung, K. K. Song, *The effect of injection pressure and fuel viscosity on the spray characteristics of biodiesel blends injected into an atmospheric chamber*, Journal of Mechanical Science and Technology, 26(9): 2941-2947; **2012**.
- [177] L. Siwale, L. Kristof, T. Adam, A. Bereczky, M. Mbarawa, A. Penninger, A. Kolesnikov, *Combustion and emission characteristics of n-butanol/diesel fuel blend in a turbo-charged compression ignition engine*, Fuel, 107: 409-418; **2013**.
- [178] C. H. Wang, K. L. Pan, G. J. Ueng, L. J. Kung, J. Y. Yang, *Burning behaviors of collision-merged water/diesel, methanol/diesel, and water plus methanol/diesel droplets*, Fuel, 106: 204-211; **2013**.
- [179] measured by VKA (RWTH Aachen) during FVV-project, **2013**.
- [180] J. Dernotte, C. Hespel, F. Foucher, S. Houille, C. Mounaim-Rousselle, *Influence of physical fuel properties on the injection rate in a Diesel injector*, Fuel, 96(1): 153-160; **2012**.
- [181] J. Dernotte, C. Hespel, S. Houille, F. Foucher, C. Mounaim-Rousselle, *Influence of Fuel Properties on the Diesel Injection Process in Nonvaporizing Conditions*, Atomization and Sprays, 22(6): 461-492; **2012**.
- [182] H. Seto, M. Nagao, Y. Kawabata, *Pressure-dependence of the bending modulus of surfactant monolayers in ternary microemulsion systems observed by neutron spin echo*, Colloids and Surfaces A: Physicochemical and Engineering Aspects, 284-285: 430-433, **2006**.
- [183] G. E. Totten, S. R. Westbrook, R. J. Shah, *Fuels and Lubricants Handbook: Technology, Properties, Performance, and Testing*, Band 1, **2003**.
- [184] J. K. Percus, G. J. Yevick, *Analysis of Classical Statistical Mechanics by Means of Collective Coordinates*, Physical Review, 110(1): p. 1-13; **1958**.
- [185] M. Teubner, R. Strey, *Origin of the Scattering Peak in Microemulsions*, Journal of Chemical Physics, 87(5): p. 3195-3200; **1987**.
- [186] H. Klemmer, *Amphiphilic Polymers in Microemulsions: The Influence on Structure and Formation Kinetics*, Cuvillier Verlag, ISBN: 978-3-95404-558-7, **2013**.



- [187] Testing of cooling lubricants; DIN 51 360-1, **1985**.
- [188] Sjogren A. Proc of the 16th Symp (Int) on Combustion, MIT, 1976. Pittsburgh, Pa: The Combustion Institute; 297, **1977**.
- [189] P. Dittmann, H. Dörksen, S. Maleknia, FVV-Zwischenbericht, **2013**.
- [190] C. Simon, R. Strey, S. Pischinger, P. Dittmann, H. Dörksen, K. Wormuth, S. Maleknia, *Systematische Untersuchung und Bewertung der Anwendbarkeit von Wasser-Diesel Mikroemulsionen in schnelllaufenden Großdieselmotoren für Bahn- und Marineanwendungen*, FVV Herbsttagung, R560: 197-225, **2012**.
- [191] C. Simon, R. Strey, S. Pischinger, P. Dittmann, H. Dörksen, C. Noll, S. Maleknia, *Systematische Untersuchung und Bewertung der Anwendbarkeit von Wasser-Diesel Mikroemulsionen in schnelllaufenden Großdieselmotoren für Bahn- und Marineanwendungen*, FVV Frühjahrstagung, R566: 105-139, **2014**.
- [192] F. Pischinger, *Motorische Verbrennung*, RWTH Aachen, **2001**.
- [193] E. Wiberg A. F. Holleman, N. Wieberg, *Lehrbuch der Anorganischen Chemie*, de Gruyter, 101; **1995**.
- [194] Kumfer, B. M. and Kennedy, I. M. (2009). *The role of soot in the health effects of inhaled airborne particles*, in: Bockhorn, H., D'Anna, A., Sarofim, A.F., Wang, H. (Eds.), *Combustion Generated Fine Carbonaceous Particles: Proceedings of an International Workshop held in Villa Orlandi, Anacapri*, KIT Scientific Publishing, 1-15, **2007**.
- [195] J.B. Maxwell, L. A. Barrie, *Atmospheric and Climate Change in the Arctic and Antarctic*, AMBIO 18 : 42-49, **1989**.
- [196] R. Lemaire, S. Bejaoui, E. Therssen, *Study of soot formation during the combustion of Diesel, rapeseed methyl ester and their surrogates in turbulent spray flames*, Fuel, 107: 147-161; **2013**.
- [197] T. Ronkko, A. Virtanen, J. Kannosto, J. Keskinen, M. Lappi, L. Pirjola, *Nucleation mode particles with a nonvolatile core in the exhaust of a heavy duty diesel vehicle*, Environmental Science & Technology, 41(18): 6384-6389; **2007**.
- [198] T. Ronkko, A. Virtanen, K. Vaaraslahti, J. Keskinen, L. Pirjola, M. Lappi, *Effect of dilution conditions and driving parameters on nucleation mode particles in diesel exhaust: Laboratory and on-road study*, Atmospheric Environment, 40(16): 2893-2901; **2006**.
- [199] E. M. Hackbarth, W. Merhof, *Verbrennungsmotoren - Prozesse, Betriebsverhalten, Abgas*, Braunschweig, Wiesbaden: Friedrich Vieweg & Sohn Verlagsgesellschaft mbH. ISBN: 3- 528-07431-0, **1998**.
- [200] F. Payri, V. R. Bermudes, B. Tormos, W. G. Linares, *Hydrocarbon emissions speciation in diesel and biodiesel exhausts*, Atmospheric Environment, 43: 1273-1279; **2009**.
- [201] P. Brookes, M. E. Duncan, *Carcinogenic Hydrocarbons and Human Cells in Culture*, Nature, 234(5323): 40; **1971**.
- [202] R. D. Landet, *PM emissions and NOx-reduction due to water in fuel emulsions in marine diesel engines*, 6, **2010**.
- [203] J. W. Park, K. Y. Huh, J. H. Lee, *Reduction of NOx, smoke and brake specific fuel consumption with optimal injection timing and emulsion ratio of water-emulsified*



- diesel*, Proceedings of the Institution of Mechanical Engineers, Part D: Journal of Automobile Engineering 215: 83-9; **2001**.
- [204] J. Park, K. Huh, K.. Park, *Experimental study on the combustion characteristics of emulsified diesel in a rapid compression and expansion mashine*, Proc.Intn Mech.Engrs, Part D, Journal of Automobile Engineering; 214(D5): 579-586, **2000**.
- [205] J.B. Heywood, *Internal combustion engine fundamentals*, New York: McGraw-Hill, **1988**.
- [206] C. E. Roberts, D. Naegeli, C. Chadwell, *The Effect of Water on Soot Formation Chemistry*, SAE paper 2005-01-3850, **2005**.
- [207] *Pallflex filters*, http://www.pall.com/pdfs/Laboratory/02.0601_Pallflex_LR.pdf.
- [208] H. Burtscher, S. Künzel, C. Hüglin, *Characterization of particles in combustion engine exhaust*, Journal of Aerosol Science; 29(4): 389-396, **1998**.
- [209] T. Ishiguro, Y. Takatori, K. Akihama, *Microstructure of diesel soot particles probed by electron microscopy; first observation of inner core and outershell*, Combustion and Flame; 108:231–4, **1997**.
- [210] M. Patel, R. B. Aswath, *Morphology, structure and chemistry of extracted diesel soot: Part II: X-ray adsorption near edge strucure (XANES) sprectroscopy and high resolution transmission electron microscopy*, Tribology International, 52: 17-28, **2012**.
- [211] A. B. Mhadeshwar, *Experimental Study of Carbon Black and Diesel Engine Soot Oxidation Kinetics Using Thermogravimetric Analysis*, Energy & Fuels, 26: 5613-5625, **2012**.
- [212] L. Pahalagedara, H. Sharma, C.-H. Kuo, S. Dharmarathna, A. Joshi, S.L. Suib, A. B. Mhadeshwar, *Structure and Oxidation Acitivity Correlations for Carbon Blcks and Diesel Soot*, Energy Fuels, 26 (11): 6757–6764, **2012**.
- [213] WHO 2003, *Health Aspects of Air Pollution with Particulate Matter, Ozone and Nitrogen Dioxide*, Report on a WHO Working Group, Bonn, Germany, **2003**; http://www.euro.who.int/__data/assets/pdf_file/0005/112199/E79097.pdf.
- [214] R. Strey, *Zur Mikrostruktur von Mikroemulsionen*, Georg-August-Universität: Göttingen, **1992**.
- [215] M. Teubner, R. Strey, *Origin of the Scattering Peak in Microemulsions*, Journal of Chemical Physics, 87(5):3195-3200, **1987**.
- [216] T. Sottmann, R. Strey, S.H. Chen, *A small-angle neutron scattering study of nonionic surfactant molecules at the water-oil interface: Area per molecule, microemulsion domain size, and rigidity*, Journal of Chemical Physics, 106(15): 6483-6491, **1997**.
- [217] K. V. Schubert, R. Strey, S.R. Kline, E.W. Kaler, *Small-Angle Neutron-Scattering near Lifshitz Lines - Transition from Weakly Structured Mixtures to Microemulsions*, Journal of Chemical Physics, 101(6):5343-5355, **1994**.
- [218] T. Sottmann, et al., *A small-angle neutron scattering study of nonionic surfactant molecules at the water-oil interface: Area per molecule, microemulsion domain size, and rigidity*, Journal of Chemical Physics, 106(15): 6483-6491, **1997**.
- [219] M. Kotlarchyk, S. H. Chen, *Analysis of small angle neutron scattering spectra from polydisperse interacting colloids*, AIP. p. 2461-2469, **1983**.

- [220] P. Lindner, T. Zemb, *Neutron, X-Rays and Light. Scattering Methods Applied to soft Condensed Matter*, Amsterdam: Elsevier Science. 552, **2002**.
- [221] Rayleigh, *The incidence of light upon a transparent sphere of dimensions comparable with wave-length*, Proceedings of the Royal Society of London, 84, **1910**.
- [222] M. Schwan, L. Kramer, T. Sottmann, R. Strey, *Phase behaviour of propane- and scCO₂-microemulsions and their prominent role for the recently proposed foaming procedure POSME (Principle of Supercritical Microemulsion Expansion)*, Phys. Chem. Chem. Phys., 12: 6247-6252, **2010**.
- [223] HFRR (High Frequency Reciprocating Rig), <http://www.pcs-instruments.com/hfrr/hfrr.shtml#page=page-1>, **2013**.
- [224] HFRR, <http://de.wikipedia.org/wiki/HFRR>, **2013**.
- [225] MTM (Mini Traction Machine), <http://www.pcs-instruments.com/mtm/mtm.shtml#page=page-1>, **2013**.
- [226] DIN 51 360, Teil 2, *Bestimmung der Korrosionsschutzeigenschaften von wassergemischten Kühlschmierstoffen*, **2013**.
- [227] AVL Smart Sampler, <https://www.avl.com/smart-sampler>, **2013**.
- [228] AVL Opacimeter, <https://www.avl.com/opacimeter>, **2013**.
- [229] AVL Smoke Meter, <https://www.avl.com/smoke-meter>, **2013**.
- [230] Zwischenbericht-FVV, VKA Aachen, *Diesel-Wasser-Mikroemulsionen*, **2013**.
- [231] VKA, Lehrstuhl für Verbrennungskraftmaschinen , RWTH Aachen, *Hochdruckeinspritzkammer*, <http://www.vka.rwth-aachen.de/index.php?id=396>, **2013**.



Erklärung

Ich versichere, dass ich die von mir vorgelegte Dissertation selbständig angefertigt, die benutzten Quellen und Hilfsmittel vollständig angegeben und die Stellen der Arbeit - einschließlich Tabellen, Karten und Abbildungen - die anderen Werken im Wortlaut oder dem Sinn nach entnommen sind, in jedem Einzelfall als Entlehnung kenntlich gemacht habe; dass diese Dissertation noch keiner anderen Fakultät oder Universität zur Prüfung vorgelegen hat; dass sie - abgesehen von unten angegebenen Teilpublikationen - noch nicht veröffentlicht worden ist sowie, dass ich eine solche Veröffentlichung vor Abschluss des Promotionsverfahrens nicht vornehmen werde. Die Bestimmungen der Promotionsordnung sind mir bekannt. Die von mir vorgelegte Dissertation ist von Prof. Dr. R. Strey betreut worden.

Köln, den 28. März 2014

Teilpublikation

C. Simon, R. Strey, S. Pischinger, P. Dittmann, H. Dörksen, K. Wormuth, S. Maleknia, Systematische Untersuchung und Bewertung der Anwendbarkeit von Wasser-Diesel Mikroemulsionen in schnelllaufenden Großdieselmotoren für Bahn- und Marineanwendungen, FVV Herbsttagung, R560: 197-225, **2012**.

C. Simon, R. Strey, S. Pischinger, P. Dittmann, H. Dörksen, C. Noll, S. Maleknia, Systematische Untersuchung und Bewertung der Anwendbarkeit von Wasser-Diesel Mikroemulsionen in schnelllaufenden Großdieselmotoren für Bahn- und Marineanwendungen, FVV Frühjahrstagung, R566: 105-139, **2014**.



Curriculum Vitae

Name: Setareh Maleknia
Born: 17.11.1985 in Teheran (Iran)
E-mail: setareh_m@yahoo.de
Marital status: single

Education

1996-2005 Erich Kästner-Gymnasium Köln:
general qualification for university entrance (Abitur)

University Studies

08/2005-12/2010 Study of *Chemistry* (diploma), University of Cologne, Germany
06/2010-12/2010 Diploma-thesis on the topic: "Efficiency boosting" in einer Wasser-Diesel-Mikroemulsion; advisor Prof. Dr. R. Strey, Institute for Physical Chemistry, University of Cologne, Germany
Since 02/2011 PhD-Thesis: "Green" Microemulsions and Nanoemulsions as Alternative Fuels

Work experience

01/2010-03/2010, Student assistant at the Institute for Physical Chemistry,
06/2010-12/2010 University of Cologne in the department of Prof. Dr. R. Strey
Since 02/2011 Research assistant at the Institute for Physical Chemistry, University of Cologne in the department of Prof. Dr. R. Strey



